Understanding the link between active galactic nuclei and their large scale environment.

RACHEL DOWSETT

Institute for Astronomy
School of Physics

University of Edinburgh
Doctor of Philosophy

October 2005

Abstract

In this thesis I present an analysis of the population of AGN in dense environments, with the aim of determining the number of AGN in galaxy clusters and investigating the effect of extended environment on the AGN. This work uses the new generation of X-ray telescopes to identify and analyse the populations of AGN, specifically focusing on clusters of galaxies.

I have undertaken the first major statistical survey to investigate the prevalence of AGN in a large sample of moderate redshift ($z > 0.1$) galaxy clusters. By comparing the X-ray source population in the fields of 140 galaxy clusters to that found in 44 non-cluster observations, the number of X-ray detected AGN associated with each galaxy cluster is determined statistically. In order to analyse the large number of observations in a fast and uniform manner, I have developed an automated pipeline which detects and evaluates the X-ray point sources in each field. The pipeline also produces a prediction of the number density and radial distribution of sources in each field, based on the non-cluster observations and detailed models of the detector characteristics. The effect of gravitational lensing, which reduces the X-ray source counts by up to 1 source per cluster field, is calculated as a function of radius, and incorporated into the predicted source distribution. I demonstrate that there is a significant population of AGN in galaxy clusters, with an average of ~ 3 AGN per cluster.

In order to evaluate the effect of different cluster environments on the AGN population, and the evolution of cluster AGN, I investigate trends in the excess of point sources as a function of cluster redshift, luminosity and morphology. It is found that low redshift ($z < 0.5$) clusters contain almost no AGN in their central regions, but that a moderate number of AGN are found between 0.5 and 1 Mpc from the cluster centre. By comparison with X-ray sources in the field it is determined that AGN are suppressed in the centres of galaxy clusters, and it is likely that they are triggered on the outskirts of clusters. At higher redshifts there is a significant increase in the number of luminous AGN in galaxy clusters, which is greater than the evolution of field AGN, indicating that the evolution of the AGN population is dependent on the extended environment. The number of AGN in galaxy clusters is found to increase in disturbed clusters, and it appears that the AGN are affected by local galaxy density rather than the properties of the galaxy cluster.

In addition to the large statistical study, I have investigated in detail the number and properties of AGN in the supercluster A901/2 (z=0.17). This supercluster is a highly complex environment, which is highlighted by analysis of the X-ray extended emission. I describe a previously unidentified cluster, A901α, and the properties of extended emission from four other clusters and groups in this region. Using deep X-ray imaging, 17-band photometric data and optical spectroscopy, I identify 11 AGN in the supercluster. Around 5% of bright ($m_R < 20$) supercluster galaxies are found to contain an AGN at this flux limit – for the most part these appear optically to be passive early-type galaxies, and there are significantly more AGN than would be expected from the optical data alone.

Using the positions and colours of over 1000 identified supercluster galaxies, I define the supercluster environments in terms of local galaxy density and local galaxy colour. Compared to other similar galaxies, AGN host galaxies are found to lie in areas of moderate density and slightly higher density with blue local colour (but not in redder environments of the same density), similar to that of groups of galaxies and cluster outskirts. A possible explanation is that AGN activity is triggered by tidal disruption or harassment when a galaxy first joins a dense environment. There is also tentative evidence for a lower X-ray luminosity in AGN in the most cluster-like environments.

Declaration

I declare that this thesis is not substantially the same as any that I have submitted for a degree or diploma or other qualification at any other University. I further state that no part of my thesis has already been or is being concurrently submitted for any such degree, diploma or other qualification.

I declare that I have written and composed this thesis, and that this thesis is the outcome of my own work except where specifically indicated in the text.

Rachel Dowsett
Edinburgh,
October 2005.

Contents

List of Figures

List of Tables

CHAPTER 1

Introduction

One of the key aims of current cosmology and extragalactic astronomy is to understand the formation and evolution of the universe. Observations of galaxies and galaxy clusters, analysis of the Cosmic Microwave Background, and large simulations have all contributed to the current model of the structure of the universe, λCDM. This model includes baryonic matter, dark matter and dark energy, and explains the structure in the universe in terms of hierarchical clustering, where small objects form first, and build up into larger objects. Although this model explains many of the observable properties of the universe there are a number of problems, in particular with predictions for the most massive galaxies, as evidenced by, for example, the number of Extremely Red Objects at $z \sim 1$ (Daddi et al. 2000), and the sharp cut-off at the high-mass end of the galaxy mass function (Benson et al. 2003). One possible solution is to include processes relating to the black hole which lies in the centre of every large galaxy; these processes are currently omitted from most simulations of hierarchical clustering. The strong correlation between the mass of the black hole and that of the galaxy bulge (e.g. Gebhardt et al. 2000, Magorrian et al. 1998) suggests that the growth of the black hole and bulge are closely related, and it is found that including feedback from accretion onto the black hole solves some of the problems with current simulations (Croton et al. 2005b). The main growth phase of the black hole coincides with the appearance of an Active Galactic Nucleus (AGN). At present very little is understood about why some galaxies contain AGN whereas others have no activity. Understanding the processes that trigger or suppress AGN activity will shed light on their role in the evolution of galaxies, galaxy clusters and the structure of the universe.

The aim of this project is to investigate the prevalence and properties of AGN in galaxy clusters, in order to add to our understanding of the processes which can cause AGN activity. In this introduction the background to this study is explained in more detail, in order to

highlight the wider context of this work, and also the reasons for choosing the particular methods that are used in this project.

This introduction is split into the following sections: Section 1.1 provides an overview of the standard model of AGN and the methods of detecting them, focusing on the advantages of X-ray surveys. Section 1.2 explains what is currently known about the evolution and fuelling of AGN, and the possible links between AGN activity and host galaxy properties. In Section 1.3 the discussion is extended to the large scale environment of galaxies, particularly focusing on galaxy clusters and superclusters. The effect of the galaxy cluster on the properties of the constituent galaxies is reviewed, and the mechanisms by which the extended environment could affect AGN are stated. Individual studies examining the external environments of AGN are reviewed in Section 1.4, with a particular focus on those studies which assess the number, properties and position of AGN in galaxy clusters. Finally, in Section 1.5 the aims and basic method of the projects in this thesis are outlined, and the layout of the thesis is described.

Throughout this thesis, the standard λCDM cosmology is used, with H_0=70 km/sec/Mpc, $\Omega_m = 0.3$ and $\Omega_\lambda = 0.7$.

1.1 Active Galactic Nuclei

Active Galactic Nuclei, or AGN, are point-like sources in the centre of galaxies, which emit a large amount radiation at a range of wavelengths. The extreme luminosities, small emission regions, unusual spectra and rapid variability of AGN has led to the conclusion that they are caused by accretion of interstellar gas onto the super-massive black hole which appears to lie at the centre of every galaxy with a stellar bulge (e.g.Gebhardt et al. 2000 and 2001, Magorrian et al. 1998).

1.1.1 The standard model

Understanding the composition of an AGN is complicated by the large range of observed properties found in different AGN. The currently accepted best model is the 'standard model', which attempts to explain many of the differences in terms of the orientation of the AGN and the accretion rate. Many advanced variants of this model have been proposed, which attempt to explain more of the complex properties of AGN.

In the standard model, material accretes onto the black hole through an optically thick accretion disk, which radiates black body emission, peaking in the ultraviolet. X-ray emission is produced through various processes in the region of the disk (see Section 1.1.3). Optical line emission is caused by the reprocessing of the disk radiation in clouds of gas surrounding the black hole – narrow lines from clouds in the outer regions and Doppler-broadened lines from the inner (broad-line) regions. The broad-line region and accretion

disk may be fully or partially obscured by dusty material (often referred to as a torus) surrounding the black hole. Radiation may also be produced in a jet of particles, emitted perpendicular to the accretion disk, which can also be the source of radio emission.

The maximum emission from an accreting source is given by the Eddington limit. At this point, the outward pressure on electrons from the emitted radiation balances with the inward gravitational force on a proton, and if radial symmetry is assumed then $L_{edd} = 1.4 \times 10^{38}(M/M\odot)$ Watts. However, most AGN are emitting at substantially less that the Eddington limit.

1.1.2 Optical characteristics

A full discussion of the many optical characteristics of AGN is beyond the scope of this introduction. Instead this section focuses on those characteristics which enable the optical identification of AGN.

The range of optical luminosities and spectral properties of AGN have given rise to many categories, which are generally broad and overlap to some extent. Quasars, or QSOs, are the most luminous AGN, followed by moderate luminosity Seyfert galaxies and finally LINERS (Low Ionisation Nuclear Emission Regions) – in this thesis all of these are covered by the term AGN. With very few exceptions, spectra are required to optically identify active galactic nuclei. The optical spectra of AGN can broadly be split into two categories, Type I, which contain both broad and narrow emission lines, and a point-like non-stellar continuum, and Type II, which only show narrow lines. Type II AGN are presumed to have their central regions obscured by a dusty torus, and at Seyfert luminosities they outnumber the Type I galaxies by at least $\sim 2:1$ (e.g. Huchra and Burg 1992, depending on the selection criteria). An intermediate population of Type 1.5-1.9 galaxies also exists, with weak (partially absorbed) broad lines and strong narrow lines.

As well as the partially obscured Type II galaxies, a significant population of AGN are largely or completely optically obscured due to absorption of the nuclear emission by large amounts of gas and dust (see for example Martini et al. 2002, and Gandhi et al. 2004). In this case very few optical photons escape, and the spectrum even lacks narrow line emission (at the resolution of most data). These AGN can be found by investigating other wavebands, but will be missing from optical studies. The ratio of obscured to unobscured AGN is not well quantified, and depends on the methods used, but it is likely that optically obscured AGN outnumber unobscured AGN by a factor of a few (see for example Martini et al. 2002, and references in Mushotzky, 2004).

The identification of AGN activity is complicated by the spectrum of the galaxy. This makes it hard to identify a weak non-stellar continuum, and, particularly if the galaxy contains significant star formation, the galaxy spectrum may have many of the same emission lines as the AGN. However AGN generally have higher ionisation emission lines (e.g. CIV,

HeII) than star-forming regions, due to the hard UV / X-ray ionising continuum. The ratios of emission lines are very different between AGN and star-forming galaxies, and so combinations of line ratios are the most common method for distinguishing between these two populations. The standard diagnostic lines depend on the rest-frame wavelengths observed - the BPT diagnostic line ratios shown in Figure 1.1 (Baldwin et al. 1981) can be used for low redshift, but at higher redshift the Lamareille et al. (2004) diagnostic diagrams, which use [OII]λ3727, [OIII]λ5007 and $H\beta$ only, are generally more appropriate. All of the methods have some difficulty in distinguishing between faint AGN and star formation, especially for galaxies that contain both star formation and nuclear activity.

Despite the missed populations and confusion with star-formation, optical surveys remain the dominant method of producing large samples of AGN. Surveys investigating the QSO population look for point like objects with unusual colours, and identify the QSOs using spectroscopy. Large samples of fainter AGN are discovered within surveys of galaxies – multi-object spectrographs can produce many galaxy spectra at once and, in addition to the AGN properties, the spectra give the redshift and properties of the host galaxy. Large surveys such as the Sloan Digital Sky Survey (e.g. Stoughton, 2002) and 2dFGRS (e.g. Lewis et al., 2002) have discovered tens of thousands of nearby AGN.

1.1.3 X-ray characteristics

The distinctive X-ray emission from AGN provides another method of identification. In the standard model, hard X-rays are produced through inverse Compton scattering of the blackbody radiation by electrons in a corona above the accretion disk. The rapid variability of the X-ray emission shows that it is predominantly produced above the central regions of the disk (Grupe et al. 2001). Further X-ray emission is produced by reflection of these X-rays by the disk, which gives a reflection spectrum with a peak at $\sim$20keV (e.g.Malzac et al., 1998). The iron line Fe Kα (6.4keV) is also produced within the disk, and is commonly found in deep X-ray spectra (Streblyanska et al. 2005).

This X-ray emission makes up a significant part of the total bolometric luminosity of AGN – between 3% and 20% of all energy is emitted in the X-ray (Ho 1999). In addition, column densities of gas and dust around AGN which would extinguish or significantly reduce the observed optical light have far less effect on the X-ray emission. However, larger column densities ($\sim 10^{23}$ cm^{-2}) can cause absorption of the softer X-rays and, in the extreme case, all the X-ray emission may be absorbed. The X-ray spectrum of unabsorbed AGN can be approximated to first order as a power law (between $\sim$0.5 and $\sim$10keV) of the form $S_\nu \propto \nu^{-\alpha}$, where $\alpha \sim 0.7$. In most observations of AGN the number of X-rays detected is not sufficient to extract a spectrum, so the ratio of hard band (2-8keV) to soft band (0.5-2keV) counts (know as the 'hardness ratio') is generally used to distinguish between X-ray absorbed and unabsorbed AGN.

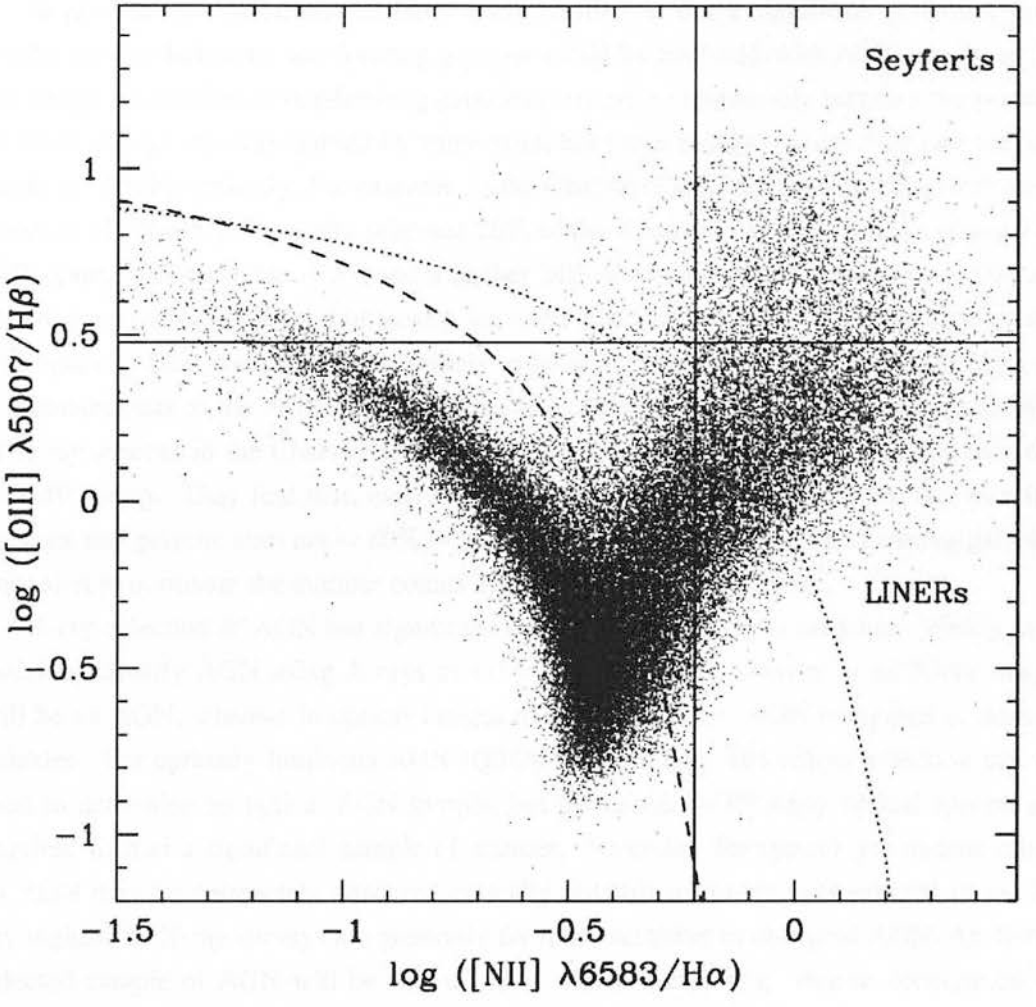

Figure 1.1: The BPT diagnostic diagram for AGN, from Kauffmann et al. (2003). Galaxies below the dashed line are predominantly star-forming, and those above the dotted line are certain AGN. The classification of LINERS and Seyferts depends on the boundaries chosen.

Like optical studies, X-ray surveys have problems distinguishing between star-formation and weak AGN activity, as strong star-formation can produce a similar X-ray luminosity to moderately weak AGN activity. However, this is not a serious problem. Luminous X-ray sources can be securely classified as AGN: a source with $L_{0.5-8\mathrm{keV}} > 3 \times 10^{42}\mathrm{erg/s}$ is extremely unlikely be purely star forming (Bauer et al. 2004), and any source with around $L_{0.5-8\mathrm{keV}} > 1 \times 10^{41}\mathrm{erg/s}$ is likely to be an AGN (see Section 4.5.3). As it is not possible to find a redshift for most AGN, even from deep X-ray data, optical observations are

required, and the ratio between X-ray and optical luminosity can also distinguish between star-formation and AGN activity. Hardness ratios can also be used to separate AGN from star-forming galaxies (Bauer et al. 2004).

In general the contamination from star-formation is not a significant problem; only nearby or very luminous star-forming galaxies could be confused with AGN and, in an X-ray image, the number of star-forming galaxies detected is significantly less than the number of AGN. X-rays are also emitted by some stars, but these are also moderately rare and are easier to identify optically. For example, in the ChaMP (Chandra Multiwavelength Project, Green et al. 2004) the optically brightest 26% of the X-ray sample was found to consist of 72% optically identifiable AGN, and a further 24% for which star-formation would be unable to account for the X-ray luminosity, leaving a maximum of 4% contaminating sources. The optically faint sources are more likely to be at high redshift, so are even less likely to be contaminants to the AGN sample. Bauer et al. (2004) investigate the optical properties of X-ray sources in the Chandra Deep Fields, which are far less X-ray luminous than the ChaMP survey. They find that, even in the soft band, the fractions of AGN, star-forming galaxies and galactic stars are $\sim 80\%$,$\sim 20\%$ and $\sim 1\%$ respectively. Star-forming galaxies only start to dominate the number counts at fluxes $\lesssim 10^{-17}$erg/cm^2/sec.

X-ray selection of AGN has significant advantages over optical selection. Firstly, it is easier to identify AGN using X-rays as the majority of point sources in an X-ray image will be an AGN, whereas in optical images there are very few AGN compared to normal galaxies. For optically luminous AGN (QSOs), morphology and colour selection can be used to determine an optical AGN sample, but for fainter AGN many optical spectra are required to find a significant sample of sources. Secondly, for typical gas-to-dust ratios an AGN may be completely obscured optically but still relatively unattenuated in the X-ray regime, so X-ray surveys are generally far more sensitive to obscured AGN. An X-ray selected sample of AGN will be free of many of the biases (e.g. due to obscuration or observation angle) that are found in optical surveys and will discover far more AGN in any region of sky.

The advantage of detection using X-rays has increased significantly with the advent of the Chandra and XMM-Newton X-ray telescopes, which were both launched in 1999. It is now feasible to conduct large-scale surveys of moderate luminosity AGN using X-rays. Both telescopes are significantly more sensitive than their predecessors, and Chandra in particular has excellent spatial resolution, allowing unique optical counterparts to be found for many sources. The characteristics X-ray detectors in general and these telescopes in particular are described in Appendices A.2, A.3 and A.4. A moderate exposure X-ray image with Chandra can easily reach 400 sources deg^{-2} (and the Chandra deep fields reach $\sim$ 7000 sources deg^{-2} Bauer et al. 2004) , whereas the maximum density for optically selected AGN is $\sim$150 deg^{-2} (Palunas et al. 2000).

1.1.4 AGN at other wavelengths

Studies of AGN at other wavelengths, particularly radio and infrared, have yielded interesting results. However, only about 10% of optically detected AGN have luminous radio emission, and the sample selected depends heavily on the frequency of the survey. As the distinction between radio-loud and radio-quiet AGN is not yet fully understood, the subsample of accreting black holes selected by radio detection cannot be assumed to represent AGN in general. Infrared detection can be used to find AGN, but dusty and starburst galaxies also have significant infrared emission. Infrared colour selection can be used to separate these samples to some extent, but finding a good sample of AGN is difficult (see Mushotzky 2004 for details of radio and infrared selected AGN).

1.2 Fuelling and triggering AGN

1.2.1 The evolution of AGN

The mass of the black hole is closely related to that of the galaxy bulge (e.g. Magorrian et al., 1998), which may indicate a significant link between the evolution of the black hole and the host galaxy. It is perhaps unsurprising that there is some relation between the black hole and the galaxy in which it grows, but the tightness of the correlation is surprising: it appears that black holes are not merely products of the evolution of galaxies, but rather that feedback from AGN has a large effect on galaxy properties and even the properties of galaxy clusters. The most massive galaxies, which typically reside in the centres of galaxy clusters, contain mostly old stars, whereas simple λCDM models predict that the most massive galaxies should be forming at the most recent times, and consequently contain younger stars. One possible explanation is the truncation of star-formation by feedback from AGN outflows (e.g. Silk and Rees 1998, Fabian 1999). Recent semi-analytic models of galaxy formation by Croton et al. (2005b) have shown that if both black hole formation and feedback through AGN outflows are included, then the models can reproduce the star-formation history of massive galaxies. Including feedback from AGN can also explain why there are far less massive galaxies in the universe than predicted by previous models. In addition, AGN feedback is a possible explanation for the lack of cool gas in the cores of galaxy clusters (Fabian et al. 2001): it has been suggested that the interaction between the jets from powerful AGN in the centre of the cluster and the intra-cluster medium might regulate the cooling of the gas and explain the "cooling flow problem" (e.g. Sakelliou et al. 2002, Voit and Donahue 2005 and Pizzolato and Soker 2005).

Recently much work has gone into studying the evolution of black holes and the galaxy population (e.g. McLure and Dunlop 2002). Observational studies are mostly limited to investigating AGN, as they are the only visible evidence for most black holes. In addition,

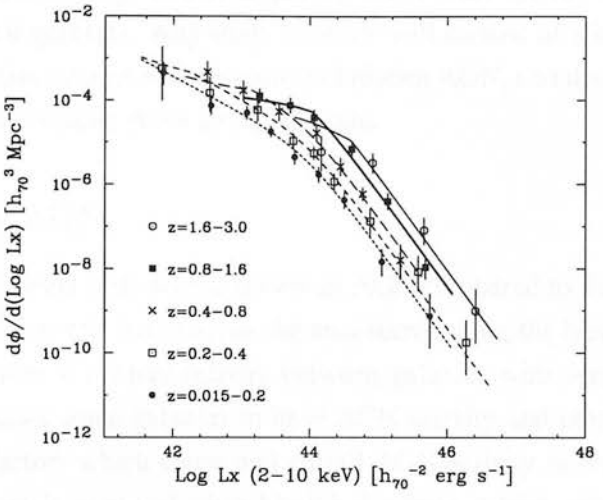

Figure 1.2: The intrinsic 2-10keV luminosity function and best fit LDDE model from Ueda et al. (2003). Low luminosity AGN peak at $z \sim 1$, whereas high luminosity AGN continue to rise above $z = 2$.

AGN are particularly useful as their accretion rates trace the growth of the black holes. In the X-ray it is found that the luminosity function can be well fitted by two power laws, with a break at a characteristic luminosity, $L_X{}^*$, above which the number of sources drops off sharply. Locally, $L_X{}^* \sim 10^{44}$ erg s^{-1}, but this evolves considerably with redshift. The evolution of the luminosity function is best described by a luminosity-dependent density evolution (LDDE) model, such as that found by Ueda et al. (2003), and shown in Figure 1.2. The distribution of intermediate luminosity ($L_X = 10^{42-44}$ erg s^{-1}) sources peaks at z $\sim$ 1, but the number density of broad line AGN, and that of high luminosity X-ray sources (which broadly cover the same population), peaks at a far higher redshift (Cowie et al. 2003). The observed luminosity function evolution of AGN is consistent with the current masses of supermassive black holes (within the uncertainties in accretion efficiency, Barger et al. 2001), and shows that the vast majority of AGN activity in massive galaxies, and hence black hole formation, occurred before z$\sim$1. In addition, the correlation between the local black hole mass function and the AGN luminosity function indicates that the majority of black hole growth must have taken place by luminous accretion.

Although the fraction of galaxies in the local universe containing luminous AGN is small (bright optical AGN were found in 1.3% of galaxies in the CfA redshift survey by Huchra and Burg, 1992), it is by no means true that there is no AGN activity at the current epoch. Luminous AGN are the top end of a continuum, which is dominated by low luminosity AGN (LLAGN) (e.g. Ho et al., 1997), and the proportion of galaxies hosting fainter AGN is far larger; in the local universe over a third of all galaxies have optically detectable LLAGN, and almost half of all galaxies appear to have AGN-like narrow emission lines

(Ho et al. 1997a). In the X-ray, Lira et al. (2000) found faint nuclear emission in the centre of $\sim$ 35% of local galaxies. Any study of AGN will consist of a balance between the higher number densities (at a given luminosity) of distant AGN, and the increase in flux and resolution available for nearby AGN and their hosts.

1.2.2 Fuelling AGN

Although it takes relatively little fuel to power an AGN compared to the galaxy mass, very little is known about how this fuel reaches the area surrounding the black hole. In the local universe, the difference in nuclear activity between galaxies with very similar properties is striking. What causes some galaxies to have AGN activity and others to be quiescent? Understanding the factors which cause and curtail AGN activity in the moderate redshift universe will help explain how and when black holes form at high redshift, and shed light on the interplay between AGN and their host galaxies.

The key problem in fuelling an AGN is not the quantity of fuel required, which is typically $\lesssim 10^{-2} M\odot$/yr for a moderate luminosity AGN[1](Ho et al. 1997a), but rather the angular momentum of the fuel. If the source of fuel is at a few kpc then the angular momentum must be reduced by a factor of 10^4 to reach the accretion disk. A range of factors, from stellar bars in the host galaxy (Shlosman et al. 1989) to mergers between galaxies (e.g Sánchez et al. 2005 and references therein, but see Grogin et al. 2005 for an example of a counter example), could cause AGN activity. These properties can broadly be divided into those internal to the host galaxy, and those due to the extra-galactic environment (from close interactions to galaxy clusters). Care needs to be taken when distinguishing between these as if the large scale environment affects the AGN it is also likely to affect the properties of the host galaxy. In addition the feedback from the AGN to the host galaxy and large scale environment complicate the system, although for moderate AGN these effects are expected to be minimal. Disentangling the interactions between AGN, galaxies and large-scale environment is a highly complex problem.

1.2.3 Linking AGN activity to host galaxy properties

Many large or moderate samples of AGN hosts have been published recently, and have confirmed results from smaller samples and revealed properties of AGN host galaxies. The results presented here are from four surveys, but the conclusions are backed by many more.

The analysis by Kauffmann et al. (2003) of over 22,000 optically selected narrow-line AGN from the Sloan Digital Sky Survey (SDSS) confirms that AGN are preferentially found

[1]Although in some models, such as convection-dominated accretion flows (Narayan et al. 2000), much of the fuel in the accretion disk is not accreted due to turbulence, so the fuel accretion rate may need to be much higher.

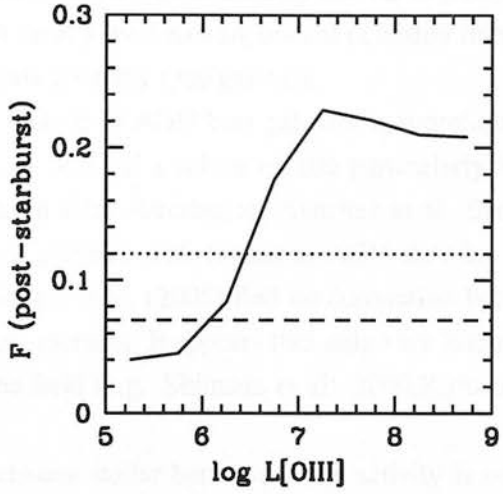

Figure 1.3: The fraction of AGN with higher than normal Hδ absorption lines, indicating a post-starburst systems from Kauffmann et al. (2003). The fraction of normal massive galaxies (dashed line) and normal massive galaxies with young stars (dotted line) are also plotted. The [OIII] line luminosity is used to measure the AGN strength. An unusually high fraction of post-starburst galaxies contain luminous AGN.

in massive galaxies. Over 50% of galaxies in the SDSS with stellar masses of $\sim 10^{11} M_{\odot}$ have optically detected AGN, compared to $< 5\%$ of galaxies of $10^{9} M_{\odot}$. This is similar to the results from Ho et al. (1997a), and as both of these values are for low redshift ($z < 0.1$) samples the typical nuclear luminosity of AGN must rise considerably towards the epoch of highest AGN activity.

The observational evidence implies a strong connection between AGN, host galaxy morphology and star-forming activity. The host galaxies of the Kauffmann et al. AGN are generally early-type (bulge dominated) galaxies. These have very similar properties to the non-AGN early-types, with one striking difference; for high luminosity AGN the average stellar age is far younger than expected, indicating that these systems have been through a period of recent star-formation (see Figure 1.3). The star-formation is spread throughout the galaxy rather than concentrated around the AGN. In addition, the same result is found for broad-line AGN. Miller et al. (2003) also investigate AGN in the SDSS, and conclude that the presence of an AGN is dependent only on the bulge component of a galaxy, and does not depend on the presence of a disk.

At higher redshift, the GEMS (Galaxy Evolution from Morphology and SEDs) sample of optically selected (mostly broad-line) AGN at $0.5 < z < 1.1$ is also dominated ($\sim 80\%$) by early-type hosts (Sánchez et al. 2004). Again, after subtracting the nuclear emission these early-type galaxies are bluer than similar non-active galaxies, indicating recent star-

formation. In optical follow up of X-ray detected AGN in the ChaMP, Silverman et al. (2005b) have found that X-ray unabsorbed AGN have the same optical colours as SDSS colour-selected quasars, which are dominated by nuclear emission. On the other hand X-ray absorbed AGN, which mostly have narrow optical emission lines, show far redder colours, indicating that their hosts are early type galaxies.

Another common feature of AGN host galaxies is morphological disturbance. Kauffmann et al. find that $\sim$ 30% of a subset of 100 particularly luminous AGN have close companions or significant tidal disturbance. Sánchez et al. find the same result at higher redshift, with $\sim$ 1/3 of galaxies with luminous AGN showing evidence for galaxy interactions. In contrast Grogin et al. (2005) find no correlation between moderate luminosity AGN and galaxy-galaxy mergers. It appears that only very luminous AGN have interaction rates higher than in the field (e.g. Shimada et al. 2000,Kirhakos et al. 1999 and Disney et al. 1995).

The correlation between stellar bars and AGN activity is not well defined. Using the Palomar Optical Spectroscopic Survey, Ho et al. (1997b) find that stellar bars increase nuclear star-formation, but have no impact on AGN activity. On the other hand, Maia et al. (2004) find that Seyferts are twice as frequent in barred/merging galaxies than expected. The difference in observation band and bar detection method may explain the apparent discrepancies between studies that link stellar bars and AGN (e.g.Knapen et al. 2000 and Laurikainen et al. 2004) and those that show no link (e.g.Mulchaey and Regan 1997). However, it is clear that not all AGN host galaxies have stellar bars, and not all galaxies with stellar bars have AGN.

A full explanation linking host-galaxy properties and AGN activity is still some way off. At the simplest level, Kauffmann et al. note that bulge-dominated, post-starforming galaxies have both a massive black hole and abundant fuel supply, and so have the ingredients for an AGN. Ho et al. (1997b) suggest that gravitational torques induced by a stellar bar are a possible method of fuelling a black hole without involving a merger or interaction with another galaxy or the extended environment. Gravitational torques from stellar bars can drive material to the inner $\sim$1 kpc of a galaxy. Other methods to further reduce the angular momentum include dynamical friction between clumps of gas, and star-formation which can drive material towards the black hole via, for example, shocks from supernovae. The star-formation may be enhanced by mergers, as well as the additional gravitational turbulence, possibly explaining the link between powerful AGN and galaxy-galaxy interactions. Furthermore, Fabian et al. (1998) suggest that isotropic nuclear star-formation, rather than a dusty torus, may be responsible for obscuring a large number of AGN.

It appears that a strong link exists between nuclear and extended activity in a galaxy, and that star-forming activity in particular causes, or is caused by the same external trigger as AGN activity.

1.3 Galaxies and their large scale environment

1.3.1 Galaxy clusters and superclusters

Any investigation of the effect of large scale environment on AGN is likely to include the effect of galaxy clusters, as they are the densest regions of the universe, and contain around 10% of galaxies at the present epoch. λCDM cosmology predicts that the largest structures in the universe are rarest and form most recently, and this is seen in the distribution of galaxy clusters. At $z > 1$ there are very few known clusters, although there are many protoclusters (which contain galaxy overdensities, but are not yet virialized Rosati et al. 2002). The number and size of clusters increases significantly towards the present epoch, and in the local universe many galaxies reside in over-dense regions (Croton et al. 2005b). Most of these galaxies lie in groups and poor clusters (with less than 50 galaxies) but there is also a large number of Abell class 1 or 2 clusters (with between 50 and 130 galaxies in the central region, Abell 1958). The richest clusters contain thousands of galaxies, and although they are more common in the local universe, they have been found at $z \sim 0.9$ (van Dokkum et al. 1999). The galaxies associated with clusters can extend to ~ 3 Mpc, but the vast majority of the baryonic mass of the cluster is concentrated in the central few hundred kpc, in the form of hot gas (the intra-cluster medium) at a temperature of $\sim 10^7 - 10^8$K (Rosati et al. 2002). The gas is mostly ionised hydrogen, with ~ 0.3 solar metallicity, and it emits strongly in the X-ray via Bremsstrahlung. In the central few hundred kpc this gas may be dense enough to affect the cluster galaxies. The gravitational potential of the cluster is dominated by dark matter, which makes up over 80% of the cluster mass and dominates the large scale gravitational force on the cluster galaxies (e.g. Gray et al. 2002).

Galaxy clusters are useful for cosmological studies and, in addition, for studies of galaxy evolution and that of AGN, because they contain many galaxies at one redshift in a small area of sky, making them ideal for selecting samples of galaxies. In addition, the cluster environment has an effect on the properties of the member galaxies, and on any galaxies joining the cluster. Galaxy clusters are still growing, and at any time will contain a population of galaxies which are joining or have recently joined the cluster, as well as those which have relaxed orbits in the cluster potential. Studies of these galaxies shed light on the processes governing galaxy evolution, the influence of the local and extended environment, and the criteria which determine galaxy activity and morphology.

Mergers of galaxy clusters, or between clusters and groups, are of particular use when investigating the effect of extended environment on galaxy properties, as the gravitational disturbance due to the cluster potential is increased, and the fraction of galaxy-galaxy interactions is also higher. If the extended environment affects AGN activity, then a disturbed environment might be expected to have an even larger effect, and indeed there is some

evidence that AGN activity is enhanced in a cluster-cluster merger (Miller and Owen 2003).

Of perhaps even more use in studies of galaxies and their environments, although comparatively rare, are superclusters of galaxies. These massive structures are made up of many clusters and groups of galaxies, joined together by filaments which also contain galaxies. These are of particular interest as they contain a very large number of galaxies at one redshift, but in a range of environments. It is increasingly clear that the distinction between cluster and field galaxies is over-simplistic, and that galaxy groups and filaments are a key transformation point for galaxies (see details in Section 1.3.2). Whereas images of galaxy clusters can be divided into centres, outskirts and the field (and possibly merging regions), in a supercluster image the distinction can be made between clusters, cluster outskirts, groups, filaments and the field, and the effect of all of the different environments can be evaluated. The scale of environmental effects can also be investigated – for example, the local galaxy density in a group is very similar to that on the outskirts of a cluster, but the large scale environment is very different.

The central galaxy of a cluster is a special case, as it lies in the centre of the potential well, so the environmental effects on this galaxy are therefore very different to those on other cluster members. The galaxy is often far larger than any other cluster galaxy, and is frequently found to have AGN activity – in particular many of the central galaxies are found to be radio-loud (Peres et al. 1998), and this produces feedback into the intra-cluster medium (e.g. Donahue et al. 2005). This provides a clear demonstration of the two-way links between environment and galaxy properties. Studies of the central galaxies are limited in the X-ray, as the emission from the intra-cluster medium obscures all but the most luminous AGN in the central $\sim$ 100 kpc of moderate clusters. The studies in this thesis are based on X-ray data, and concentrate on understanding the AGN activity in the other cluster galaxies.

1.3.2 Properties of cluster galaxies

The impact of the cluster environment on the properties of galaxies has been an area of considerable research over the past decade. This section focuses on the properties of galaxies in clusters, neglecting nuclear activity. These are now moderately well defined, and will have a large effect on the cluster AGN population.

Conclusions have been drawn regarding the activity, colour, star formation history and morphology of cluster galaxies, and how these change with cluster properties, epoch and the galaxy position in the cluster. These results will affect any study of AGN in galaxy clusters in two ways. Firstly, as AGN properties are linked to those of the host galaxies, the number and distribution of AGN in a cluster will depend on the distributions of different galaxy populations. Secondly, it may be that AGN are triggered or suppressed by direct interaction with the cluster environment (such as gravitational instabilities), rather than indirectly

through changes in their host galaxy properties (such as the morphological transformation of the host).

The galaxy colour - density relation: In the local universe, clusters are dominated by red, early-type ellipticals, which have a tight correlation between optical colour and magnitude (the colour-magnitude relation, see for example Bower et al., 1992). The colour-magnitude relation evolves passively out to at least z = 1.27, and it appears that the majority of the stars in these galaxies were formed at $z > 2$ (van Dokkum and Stanford 2003). In the cores of compact clusters (the inner 30% of galaxies), galaxies that are significantly bluer than the colour-magnitude relation are very rare, and spiral galaxies tend to be redder than those in the field. Butcher and Oemler (1984) found that the ratio of spiral to blue galaxies (> 0.2 magnitudes bluer than the B-V colour-magnitude relation) in all clusters is typically 4:1, compared to a field value of 4:3. Whereas the cores of galaxy clusters are dominated by the red population, there are far more blue galaxies found towards the edges of clusters. Recent work has shown that the fraction of blue galaxies is a function of local, rather than extended, galaxy density (Wake et al. 2005), and in particular that the colour of local cluster galaxies does not depend on the optical (De Propris et al. 2004) or X-ray (Wake et al. 2005) properties of the cluster. This distinction between local and extended effects is important when investigating the properties of galaxies in clusters.

Evolution of the fraction of blue galaxies: The question of whether the blue fraction in cluster cores has changed significantly recently, and in particular whether it has evolved faster than in the field, is key to understanding whether the cluster environment has an effect on galaxy properties. At redshifts over 0.1 the fraction of blue galaxies, f_B, within the central regions of both compact and open clusters may increase significantly with distance (Butcher and Oemler 1984). This "Butcher-Oemler effect" states that the average value of f_B increases from ~ 0.03 at z=0.1 to ~ 0.25 at z=0.5, and so these blue galaxies in higher redshift clusters must be the progenitors of some of the local passive cluster members. Such rapid evolution in the local universe is perhaps unlikely and Dressler (1984) explains how a number of selection effects could cause or boost the apparent rise in blue galaxies. De Propris et al. (2003) find evidence that the excess blue galaxies at higher redshift which cause the Butcher-Oemler effect are in fact optically boosted, low mass cluster galaxies, which are undergoing a burst of star-formation before evolving into dwarf galaxies. The large variation in f_B between clusters makes it hard to draw firm conclusions on the evolution of the number of star-forming galaxies.

The star-formation rate - density relation: The dominance of red galaxies in cluster cores, compared to blue galaxies in the cluster outskirts, is due to the change in star-formation between galaxies in these regions. The lack of star formation in cluster cores appears to

hold below z = 1.5 (see for example Couch et al. (2001) and Balogh et al., 2002), in optical, infrared and radio studies. Dressler et al. (1999) found a large number of E+A[2] galaxies in clusters, indicating a recent history of star formation in these galaxies. An important question is whether the radial star formation gradient in clusters is due to accretion of star forming galaxies from the field (which was more active in the past) followed by suppression in the cluster cores, or whether star-formation is enhanced on the cluster outskirts.

Many studies have come to the conclusion that star-formation is suppressed in the cluster cores. Results from the SLOAN (Gómez et al. 2003) and 2dFGRS (Lewis et al. 2002) surveys show that the fraction of star-forming galaxies is significantly higher in the outskirts of the cluster than at the centre. Their results show that the star formation rate is best viewed as a function of local density, rather than clustercentric radius, and is independent of cluster size. If cluster centres are removed from the 2dFGRS sample, the same dependence of activity on local density is seen, leading to the conclusion that star formation is stopped when galaxies are members of in-falling groups or chains of groups (Lewis et al. 2002), rather than triggered in the cluster outskirts. This trend is slightly complicated by the fact that not all galaxies move from less dense to more dense regions – the results may be confused by galaxies which were originally in the core moving towards the outskirts at recent times, as seen in simulations by Balogh et al. (2000). Gray et al. (2004) show that star-formation is suppressed as a function of dark-matter density, and that the fraction of star forming galaxies is slightly lower in the cluster outskirts than in the field. This result is supported by many other studies (see, for example, Gómez et al. (2003) and Balogh et al., 1999)

However, this situation is complicated by the recent discovery by Wolf et al. (2005), that the supercluster A901/2 contains a significant population of dusty star-forming galaxies in areas of medium density, which are not visible either in the field or the cluster cores (see Figure 1.4). Wolf et al. postulate that these are galaxies in the process of transformation from the field to the cluster population, possibly as a result of minor mergers or other effects of the cluster environment, although they could also be mergers between early-type cluster galaxies and smaller galaxies accreted from the field. Either way, the obscured star-formation and dusty nature of these galaxies indicates that there is significant disruption to galaxies in the cluster outskirts.

Galaxy-galaxy mergers: A large fraction of galaxies in high redshift clusters are undergoing mergers (e.g. van Dokkum et al., 2000), and this could also be a trigger of galaxy activity. There is also evidence from field galaxies that interactions between close pairs of galaxies, rather than mergers, cause enhanced star formation rates (e.g. Barton Gille-

[2]E+A galaxies have spectral properties of elliptical galaxies, with the addition of Balmer lines from A-type stars. The short lifetime of A stars shows that these are post-starburst systems.

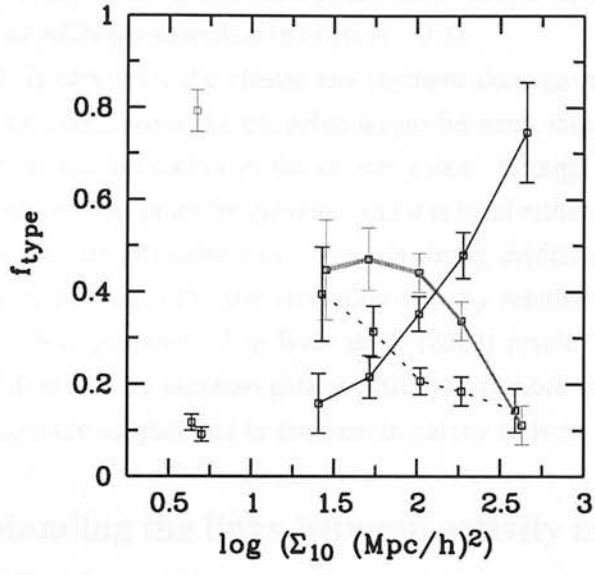

Figure 1.4: The excess of dusty red galaxies found by Wolf et al. (2005). The fraction of blue galaxies (thick grey line) decreases with local galaxy density, and the fraction of dust-free red galaxies increases (thin black line). In contrast, the fraction of dusty red-sequence galaxies (dotted line) peaks at moderate density, and they are rare in both dense and field environments.

spie et al., 2003). Although mergers are not common enough to cause the change in star-formation rate, they may cause other activity, such as AGN.

The morphology-density relation: Another galaxy property which depends strongly on the cluster environment is the morphology. Like the star-formation rate, this is important in the study of AGN in clusters since galaxy morphology and AGN activity appear to be linked, as well as in determining the effect of the environment on galaxies. It is well established that the morphology of galaxies in clusters is strongly dependent on the cluster density. At low redshift, the lowest density clusters are spiral rich, and similar to the field. S0 galaxies dominate in moderate density clusters and the densest clusters are rich in elliptical galaxies (Oemler 1974, Dressler 1980). A study of the rich cluster CL 1358+62 at z=0.33 (van Dokkum et al. 1998) found that star formation in S0 galaxies decreased in the central regions of the cluster. Dressler et al. (1997) found a large decrease in the ratio of cluster S0 to elliptical galaxies with increasing redshift, and a proportional increase in the number of spiral galaxies, up to z=0.5. Later studies confirmed this measurement (see Kodama and Smail 2001 and references therein). The simplest conclusion is the transformation of spiral galaxies into S0s: Kodama and Smail showed that this was feasible, as long as the galaxy accretion rate is high (half of all cluster galaxies accreted since z=0.5) and the majority of spirals become S0. This transformation may be of importance in the fuelling of AGN, as $> 70\%$ of local (e.g Eskridge et al. 2002) and a significant number of more distant

spiral galaxies (e.g. Sheth et al. 2003) have stellar bars, which are a possible method of transporting fuel to an AGN (as described in Section 1.2.3).

In conclusion, it is clear that the cluster environment does have an effect on galaxy properties[3]. The main conclusions are the relationship between morphology and density, and the suppression of star-formation in the cluster cores. Groups and cluster outskirts appear to be the transformation point for galaxies, and it is local rather than extended galaxy density that changes the star-formation rate. There is strong evidence for evolution in the morphology–density relation, but the star-formation–density relation appears to evolve in the same way as for field galaxies. The Wolf et al. (2004) results indicate that regions of moderate galaxy density may increase galaxy activity, but more studies are required to understand what causes the suppression or increase in galaxy activity.

1.3.3 Understanding the links between activity and large scale environment

The physical processes which could affect the galaxy properties in the cluster can be broadly split into three categories; ram-pressure stripping, mergers and close interactions, and suffocation. These processes, together with their possible effects on the galaxy, are outlined below.

- Ram-pressure stripping is when cold gas in the disk of a galaxy is removed when it travels through the intra-cluster medium. Up to 80% of the gas may be removed if a galaxy passes through the core of a very rich cluster (Abadi et al. 1999). Simulations by Quilis et al. (2000) show that massive galaxies, which might be expected to be resistant to loosing their gas due to harassment or suffocation, can have most of their gas removed by ram-pressure stripping in $\sim 10^8$years, far less than the orbital time for a galaxy in a cluster. This is a possible method for truncating star-formation and transforming morphology. A further effect in this category is the evaporation of the intra-galactic medium into the hot intra-cluster medium. However, these effects are only significant in the cores of massive clusters. As the changes in galaxy morphology and activity are seen at large radii, and also in poor clusters and groups, this is unlikely to be the dominant mechanism for the truncation of star formation.

- Mergers and close interactions cause tidal disturbances in galaxies, which tend to draw gas towards the centre of the galaxy, especially in slow encounters such as those in infalling groups of galaxies (Mihos 2004). This can trigger a starburst, which

[3]There is a possibility that the difference between cluster outskirts and cores is due to galaxies that are now at the centre of clusters having formed in different circumstances to galaxies that are now in the field. Bower and Balogh (2004) conclude that this is unlikely given the large spread in halo masses at z=2 that have evolved into present day cluster cores.

can eject significant quantities of gas from smaller galaxies (Martin 1999), thus suppressing star formation. One close encounter, or the cumulative effect of many weak encounters may be enough to suppress star formation throughout the galaxy. The starburst scenario is weakened by the fact that no significant increase in star-formation is seen between the field and cluster outskirts, although this may be obscured by dust (as described in Section 1.3.2). Typical timescales for collisions and harassment induced changes are $\sim 10^8$years (e.g. Barnes (2002) and Iono et al., 2004).

- A third possibility is that the galaxies are "suffocated" by joining the cluster. Hierarchical models of galaxy formation require the gas in the disk to be supplemented from a reservoir in the halo (Cole et al. 2000). Galaxies joining cluster environments may have this gas reservoir partially removed by gravitational forces, suppressing further star formation. The typical timescales for suffocation are $\gtrsim 10^9$years.

The relative influence of the latter two factors depends on the nature of the halo and the ejection power of starbursts, as well as the rate and strength of tidal interactions. The time scales of the star formation suppression (a few gigayears) appears to favour suffocation as the main cause (Balogh et al. 2000), but there is still a large degree of uncertainty as to what causes or suppresses activity in cluster galaxies.

1.4 The environments of AGN

The strong correlation between galaxy properties and local density leads us to expect a similar correlation with AGN activity, as AGN are related to their host galaxies. In addition, the cluster environment may have a direct effect on the AGN activity as well as the indirect effect via changes in the host galaxy properties. The physical processes which may affect galaxy properties in clusters (Section 1.3.3) could also affect AGN activity - either stopping it (possibly by truncating star-formation so that the mechanisms for driving fuel towards the black hole are reduced) or increasing it (by driving fuel directly towards the black hole).

In this section, the major results concerning AGN activity and large scale environment are reviewed. Results from both studies of AGN within galaxy clusters and studies of the clustering of AGN are discussed. The presence of AGN in galaxy clusters is evaluated in different wavebands, and a critique of the results from the latest X-ray studies is presented.

1.4.1 Optical studies

A study to discover the fraction of emission-line galaxies in field and cluster environments was undertaken by Dressler et al. (1984), who analysed optical spectra of the galaxies in 14 rich clusters, and the surrounding fields. On average, 1% of cluster galaxies were identified as AGN, compared to 5% of the field galaxies in the same images. However the sample was

magnitude limited, with more luminous field galaxies than cluster galaxies, which could bias the results (Edge 1992). A further study of 10 clusters out to redshift 0.5 also gave an AGN fraction of $1-2\%$ (Table 7 of Dressler et al., 1999), and this result is independent of redshift. Edge (1992) cross correlated optically bright AGN with clusters at $z < 0.3$ and found the AGN hosts were indistinguishable from the general galaxy population in position and velocity.

The large optical catalogues that have recently been released have allowed more detailed studies of the environment of AGN. Coldwell et al. (2002) compare the Véron-Cetty and Véron (2001) catalogue of bright AGN with $0.1 < z < 0.2$ with the APM optical catalogues[4], and find that the AGN do not lie in dense regions (similar to rich or moderate clusters) or regions with a dominant red galaxy population. When the same AGN sample is compared to the 2dFGRS (Coldwell and Lambas 2003), they are found to lie in areas of higher activity (areas containing a higher fraction of galaxies with emission lines) than a control sample of luminous early-type galaxies. The quasars (defined as $M_B < -23$) are found to have an overdensity of emission line galaxies within $\sim 3h^{-1}$ Mpc, and AGN ($M_B > -23$) have an overdensity within $\sim 1h^{-1}$ Mpc. Kauffmann et al. (2004) investigate the environment of AGN in the SDSS, and find that luminous AGN are twice as likely to occur in galaxies in low-density regions than in similar galaxies in high-density regions, suggesting that AGN activity is suppressed in regions such as galaxy clusters. These results are shown in Figure 1.5.

In contrast, Miller et al. (2003) also use the SDSS, and find that luminous AGN do lie in galaxy clusters, but only at a number proportional to the galaxy density. Using bright AGN with $0.05 < z < 0.1$, selected from the SDSS, they find that the fraction of luminous galaxies with an AGN is independent of local density. The main difference between this sample and the Kauffmann et al. sample is the technique for producing the AGN sample, and it is possible that the difference is due to different luminosity AGN being investigated. The lack of environmental dependence on AGN activity is backed by Wake et al. (2005), who also use the SDSS to show that at $0.05 < z < 0.2$ bright, low redshift AGN have an auto-correlation function consistent with that for galaxies in general. In contrast they find that faint AGN have a higher correlation function, indicating that their host galaxies are more massive. Finally, at higher redshift ($0.8 < z < 2.1$) Porciani et al. (2004) conclude that the clustering amplitude of AGN increases with redshift, probably tracing the increase in AGN in massive galaxies.

In summary, the optical evidence for AGN in galaxy clusters is confused, with different clustering properties for different samples and redshifts, and a possible correlation with regions of high star-formation. The strongest evidence implies that there is no link between AGN and local environment. However, it seems surprising that the probable link between

[4]see http//:www.ast.cam.ac.uk/~apmcat

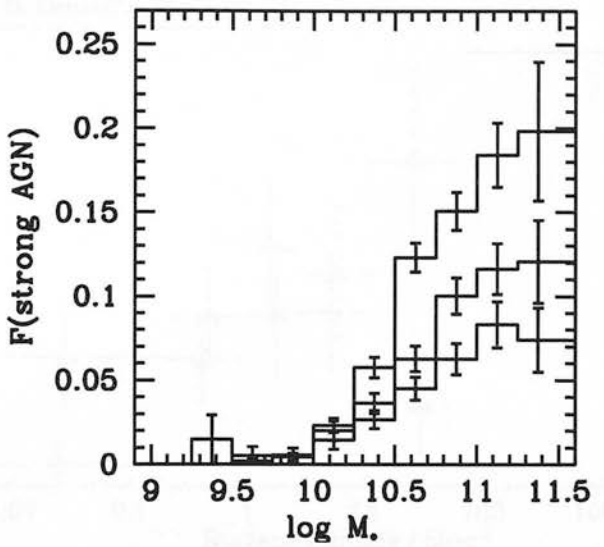

Figure 1.5: The fraction of galaxies containing luminous AGN as a function of host stellar mass, from Kauffmann et al. (2004). The top line is for galaxies in low density environments, followed by medium density and the lowest line is for the densest environments. There is a clear environmental dependence on the number of galaxies hosting AGN.

star-formation and AGN activity, and between star-formation and local density, do not result in a clear correlation between AGN activity and density. Optical samples are incomplete, and particularly prone to missing dust-enshrouded AGN, so the picture may be clearer if other wavebands are investigated.

1.4.2 Radio studies

Radio AGN are not representative of AGN as a whole. However, it is worth mentioning the strong correlations between radio detected AGN and extended environment.

In low redshift ($z < 0.09$), rich clusters Ledlow and Owen (1996) find that the radio properties of cluster galaxies are indistinguishable from those of field galaxies. In contrast, Reddy and Yun (2004) investigate the seven nearest clusters and find that 11% of luminous cluster galaxies are radio loud, compared to 1% in a field sample. This corresponds to 1 or 2 extra radio sources per cluster. At least 70% of these galaxies are AGN (the others are likely to be star-forming), and they are preferentially found towards the centres of the clusters. Best (2004) combines the 2dFGRS with the NVSS (NRAO Very Large Array Sky Survey) to investigate links between radio-loud AGN and galaxy clusters. The AGN show very little correlation with local galaxy density, but a strong correlation with larger scale density, with AGN lying preferentially in moderate groups or poor clusters of galaxies. Best

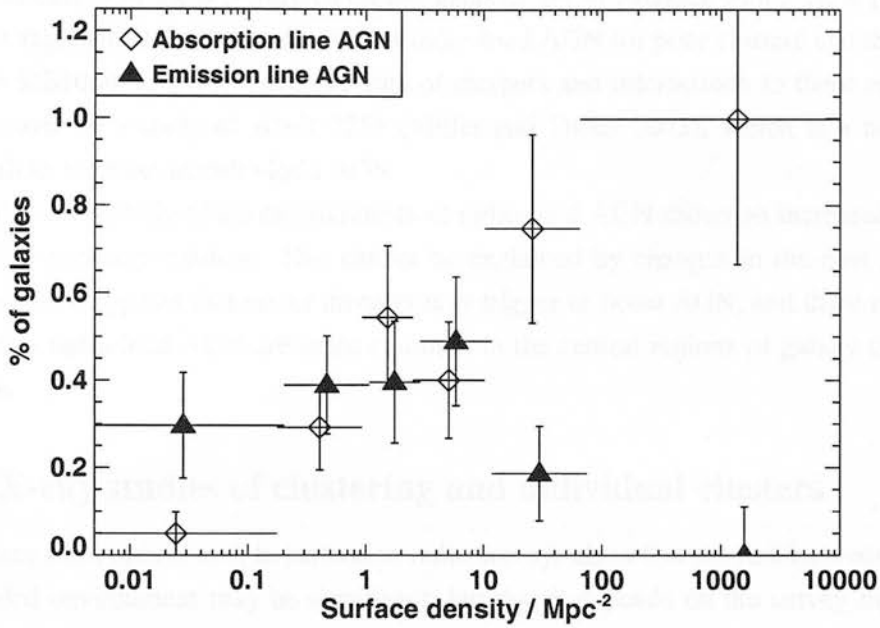

Figure 1.6: The fraction of elliptical galaxies with $M_B < -19$ containing a radio-loud AGN as a function of galaxy density, from Best (2004). The absorption line sources are found in galaxy clusters, whereas the emission line sources are found in less dense regions.

concludes that the AGN activity does not trace the galaxy population (in terms of the bulge size) but rather that it is triggered or boosted by the external environment. In addition, the majority of the AGN in dense environments are optically absorption line sources, so would be missing from optical studies, explaining the disagreement with some of the optical results. Emission-line AGN are found in low and moderate density regions only (see Figure 1.6). Again, the biases in various methods of selecting AGN are highlighted - it is clear that optical selection on line emission can miss many AGN in cluster centres.

At higher redshifts there is further evidence linking cluster galaxies and AGN. Barr et al. (2003) find that around half of their sample of powerful, radio-loud AGN at $z > 0.6$ are associated with galaxy groups or clusters, and that they do not necessarily lie in the central galaxy. There is some evidence for two populations of radio sources in clusters, one high and one lower luminosity (Dwarakanath and Owen 1999), and it appears that the brighter population does not evolve up to z$\sim$0.9 (Stocke et al. 1999 and Barr et al. 2003). Dwarakanath and Owen postulate that the lower luminosity population of AGN may be correlated with the presence of a high fraction of blue galaxies in the cluster, although there is not a direct correlation between the star-forming galaxies and the AGN. This conclusion is backed by the excess of low-luminosity radio sources in the rich, high redshift cluster MS1054-03 (Best et al. 2002), which predominantly lie in the central 1Mpc. This cluster also contains a large fraction of merging galaxies, and although none of the AGN are in

merging systems, 4 of the 8 confirmed cluster galaxies are in galaxies with a close partner. A possible explanation for the preference of radio-loud AGN for poor clusters and the high number in MS1054-03 is the increased rate of mergers and interactions in these regions. This is backed by a study of Abell 2255 (Miller and Owen 2003), which is a merging cluster with an increase in radio-loud AGN.

Virtually every study of the environments of radio-loud AGN shows an increased number of AGN in galaxy clusters. This cannot be explained by changes in the host galaxy population, but it appears that minor mergers may trigger or boost AGN, and there is some evidence that radio-loud AGN are more common in the central regions of galaxy clusters and groups.

1.4.3 X-ray studies of clustering and individual clusters

The evidence from optical and, in particular, radio surveys show that the link between AGN and extended environment may be significant, but that it depends on the survey methods used. X-ray detections of AGN remove many of these uncertainties, providing a larger and less biased sample. However, they are complicated by the presence of the galaxy cluster, which is also a source of X-ray emission.

The first detection of X-ray point sources in a cluster other than Virgo was the discovery that, of eight point sources in the field of A1367, three were X-ray emitting cluster galaxies (Bechtold et al. 1983). Henry and Briel (1991) studied a ROSAT image of A2256 (z=0.06) and found 14 X-ray sources (selected by eye) in part of the field, where only 7 would be expected from a cluster free field. Two of the sources were confirmed to be cluster members, and all have relatively high X-ray luminosities ($\sim 10^{42}$ erg s^{-1}) if they are cluster members. They also found evidence that the source positions were not random, with the excess being found between 70 and 250 kpc from the cluster centre. Lazzati et al. (1998) applied a wavelet analysis technique to improve detection of point sources. They found a significant excess of sources in observations of two nearby clusters, A1367 (z=0.02) and A194 (z=0.0215), compared to that expected from non-cluster observations. Around 20 point sources were found in the central $\sim$ 0.7 Mpc of each field, where less than 9 would be expected from the field alone. All of the sources would have luminosities of less than 10^{42} erg s^{-1} at the cluster redshift, so could be bright starburst galaxies or AGN. A1367 is a rich (Abell class 2) irregular cluster, whereas A194 is poor (Abell class 0), suggesting that AGN or low luminosity AGN (LLAGN) occur in differing cluster environments.

The launch of the Chandra X-ray telescope in 1999 revolutionised the study of AGN in X-rays. The excellent spatial resolution ($\sim 0.7''$ FWHM on-axis) enables AGN to be identified, and easily distinguished from the extended intra-cluster medium. This has resulted in investigations of AGN in a number of galaxy clusters, to try to determine the number and properties of cluster AGN. Most studies involved comparing the number counts in the

cluster observation to that found in a typical non-cluster ('blank') field.

In the majority of searches for AGN in clusters with Chandra, more point sources than expected have been found. However, the size of the excess and the nature of the sources varies considerably and as yet no clear picture of the factors governing AGN in clusters has emerged. In particular the field-to-field variance in the number of background sources makes it hard to determine how many point sources are due to the cluster, and in addition it is not certain that the published results are representative of the cluster population, as fields which have no statistical excess of sources may not have been published. Analysis of published results for individual clusters at $z \leq 0.5$ has found evidence for AGN in many of them. Significant overdensities of X-ray sources have been found in A2104, at z=0.15 (Martini et al. 2002), A1995 (z=0.32) (Molnar et al. 2002) and two z=0.5 clusters, 3c295 and RXJ003033.2+261819 (hereafter RXJ0030) (Cappi et al. 2001). However, the region around MS0451-03, also at z=0.5, has no excess point sources (Molnar et al. 2002).

The excess sources around 3c295 and RXJ0030 have luminosities of L_X(0.5-2keV) $\gtrsim 10^{42}$ erg s^{-1}, ruling out all but the most powerful starburst galaxies, and hardness ratios typical of unabsorbed AGNs. In comparison, the excess around A1995, which is significant to 3σ, is made up of sources that are an order of magnitude lower in X-ray luminosity if they are cluster members. The lower hardness ratio of these sources suggests starburst galaxies as the cause. If A1995 was moved to the redshift of 3c295 and RXJ0030 (z=0.5), it would have no detectable excess, as seen in MS0451-03, which is at the same redshift.

Recently, there have also been studies of X-ray AGN in clusters and protoclusters at redshift $\gtrsim 0.5$. Johnson et al. (2003) studied MS1054-03, a rich cluster at redshift 0.83. An excess of bright sources was found, that could not be explained by lensing or by cosmic variance, and two of the sources are spectroscopically confirmed cluster members. Pentericci et al. (2002) examined the protocluster around the radio galaxy MRC 1138-262 at redshift 2.16. They also found an excess of soft point sources, with a significance of $\sim 1.5\sigma$. Most of these sources are AGN, and optical observations identify 2, and plausibly up to 6, of the AGN as protocluster members.

The uncertainties in the number of excess sources in an observation come partly from the Poissonian errors on the small number of sources, but also from cosmic variance due to large-scale clustering of the background AGN. The scale of this variance is not well defined (e.g. Gilli et al., 2005) and depends on the flux limit of the sample and the field of view. The ChaMP team (Kim et al. 2004b) find that there is no non-Poissonian difference in number counts between fields when examining typical Chandra observations. Other studies find that some degree of clustering does exist, but it is expected to be less than $\sim 25\%$ (see for example Cappelluti et al. (2005) and references therein). A large sample of clusters and blank fields can be used to reduce this effect and the uncertainties due to small numbers of sources. Alternatively the X-ray images can be combined with optical data to identify the cluster AGN.

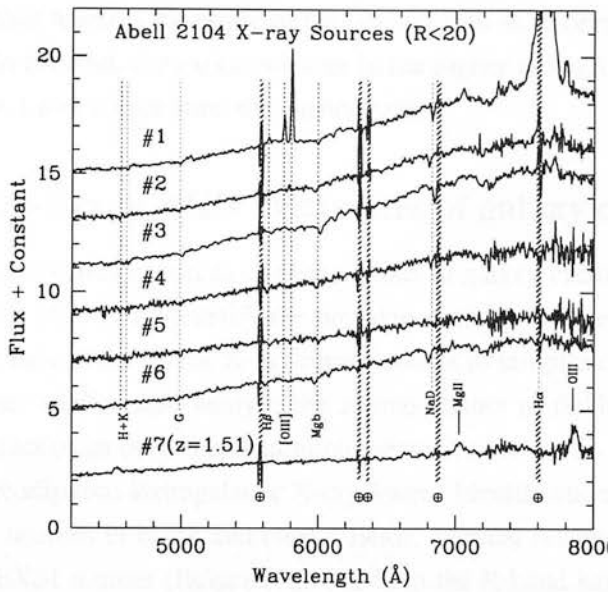

Figure 1.7: The optical spectra of six X-ray identified cluster AGN, from Martini et al. (2004). Only source #1 would have been identified in an optical survey, highlighting the need for X-ray data to obtain a large sample of cluster AGN.

Using the latter technique, Martini et al. (2004) combine X-ray observations with optical colour-magnitude diagrams to identify cluster AGN. These are found in the fields of four clusters (A2550, AC114, A2104 and MS0451-03), from z=0.11 to 0.54, with between 2 and 6 confirmed AGN per cluster. Davis et al. (2003) also combine optical and X-ray data to identify at least three, and possibly five AGN in the z=0.08 cluster A2255. In Abell 2104, only one of the six cluster AGN would have been identified by the optical spectra alone (see Figure 1.7), reinforcing the need for X-ray studies of AGN. The contrast between different clusters is striking - in A2104 the AGN host galaxies are all red, early-type galaxies, whereas spectral analysis of the AGN host galaxies around AC114 (z=0.31) show that several AGN in the cluster have host galaxies with recent or ongoing star-formation. The Martini et al. optical sample includes MS0451, which had no statistical excess of sources compared to a blank field, but has at least 2 confirmed cluster AGN. This highlights the need for either optical identification of cluster AGN candidates, or a large sample of clusters in order to increase the statistical significance and reduce the effect of cosmic variance.

The radial positions of the AGN excess is interesting as it shows whether AGN are uniformly distributed throughout the cluster, or whether they are triggered or suppressed as a function of radius. In contradiction to the optical results from Edge (1992), Martini et al. (2002) find that the identified host galaxies in A2104 have an average redshift offset of $\sim$ 1000 km s^{-1} from the cluster mean, suggesting that AGN are triggered by in-fall. Surprisingly though, they all fall near the cluster colour-magnitude relation, rather than being

blue star-forming or post-star-forming galaxies. The excess in the images of 3c295 and RXJ0030 were greatest towards the centre of the cluster, with no excess seen at distances of above $\sim$ 1.2Mpc. In contrast, the excess sources in the higher redshift cluster MS1054-03 were found between 1 and 2 Mpc from the cluster centre.

1.4.4 X-ray studies of AGN in samples of galaxy clusters

The Chandra archive contains hundreds of observations of galaxy clusters, of varying quality and properties. To attempt to quantify the prevalence and properties of AGN in galaxy clusters, two groups have analysed the X-ray source counts in samples of 10 or more galaxy clusters. Two further studies also analyse the source counts in fields containing galaxy clusters as a by product of an overall serendipitous search for X-ray sources.

The SEXSI (Serendipitous Extragalactic X-ray Source Identification) and ChaMP projects both identify X-ray sources in blank and cluster fields. Optical imaging of the hard band, intermediate flux SEXSI sources (Eckart et al. 2005) in the R-band has found that there is no significant overdensity of optical sources within $1'$ of the AGN, showing that they do not lie in the centre of massive clusters. The ChaMP study (Kim et al. 2004a and 2004b) compares the number counts at each flux (the Log(N)-Log(S) distribution) for 33 blank fields with those containing high redshift clusters (29 fields with $z > 0.3$), to determine whether there are excess sources in the cluster fields. They find no statistical difference between the two samples. However, the sample is limited to sources with > 20 X-ray counts, and does not take into account the increase in background counts due to the intra-cluster medium. This reduces the sensitivity in cluster images compared to the blank fields, and needs to be taken account of when evaluating the sky area available at each flux. The fact that their Log(N)-Log(S) distributions agree without this correction implies that the true cluster Log(N)-Log(S) distribution should be higher than that of the blank fields. In addition, this sample misses fainter sources associated with the galaxy clusters.

The studies which deliberately target galaxy clusters have found significant excesses of sources. Cappelluti et al. (2005) use deep observations of 10 clusters in the range $0.24 < z < 1.2$, and find that regions of four fields contain around twice as many sources as expected, corresponding to a 2σ excess per field. The careful evaluation of the reduced sensitivity due to the emission from the intra-cluster medium, following Johnson et al. (2003), and use of five blank fields to account for cosmic variance, make these results robust. However, as shown in Figure 1.8, they do find slightly more under-dense cluster fields than blank fields, which is surprising as the cluster fields should contain at least as many sources per square degree as the blank fields, unless they contain a deficit of background sources due to gravitational lensing. Cappelluti et al. do not correct their sample for gravitational lensing, which can slightly decrease the number counts at fainter fluxes. The clusters are observed using the ACIS-I array, which has four chips, and the excess sources are calculated for each

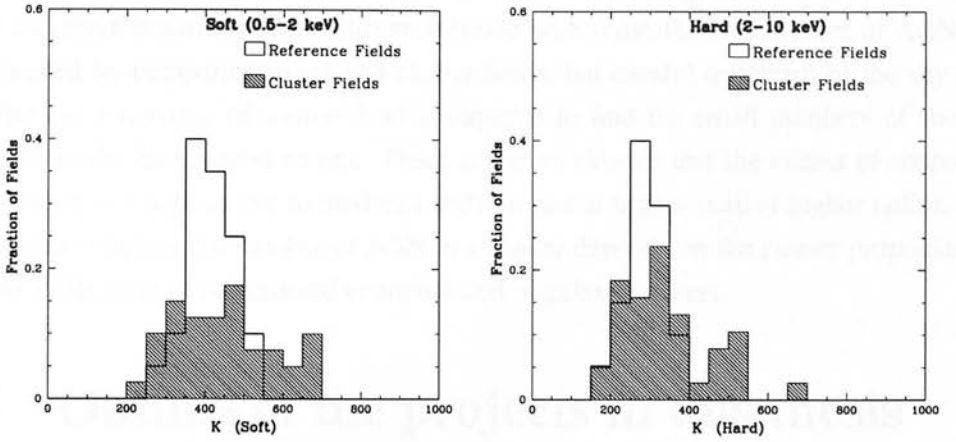

Figure 1.8: The distribution of number count normalisations for Chandra blank field and cluster observations, from Cappelluti et al. (2005). The normalisations, which show the source density, are calculated for each chip (4 per observation) and there are clearly more chips with high source densities in the cluster fields than the blank fields, in both the hard and soft bands. The larger number of under-dense cluster fields is, however, surprising as the cluster fields should always contain at least as many AGN as the blank fields.

chip individually. Four cluster fields, at a range of redshifts, have a significant source excess on at least one chip, and in three of the cluster images an excess is found on the chip containing the cluster centre. As the cluster is not in the centre of the chip, it is hard to draw any firm conclusions regarding the radius of these excess sources, but it is clear that they are associated with the cluster and Cappelluti et al. speculate that they are tracing filaments on the outskirts of the cluster. If associated with the cluster, these sources have luminosities of $\sim 10^{42-44.5}$erg/cm^2/sec, confirming that they are AGN. There is evidence that the number of excess sources rises with redshift, but this could also be due to changes in the cluster properties.

Ruderman and Ebeling (2005) analyse point sources around a larger sample of 51 massive galaxy clusters at $0.3 < z < 0.7$, and 20 control fields. They find an excess of sources within 3.5 Mpc of the cluster centre, consisting of a spike of central sources and an excess towards the outskirts of this region. This survey only investigates the brightest sources ($\sim$ 10 per cluster field) and, like the ChaMP, does not take into account the changes in sensitivity due to the cluster emission. In addition, Ruderman and Ebeling (2005) finds that the density of sources at the edge of the images, beyond the region in which lensing could reduce the source counts, is *higher* in the blank fields than the cluster fields. As a selection of blank fields should always have less sources than the cluster fields (as long as the sample is large enough to eliminate cosmic variance), this suggests an incorrect treatment of the sky area available at each flux. These results are discussed further and compared to those from this project in Section 3.4.

In conclusion, it is clear that galaxy clusters can contain significant numbers of X-ray AGN, and there is some evidence for an increase with redshift. The number of AGN can be estimated by comparing blank and cluster fields, but careful treatment of the sky area available (as a function of source flux) is required to find the small numbers of sources compared to the background counts. There is some evidence that the excess of sources is found within $\sim$ 1 Mpc at low to moderate redshift and at higher radii at higher radius. It is not yet clear whether the number of AGN in a cluster depends on the cluster properties, or whether AGN activity is increased or suppressed in galaxy clusters.

1.5 Outline of the projects in this thesis

This thesis contains two projects designed to tackle the key question of how the extended environment affects the fuelling of AGN. These projects are designed to add significantly to the understanding of the number and properties of AGN in cluster environments, and the effect of different environments on the AGN.

The first project makes use of the vast number of observations of galaxy clusters in the Chandra archive – there are over 140 moderate to deep observations of galaxy clusters with $z > 0.1$ currently available. This project extends the analysis, described above, of point sources in a few cluster fields, to utilise all of the available data by using an automated pipeline to analyse the images. The X-ray sources in the cluster fields are compared to those in a sample of blank fields, and the number, flux and distribution of X-ray sources associated with the cluster is determined statistically for each observation. Although there are large uncertainties in the results for individual fields, by combining over 140 fields the number of AGN in galaxy clusters on average is determined. In addition, the large redshift range and differences in cluster properties enables the sample to be split, and the dependence of AGN properties on cluster redshift, morphology and luminosity is evaluated.

The second project combines X-ray and optical data to study in detail the AGN in the supercluster A901/2. By combining deep X-ray data with the optical spectroscopic and photometric redshifts, optical images and best-fit template SEDs available for sources in this field (from the COMBO 17 survey, Wolf et al. 2003), the AGN which lie in supercluster galaxies are found and their host galaxies evaluated. The wealth of optical and X-ray data for this field enables the local and extended environment of the AGN to be investigated in terms of galaxy density, galaxy properties and position within the large scale structure. This project complements the larger, statistical study by focusing on one set of AGN, and determining exactly where the AGN lie. By comparing AGN hosts to other similar galaxies, this project determines whether AGN activity is triggered or suppressed in dense environments.

The thesis is presented as follows:

- Chapter 2 describes the automated pipeline used to reduce the archival data for the

survey of over a hundred galaxy clusters. The source detection and models of expected sources for each field are described, and the possible sources of bias evaluated.

- In Chapter 3 the results of this survey are presented, together with an interpretation of the data and comparison to previous work.
- Chapter 4 describes the analysis of the supercluster A901/2 and the properties and distribution of the AGN.
- Chapter 5 provides a summary of the results of both projects, and also a discussion of the future work planned with this dataset.

CHAPTER 2

Investigating the AGN in galaxy clusters - the reduction pipeline

2.1 Introduction

The large number of observations of galaxy clusters in the Chandra[1] archive provide an excellent basis for investigating the prevalence of AGN in galaxy clusters. By comparing the point source distribution in 'blank field' observations with that from cluster observations, the number, flux and radial distribution of the sources associated with the cluster can be determined statistically. As described in Sections 1.4.3 and 1.4.4, this method has been used in the past to investigate small samples of galaxy clusters, but these contain significant statistical errors and field-to-field variance. This study is a significant advance over previous studies, both in size and methodology. By analysing over 140 galaxy clusters the statistical variance seen in the smaller studies is significantly reduced, and the properties of the cluster AGN population can be identified. In addition, a sample of this size can be split into sub-samples without introducing significant errors from the field to field variance. The dependence of the AGN population on cluster redshift, mass (from the X-ray luminosity) and morphology can therefore be found. This analysis requires careful data reduction and modelling of the sensitivity of each observation, and is performed using an automated pipeline developed for this purpose.

[1]The Chandra archive was used, rather than images from XMM-Newton, as Chandra has superior spatial resolution. Although XMM has better sensitivity (in terms of photons detected), for faint sources the large PSF (point spread function) makes point sources hard to detect. In Chandra images, despite the reduced photon numbers, the improved PSF means that fainter point sources can be detected. Unlike in XMM, these can easily be distinguished from the extended intra-cluster medium, and in addition point source blends are far rarer. See Appendix A for more details of the Chandra and XMM-Newton telescopes.

The key steps in investigating the point sources in the cluster observations are as follows:

- Observations of galaxy clusters and 'blank' fields are chosen from the Chandra archive.
- Each cluster is assigned a morphological class, and the cluster luminosities are found. This allows a later comparison of the AGN content of clusters as a function of cluster properties, as well as an estimate of the effect of gravitational lensing.
- Point sources are identified in the fields, and their properties are calculated.
- For each observation a 'flux-limit map' is produced, showing the detection sensitivity at each point of the image. This accounts for the detector response, PSF (point spread function) size, and the presence of the background intra-cluster emission.
- The Log N($> S$) - Log S distribution is calculated for each blank and cluster field, taking into account the sky area sensitive to sources of each flux.
- The radial distribution of sources in each field is calculated. A predicted radial distribution, assuming no cluster AGN, is produced from the blank field source distribution and the flux-limit map.
- The effects of gravitational lensing by the galaxy cluster are modelled, and the Log N($> S$) - Log S distributions and predicted radial distributions are corrected for this effect.

This Chapter includes the details of the automated pipeline and data reduction as follows: Section 2.2 describes the initial sample of observations from the Chandra archive and the selection of blank fields as a control sample. Section 2.3 explains the initial data reduction and detection of point sources in these observations. In Section 2.4 the final sample of cluster observations is presented, and the derivation of cluster morphologies and luminosities is described. Section 2.5 details the analysis of the point sources in each field. Section 2.6 explains the method of predicting the source distributions in each observation, including the correction for gravitational lensing. Finally Section 2.8 summarises the automated pipeline.

2.2 Initial data selection

2.2.1 Observations of galaxy clusters

There are over 500 observations marked as 'Clusters of Galaxies' in the Chandra archive - some of these are so close that only the central regions are visible in the Chandra field of view, some will not have deep enough observations to detect significant numbers of AGN

and others may not be genuine galaxy clusters. Observations of interest were selected as described below, and all put through the first stage of the pipeline. The final sample was only defined after data reduction, as the full nature of the target is not always clear until the data are properly reduced.

As an initial step all observations with total exposure time $>$ 10ksec, taken with the ACIS-I or ACIS-S array (see Appendix A.3.1) which were assigned to the 'Clusters of Galaxies' category were considered. The NASA Extragalactic Database (NED) was used to select observations from this sample with a confirmed galaxy cluster within $5'$ of the aim-point. In addition observations with a cD galaxy, other bright galaxy, QSO, or galaxy overdensity at one redshift, were also selected. These were included in the initial sample as they all indicate the possible presence of a galaxy cluster, and were all targeted in studies of galaxy clusters. In particular, a cD galaxy or list of cluster galaxies may be published without the galaxy cluster explicitly appearing in the NED. All observations where the target cluster or overdensity was within $5'$ of the aim-point were included, as many listed clusters are optically identified and have inaccurate positions, particularly if they have few identified galaxies.

As a second step the NED was used to select only those observations with targets at $z > 0.1$, so as to ensure the outskirts of the cluster were observed. A $z = 0.1$ cluster observed with the ACIS-S array would be observed to a radius of at least 220kpc in all directions, and with ACIS-I this increases to at least 440kpc. Observations with more than one published redshift or named cluster were also retained for this step, as the redshift could be incorrect, or the cluster could have been identified twice.

The archive was examined up to July 2005 and 156 targets were selected, of which 37 were observed on more than one occasion (with the same detector array). The selection of the sample from this set of targets is described in Section 2.4.

This set of cluster observations will be heavily biased, as clusters are selected depending on the requirements of the observer. In particular the sample will be biased towards relaxed clusters, which are used to constrain cosmological parameters (e.g. Allen et al. 2004), and highly disturbed, rich clusters, used to study cluster mergers for example. Some targets were selected using previous X-ray surveys and others targeted optically discovered clusters. In addition some observations were searches for cluster emission, such as around a QSO or optical overdensity. Some of these may fail to find a cluster, but this cannot be determined until the data are reduced, so these observations were retained for the time being. The biases in the sample selection were parameterised as far as possible by examining the X-ray properties of the clusters, and taken into account later in the analysis.

2.2.2 Blank fields

It is necessary to have a control sample of blank fields in order to calculate the expected distribution of point sources in a typical observation with no targeted foreground sources, and hence calculate the number of sources expected to be in the galaxy cluster. To avoid biases due to large scale structure and statistical variance due to low counts it is desirable to have as large a sample as possible of blank fields.

Many surveys have been conducted which aimed to constrain the general X-ray source population and were therefore not targeted at a specific object. These are ideal for determining the expected background X-ray source population (the sources that are not due to the galaxy cluster). Extensive catalogues of sources in these fields have been published, but in order to compare them to the cluster sample they were re-analysed in the same manner as the clusters, using the reduction pipeline. All of the observations in the "Extragalactic diffuse emission and surveys" category of the Chandra archive were examined to determine their suitability for this blank field sample. The purpose of the observation was determined from the proposal abstract[2] and from published papers, and deliberately targeted blank field observations were selected. The target fields were also checked with the NED and those that contained galaxy clusters which were discovered independently of the blank field observation, were removed (such as the XMM 13hr field, which contains a ROSAT selected galaxy cluster). Many blank field surveys were far deeper than the cluster observations so it was not necessary to select all of the observations - instead, if possible, observations which covered the largest area without overlap were selected and treated as independent fields. The final sample of true blank fields is selected from the following surveys:

- **William Herschel Deep Field** - one 75ksec observation
- **XMM 1hr field** - Two fields were selected, each with 30ksec exposure time. There was some overlap between the fields, so they were treated as one merged observation (see Section 2.3.4).
- **Extended Chandra Deep Field South** - as described in Virani et al. (2005), this field consists of 4 pointings around the Chandra Deep Field South. This covers a larger area than the Chandra Deep Field to a depth of 250ksec, which is sufficient for this study. The four fields have minimal overlap, so are treated as independent fields (the overlap regions are in fact rejected later in the analysis, as areas of large PSF are rejected). [For one of the four pointings there were complications in the data reduction so only 80ksec was used].
- **Lockman Hole North-West** - Four of the 40ksec fields were chosen such that there was no overlap between the observations. For details see Yang et al. (2004).

[2] see http://cxc.harvard.edu/target_lists/index.html

- **Swire-Lockman region** - This is the Lockman Field of the SIRTF/SWIRE Legacy Survey (see for example Franceschini et al.,2004). Of the nine 70 ksec observations the four most spatially extreme positions were taken, as they do not overlap and can be treated as four separate blank fields.

- **DADDI** - Three 30ksec observations, with significant overlap, were selected. The field was observed as part of a study of EROs.

- **Hubble Deep Field North** - Two of many pointings were chosen, giving a total time of 220ksec (see for example Brandt et al., 2001). Although galaxy clustering has been discovered in this field, this is due to the depth with which it has been studied. As the clusters were not identified by previous missions (such as ROSAT) this area is still included as a blank field.

- **Groth-Westphal** - Three observations of this area, totalling 200ksec, were used (for details see Nandra et al., 2005).

- **Extended Groth Strip (EGS)** - Two of the four 100ksec observations, which did not overlap, were chosen. These are near, but do not overlap with, the Groth-Westphal observations.

- **Elais N1 and N2** - These observations were not categorised as blank fields in the Chandra archive but are valid for this analysis (for details of this field see Manners et al., 2003). The two faint clusters found in these regions are serendipitous, so it is valid to include the regions as blank fields.

In addition to the 'true' blank fields, observations of high redshift ($z > 2$) quasars or radio galaxies were also used. These were added to increase the sample size, and hence reduce the errors due to low source counts (particularly at high fluxes) and reduce the effect of particularly over or under-dense fields. In addition, all of the blank field observations used the ACIS-I detector, so observations with the ACIS-S detector were required to test for differences in the source detection or properties. The fields were selected from the "Active galaxies and quasars" category (and also misclassified QSO observations in the "Extragalactic diffuse emission and surveys" category), with observation times $>$ 10ksec and redshifts in the NED.

In most of these fields the QSO is visible at the aim-point and it is possible that there are extra sources at the redshift of the QSO due to either clustering or lensing (these extra sources will be rare as the observations are shallow and the target QSOs very distant, so only luminous QSOs associated with the target source would be detected). The target and any associated QSOs will falsely boost the blank field number counts, so they were removed by masking a portion of the image. To do this, the fields were compared to the objects in the NED, to look for additional objects associated with the target QSO, or confirmed galaxy

clusters. One field was rejected as it contained significant large scale structure, with QSOs at the same redshift as the target up to 250″ from the aim-point. A second field had a region removed around a nearby galaxy with extended emission, as the point sources seen may be within the galaxy. In all images a circle of radius 25″ was removed from around the aim point, as this radius excludes all other objects identified in NED at the QSO redshifts (with the exception of the rejected field). These regions were excluded from the analysis using the masks described in Section 2.6.5.

Once the data were reduced, the blank field number counts were checked to ensure that including the high redshift QSO fields does not bias the background (see Section 2.6.10). The final sample of blank fields consists of 22 true blank fields and 22 QSO fields, which are listed in Table 2.1. Four of the blank fields have exposures of over 200ksec, which is sufficiently deep to compare to the maximum exposure of 190ksec for the deepest selected cluster field (and 117ksec for the deepest cluster field in the final $z < 1$ sample).

2.3 Data reduction

To reduce the initial cluster and blank field samples, an automated pipeline was developed, using a range of CIAO[3] tools and other programs. This ensured that the reduction was uniform, and allowed the whole sample to be reduced efficiently.

In order to obtain the maximum number of sources around each cluster, all four ACIS-I chips were used for observations focused on the ACIS-I array, and the three chips nearest to the aim-point were used for ACIS-S observations (or less if not all were turned on). Due to the off-axis degradation of the PSF the other chips were not investigated as the errors become too large. In addition parts of the selected chips were later excluded as the analysis was restricted to a maximum radius from the aim-point (see Section 2.6.4).

2.3.1 Calibration

For each observation the data were re-reduced from the level 1 event list (uncalibrated data, with only in-flight filtering applied) so as to ensure the most recent calibrations were applied to all files, using standard CIAO 3.0.1 tools (see the CIAO detect manual (2003) for details). Aspect files, containing information on the telescope pointing and dither, were merged if more than one applied to the observation. The *fix_batch*[4] script was used to check and correct the astrometry for systematic aspect offsets.

Level 2 X-ray files contain the physical properties of the detections, such as the photon energies, which are deduced from detected properties and calibration files. The 'gain' is

[3]CIAO (Chandra Interactive Analysis of Observations) is the software package designed specifically for reducing and analysing Chandra data.

[4]see http://cxc.harvard.edu/cal/ASPECT/fix_offset/fix_offset.cgi

the mapping between detected pulse height and actual photon energy, and is spatially and energy dependent. In addition the gain has been decaying, so a time dependent gain decay, or charge transfer inefficiency, has to be applied in all observations taken after 29 January 2000[5].

The Quantum Efficiency (QE) of the detectors is also spatially, energy and time dependent. The spatial and energy dependence are well calibrated, but the QE is decaying due to the build up of contaminants on the telescope. This has been modelled by a time dependent decay rate[6]

$$R(t) = n \times e^{-t_0\left(1-e^{-t/t_1}\right)} \tag{2.1}$$

where $n = 0/00722$, $t_1 = 620 \pm 66$ days, $t_0 = 0.582 \pm 0.024$ and t is the time of the observation from 20/07/1999 in days. This only applies at energies below $\sim$ 1keV and is uniform across the detector. The net change is up to 10% per year at low energies, which is a small effect for one field, but is significant enough to affect this large sample. Initially the fluxes of all sources were corrected using an assumed spectrum of $F \propto E^{-1.7}$, as the spectra of the individual sources are not known. However, a recent calibration file, CALDB 2.26, corrects for this effect in more detail, using a more complex formula, so was used on the final sample.

A new level 2 file was created using the *acis_process_events* tool in CIAO 3.0.1, which accounts for the spatial, energy, and time dependence of the gain, and CALDB 2.26 to correct for the degradation of the QE.

2.3.2 Filtering

For each observation the level 2 file was filtered to remove non-cosmic X-rays and other contaminants, and enable sources to be detected. Only detections which had standard grades (0,2,3,4,6 - see Appendix A.3.2), status=0 (Appendix A.3.3), and were in the default good time interval (GTI) were selected, so as to remove the majority of particle and cosmic ray background. Further GTI filtering was performed by manually masking the brightest sources and removing times where the count rate in the remaining area was more than 3-sigma above the quiescent rate. This filtering was performed separately for each chip as the background rates vary between chips due to changes in sensitivity and chip design.

In addition, CCD 8 was destreaked (Appendix A.3.4) and the data were filtered for bad pixels. Finally, the data were filtered for energies between 0.5 and 8 keV to allow better detection of AGN: above 8keV the particle background makes it harder to detect sources (see Appendix A.2.1), and below 0.5 keV the absorption and emission from our own galaxy reduce the detection efficiency for extragalactic sources. Also, at energies < 0.5 keV the

[5] after the ACIS focal plane temperature was lowered. See http://cxc.harvard.edu/cal/Acis/Cal_prods/tgain/index.html and the CIAO threads at http://cxc.harvard.edu/ciao/threads/

[6] modelled by G. Chartas - see http://cxc.harvard.edu/chandra-users/0323.html

Target Name	Observation RA	Observation DEC	OBSID	Good Exp. (ksec)	Array	QSO
HS0017+2116	00:20:10.80	+21:32:51.00	3063	10.0	ACIS-S	Y
3C9	00:20:25.20	+15:40:53.00	1595	17.5	ACIS-S	Y
WHDF	00:22:33.30	+00:20:55.00	2252	71.0	ACIS-I	
GSGP4X:048	00:57:17.10	-27:21:47.00	2242	10.5	ACIS-S	Y†
XMM1HR-3&4	01:45:38.18	-04:41:24.48	4275,4276	52.1	ACIS-I	
CADIS01HFIELD	01:47:36.20	+02:20:03.30	2240	28.3	ACIS-I	
J0305+3525	03:05:47.40	+35:25:13.40	4142	12.3	ACIS-S	Y
EXTENDEDCDF-S3	03:31:48.79	-27:57:08.10	5019,5020	240.2	ACIS-I	
EXTENDEDCDF-S2	03:31:52.60	-27:41:44.92	5017,5018	219.2	ACIS-I	
EXTENDEDCDF-S4	03:33:01.78	-27:57:09.61	5022	78.7	ACIS-I	
EXTENDEDCDF-S1	03:33:06.10	-27:40:53.50	5015,5016	237.6	ACIS-I	
0406-244	04:08:51.50	-24:18:16.50	3058	18.2	ACIS-S	Y
HS0818+1227	08:21:39.10	+12:17:29.00	3571	19.7	ACIS-S	Y
0828+193	08:30:53.40	+19:13:15.60	3059	17.4	ACIS-S	Y
APM08279+5255	08:31:41.60	+52:45:16.80	2979	88.3	ACIS-S	Y
SDSS091316+591921	09:13:16.60	+59:19:21.50	3034	9.8	ACIS-S	Y
QSO0910+564	09:14:39.30	+56:13:21.00	4821	22.9	ACIS-S	Y
BRI0952-0115	09:55:00.10	-01:30:05.00	5194	19.8	ACIS-S	Y
PC1000+4751	10:03:52.80	+47:36:54.30	4152	13.7	ACIS-S	Y
FSC10214+4724	10:24:34.50	+47:09:09.80	4807	21.4	ACIS-S	Y
LH-NW-4	10:32:06.00	+57:37:24.99	3345	38.3	ACIS-I	
LH-NW-6	10:33:22.00	+57:55:25.00	3343	33.5	ACIS-I	
LH-NW-5	10:34:02.10	+57:28:25.00	3346	38.1	ACIS-I	
LH-NW-9	10:35:16.00	+57:46:24.99	3348	39.4	ACIS-I	
PC_1035+4747	10:38:08.20	+47:31:36.60	4154	8.8	ACIS-S	Y
SWIRELOCKMAN7	10:43:27.23	+59:10:15.07	5029	70.8	ACIS-I	
SWIRELOCKMAN1	10:44:46.15	+58:41:55.45	5024	63.7	ACIS-I	
SWIRELOCKMAN9	10:47:13.85	+59:20:06.95	5031	65.0	ACIS-I	
SWIRELOCKMAN3	10:48:32.77	+58:51:47.33	5026	68.7	ACIS-I	
Q1208+1011	12:10:56.90	+09:54:26.80	3570	10.0	ACIS-S	Y
HDF-N	12:36:49.40	+62:12:58.00	2421,3293	222.0	ACIS-I	
SDSSJ130216+003032	13:02:16.10	+00:30:32.10	3958	10.7	ACIS-S	Y
SDSS1306+0356JE	13:06:09.30	+03:56:43.50	3966	117.6	ACIS-S	Y
F864X:052	13:44:07.30	-00:28:33.00	2250	9.5	ACIS-S	Y†
GROTH-WESTPHAL	14:17:43.60	+52:28:41.20	3305,4357,4365	191.3	ACIS-I	
EGS-3	14:20:28.00	+53:02:01.30	5845,5846	97.6	ACIS-I	
EGS-1	14:22:42.30	+53:25:37.51	5841,5842	90.6	ACIS-I	
SDSSJ144231+011055	14:42:31.70	+01:10:55.30	3960	10.8	ACIS-S	Y
DADDIFIELD	14:49:09.10	+09:01:36.00	5032,5033,5034	87.2	ACIS-I	
QSO1508+5714	15:10:02.90	+57:02:43.40	2241	88.5	ACIS-S	Y
ELAIS:N1	16:10:21.90	+54:33:36.00	888	71.9	ACIS-I	
ELAIS:N2	16:36:48.48	+41:01:45.90	887	73.1	ACIS-I	
2036-254	20:39:24.50	-25:14:30.40	3060	19.6	ACIS-S	Y
2048-272	20:51:03.40	-27:03:04.60	3061	17.7	ACIS-S	Y

Table 2.1: Observations of blank fields. The fields containing deliberately targeted QSOs are indicated - those marked † were in the "Extragalactic diffuse emission and surveys" category as a search for ROSAT identified NELGs, but no emission was seen at the target point so they were treated as blank fields.

emission from the intra-cluster medium is highest, making it harder to detect AGN near the cluster centres.

2.3.3 Source detection

Images and exposure maps (in $\sec^{-1}\mathrm{cm}^{-2}$, see Appendix A.3.5) were made using unbinned data, and using calibration files which take into account the difference in quantum efficiency between back and front illuminated chips[7]. The exposure map is energy dependent, and includes the effect of bad pixels, CCD gaps and vignetting as well as the good exposure time for each chip. Exposure maps were made assuming the sources have a photon index of $\Gamma = 1.7$, typical of unobscured AGN at the sample flux limits (see for example Figure 3 of Tozzi et al., 2001). Changing the spectral index to other realistic values does not change the sources detected or their significances.

Sources were detected on the unbinned images using the WAVDETECT mexican hat wavelet (Appendix A.1.3), with wavelet scales of 1,2,4,8 and 16 pixels to match the variation of the PSF from the centre to the outskirts of the image. Tests using different wavelet scales suggest that very close sources may sometimes be missed using scales separated by a factor of 2, whereas scales separated by $\sqrt{2}$ are more accurate. However sources which can be distinguished by the finer scale separation but not the coarser one are very rare ($\ll 1\%$) in typical Chandra images out to the radii used in this sample. Running with twice as many wavelet scales doubles the time taken to detect sources in this large sample, so it was not considered necessary to correct for this effect.

WAVDETECT was run with a significance threshold of 10^{-6}, corresponding to around 1 expected false source per chip, but the significance of all the sources was re-assessed later on in the analysis and a more conservative cut was used. This was necessary in order to be able to predict the expected source distribution over the chips, taking into account the background variation (see Section 2.6). Point source detections were determined within WRECON using details of the 1-sigma encircled energy PSF size at 1.4 keV. Source sizes were output as 3-sigma ellipses, assuming a gaussian PSF (an example of the detected sources is shown for the case of multiple observations in Figure 2.1).

Due to the large size of many of the images it was necessary to cut them into sections before running WAVDETECT, then combine the source lists. The sections overlapped to ensure that no sources were missed or affected by being at the edge of the image, and duplicate detections in the overlap regions were removed manually. As a final stage the source list output from WAVDETECT was examined by eye to remove detections of the extended cluster emission.

[7] In CADLB 3.0.1, see http://cxc.harvard.edu/cal/docs/cal_present_status.html#abs_eff for details

2.3.4 Fields with multiple observations

Many clusters and blank fields were observed more than once, and in these cases data from up to three observations were merged before the sources were detected, to give far deeper images and maximise the number of sources. The process is similar to that for single observations with the following additions:-

The astrometry of the images was adjusted using the *align_evt* routine[8] as, even after correcting the aspect files, small offsets often exist between images. To do this sources were detected in the central 4 arcmin of each image, where the PSF is smallest, using a fast sliding box technique. The median offsets in RA and DEC were then used to correct the central co-ordinates of the image (by translation only, no rotation was applied). To ensure only sources with accurate positions were used, only those with signal to noise (SNR) > 3 were matched. If the image centres differed by over 4 arcmin then a larger area was searched, and if there were too few SNR > 3 sources then SNR > 1 was used. Manual inspection showed that the matching was accurate even in extreme cases of only six sources with SNR > 1, and that no rotation was required to match the images accurately.

Individual images were made, and exposure maps created for each observation. A combined image was computed using the astrometry corrected event files and the *merge_all* script. The combined exposure map was made by summing the individual exposure maps as the CIAO *merge_all* exposure map was often found to contain errors. Sources were detected on the combined image using the combined exposure map.

WAVDETECT determines whether a source is real based on the source extent and the size of the PSF, which is complex for merged images with different aim points. In this case the combined PSF size at each point was calculated by combining the PSF sizes of the individual images. The input PSFs for the individual images were taken from the CIAO file psfsize20010416.fits, which is also the input file for a standard run of WAVDETECT. This file contains separate PSF distributions for the ACIS-I and ACIS-S detectors, which were applied to the corresponding observations (at no point were ACIS-I and ACIS-S images merged as this is too complex). At each point the PSFs from each image were assumed to be a 2-D gaussian distribution, with the given PSF size. The combined PSF size at each pixel is then given by summing the gaussian distributions, weighted by the exposure map values at that point in the image, and finding the the 3-sigma encircled energy of the resulting distribution. Obviously regions covered by only one pointing have the PSF of that pointing only. These PSF sizes were input into WRECON[9] in order to give detections and sizes that are comparable to the standard WAVDETECT results for single images.

As an illustration of this technique, Figure 2.1 shows the sources detected in a combined image of MACS J1149+22, which was observed twice. The combined exposure map and expected PSF distribution are also shown.

[8] ALIGN_EVT v1.6, written by Tom Aldcroft

[9] Using a more flexible version, kindly provided by Peter Freeman (private communication).

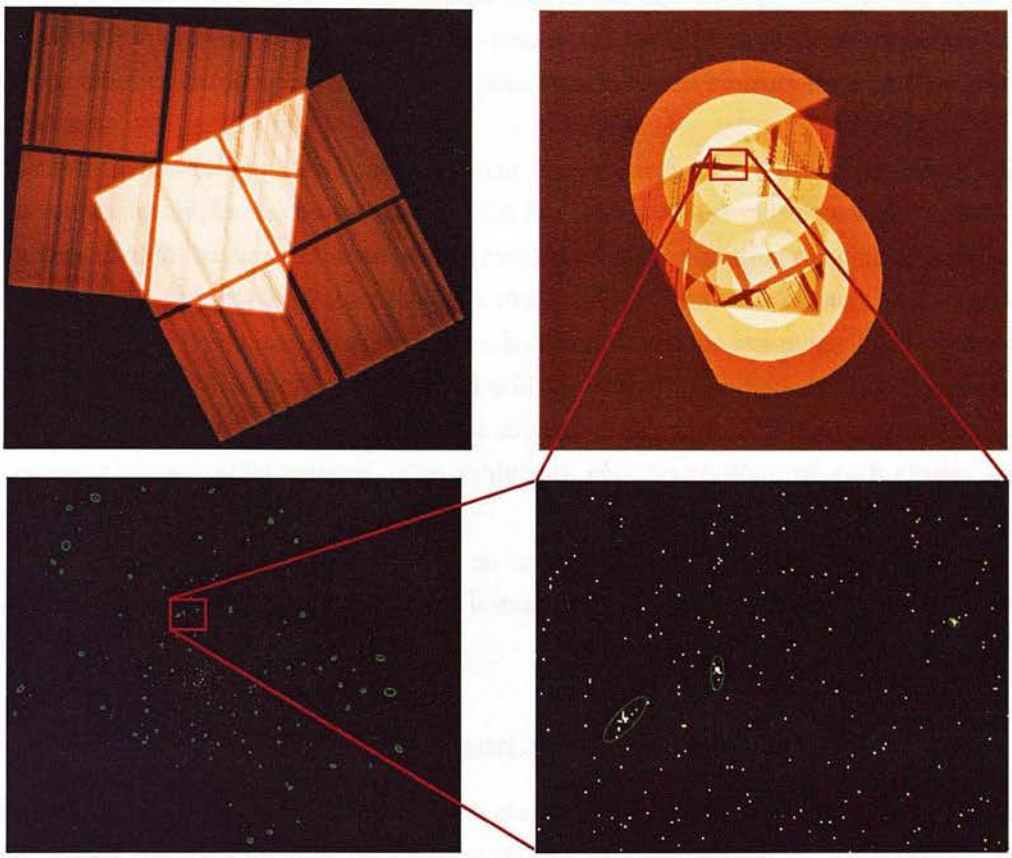

Figure 2.1: Source detection inputs and outputs for MACS J1149+22. The top panel shows the exposure map (left) and calculated expected PSF size distribution (right) for this observation (the PSF distribution is given as the maximum value in areas of no exposure). In the areas only covered by one exposure the PSF clearly expands radially, but it becomes far more complex in the merged areas. The lower panel shows the sources detected on the combined image, using these inputs, and a enlarged portion of the image. The enlarged portion covers an area where the expected PSF size varies rapidly due to chip gaps. It is clear that the input PSF size distribution, combined with the detection power of WAVDETECT, accurately finds the true source centre and extent. Some detected sources could be background fluctuations, but these are later removed as described in Section 2.5

2.4 The Cluster Sample

2.4.1 Cluster fields

The initial selection of possible cluster fields is described in Section 2.2. To summarise, all observations labelled 'Clusters of Galaxies' with a confirmed cluster, optical overdensity, QSO, bright galaxy or cD galaxy at $z > 0.1$ within the field of view, and total observation time $>$ 10ksec, were selected.

It is necessary to determine the reality of the clusters in the initial sample, as the objects in the 'Clusters of Galaxies' category the Chandra archive consist of a wide range of

observations, including searches for clusters that failed, and wrongly categorised observations. It is also important to find the X-ray position of the cluster as the AGN distribution may depend on cluster radius, and many optically discovered clusters have poorly defined positions.

In addition to finding the clusters it is interesting to determine their properties. If AGN are affected by cluster environments then the luminosity of the cluster and the degree of disturbance might be expected to affect the number of AGN. Splitting the cluster sample by luminosity will determine whether there are more AGN in luminous clusters, which generally have more galaxies, and whether fainter, less rich cluster environments have significant populations of AGN. A morphological split will allow distinction between highly disturbed environments, such as cluster mergers, and relaxed clusters, and determine whether cluster mergers trigger AGN activity. The luminosity and morphology of each cluster were determined as described below.

The cluster luminosity also provides an estimate of the mass, which can be used to correct the predicted source counts for each image for the effect of gravitational lensing, as described in Sections 2.6.11–2.6.13.

2.4.2 Cluster reality, centre and morphology

The morphology, centre and reality of each cluster was determined by examining the full-band images and the smoothed background images (see Section 2.6.3). The cluster centre was taken to be the peak of the smoothed background image, and this position is listed in Table 2.3. In most images the cluster centre or dominant cluster was obvious, but where the cluster appeared to be a major merger, consisting of two distinct peaks of similar brightness, the mid-point between the two peaks was chosen.

The reality and morphology were determined by eye, using the full and smoothed images (described in Section 2.6.3). The morphological classifications clearly involve a certain amount of subjectivity, but in broad terms they will be sufficient to distinguish the general types of cluster morphology. The following categories were used, and are illustrated in Figure 2.2.

0. No cluster emission visible against the background fluctuations.

1. One relaxed cluster visible. It may be elliptical or have edge structure, but not enough to fall into another category.

2. One disturbed cluster visible. The disturbance must be such that the cluster is clearly not simply elliptical or an asymmetric ellipse. The disturbance must be joined to the cluster by visible emission, and not enough to class as 'merging'.

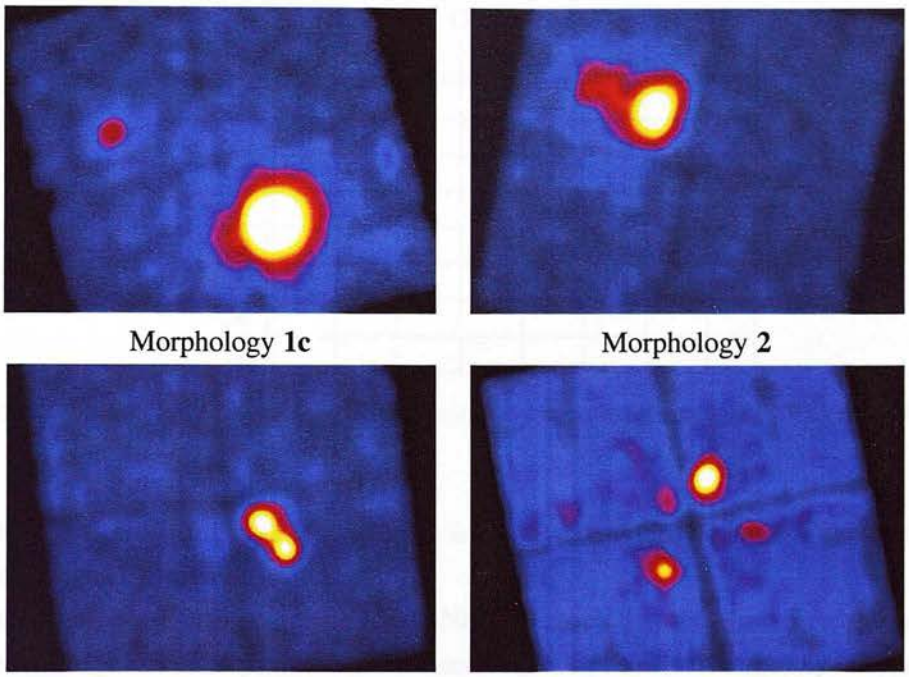

Morphology **1c** Morphology **2**

Morphology **3** Morphology **4**

Figure 2.2: Examples of cluster morphology categories.

3. Merging cluster. A double-peaked system, with a sub-clump with peak emission (in the smoothed image) $> 20\%$ of the main cluster, joined to the main cluster by visible emission.

4. Two clusters. A second cluster with peak emission $> 20\%$ of the main cluster but not clearly associated with it.

1c, 2c, 3c. As **1, 2** and **3**, but with a small contaminating cluster or group in the field of view. The second clump must have peak emission $< 20\%$ of the main cluster and not be clearly associated with it.

The possible cluster images were assigned a category by two observers, who were broadly in agreement as seen in Table 2.2. The few discrepancies are mainly due to small contaminating clusters or other extended emission that may be background fluctuations, and cases of uncertainty over the degree of disturbance. The morphologies of Observer 1 (the author) were adopted as they are slightly more conservative.

The optical data (from the NED) for the cluster fields was used to check for optically detected contaminants. Four fields were moved from morphology class **1** to **1c** as they contained optically confirmed (but X-ray faint) clusters at a significantly different redshift and position from the main cluster (these are flagged in Table 2.3). Fields that contained

Observer 2 \ Observer 1	0	1	1c	2	2c	3	3c	4
0	11							
1		96	3	2				
1c			11		1			
2		1		12				
2c			1		1			
3						10		
3c								
4								7

Table 2.2: Morphology classes assigned to clusters by two observers (using X-ray data alone).

"candidate clusters" in the NED were not classed as contaminated unless the "candidate clusters" also had X-ray emission.

The images were then compared to the NED to check that the chosen redshifts corresponded to the peak in X-ray emission, if it was visible. Redshifts from galaxy clusters were accepted if their given position was less than 3′ from the centre of the X-ray emission. Two cluster observations were removed from the final list as their redshift did not correspond to the observed emission. In many cases a bright galaxy (often found in the Sloan Digital Sky Survey) was found to coincide with the peak of the X-ray emission, and in these cases the redshift of the galaxy, if known, was also checked. For clusters that had more than one redshift measurement (for example a cluster redshift and a cD galaxy redshift) the cluster redshift was accepted if $\delta z/z < 0.1$. Otherwise the literature was examined in detail to determine the most accurate redshift - these clusters are flagged in Table 2.3. In addition one bright cluster has a revised redshift due to an iron emission line in the X-ray spectrum, as described in Section 2.4.4 (all of the other bright clusters had any X-ray emission lines at the same redshift as the optical data).

2.4.3 The final cluster sample

A final sample of uncontaminated confirmed clusters was constructed to ensure that the analysis is not affected by additional clusters in the field of view. These contaminating clusters could contain AGN, which would confuse any analysis of the cluster AGN population at a given cluster redshift or morphology. In addition these clusters may contribute to the lensing of background AGN (see Section 2.6.11), although this is likely to be minimal in the case of **1c, 2c** and **3c**. This sample therefore consists of those observations with morphology class **1, 2** or **3**, with $0.1 < z < 1$.

Weakly contaminated cluster fields (**1c, 2c** and **3c**) were included in a second sample, as the contamination may have a minimal effect on the number of AGN, and if this is true

then including these data may increase the statistical significance of any results.

The eight $z > 1$ cluster observations were placed in a third sample, regardless of the reality or extent of their emission, as at this redshift range the observed clusters are all centred on active galaxies, and often the extended emission may be too faint to detect. In some cases the 'cluster' emission is clearly highly disturbed, and possibly emitted by AGN jets or, if the cD galaxy contains a radio source, scattering of the CMB by non-thermal electrons (Fabian et al. 2003). In general these objects are better classified as proto-clusters, and so are analysed separately from the rest of the sample.

The fields with no observable cluster emission, and with $z < 1$, were removed from the sample, as the cluster cannot be confirmed, and the centre cannot be found other than by the position of the source with the optical redshift, which may not be the true cluster centre.

The final cluster fields, split into the above categories, are described in Table 2.3. The table columns are listed below, and entries marked with a note ('N'), are explained in the notes for Table 2.3[10]

- Name - Name of cluster (in the Chandra observation log)
- NED Name - Name of cluster in the NED. If more then one cluster name exists then the nearest is given. If there is no cluster within 2′ then the nearest object name at the cluster redshift is given.
- OBS ID - Chandra Observation ID

[10]Notes for Table 2.3:

N0 - the NED gives z=0.35, but the X-ray spectral data is fit far better with z=0.38.
N1 - the NED gives two redshifts, but only one is given in the paper which NED refers to.
N2 - the contaminating cluster is not visible in the X-ray image, but is confirmed from optical data.
N3 - the contaminating cluster is not visible in the X-ray image, but has been detected using weak lensing analysis.
N4 - this field contains two contaminating clusters, one X-ray detected and confirmed optical cluster, which are not co-incident.
N5 - the average of two quoted redshifts (for two spatially nearby clusters) is given.
References are as follows: [1]-LaRoque et al. (2003); [2]-Stocke et al. (1991); [3]-Smail et al. (1993); [4]-Böhringer et al. (2000); [5]-Vikhlinin et al. (1998); [6]-Struble and Rood (1999); [7]-de Grandi et al. (1999); [8]-Caccianiga et al. (2000); [9]-Ebeling et al. (1998); [10]-Gioia et al. (1998); [11]-De Grandi and Molendi (2002); [12]-Wei et al. (1999); [13]-Gómez et al. (2000); [14]-Aller et al. (1992); [15]-Roukema and Bajtlik (1999); [16]-Schindler et al. (2001); [17]-Mullis et al. (2003); [18]-Ebeling et al. (1996a); [19]-Allen et al. (1992); [20]-SDSS DR3, see Stoughton (2002); [21]-Perlman et al. (2002); [22]-Böhringer et al. (2004); [23]-Gioia and Luppino (1994); [24]-Borgani and Guzzo (2001); [25]-Ebeling et al. (2001b); [26]-Spinrad et al. (1985); [27]-SDSS DR1, see Stoughton (2002); [28]-Holden et al. (2002); [29]-Ponman et al. (1994); [30]-Schindler et al. (1995); [31]-Cohen and Kneib (2002); [32]-Schade et al. (1997); [33]-Böhringer et al. (2004); [34]-Liang et al. (2000); [35]-Edge et al. (2003); [36]-Yee et al. (1996); [37]-Abell et al. (1989); [38]-Couch et al. (1998); [39]-Goto et al. (2002); [40]-Jones et al. (2003); [41]-Cao et al. (1999); [42]-Henry et al. (1997); [43]-Caretta et al. (2002); [44]-Della Ceca et al. (2000); [45]-White (2000); [46]-Tucker et al. (1998); [47]-Postman et al. (1988); [48]-SDSS DR2, see Stoughton (2002); [49]-Willick et al. (2001); [50]-Arnaud (1992); [51]-Schwope et al. (2000); [52]-Pierre et al. (1997); [53]-Molinari et al. (1994); [54]-Stern et al. (2003); [55]-Stanford et al. (2002); [56]-Benoist et al. (2002); [57]-Pentericci et al. (2000); [58]-Blakeslee et al. (2003); [59]-Hewitt and Burbidge (1991); [60]-Donahue et al. (2002); [61]-Ellis and Jones (2004); [62]-Pascarelle et al. (1996)

- RA & DEC - Position of cluster as determined from the X-ray emission (J2000)
- Array - Detector or CCDs used
- Time - Good exposure time after filtering (average over the selected chips)
- F_x - Cluster observed frame 0.5-8keV flux (10^{-12}erg/cm^2/sec)
- L_x1 - Cluster rest frame 0.5-8keV luminosity (10^{44}erg/sec)
- L_x2 - Cluster rest frame 0.1-2.4keV luminosity (10^{44}erg/sec)
- rχ^2 - reduced χ^2 of the XSPEC fit to the cluster spectrum
- Morph - Morphology category
- Redshift - Cluster redshift
- Ref - Source of cluster redshift, see the footnote of notes for Table 2.3.

2.4.4 Cluster luminosities and temperatures

To compare clusters at different redshifts, luminosities need to be found in the same rest-frame band for each cluster. This information cannot be extracted directly from the image without assuming a spectrum, which is a rather crude method given the quality of the data. Instead, to get accurate luminosities a spectrum was extracted from the level 2 data for each cluster and fit with a thermal model, which was then evaluated in the given band. The following analysis is only valid for clusters with morphology classes 1-3, and excluding any contaminating clusters, as listed in Table 2.3. If an observation consists of a merger between two sub-clusters, a model spectrum with a single temperature may not be valid, but as shown later this has minimal effect on the calculated luminosities.

Energy calibration is obviously far more important for spectral analysis than for the image analysis, and it was found to be necessary to re-reduce some of the data. For the spectral analysis any observations taken with a non standard focal plane temperature ($\gtrsim$ 153K) were re-reduced with the appropriate gain files to ensure that the energies assigned to each photon were correct. The energy corrections are small, so neglecting to correct for this has no effect on the point source properties, only the cluster spectrum. As the event files were previously filtered for energies of $0.5 - 8$keV the spectra were extracted and fit over this energy range.

Spectra were extracted from circular apertures centred on the cluster centre, which was defined as the maximum of the smoothed, source-subtracted image described in Section 2.6.3. The aperture was selected to include $\sim$ 99.5% of the cluster counts, assuming a constant background rate outside the cluster. The background was taken from an annulus with inner and outer radii of 1.1 and 1.49 times the cluster annulus, which gives the same

Table 2.3

Name	NED Name	OBS ID	RA	DEC	Array	Time	F_x	L_x1	L_x2	rχ^2	Morph	Redshift	Ref
Morphology 1 clusters:													
MS0015+16	CL 0016+1609	520	00:18:33.6	+16:26:12.6	I	67.2	2.32	23.06	8.31	0.92	1	0.544	1,2
CL0024+17	ZwCl 0024.0+1652:[DG9	929	00:26:35.8	+17:09:41.1	S	38.9	0.50	2.71	1.32	0.90	1	0.39	3
RXJ0027+26	RX J0027.6+2616	3249	00:27:45.4	+26:16:22.5	I	9.9	0.83	3.51	1.35	0.96	1	0.367	4
RXJ0030+26	CRSS J0030.5+2618	1190,1226	00:30:34.0	+26:18:09.9	S	37.1	0.27	2.37	0.94	1.03	1	0.50	5
A68	RX J0037.0+0909	3250	00:37:06.4	+09:09:29.3	I	10.0	4.18	7.61	2.87	0.91	1	0.255	6
A209	APMUKS(BJ) B012925.89	522,3579	01:31:53.4	-13:36:44.1	I	19.9	6.94	8.03	3.58	0.99	1	0.206	6
RXJ0232-44	RXC J0232.2-4420	4993	02:32:18.5	-44:20:48.2	I	18.0	6.89	16.55	7.42	1.11	1	0.284	7
A383	APMUKS(BJ) B024532.67	524,2320	02:48:03.5	-03:31:44.4	I	29.2	5.46	5.36	2.79	1.19	1	0.187	6
MS0302+16	Cl 0302+1658	525	03:05:31.6	+17:10:08.6	I	10.0	0.45	2.84	1.19	0.38	1	0.424	2
MACS_J0417-11	RBS 0531	3270	04:17:34.7	-11:54:35.7	I	12.0	6.33	39.05	14.67	0.98	1	0.44	8
RXJ0439+07	RX J0439.0+0715	526,1449,3583	04:39:00.7	+07:16:05.6	I	27.0	5.19	7.66	2.86	0.95	1	0.23	9
RXJ0439+05	RX J0439.0+0520	527	04:39:02.3	+05:20:44.0	I	9.5	3.73	4.55	2.00	0.72	1	0.208	9
MS0440+02	MS 0440.5+0204	4196	04:43:09.9	+02:10:19.7	6,7	45.1	1.55	1.53	0.63	1.22	1	0.19	2,10
RXJ0528-39	RBS 0653	4994	05:28:52.8	-39:28:20.5	I	16.8	4.42	10.48	4.66	0.90	1	0.284	7
MACS_J0647+70	MACS J0647.7+7015	3196,3584	06:47:50.3	+70:14:54.6	I	39.0	1.68	19.07	6.33	0.83	1	0.584	1
MS0735+74	ZwCl 0735.7+7421	4197	07:41:44.6	+74:14:37.3	6,7	45.3	5.77	7.81	3.92	1.38	1	0.216	2
MACS_J0744+39	MACS J0744.8+3927	3197,3585,6111	07:44:52.7	+39:27:26.9	I	89.0	1.39	24.35	8.58	1.15	1	0.686	1
PKS0745-19	PKS 0745-19 Cluster	508,2427	07:47:31.4	-19:17:41.7	S	36.8	57.56	14.87	4.24	1.56	1	0.103	11
RXJ0819+63	RX J0819.6+6336	2199	08:19:26.0	+63:37:24.0	S	14.5	2.98	1.10	0.60	1.11	1	0.119	9
RXJ0821+07	RX J0820.9+0751	1647	08:21:02.0	+07:51:48.8	S	8.2	1.63	0.51	0.33	1.02	1	0.11	12
A665	ZwCl 0826.1+6554	531,3586	08:30:58.7	+65:50:31.4	I	38.6	9.12	10.99	4.50	1.13	1	0.1819	6,13
4C55+16	4C +55.16	4940	08:34:55.0	+55:34:21.2	6,7	92.0	3.59	6.35	3.29	1.44	1	0.242	14
MS0839+29	NSC J084254+292723	2224	08:42:55.9	+29:27:25.5	S	29.4	3.14	3.39	1.84	1.25	1	0.194	2
A697	ABELL 0697	532,4217	08:42:57.5	+36:21:56.1	I	23.6	7.30	16.61	6.50	1.10	1	0.282	6
ZW1953	RX J0850.1+3604	1659	08:50:06.7	+36:04:17.1	I	22.1	2.94	12.99	5.19	0.93	1	0.378	4,9
I09104	MACS J0913.7+4056	509	09:13:45.4	+40:56:27.6	S	7.8	1.46	10.00	4.18	0.87	1	0.442	15
A773	RXC J0917.8+5143	533,3588,5006	09:17:52.9	+51:43:39.2	I	30.4	6.57	8.54	3.87	1.03	1	0.217	4,6
RBS797	MACS J0947.2+7623	2202	09:47:13.0	+76:23:14.2	I	11.7	6.30	24.61	11.48	0.91	1	0.35	16
MACS_J0949+17	1RXS J094953.8+170803	3274	09:49:51.8	+17:07:08.1	I	14.3	3.19	14.28	5.42	0.73	1	0.383	4
ZW2701	ZwCl 0949.6+5207	3195	09:52:49.3	+51:53:04.9	S	26.5	4.35	5.87	3.26	1.01	1	0.214	9

Continued on next page...

Table 2.3 – Continued

Name	NED Name	OBS ID	RA	DEC	Array	Time	F_x	L_x1	L_x2	$r\chi^2$	Morph	Redshift	Ref
CL0956+41	RX J0956.0+4107	5294	09:56:03.4	+41:07:09.3	I	17.3	0.24	3.35	1.57	0.66	1	0.587	17
A907	ABELL 0907	535,3185,3205	09:58:21.9	-11:03:50.9	I	104.6	8.58	5.31	2.44	1.42	1	0.153	18
MS1008-12	MS 1008.1-1224	926	10:10:32.3	-12:39:34.5	I	43.6	2.21	6.00	2.40	1.23	1	0.301	2
ZW3146	ZwCl 1021.0+0426	909	10:23:39.7	+04:11:09.2	I	45.8	10.14	25.66	11.40	1.00	1	0.2906	18
A1068	ABELL 1068	1652	10:40:44.6	+39:57:10.2	S	26.7	10.63	5.41	3.22	1.50	1	0.1375	6
MACS_J1108+09	SDSS J110855.36+09060	3252,5009	11:08:55.3	+09:05:58.5	I	34.1	1.18	8.73	3.77	0.86	1	0.463	20
CL1113-26	WARP J1113.0-2615	915	11:13:05.1	-26:15:38.8	I	104.2	0.10	2.46	1.01	1.09	1	0.725	21
A1204	ABELL 1204	2205	11:13:20.4	+17:35:38.7	I	23.5	6.78	5.52	3.41	1.24	1	0.1706	4,6
MACS_J1115+53	SDSS J111514.85+53195	3253	11:15:15.6	+53:19:54.0	I	8.8	2.03	14.22	5.73	0.92	1	0.466	20
MACS_J1115+01	SDSS J111551.90+01295	3275	11:15:51.9	+01:29:55.6	I	14.6	4.84	18.57	7.72	0.93	1	0.38(N0)	22
V1121+23	RX J1120.9+2326	1660	11:20:57.4	+23:26:33.1	I	70.6	0.25	3.30	1.79	0.95	1	0.562	17
MS1137+66	MS 1137.5+6625	536	11:40:22.3	+66:08:16.1	I	117.2	0.27	7.21	2.94	0.87	1	0.782	23
A1361	ABELL 1361	2200,3369	11:43:39.7	+46:21:20.0	S	15.9	4.60	1.64	0.97	1.07	1	0.117	4,6
A1413	ABELL 1413	537,1661,5003	11:55:18.0	+23:24:16.2	I	94.1	16.17	8.33	3.65	1.28	1	0.142	4,6
A1483	RX J1157.3+3336	538	11:57:17.3	+33:36:39.9	I	9.8	3.22	4.15	1.98	0.91	1	0.2138	4,6
MACS_J1206-08	RXC J1206.2-0848	3277	12:06:12.4	-08:48:03.9	I	23.4	4.70	28.82	10.65	1.07	1	0.441	22,24
CL1216+26	RX J1216.3+2633	4931	12:16:19.9	+26:33:12.4	I	17.5	0.20	1.41	0.80	0.86	1	0.428	5
V1221+49	RX J1221.4+4918	1662	12:21:26.3	+49:18:27.2	I	78.7	0.38	7.47	3.26	0.95	1	0.7	5
CL1226+33	CL J1226.9+3332	3180	12:26:57.9	+33:32:47.4	I	31.6	0.77	24.28	9.35	0.85	1	0.89	25
3C280	3C 280	2210	12:56:58.2	+47:20:22.2	S	45.7	0.01	0.55	0.15	0.46	1	0.996	17,26
A1664	ABELL 3541	1648	13:03:42.4	-24:14:45.3	S	9.7	7.78	3.35	1.80	1.28	1	0.128	6
MACS_J1311-03	SDSS J131101.79-03103	3258,6110	13:11:01.7	-03:10:38.5	I	77.8	1.12	9.92	4.80	0.96	1	0.49	27
A1689	ABELL 1689:[TCG90] 00	540,1663,5004	13:11:29.5	-01:20:30.1	I	40.8	20.84	18.35	7.78	1.12	1	0.1828	6
RXJ1317+29	RDCS J1317+2911	2228	13:17:21.5	+29:11:16.2	I	111.0	0.01	0.58	0.31	0.72	1	0.805	28
RXJ1340+40	RX J1340.5+4017	3223	13:40:32.9	+40:17:38.7	S	46.4	0.16	0.13	0.13	1.05	1	0.171	29
RXJ1347-11	LCDCS 0829	3592	13:47:30.8	-11:45:10.1	I	57.4	10.78	68.09	23.48	1.16	1	0.451	30,31
RXJ1350+60	RDCS J1350+6007	2229	13:50:48.3	+60:07:06.0	I	58.1	0.12	3.99	1.98	1.05	1	0.804	28
ZW1358+62	ZwCl 1358.1+6245	516	13:59:50.6	+62:31:02.9	S	52.1	2.42	8.31	3.80	1.11	1	0.328	2
A1835	ABELL 1835	495,496	14:01:02.0	+02:52:41.6	S	30.2	18.40	34.36	14.89	1.58	1	0.253	6
3C295	3C 295 CLUSTER	578	14:11:20.4	+52:12:10.0	S	17.9	0.87	6.92	3.43	1.21	1	0.46	32
V1416+44	RX J1416.4+4446	541	14:16:27.9	+44:46:44.5	I	30.7	0.58	3.38	1.80	1.02	1	0.4	5

Continued on next page...

Table 2.3 – Continued

Name	NED Name	OBS ID	RA	DEC	Array	Time	F_x	L_x1	L_x2	rχ^2	Morph	Redshift	Ref
MACS_J1423+24	MACS J1423.8+2404	4195	14:23:47.9	+24:04:42.6	6,7	115.2	1.92	22.14	9.91	1.20	1	0.545	1
A1914	ABELL 1914	542,3593	14:26:02.0	+37:49:32.8	I	26.7	19.03	14.54	6.18	1.00	1	0.171	6
RXJ1504-02	RBS 1460	4935	15:04:07.5	-02:48:17.7	I	13.3	23.76	30.82	13.27	1.29	1	0.2153	33
A2034	ABELL 2034	2204	15:10:11.8	+33:30:54.3	I	53.8	10.73	3.41	1.59	0.97	1	0.113	6
RXJ1532+30	RX J1532.5+3021	1665	15:32:53.8	+30:20:58.6	I	9.9	5.92	22.92	11.18	1.08	1	0.345(N1)	9
A2111	ABELL 2111	544	15:39:41.3	+34:25:06.7	I	10.3	3.57	5.18	2.26	1.02	1	0.229	6
A2104	ABELL 2104	895	15:40:07.9	-03:18:17.5	S	49.0	8.94	5.42	1.80	1.72	1	0.1554	6,34
RXJ1552+20	WARP J1552.2+2013	3214	15:52:12.8	+20:13:39.9	S	14.9	0.23	0.11	0.08	1.06	1	0.136	5
MACS_J1621+38	MACS J1621.4+3810	3594,6109,6172	16:21:24.7	+38:10:08.5	I	77.2	1.50	11.50	5.46	1.03	1	0.465	35
A2204	ABELL 2204	499	16:32:46.9	+05:34:31.5	S	10.0	32.58	19.81	8.68	1.24	1	0.152	6
A2218	ABELL 2218	553,1454,1666	16:35:51.5	+66:12:36.8	I	60.3	5.76	4.77	2.11	0.96	1	0.176	6
A2219	ABELL 2219	896	16:40:19.9	+46:42:35.3	S	42.1	16.04	22.61	9.30	1.57	1	0.226	6
A2259	ABELL 2259	3245	17:20:08.4	+27:40:11.0	I	10.0	6.37	4.58	2.14	0.99	1	0.164	6
RXJ1720+26	RBS 1639	1453,3224,4361	17:20:10.1	+26:37:30.8	I	54.4	14.37	10.30	4.69	1.22	1	0.164	9
MACS_J1720+35	MACS J1720.2+3536	3280	17:20:16.7	+35:36:23.1	I	20.8	2.86	14.33	6.18	1.08	1	0.391	35
A2294	ABELL 2294	3246	17:24:12.0	+85:53:10.8	I	9.6	7.97	6.48	2.23	1.06	1	0.178	6
MS2053-04	MS 2053.7-0449	551,1667	20:56:21.1	-04:37:46.3	I	88.4	0.21	2.72	1.13	0.96	1	0.583	2
MACS_J2129-07	MACS J2129.4-0741	3199,3595	21:29:26.0	-07:41:28.2	I	36.7	1.61	18.25	6.57	1.00	1	0.57	1
RXJ2129+00	RBS 1748	552	21:29:40.0	+00:05:19.7	I	9.9	6.72	9.54	4.24	0.98	1	0.224	9
MS2137-23	MS 2137.3-2353	928	21:40:15.2	-23:39:40.1	S	39.4	3.69	11.63	5.54	1.34	1	0.313	2
A2390	ABELL 2390	4193	21:53:39.0	+17:41:15.3	6,7	93.7	16.19	23.69	9.01	1.66	1	0.23	6,36
A2409	ABELL 2409	3247	22:00:52.9	+20:58:22.3	I	10.2	8.75	5.00	2.15	0.97	1	0.148	6
MACS_J2211-03	1RXS J221144.6-034947	3284	22:11:45.9	-03:49:46.6	I	17.7	7.06	14.29	5.13	1.04	1	0.27	33
MACS_J2245+26	1RXS J224505.2+263758	3287	22:45:04.7	+26:38:03.5	I	16.1	3.36	9.52	4.02	1.05	1	0.304	4
RXJ2247+03	RX J2247.4+0337	911	22:47:28.0	+03:37:00.8	I	48.7	0.12	0.11	0.08	1.02	1	0.18	5
AS1063	ABELL S1063	4966	22:48:44.8	-44:31:46.4	I	26.6	11.12	40.28	16.32	1.09	1	0.348	22
AC114+AS1077	ABELL S1077:[CN84] 00	1562	22:58:48.2	-34:48:07.3	S	72.1	4.74	13.72	5.69	2.18	1	0.31	37,38
A2631	ABELL 2631	3248	23:37:38.7	+00:16:08.5	I	9.1	4.12	9.19	3.78	1.05	1	0.278	6,22
A2667	NVSS J235139-260514	2214	23:51:39.3	-26:05:03.5	S	9.6	11.90	17.72	8.71	1.14	1	0.226	22,25

Continued on next page...

Table 2.3 – Continued

Name	NED Name	OBS ID	RA	DEC	Array	Time	F_x	L_x1	L_x2	rχ^2	Morph	Redshift	Ref
Morphology 2 clusters:													
MACS_J0404+11	RX J0404.6+1109	3269	04:04:32.9	+11:08:08.0	I	21.7	0.89	3.42	1.14	0.95	2	0.3548	4
CL0552-36	RX J0522.2-3625	4926	05:22:15.2	-36:25:02.6	I	18.5	0.21	1.71	0.75	0.73	2	0.472	17
MS1006+12	ZwCl 1006.1+1201	925	10:08:47.5	+11:47:36.1	I	29.3	2.63	3.61	1.61	1.25	2	0.221	2
A1201	ABELL 1201	4216	11:12:54.6	+13:26:02.4	S	34.2	3.21	2.51	1.29	1.22	2	0.1688	6
Q1213-00	SDSS J121531.35-00371	4201	12:15:30.2	-00:37:03.0	I	43.1	0.40	1.95	0.63	1.28	2	0.413	39
RXJ1256+25	RX J1256.0+255	3212	12:56:02.5	+25:56:38.0	S	26.9	0.13	0.22	0.14	0.91	2	0.232	5,40
A1763	ABELL 1763	3591	13:35:18.3	+41:00:00.7	I	19.6	5.85	8.08	3.78	1.26	2	0.223	41
MS1621+26	MS 1621.5+2640	546	16:23:35.2	+26:34:21.3	I	29.9	1.10	6.54	2.60	1.02	2	0.426	2
RXJ1716+67	RX J1716.4+6708	548	17:16:48.9	+67:08:25.4	I	51.6	0.32	8.82	3.18	0.76	2	0.813	42
A2261	ABELL 2261	550,5007	17:22:27.2	+32:07:57.0	I	33.3	9.02	12.53	5.16	1.08	2	0.224	6
MACS_J1824+43	MACS J1824.3+4309	3255	18:24:18.5	+43:09:54.2	I	14.9	0.03	0.41	0.36	0.07	2	0.487	35
MACS_J2228+20	RX J2228.5+2036	3285	22:28:33.2	+20:37:12.9	I	19.8	2.99	16.25	6.30	0.81	2	0.412	4
A2550	APMUKS(BJ) B230856.99	2225	23:11:35.7	-21:44:46.8	S	58.6	1.03	0.42	0.34	1.23	2	0.123	43
Morphology 3 clusters:													
A2744	ABELL 2744	2212	00:14:19.1	-30:23:23.1	6,7	24.7	8.18	23.31	9.55	1.25	3	0.308	6
3C28	EXSS 0053.1+2608	3233	00:55:50.5	+26:24:35.5	I	49.6	2.98	3.28	1.65	1.02	3	0.197	6
CL0152-13	CL J0152.7-1357	913	01:52:44.4	-13:57:17.4	I	36.3	0.19	5.12	1.94	0.99	3	0.831	44
A521	ABELL 0521:[FMC2003]	901	04:54:06.6	-10:13:09.4	I	38.5	3.50	6.48	2.72	1.09	3	0.253	45
A520	RXC J0454.1+0255	528,4215	04:54:10.1	+02:54:40.7	I	75.5	6.38	7.14	2.81	1.20	3	0.203	4,6
1E0657-56	1RXS J065830.3-555702	554,3184	06:58:30.3	-55:56:34.6	I	112.4	13.22	32.58	11.24	1.14	3	0.296	46
Z5247	RXC J1234.2+0947	539	12:34:21.7	+09:46:56.9	I	9.1	2.43	3.66	1.83	0.79	3	0.229	4
A1682	ABELL 1682	3244	13:06:50.5	+46:33:25.3	I	8.9	4.51	6.83	2.86	1.12	3	0.234	6
A1758	RBS 1283	2213	13:32:42.8	+50:32:55.0	6,7	55.8	7.49	17.28	7.26	1.43	3	0.28	4,6
A2069	RX J1524.1+2952	4965	15:24:08.7	+29:53:00.3	I	52.2	3.19	1.09	0.56	1.08	3	0.116	6,47
Morphology 1c clusters:													
A267	SDSS CE J028.177532+0	1448,3580	01:52:42.2	+01:00:40.5	I	27.4	4.16	6.27	2.81	1.13	1c	0.23	4,6
MACS_J0159-08	SDSS J015949.34-084958.7	3265,6106	01:59:49.3	-08:49:59.9	I	52.8	4.18	21.81	9.66	1.07	1c	0.4	48
MS0451-03	MACS J0454.1-0300	902	04:54:11.2	-03:00:51.3	S	43.5	2.37	25.07	9.06	1.08	1c	0.55	1,23

Continued on next page...

Table 2.3 – Continued

Name	NED Name	OBS ID	RA	DEC	Array	Time	F_x	L_x1	L_x2	rχ^2	Morph	Redshift	Ref
MACS_J0717+37	MACS J0717.5+3745	1655,4200	07:17:31.3	+37:45:29.5	I	78.7	3.69	35.91	11.53	1.17	1c	0.548	1
A586	ABELL 0586	530	07:32:20.3	+31:37:56.2	I	10.0	7.14	5.51	2.27	1.02	1c	0.171	6
A611	ABELL 0611	3194	08:00:56.7	+36:03:23.2	S	35.9	3.82	9.62	4.18	1.22	1c	0.288	6
MS0906+11	MS 0906.5+1110	924	09:09:12.8	+10:58:33.0	I	29.6	4.69	3.85	1.73	0.94	1c	0.175	2,4,6
CL0926+12	RX J0926.6+1242	4929	09:26:36.5	+12:43:06.3	I	18.6	0.26	2.50	1.30	0.61	1c	0.489	17
A963	NSC J101706+390221	903	10:17:03.6	+39:02:53.4	S	36.2	7.98	9.54	4.53	1.16	1c	0.206	4,6
MS1054-03	MS 1054.4-0321	512	10:56:59.0	-03:37:35.0	S	85.7	0.63	18.13	6.77	1.04	1c(N2)	0.8231	23,49
CL1117+17	RX J1117.5+1744	4933	11:17:30.0	+17:44:49.5	I	18.7	0.12	1.50	0.61	0.43	1c(N2)	0.584	17
MACS_J1149+22	MACS J1149.5+2223	1656,3589	11:49:35.0	+22:24:06.7	I	38.5	2.20	1.82	0.83	1.06	1c	0.1761	1,4
MACS_J1319+70	RX J1320.0+7003	3278	13:20:07.9	+70:04:36.8	I	20.5	1.74	5.74	2.58	0.73	1c(N3)	0.328	4,6
MS1455+22	ZwCl 1454.8+2233	543,4192	14:57:15.0	+22:20:34.7	I	101.4	5.97	11.96	6.04	1.28	1c	0.2578	19
A2163	RBS 1571	545,1653	16:15:45.8	-06:09:01.8	I	80.3	24.45	25.75	7.58	1.65	1c	0.203	50,51
RXJ2011-57	1RXS J201127.9-572507	4995	20:11:27.1	-57:25:10.1	I	23.9	1.55	3.75	1.91	0.77	1c	0.2786	33
MACS_J2311+03	RX J2311.5+0338	3288	23:11:33.2	+03:38:05.0	I	13.1	4.09	10.81	4.19	1.05	1c(N4)	0.2998	4,6
Morphology 2c clusters:													
MACS_J1131-19	1RXS J113153.7-195543	3276	11:31:54.8	-19:55:49.5	I	13.8	4.47	12.36	4.74	0.90	2c	0.307	6,52
A1942	ABELL 1942:[SED2002]	3290	14:38:21.9	+03:40:09.7	I	56.7	1.14	1.56	0.73	0.96	2c	0.22	53
High redshift (proto)clusters:													
CL0442+02	CXO 02	3242	04:42:25.6	+02:00:07.0	I	43.4	0.00	0.00	0.00	0.00	0	1.11	54
RXJ0910+54	[SHR2002] 024	2227,2452	09:10:44.6	+54:22:03.8	I	168.8	0.02	1.46	0.57	1.02	4	1.11	55
EIS0954-20	EIS J0954-2023b	4378	09:54:45.1	-20:22:26.4	S	14.8	0.00	0.00	0.00	0.00	0	1.04(N5)	56
B1138-262	PKS 1138-26:[SID2003]	898	11:40:46.1	-26:30:20.7	S	32.5	0.00	0.00	0.00	0.00	1	2.16	57
RDCS1252-29	RDCS J1252-2927	4198,4403	12:52:54.5	-29:27:17.1	I	188.2	0.05	4.52	1.53	1.12	1	1.23	58
3C294	3C 294	3207,3445	14:06:44.0	+34:11:26.1	6,7	190.9	0.01	4.08	1.54	0.47	2	1.78	59,60
CL1415+36	WARP J1415.1+3612	4163	14:15:11.0	+36:12:03.5	I	88.8	0.13	7.16	2.98	0.91	1c	1.03	61
53W002	HERC:[Fnn2002] 02	2221	17:13:52.2	+50:15:22.6	S	37.4	0.00	0.00	0.00	0.00	0	2.39	62

Table 2.3: The cluster sample, split by morphological class. Details of the columns, references and notes are given in the text.

area as the cluster aperture and has negligible contamination from the cluster. Point source regions were subtracted from both the cluster and background apertures using the WAVDETECT output source ellipses for all sources with significance > 3 (Equation 2.8). These regions were removed from the analysis, and as they are so small (typically $\ll 1\%$ of the area) no correction for the removed area was made. The regions for bright point sources within the apertures were checked, and enlarged if necessary, to ensure that they did not contaminate the cluster emission. Mask files were also used to remove areas of bad or no exposure in the selected regions.

The response functions for the detector (RMF and ARF, see Appendix A.3.6) were calculated using the MKRMF and MKARF tools in CIAO. The response was calculated for the central point of the cluster aperture, rather than finding a weighted response over the full aperture, due to the time required to calculate weighted response files for each cluster. The response for the background annulus was assumed to be the same as that for the cluster aperture, so the same files were used. This is a valid assumption as the maximum variation in exposure map over a chip (excluding bad columns) is $\sim 20\%$, measuring corner to corner. In general the annulus does not cover a whole chip, and falls toward the centre, so the maximum change in exposure map is $\lesssim 10\%$. Furthermore, as the background is selected from around the cluster, and as the cluster does not generally lie at the point of maximum exposure map, the changes of exposure in the background annulus largely cancel out and the mean is a good estimate of the true background behind the cluster. Other changes in response, such as quantum efficiency, were not found to vary significantly over the area. Tests on three clusters found that the difference in flux using a single central response compared to weighted responses (calculated over all pixels for both the aperture and background annulus) was $< 2\%$, which is negligible compared to the errors in fitting the model.

Where more than one observation of a cluster existed the apertures were defined using the merged final images. Spectra were extracted, and response functions calculated, for each observation of the cluster.

Spectra were fitted using XSPEC v11.3.1. The spectra were binned to a minimum of 25 counts per energy interval and fitted over the range $0.5 - 8$keV. An absorbed Raymond-Smith model (Raymond and Smith 1977) was used for all clusters. For each observation the galactic neutral hydrogen density was fixed at the local values (Dickey and Lockman 1990), and the redshift fixed to the value in Table 2.3. The best fit temperature, metal abundance and normalisation of the model were found by minimising χ^2. For clusters with more than one observation the multiple spectra were fit simultaneously, taking into account the differences in exposure time.

The absorbed Raymond-Smith model is a good fit to the cluster data, as seen by the reduced χ^2 values in Table 2.3. Although some of these clusters might have cooling flows, cooling flow models were not fitted to the data. The number of free parameters in a cooling

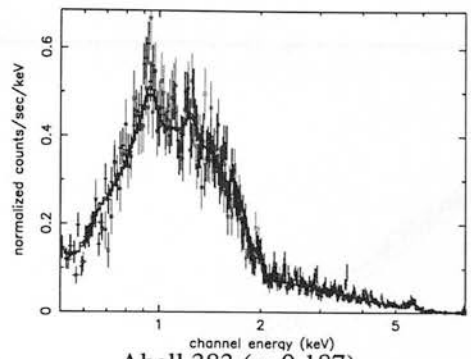

Abell 383 (z=0.187)

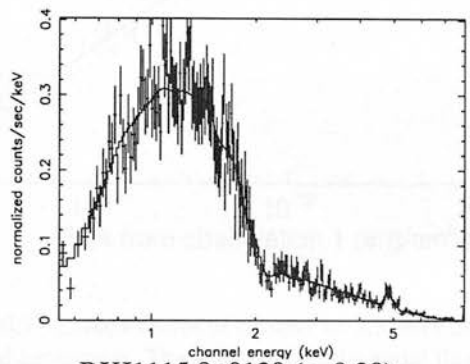

RXJ1115.8+0129 (z=0.38)

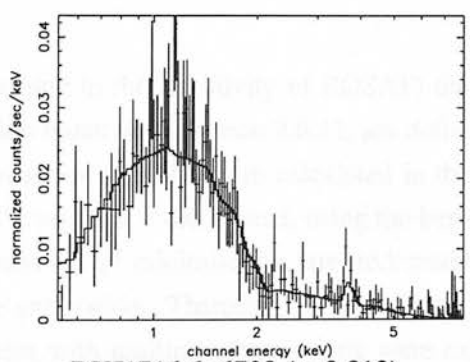

RXJ1716.6+6708 (z=0.813)

Figure 2.3: Spectra and best-fit models for three clusters at a range of redshifts. Abell 383 has two observations with similar exposure times, and the different data points are marked with lines and boxes. The emission line in RXJ1115.8+0129 was used to constrain the redshift in Table 2.3. The best fit temperatures are 4.4 ± 0.1 keV, 7.6 ± 0.5 keV and 8.8 ± 1.6 keV respectively.

flow model make it unrealistic to extract meaningful parameters for many of the fainter clusters, and the luminosities obtained from the absorbed Raymond-Smith model are accurate enough for this study. The spectra and best-fit models for three bright clusters are shown in Figure 2.3.

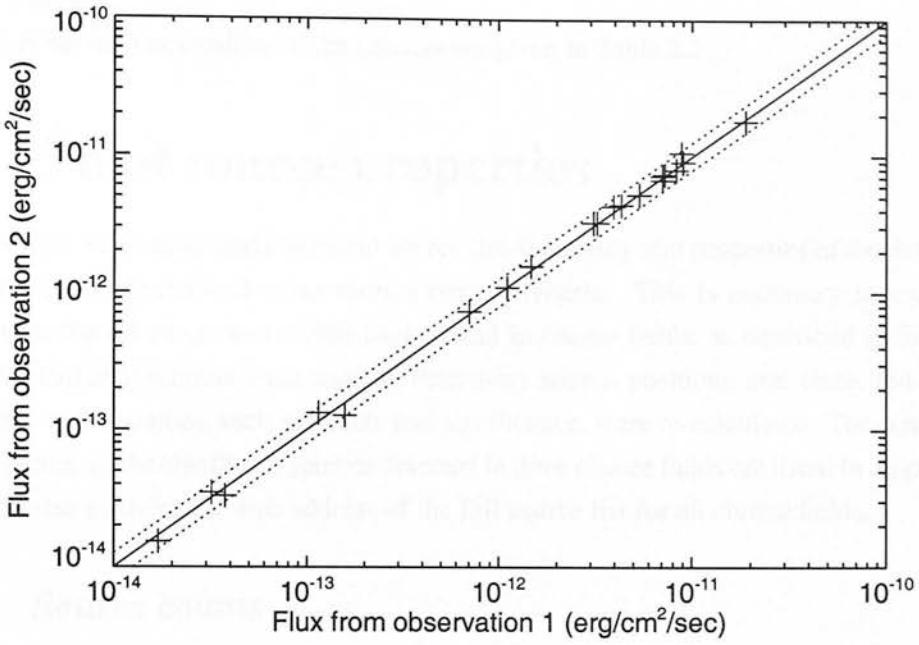

Figure 2.4: The rest-frame 0.1−2.4keV fluxes of clusters which were observed twice. The fluxes for each observation are in good agreement. The solid line marks equal fluxes for the two observations, and the dotted line is the 0.1 dex error.

For historical reasons (due to the sensitivity of ROSAT) the cluster scaling relations, such as the $L_X - \sigma$ relation required in Section 2.6.11, are defined in the rest-frame $0.1 - 2.4$keV. The cluster luminosities were therefore calculated in the rest-frame $0.1 - 2.4$keV band as well as in the rest-frame $0.5 - 8$keV band, using the best-fit model.

The model errors, found by χ^2 minimisation, are underestimated as they do not take into account errors in the calibration. Therefore, to get a better measure of the accuracy of the luminosities, clusters with multiple observations were examined. The spectra for each observation of the same cluster were fitted individually, and the difference between the luminosities found. The results, shown in Figure 2.4, show that the errors in the flux (and therefore luminosity) in the rest-frame $0.1 - 2.4$keV band, due to calibration differences between observations, are less than 0.1 dex at all fluxes.

Using the same method, the errors on the temperature are found to be generally less than 0.1 dex, and always less than 0.3 dex. However, the cluster temperatures found from the best-fit XSPEC model are often highly dependent on the neutral hydrogen density, nH. For example, for Abell 2163 the best-fit temperature for the Dickey and Lockman value of nH is 24keV, but the best-fit model when nH is allowed to vary has a temperature of 15keV (close to the value from Reiprich and Böhringer 2002) with nH increased by 50%. However, even the most extreme change in the temperature and neutral hydrogen density give very similar

shaped models, and the cluster 0.1-2.4keV luminosity, which is the key result here, changes by less than 4%.

The observed luminosities of the clusters are given in Table 2.3.

2.5 Point source properties

To determine an accurate and consistent source list, the reality and properties of the detected sources were re-determined using more stringent criteria. This is necessary in order to account for the effect of the variable background in cluster fields, as described in Section 2.6. WAVDETECT outputs were used to determine source positions and sizes, but other properties of the sources, such as counts and significance, were re-calculated. The positions and properties of the significant sources detected in three cluster fields are listed in Appendix B, which also contains the web address of the full source list for all cluster fields.

2.5.1 Source counts

The output source counts from WAVDETECT can be inaccurate for very faint sources, such as those found in these images. In particular the source counts may be incorrect in regions with large background gradients, such as near the cluster emission, which is a major factor for this study. In addition, for faint sources (particularly those near the axis), a small background fluctuation on the edge of the source can be included in the source, so that WAVDETECT finds a more elliptical region with too few background counts and too many source counts. The source properties were therefore calculated using aperture photometry, as this was found to yield more accurate results.

In order to maximise the signal to noise for individual sources, the WAVDETECT source sizes were used to determine the aperture size for each source, as the current Chandra PSF models are only measured at a few radii, and do not take into account the PSF shape. The orientation of faint WAVDETECT sources can easily be influenced by fluctuations in the background so a circular aperture was used. Although this decreases the signal to noise ratio for elliptical sources it ensures that the detection is uniform across the field. The aperture had radius $1.2 \times r_{\rm max}$, where $r_{\rm max}$ is the semi-major axis of the WAVDETECT 3-sigma ellipse. Extensive testing showed that this radius of aperture maximised the signal to noise for the sample whilst minimising the missed source counts.

Examples of the sources detected by WAVDETECT and the apertures used to calculate the count rates are shown in Figure 2.5.

In X-ray images many sources either overlap with other sources or with areas of bad exposure such as chip gaps (examples of these are shown in Figures 2.5 and 2.6). Rejecting these sources would remove a large proportion of the sample, and make the sky area hard to calculate, so the pipeline corrects for the bad pixels within each source aperture. Pixels

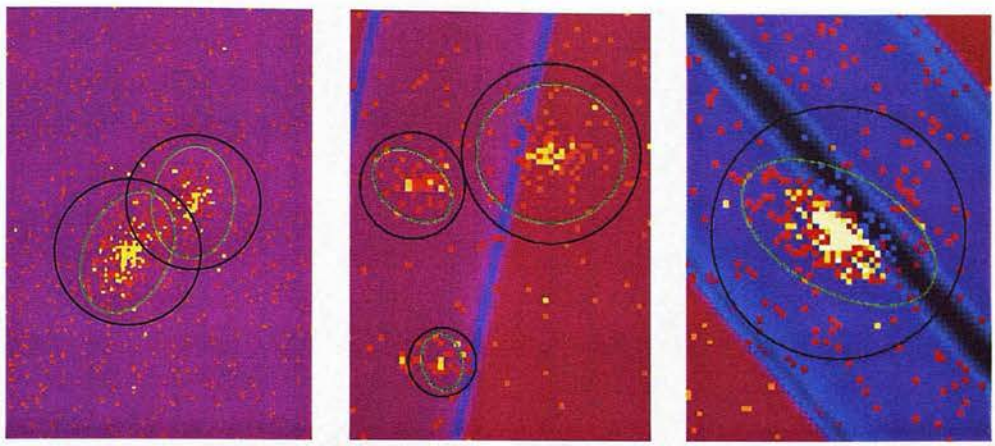

Figure 2.5: Examples of WAVDETECT source regions (green ellipses) and source apertures used (black circles). The sources are plotted over an image combining the exposure map (background colour - pink for highest exposure) and the source counts (orange for one photon, yellow for two). The first image shows two sources which overlap: the overlap region is replaced by the mirror region when calculating the source counts (this effect is obviously more important for bright-faint source pairs). In the second image it is clear that the WAVDETECT source ellipse often misses source counts, whereas the circular aperture is more effective (although not perfect). The third image shows a source overlapping areas of bad exposure (black): these are also replaced by their reflection in the calculations.

in the source aperture were rejected if they were within the aperture of another source, or had exposure below 10 percent of the median value. Due to the elliptical nature of the PSF these pixels were replaced by their reflection on the opposite side of the aperture if possible, or other pixels at the same radius if both sides of the aperture were rejected. Around 3% of the sources detected required some degree of correction, but most had very small areas rejected. This correction resulted in accurate source counts for all sources which had over half of their aperture in good regions - over 99.5 percent of the sample. The remaining sources had significant overlaps with other sources or regions of bad exposure. Their count rates and fluxes are only accurate to within around a factor of 2, and they are flagged in Appendix B.

2.5.2 Background counts

The mean background count rate per pixel was calculated in an annulus of area 10000 pixels, with an inner radius of $1.5 \times r_{\rm max}$. Again, any pixels within $1.5 \times r_{\rm max,i}$ of a nearby source, i, or with exposure less than 10 percent of the median, were rejected.

The background area was chosen to be large enough that statistics for all sources are not limited by uncertainties in the background rate (especially important in low exposure observations), but small enough to cover only the local background. An on-axis source of

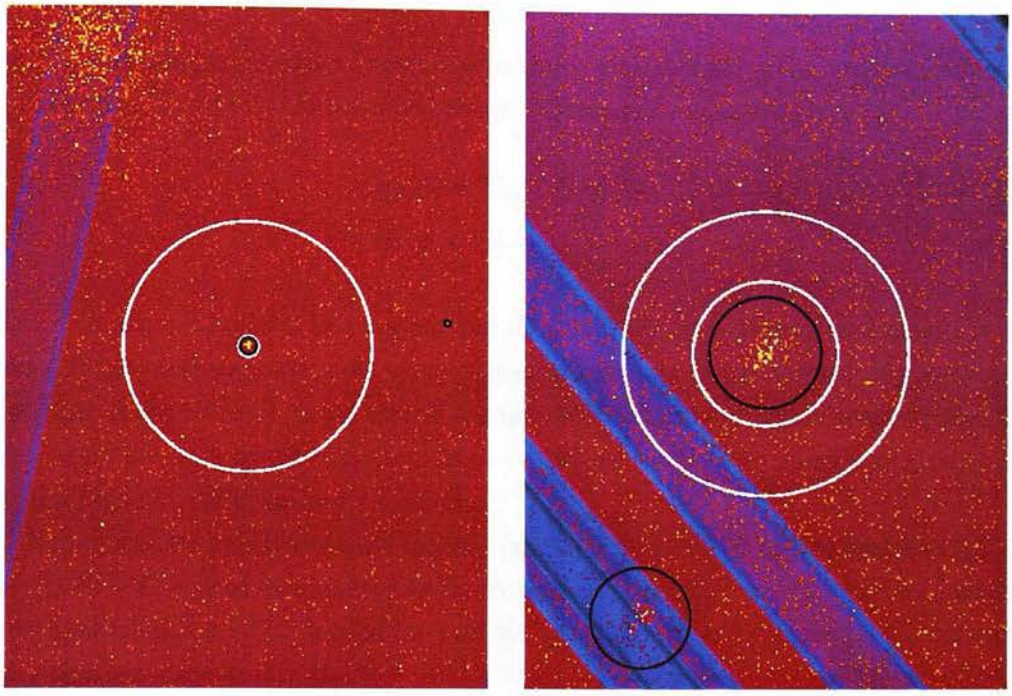

(a) (b)

Figure 2.6: Examples of background regions for a small and large source. By fixing the area of the background annulus only the local background is sampled. The cluster emission is visible in the top left of the first image - if this was near the source then the background may be over-estimated. The image components are as described in Figure 2.5, with the background annulus marked in white.

$r_{\max} = 2$ pixels would have the background calculated between a radius of 3 and 57 pixels, whereas one with $r_{\max} = 30$ on the edge of the chip would have a background region between 45 and 72 pixels radius. Because of the large variations in the PSF, this method works far better than an annulus scaled with aperture size. Two examples of the background region are shown in Figure 2.6.

This background rate is sometimes inaccurate when a source is in or near an area of highly varying background, such as very near a small cluster or in a cluster centre, and this can affect the source flux. However manual examination of cluster fields showed that this is only important when a small cluster is just within a background region, and of six small clusters examined, only one source in one field was affected. This effect is therefore minimal in calculating source significance, and negligible when calculating the properties of the sample as a whole.

2.5.3 Source statistics

Source significances and signal to noise ratios were calculated using the aperture and background counts from the areas described above. The source counts are given by

$$\text{Counts} = C_A - \text{Bkg} \tag{2.2}$$

$$\text{Bkg} = C_B \frac{N_A}{N_B} \frac{E_A}{E_B} \tag{2.3}$$

where C is the total counts in a region, and Bkg the calculated background counts in the region. E the mean exposure map value of good pixels, and N the number of good pixels. Subscripts A and B refer to the source aperture and background region respectively. C_B is scaled by the ratio of the exposures as in $\sim 18\%$ of sources the mean background and aperture exposure differ by over 10 percent.

Throughout the calculations the Gehrels (see Appendix A.1.4) approximation $G(C) = 1 + \sqrt{0.75 + C}$ is used to approximate the Poissonian 1-sigma positive error. As a conservative approximation $G(C)$ is used for both the upper and lower 1σ errors on C, and errors of n-sigma are taken as $n \times G(C)$.
The error on the counts is given by

$$\sigma^2_{\text{Counts}} = (G(C_A))^2 + (\sigma_{\text{Bkg}})^2 \tag{2.4}$$

where the error on the calculated background counts in the annulus, σ_{Bkg}, is

$$\sigma^2_{\text{Bkg}} = \left(G(C_B)\frac{N_A}{N_B}\frac{E_A}{E_B}\right)^2 + \left(G\left(C_B\frac{N_A}{N_B}\frac{E_A}{E_B}\right)\right)^2 \tag{2.5}$$

which is the combination of the error on the estimation of the background count rate, and the error on applying this (low) background value to the aperture. This is best illustrated in the example of a source such as that in Figure 2.6(a). Assume that there are 100 background counts, the exposures are equal and the background area is 50 times the source area. The error on 100 counts is $G(100) = 11.0$ - which scaled by the area gives 2 ± 0.2 background counts. However, the background counts are discrete, so there is also a positive error of $G(2) = 2.65$ on this value - so the background counts could be as high as 4 within the 1σ error.
The source signal to noise (SNR) is then

$$SNR = \text{Counts}/\sigma_{\text{Counts}} \tag{2.6}$$

and the significance, SIG is defined as

$$C_A = \text{Bkg} + \text{SIG} \times \sigma_{\text{Bkg}} \tag{2.7}$$

so that

$$\mathrm{SIG} = \mathrm{Counts}/\sigma_{\mathrm{Bkg}}. \tag{2.8}$$

A cut of $SIG > 3$ was applied to construct a catalogue of real sources. A significance of above 3 means that the source is not a background fluctuation with above a 3-sigma probability. The correlation between SIG and the SNR is very good, with a significance cut of 3 corresponding to a SNR of around 1.5. This cut is more conservative than the WAVDETECT significance parameter, and produces a more robust source list. On average it reduces the WAVDETECT source list by around 18%.

2.5.4 Hardness ratios

For each source a hardness ratio, HR, was calculated by comparing the counts[11] in the hard (2-8keV), H, and soft (0.5-2keV) band, S. The hardness ratio was defined as $HR = \frac{H-S}{H+S}$, and ranges from 1 (hard) to -1 (soft). Images for each observation were created in both of these bands, and the same apertures used as for the full band. To check that the full band aperture sizes are valid (as the PSF is energy dependent) WAVDETECT was run on the hard and soft images for one observation. The source counts derived using these apertures were within the errors of those using the full band apertures with no systematic offset.

Sources were assigned a significance in the hard and soft band images, following the method for the full band image. Those with $SIG > 3$ in the hard and full band images only were assigned $HR = 1^{+0}_{-1}$ and those with $SIG > 3$ in the soft and full band images only were assigned $HR = -1^{+1}_{-0}$. Sources which were significant in the full band image only were given $HR = 0^{+1}_{-1}$. The mean hardness ratio for sources which were significant in both the soft and hard bands is -0.26, and is independent of the off-axis angle of the source.

2.5.5 Fluxes and luminosities

To calculate fluxes (in erg/cm^2/sec, for the 0.5-8 keV band) the exposure map value at each pixel (in cm^2/sec) was combined with the counts;

$$\mathrm{Flux} = \frac{1}{k} \times \left(\sum_{i \in A} \frac{C_i}{E_i} - \frac{N_A}{N_B} \frac{E_A}{E_B} \sum_{i \in B} \frac{C_i}{E_i} \right) \tag{2.9}$$

where the summation over i is over the individual pixels in a region. k is the conversion from counts to ergs assuming the source has a spectrum with $F = \nu^{-1.7}$ between 0.5 and 8 keV, and energy dependent absorption by galactic hydrogen following Morrison and McCammon (1983) with column density from Dickey and Lockman (1990).

[11] The common convention of defining a hardness ratio in terms of the image counts is used. This is dependent on the instrumental response, and as such the hardness ratios for front and back-illuminated chips will differ slightly, and the hardness ratio does not simply translate into a flux ratio.

Missing one or two outlying counts in a faint source can significantly affect the flux, and this is a bigger effect for faint sources where WAVDETECT may also underestimate the source area. For each source the random error on the net counts is far larger than this factor, but the missed counts cause a systematic error which is a function of count rate, so will cause problems when comparing fluxes for observations with different exposure times. In order to correct for this, source counts were calculated for apertures of 1.2 $r_{\max}$ (as used in Section 2.5.1) and 1.5 $r_{\max}$, using the same background area, and compared (Figure 2.7). The aperture of 1.5 $r_{\max}$ has larger random errors, but includes more of the source counts. The ratio of the source counts in the two apertures, averaged as a function of counts, gives a correction factor of up to 4 percent. This is applied to the counts from the standard aperture of 1.2 $r_{\max}$ to correct for the missed counts. The function of the correction factor is shown in Figure 2.7. This correction does not account for missed counts in every source, but does give a population that has no systematic errors in flux at a given count level.

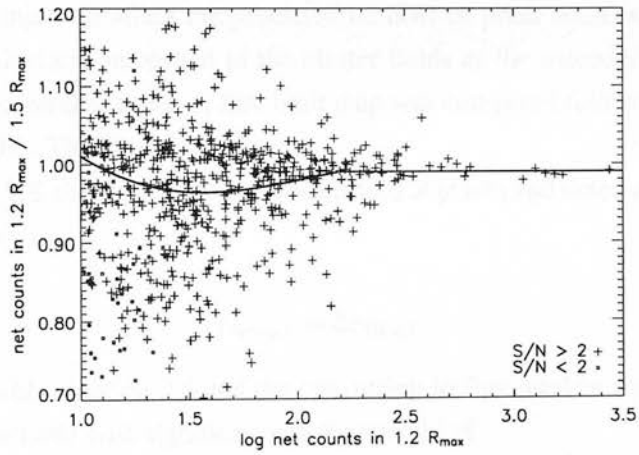

Figure 2.7: The correction factor for source fluxes as a function of source counts. Source counts were calculated, using the same background area, for two aperture sizes. The large scatter is accountable for by the errors, especially in applying the background rate to the aperture, but there is also a systematic offset. For bright sources typically 1% of the counts are missed. For most moderate (~30 counts) sources the smaller aperture results in slightly higher net counts, but for some sources a significant fraction of counts are missed in the smaller aperture. This gives a systematic offset of around 4% for moderate sources. Most sources with < 10 counts are rejected due to low significance, but those kept were corrected by the value at 10 counts. Tests using an aperture of 1.8 $r_{\max}$ gave a similar correction factor, but with larger errors.

2.6 Predicted source distributions

To interpret the number counts of point sources in each image an accurate model of each observation is required to determine the number of sources expected if there were no AGN in the cluster. This model requires the minimum flux detectable at each pixel and the number of blank field sources as a function of flux. The minimum flux model is described in Sections 2.6.1 to 2.6.7. Sections 2.6.8 to 2.6.9 describe the calculation of the expected number of sources for each observation, and Sections 2.6.11–2.6.13 explain the correction of this prediction due to gravitational lensing by the cluster.

2.6.1 Determining the detection sensitivity

A sensitivity model is required for each observation, to calculate the sky area at which a source of a given flux could be detected. Obviously different observations have different characteristics, such as exposure time, PSF variation (for different detectors) and background level, and this will affect the predicted number of point sources. The changes in sensitivity are particularly important in the cluster fields as the extended cluster emission may obscure faint central sources. A flux limit map was computed following the method of Johnson et al. (2003). This is as follows.

From equation 2.8, the counts for a source centred at pixel i and detected at the minimum significance of 3 is

$$C_{min,i} = 3\sigma_{\mathrm{Bkg,i}} \tag{2.10}$$

which combined with equation 2.5 and the conversion to flux used in equation 2.9 gives a minimum flux detectable with significance > 3 at pixel i of

$$S_{\mathrm{min,i}} = \frac{C_{\mathrm{min,i}}}{E_i k} \tag{2.11}$$

$$= \frac{3}{E_i k} \times \left(\left(G\left(R_{B,i} N_{B,i}\right) \frac{N_{A,i}}{N_{B,i}} \right)^2 + \left(G(R_{B,i} N_{A,i})\right)^2 \right)^{1/2} \tag{2.12}$$

where $S_{\mathrm{min,i}}$ is the minimum flux detectable with significance > 3 at pixel i. Subscript A indicates values for the predicted source and B the predicted background, and R is the rate in counts/pixel/sec. This model assumes that the exposure in the background region is equal to that in the aperture, which is not true for an individual source, but is valid for the sample as a whole as some sources have higher exposures in the background region and others in the source region. In addition N_B is taken as 10000 for all sources as there is no way of calculating the probability and effect of overlapping sources at each pixel. These assumptions make a negligible impact on the prediction.

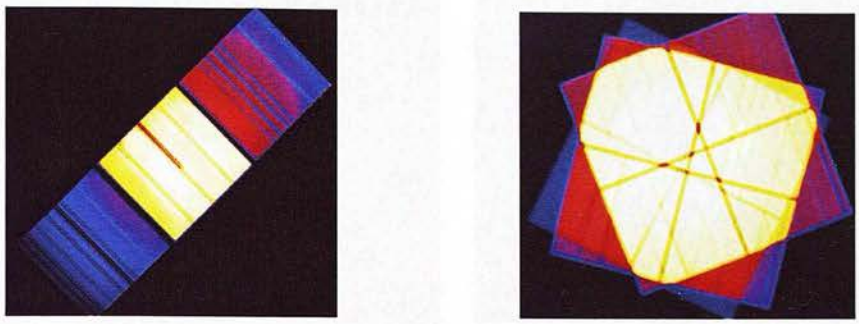

Figure 2.8: Exposure maps for two cluster observations, Abell 1068 (left) and RX J1720+26 (right). The first observation is using the ACIS-S array and the second image is three observations using ACIS-I. Yellow areas have highest exposure.

The inputs for the prediction are then the exposure E_i, source size $N_{A,i}$ and background count rate $R_{B,i}$ at each point on the image. The exposure can be found directly from the exposure map, and the source size and background rate are calculated from the individual images and from the whole sample. The calculation of these values are described in the next three sub-sections.

2.6.2 Exposure at each pixel

The exposure is simply the sum of the individual exposure maps described in Section 2.3.3. There are regions where the gradient in exposure will make source detection difficult, and these are masked out later as described in Section 2.6.5. As an illustration the combined exposure map for the single observation of Abell 1068 and the three observations of RX J1720+26 are shown in Figure 2.8.

The errors in the exposure map are not easily calculable as depends on by many calibration factors. In particular the exposure map is calculated using an assumed spectral index ($\Gamma = 1.7$). Changing this to $\Gamma = 1.2$ gives a systematic offset of $\sim 10\%$, but systematic errors which affect all observations are not important in this analysis as they affect the blank and cluster fields in the same way. The radial variation in the exposure map caused by changes in Γ is $\lesssim 1\%$ so is negligible. The effect of errors between ACIS-I and ACIS-S images are discussed in Section 2.6.10. As the calibration errors cannot be quantified, and are generally systematic, and as they will affect blank and cluster fields in the same way, errors on the exposure map are not included.

2.6.3 Background rate at each pixel

For each observation the background rate, including the diffuse cluster emission, was calculated by replacing the pixels in each point source (within $1.5 \times r_{\rm max}$) with randomly chosen

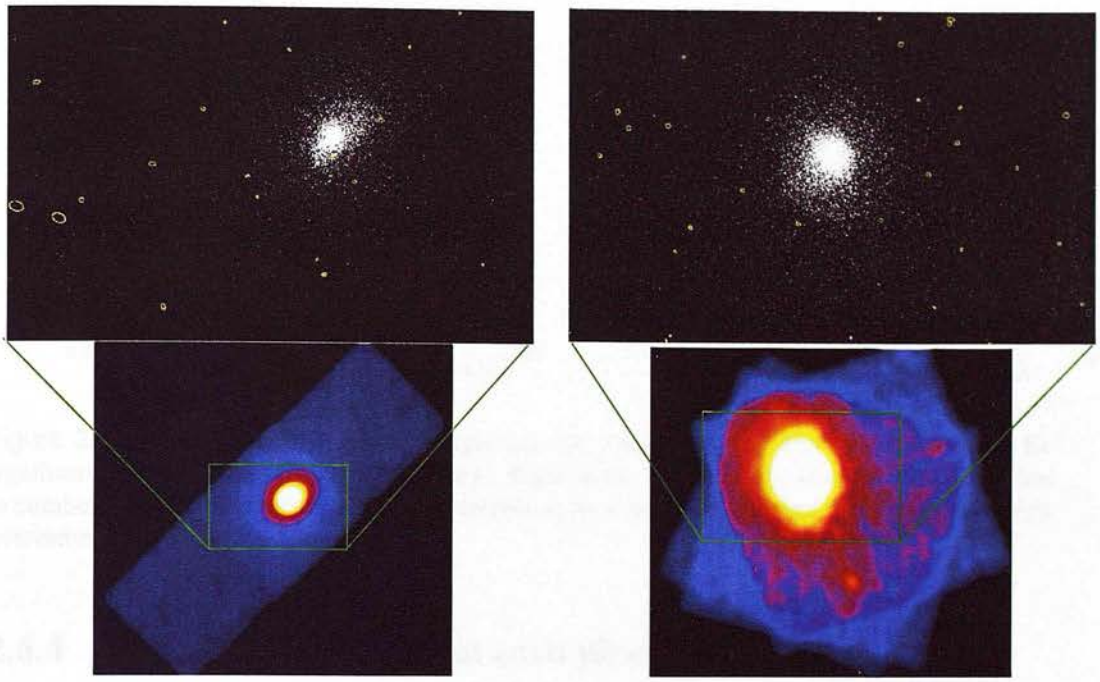

Figure 2.9: Background images for two cluster observations, Abell 1068 (left) and RX J1720+26 (right). The top panel shows the the central region of the images, with sources removed and the source regions marked by ellipses. The bottom panel shows the full smoothed background images (with a square root scale).

values from the good pixels in the background region of that source. This image was then smoothed using the CIAO tool *csmooth* with a gaussian kernel of radius 40 pixels. Figure 2.9 shows an example of the background images produced.

To find the error on the background it is easiest to assume that the smoothed background rate is given by the average of the counts in a circle, rather than calculating the errors on the true gaussian convolved image. In other words, $R_{B,i} \approx \sum_{j \in \text{Area}} C_j/\text{Area}$ where the area is a circle of radius 40 pixels centred on i. This gives a simple equation for the error - $\sigma_{R_{B,i}} \approx \sqrt{\frac{R_{B,i}}{\pi 40^2}}$. Using this assumption the error can easily be found at each point from the smoothed background count rate, $R_{B,i}$.

To test the model background, the background rate for each detected source (using aperture photometry) was compared to that from the smoothed images at the same position. As shown in Figure 2.10, the model background accurately reproduces the calculated background for the detected sources (with SIG > 3), with no systematic offset. Only 5% of sources have background rates $> 1\sigma$ less than the predicted value, and 10% have rates $> 1\sigma$ more than the prediction. The prediction is not very sensitive to the gaussian kernel size, as using a kernel of radius 10 pixels only changes the prediction by 1%, which is negligible compared to the statistical errors.

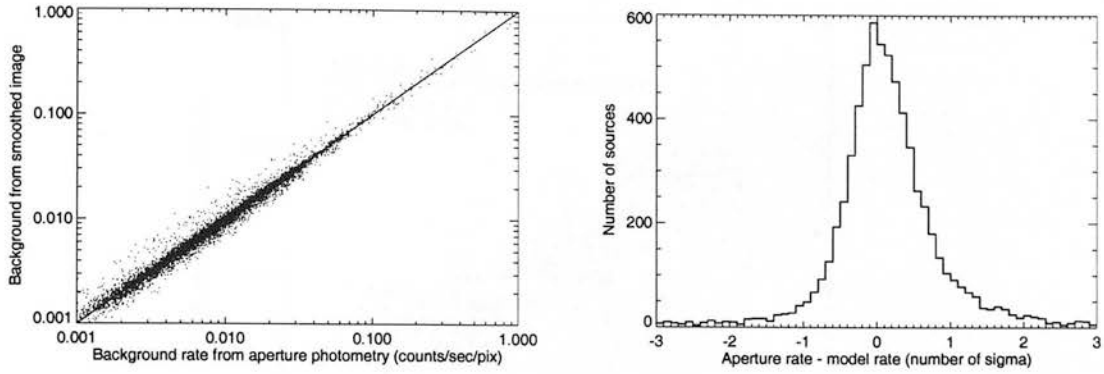

Figure 2.10: Left panel: The model background rate compared to the true background rate for significant sources (from aperture photometry). Right panel: The deviation from the model, plotted in number of $\sigma_{R_{B,i}}$. The model accurately reproduces the calculated rate, and the errors are slightly overestimated.

2.6.4 Expected source size at each pixel

The expected source size was calculated using the apertures for the detected sources from 8 blank fields, comparing the aperture size with off axis angle (see Section 2.5.1 for details of the aperture sizes). Apertures derived from the WAVDETECT output were used instead of the given PSF size as the minimum flux detectable depends on whether the source is detected by WAVDETECT and whether it has significance > 3, calculated from the WAVDETECT source size. Blank fields were used to determine the source size as the background level is relatively uniform, whereas in the cluster fields there are less small, central sources for calibration due to the cluster emission.

The radial distribution of aperture sizes is shown in Figure 2.11, which also shows the chosen model radial source size distribution. This model was determined from the data for significant, low flux sources ($S < 0.25 \times 10^{-14}$ erg cm^{-2}s^{-1}) as these faint sources generally have slightly smaller WAVDETECT sizes than brighter sources, and these are the sources nearest the detection limit, which is the aim of this calculation. The scatter in the PSF size is due mainly to the random distribution of the photons in fainter sources, which makes finding the edge of the source difficult. The aperture size was found to jump at radii of 480, 750 and 1010 pixels, due to the behaviour of the PSF combined with the wavelet scales chosen (this is illustrated by the fact that the brighter sources, marked by dots in Figure 2.11, are far closer to a constant slope, as they are affected less by the wavelet scales and trace the true change in PSF). The aperture size was modelled between each jump with a best-fit quadratic fit to the linear aperture size, with the 1-sigma error determined by the distribution of sources around this fit. At a radius of 1010 pixels the aperture size jumps considerably giving large uncertainties, and no significant faint sources, so all sources above

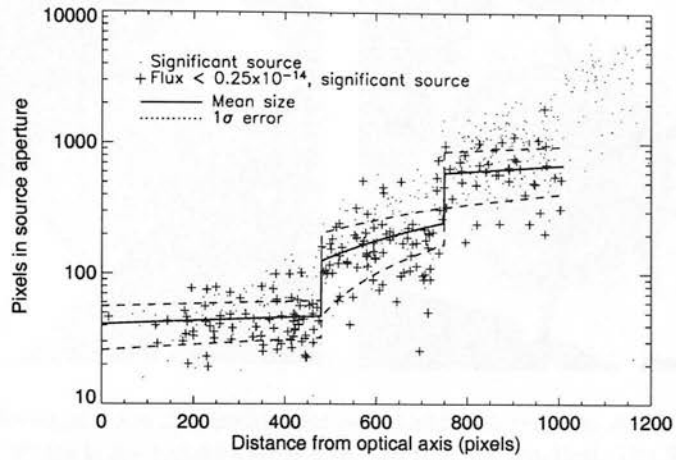

Figure 2.11: Source size as a function of distance from the optical axis. The mean size and 1σ errors are calculated for the faint sources. This is then the expected source size for sources near the flux limit at each pixel.

this radii were rejected, and this area was removed from the calculation. Re-fitting the data including sources of higher fluxes gives generally larger source sizes, and a steeper gradient within each fit region, but increasing the flux limit by a factor of two still gives source sizes well within the 1σ error.

Again, comparison with the actual source sizes shows that this model is accurate to within the errors and has no systematic error. The expected source sizes were also calculated separately for all faint ACIS-I sources, and for all faint ACIS-S sources (in all fields, including the cluster observations). Both source size distributions were within the 1σ error of the distribution in Figure 2.11, with no systematic offset. Using the ACIS-S or ACIS-I source size distribution alone made very little difference to the sky area visible at a given flux, and resulted in a $< 0.4\%$ change to the number of sources per square degree at any flux. It is therefore unnecessary to use different source size distributions for the different detector arrays.

The source size distribution was calculated for each image, taking into account the optical axis of each observation. For multiple observations the source size distribution was calculated for each observation, then combined weighted by exposure map, in the same way as for the combined PSF map input into WRECON (Section 2.3.4). It was assumed that the errors on the combined source sizes scale with source size in the same way as those for the single observation case, as shown in Figure 2.11.

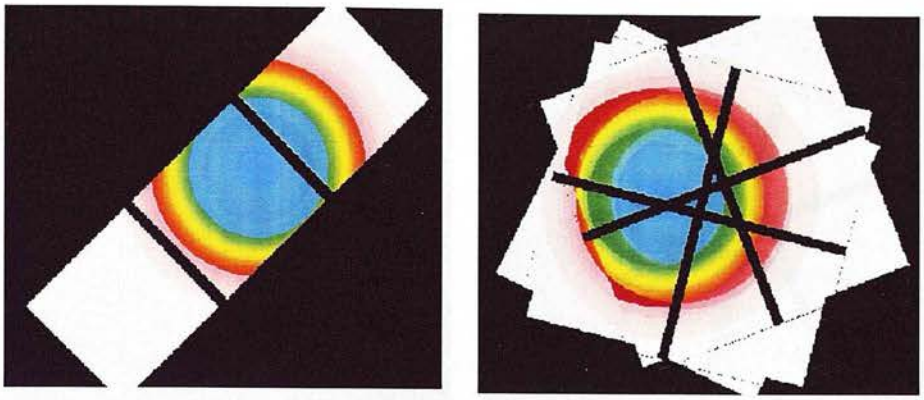

Figure 2.12: Model source size distributions for two cluster observations, Abell 1068 (left) and RX J1720+26 (right). White is the largest source size, and blue the smallest. For RX J1720+26 three source size distributions have been combined, each weighted by the masked exposure map of the corresponding image. The masked regions are described in Section 2.6.5.

2.6.5 Regions where the model is valid

A mask was constructed to restrict the area to regions where the model is accurate. This removes the effects of chip gaps, chip edges and errors in the modelling. Sources outside the masked area were removed from the analysis, and only the mask area was included in the calculations of sky area and sensitivity.

The edges of the chips were determined using the CIAO procedure SKYFOV, which marks the area of the image covered by each chip, including dithering. Edge effects are an important issue as the estimation of the background is too low wherever the *csmooth* routine smoothes between an area of good exposure and one of no exposure. This effect was found to be important within 60 pixels of any chip boundaries that butt onto an area of no exposure (rather than another chip), so these areas were removed. In the merged images the same criteria were applied to the image *after* merging, so as not to remove areas where the exposure jumps from two images to one.

Although the gaps between chips are filled in to some extent by the dither of the telescope, the rapid fluctuation in exposure (as seen in Figure 2.8) makes it difficult to detect faint sources, and the model was found to be inaccurate in these regions. A 'chip boundary' condition was applied to each chip - any chip edges which butted against another chip were moved inward by 40 pixels. The resulting mask for one observation is shown in the first panel of Figure 2.13.

For merged images the same 'chip boundary' area was removed where the individual images did not overlap. For overlap regions it would be wasteful to reject the 'chip boundary' areas in one image if they were well covered by the other images, as the combined image then has a low exposure gradient. For each image, i, the 'chip boundary' area was

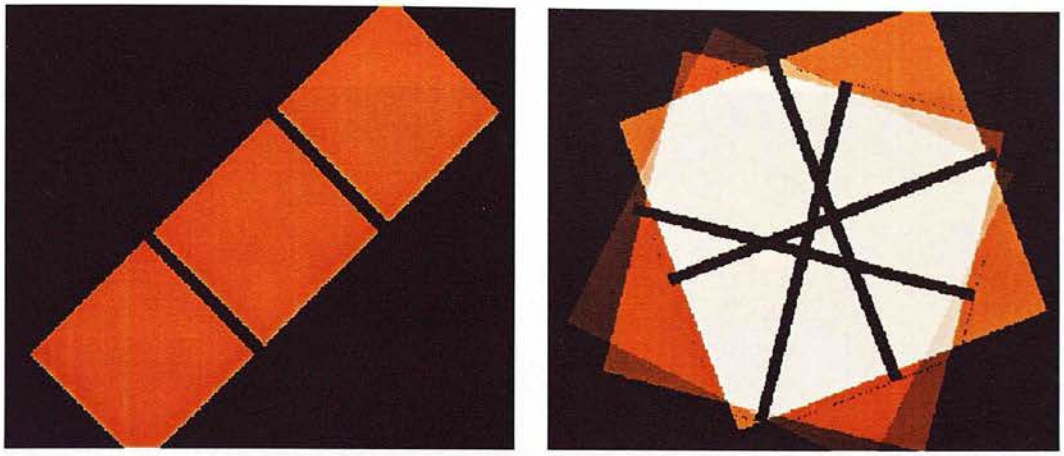

Figure 2.13: Regions included from the model after correcting for effects due to chip boundaries, for Abell 1068 (left) and RX J1720+26 (right). For RX J1720+26 all of the coloured areas were included - two of the three images had high exposure, so their 'chip boundary' areas were removed, giving the two cross shapes in the image. The third image had a lower exposure and so did not affect the combined exposure map much - the chip boundary area was therefore retained.

included if $E(\max)_i < 0.5 \times \Sigma_{j=good} E(\max)_j$, where $E(\max)$ is the on-axis exposure of an image and the sum is over all images, j, with good exposure in the 'chip boundary' area. This is illustrated for a case with 3 merged images in the second panel of Figure 2.13.

As described in Section 2.6.4, regions where the model source size is greater than 700 pixels were also removed. This corresponds to a radius of 1010 pixels for a single observation, but for merged observations it depends on the output source size prediction.

In addition, for the blank fields containing a QSO (Section 2.2.2) a circle of radius 50 pixels was removed from around the aim-point.

2.6.6 Checking the flux limit values

The final flux limit model for the two example fields is shown in Figure 2.14, where all cuts and masks have been applied.

To check the flux limit model the fluxes of all detected sources were compared to the minimum flux detectable at the source position. Figure Figure 2.15 shows that almost all ($> 97\%$) of sources are brighter than the flux limit at their position. Those that are slightly fainter than the corresponding flux limit have large errors on their flux, so that $\ll 1\%$ of sources are over 1σ fainter than the calculated flux limit at their position.

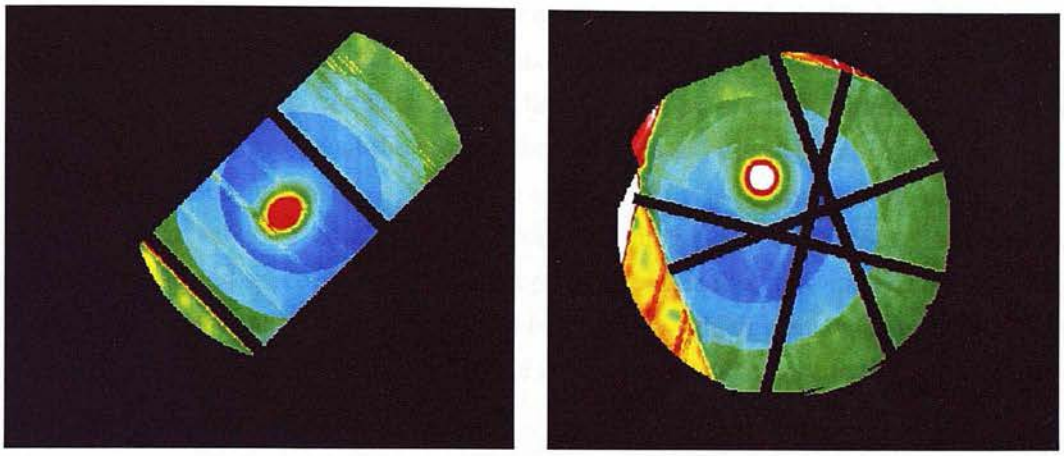

Figure 2.14: The final flux limit model for Abell 1068 (left) and RX J1720+26 (right). Blue areas are the most sensitive and have the lowest limiting flux (1.7×10^{-15}erg/cm^2/sec and 1.2×10^{-15}erg/cm^2/sec respectively), and red and white are the least sensitive (7.5×10^{-15}erg/cm^2/sec and 1.1×10^{-14}erg/cm^2/sec). The PSF size, exposure map and cluster background all clearly affect the final limiting flux distribution.

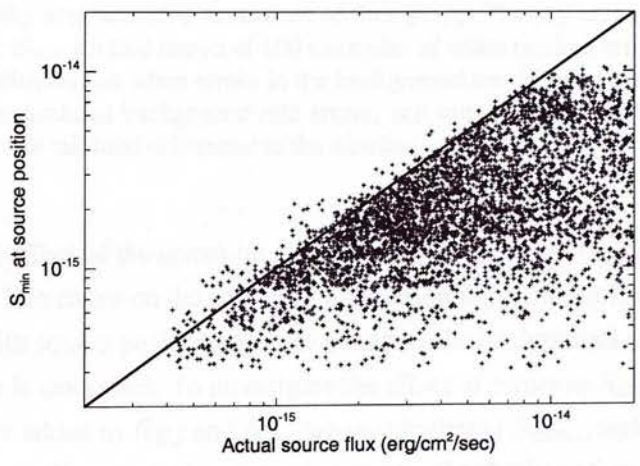

Figure 2.15: Source flux plotted against minimum detectable flux at the source position, for over 6000 good sources. Very few sources are fainter than the calculated flux limit, and these have large errors on their flux.

2.6.7 Errors on the flux limit and sky area

The sky area at which a source of flux S could be detected is found by summing all pixels, i, with $S_{\min,i} < S$ over the image. The error on $S_{\min,i}$ is required to calculate the error on the sky area, and hence on the number of sources per square degree at each flux.

The inputs required to calculate the flux limit at each pixel can be seen from Equation 2.12. The sections above detail the error in the background rate, σ_{R_B}, and the source size, σ_{N_A}, and the reason for setting $\sigma_E = 0$. In addition there is an error on the derived flux from the flux conversion factor, k, which is found by applying galactic absorption for each image to an assumed spectrum. However, the purpose of this flux limit image is to combine it with the number densities of sources from blank fields, which were calculated using the same values of k. An error on k will therefore not make any difference to the results.

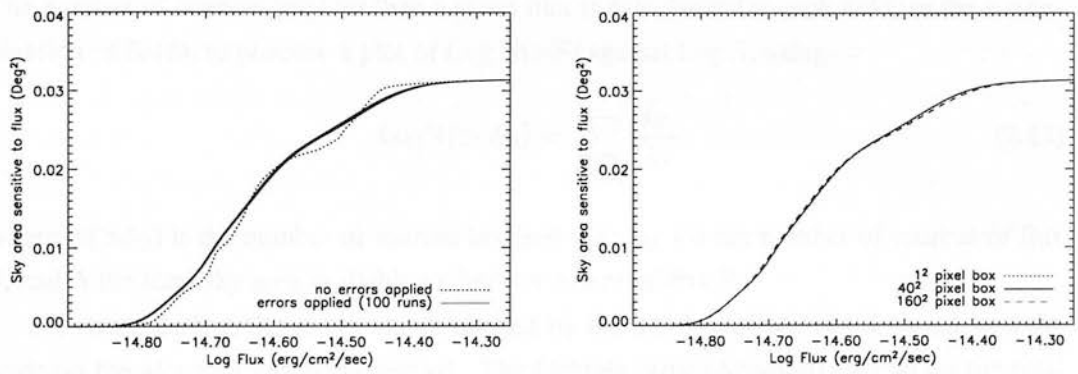

Figure 2.16: The sky area sensitive to sources of flux S. (a) The sky area distribution when no errors are applied to $S_{\min}$ (dotted line) and 100 examples of when random errors are applied (solid lines) (b) Sky area distribution when errors in the background are correlated over a fixed box size. The extremes of uncorrelated background rate errors, and rate errors that were fixed in a box of 160 × 160 pixels, make minimal difference to the distribution.

The combined effect of the errors on $S_{\min,i}$, summed over the image, is not straightforward to calculate. The errors on the source size are essentially uncorrelated (as the variation is nothing to do with source position), but the errors on the background are correlated as the background image is smoothed. To investigate the effect of errors in $S_{\min,i}$ on the sky area, random errors were added to $R_{B,i}$ and $N_{A,i}$ when calculating $S_{\min,i}$, and the sky area recalculated. The error on $N_{A,i}$ was taken from a gaussian distribution of errors with σ_{N_A} from Figure 2.11. The error on the background rate was also taken from a gaussian distribution with σ_{R_B} as described in Section 2.6.3. To ensure some degree of correlation the background points in each 80 × 80 pixel square were changed by the same (randomly selected) number of sigma.

Figure 2.16 shows the effect of these errors. The sky area without errors has quite steep

jumps due to the sudden changes in the model PSF (due to the wavelet scales). Applying random errors to the flux limit at each pixel smoothes this distribution and makes a significant difference. The random errors were simulated 100 times, but the sky area at a given flux hardly varied between the simulations. In addition the area over which the background errors were fixed was varied from a 160 × 160 box to uncorrelated errors, but this also had minimal effect on the sky area. The sky area is therefore found by producing one simulation of random errors and calculating the distribution of $S_{\rm min}$. As Figure 2.16 shows, the errors on this method are very small - the final error on the number density of sources is completely dominated by the error on the detected number of sources, and the error on the sky area can be neglected.

2.6.8 Log N(>S) - Log S distributions

The number of sources brighter than a given flux is calculated for each field, or for a combination of fields, to produce a plot of Log N(>S) against Log S, using

$$\mathrm{LogN}(>S_0) = \sum_{S>S_0} \frac{i_S}{A_S} \tag{2.13}$$

where N(>S_0) is the number of sources brighter than S_0, i is the number of sources of flux S, and A the total sky area available to detect a source of flux S.

As stated earlier, the errors are dominated by the number of sources detected, and the error on the sky area can be neglected. The Gehrels error (Appendix A.1.4) on the total number of sources was used for the brightest sources, where the sky area is constant, such that;

$$\sigma_{\mathrm{N}(>S_0)} = \frac{G(i_{S>S_0})}{A} \tag{2.14}$$

for $A > 0.99 \times A_{max}$. When the sky area starts to decrease (as lower flux), $\sqrt{i}$ errors are used as they area able to take account of the weighting by sky area; at these fluxes the number of sources is relatively large ($i \gtrsim 10$) and the difference between Gehrels and $\sqrt{i}$ approximations becomes minimal. The error is then given by

$$\sigma_{\mathrm{N}(>S_0)} = \sqrt{\sum_{S>S_0} \frac{i_S}{A_S^2}} \tag{2.15}$$

It is worth noting here the effect of the Eddington bias (Eddington 1913), whereby random flux errors can change the measured source counts above a given flux. In a distribution with more faint than bright sources it is more probable that a faint source is moved above a given flux than that a source above that flux is moved below, so that the source counts above the flux are boosted. This effect depends on the slope of the number counts (highest at bright fluxes) and the error on the flux (which is highest at the flux limit), and is equiv-

alent to convolving the Log N(>S) - Log S distribution with a gaussian distribution with width σ_S (which varies as a function of S). The resulting change in the Log N(>S) - Log S is a slightly higher number of sources at each flux. In general this changes the results for all observations in the same way, although the effect at a given flux will be slightly higher for shallower observations, as the value of σ_S is higher. Manners (2002) show that the net effect for one field is $\sim 1\%$ extra sources above the flux limit. Since this is a small effect, and is only weakly dependent on the limiting flux of the observation, it will largely cancel when comparing the cluster and blank field samples, and therefore Eddington bias effects can be neglected in this analysis.

2.6.9 Predicted source distributions for each observation

For each field, in addition to the Log N(>S) - Log S distribution, the radial distribution of sources was found and compared to the radial prediction assuming no cluster sources. This was calculated using the blank field Log N(>S) - Log S and the $S_{\rm min}$ map for each field.

Errors on the predicted radial distribution were found by applying the Log N(>S) - Log S distribution with 1σ errors to the $S_{\rm min}$ map. In all cases the few pixels that had a lower $S_{\rm min}$ than the lowest flux reached by the blank field Log N(>S) - Log S (due to the errors applied) were assigned the maximum blank-field value of Log N(>S), and those which had $S_{\rm min}$ higher than the brightest blank field source were assumed to detect no sources.

The predicted and actual radial distributions were calculated from the cluster centre, which was selected as the maximum of the smoothed background image if a clear cluster was visible. Where the cluster emission was highly irregular, or multiple clusters were visible, the central point of the brightest cluster was selected. If no cluster was visible (in the $z > 1$ sample), or in the blank fields, the radial distribution is calculated from the aim-point.

The combined radial distribution for all blank field sources is shown in Figure 2.17. As the radial prediction is based on the blank field Log N(>S) - Log S, the predicted and actual counts should be constrained to the same value at the maximum radius – this plot confirms that the method works correctly. The maximum deviation from the prediction is a little over 1σ, and the variance in the deviation shows no strong radial traits.

In addition, this radial analysis is not affected by Eddington bias as the blank field Log N(>S) - Log S contains random flux errors on the detected sources. The predicted radial distribution is based on the blank field Log N(>S) - Log S and so also accounts for the slight over-detection of sources above a given flux. The model and data therefore contain the same systematic errors, which can safely be neglected.

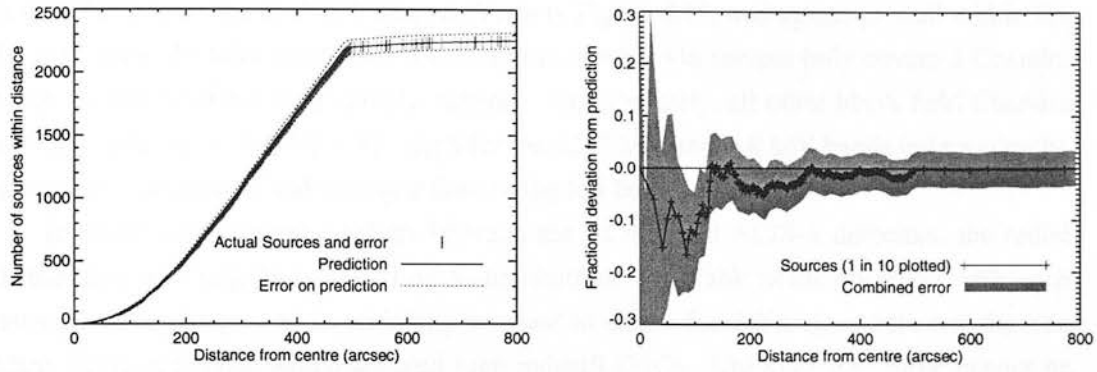

Figure 2.17: Left panel: The radial prediction and actual distribution for all blank fields. Right panel: The fractional deviation from the predicted number of sources. Only one in ten sources are plotted to illustrate the source density. Errors from the prediction and number of sources are combined in quadrature to give the shaded region.

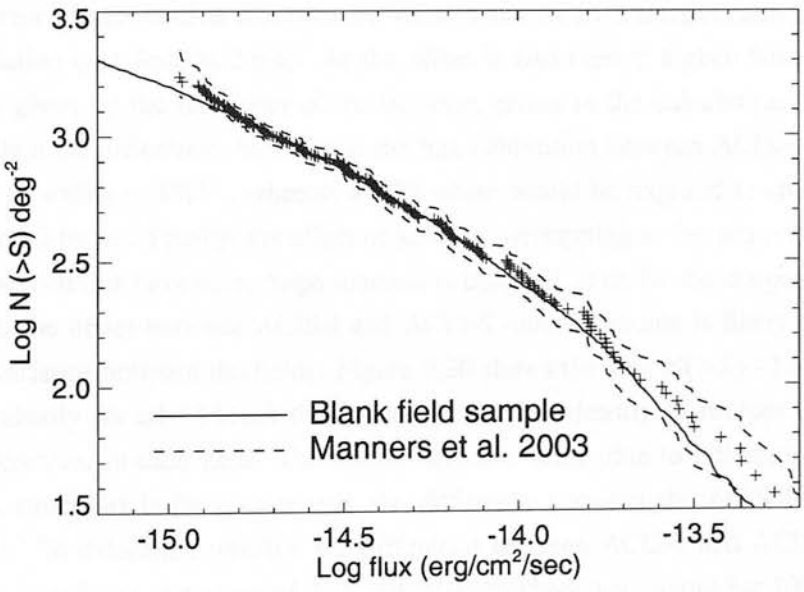

Figure 2.18: The blank field Log N(>S) - Log S plot compared to that from the ELAIS fields of Manners et al. (2003). The crosses mark the data points and the dashed lines the 1σ errors from the ELAIS fields.

2.6.10 Checking the blank fields

The blank field log N($> S$) - log S distribution was compared with that derived by Manners et al. (2003) from the ELAIS fields, as shown in Figure 2.18, and agrees to well within the 1σ error bars. As with most blank field surveys, the ELAIS sample only covers 2 Chandra fields so will be affected by sample varience. Unfortunately, all other blank field Chandra surveys calculate the log N($> S$) - log S for the 0.5-2 keV and 2-8 keV bands independently, so can only be used to find an upper limit to the full band value[12].

To check for systematic offsets between the ACIS-I and ACIS-S detectors, the radial distribution and Log N($> S$) - Log S distributions for blank fields observed with each detector were compared. In addition, we want to check for differences between the true blank fields and those which targeted high redshift QSOs. Unfortunately these cannot be done independently as all of the high redshift QSOs were observed with ACIS-S, and all of the true blank fields with ACIS-I.

Figure 2.19 shows the Log N(>S) - Log S distributions for the combined 'true' blank and QSO fields. The QSO fields (ACIS-S) have a Log N(>S) - Log S distribution that is around 1σ *lower* than the 'true' blanks (observed with ACIS-I), so it is concluded that there are no significant extra sources in the high redshift QSO fields, and they can be treated as valid blank fields.

The 1σ offset between the ACIS-I and ACIS-S (which correspond to the QSO and 'true' blank fields) does not appear to be produced by any systematic errors in the calculation. The small difference in the source size between ACIS-I and ACIS-S images cannot account for the 1σ variation (see Section 2.6.4). As the offset is also seen at higher fluxes, where the sky area is given by the total area of the detector, errors in the calculation of S_{min} also cannot explain the difference. In addition the flux calibration between ACIS-I and ACIS-S is accurate to within $\sim 5\%$[13] , whereas a 10% offset would be required to change the Log N(>S) - Log S by 1σ. Finally, the effect of sources overlapping at the edges of the images (ACIS-I observations have more large sources) is minimal, even for the deepest fields.

Instead, the offset between ACIS-I and ACIS-S number counts is likely to be simply statistical variance between the fields. Figure 2.20 shows the Log N(>S) - Log S distributions individually for all 44 blank fields, and the number density of sources brighter than 10^{-14} erg/cm^2/sec in each field. The scatter between fields (due to Poissonian errors and large scale structure) is far greater than the difference between the ACIS-I and ACIS-S subsamples. To determine whether the difference between ACIS-I and ACIS-S fields is statistically significant, the value of $N > 10^{-14}$erg/cm^2/sec was found for 1000 randomly

[12]The soft and hard band log N($> S$) - log S distribution for this sample were not calculated for this sample, as they would be of little scientific value compared to more extensive blank field studies. In addition the sources would have to be re-detected in each band, and the dependence of the PSF variation and flux correction would have to be re-calculated for each band. This would therefore not serve as a good test of the full band method, due to the different correction factors applied.

[13]see details in http://cxc.harvard.edu/cal/docs/cal_present_status.html as of 07/2005

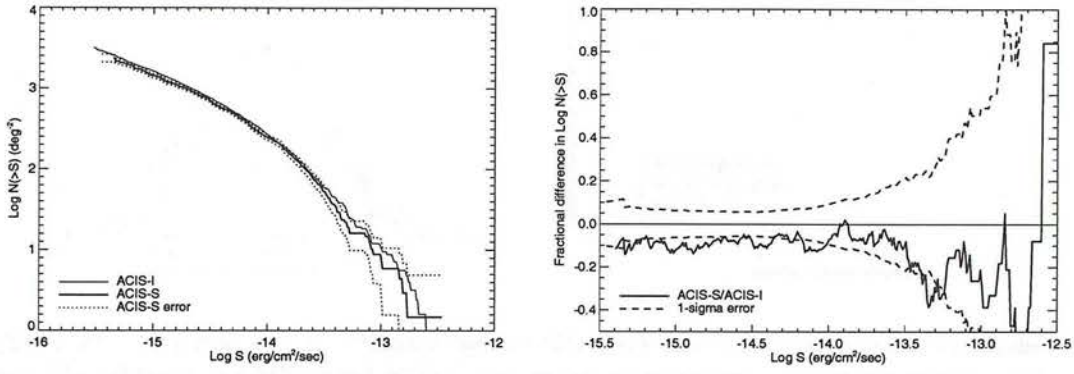

Figure 2.19: Left panel: The Log N(>S) - Log S plots for blank fields observed with ACIS-I and ACIS-S. Errors are only shown for ACIS-S for clarity – ACIS-I errors are smaller. Right panel: Fractional difference between the Log N(>S) - Log S plots for ACIS-S and ACIS-I blank fields. The 1σ errors are shown relative to the ACIS-I line, and are found by combining the errors on the two Log N(>S) - Log S distributions. The ACIS-S distribution is around 1σ lower than the ACIS-I distribution at all fluxes.

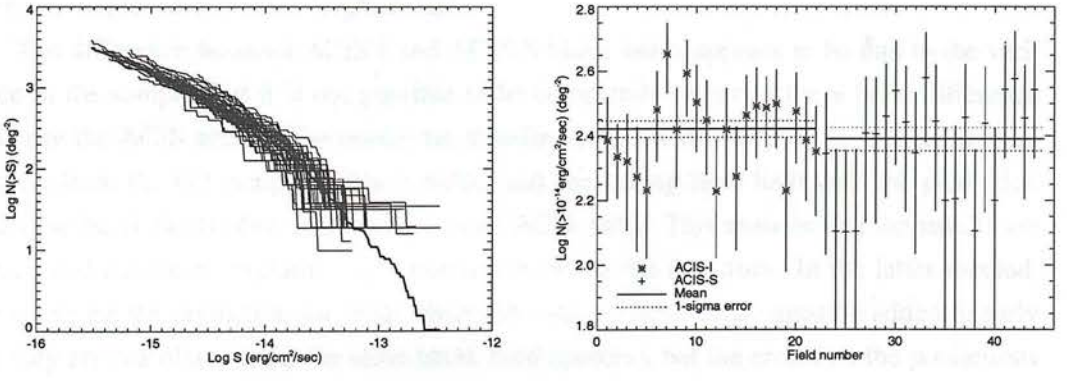

Figure 2.20: Left panel: Log N(>S) - Log S plots for the individual blank fields, with the combined distribution shown by a thick line. The scale is the same as that in Figure 2.19, and the large degree of variance between individual fields is clear. Right panel: A slice through the Log N(>S) - Log S distribution at 10^{-14} erg/cm^2/sec. The ACIS-S fields have a larger spread in Log N as they are typically smaller in area, and the 1σ difference between the means can probably be attributed to the sample variance.

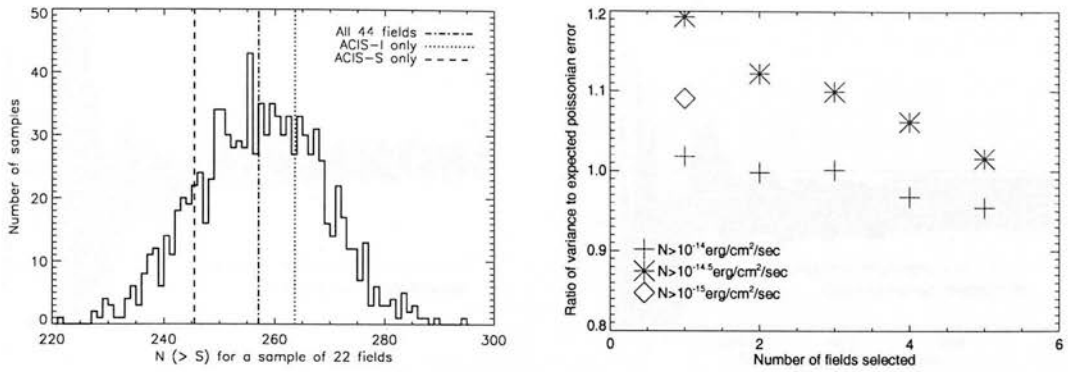

Figure 2.21: Left panel:$N > 10^{-14}$erg/cm^2/sec for 1000 randomly chosen subsamples of 22 blank fields. The values for the ACIS-I and ACIS-S subsamples are consistent with random samples, and there is no evidence of a systematic offset between the detectors. Right panel: The ratio of actual variance to expected (Poissonian) variance for 1000 sub samples of blank fields. Sub-samples of 1 - 5 fields are investigated at three flux values. The increase in errors due to cosmic variance is small for bright sources, and for samples of > 5 fields. This plot is only an indication of the variance due to clustering for two reasons: The subsamples were picked from the same parent population (in particular at $N > 10^{-15}$erg/cm^2/sec only 17 blank fields were available) so the overlap between subsamples reduces the observed variance for moderate sample sizes. Secondly the values can also be < 1 as the Poissonian errors were calculated from the mean field value, whereas in reality some fields are larger so have smaller errors.

chosen subsamples of 22 blank fields. The distribution is shown in the left panel of Figure 2.21, and shows that the ACIS-I and ACIS-S samples are fully consistent with randomly chosen samples at $S > 10^{-14}$erg/cm^2/sec.

The difference between ACIS-I and ACIS-S blank fields appears to be due to the variance in the sample, but it is not possible to be completely sure that there is no difference between the ACIS arrays. The results are therefore calculated in two ways – using the prediction from the full sample of blank fields, and comparing each field with the prediction from the blank fields observed with the same ACIS array. This ensures that the results are robust and cannot be explained by variations between the detectors. In the latter method, the errors on the prediction for fields observed with the same array must be added linearly (as they are calculated from the same blank field sources), but the errors on the predictions for the ACIS-I and ACIS-S subsamples are independent, and so are added in quadrature.

The error calculations used here are based on the Poissonian errors on the sources detected, assuming that they are randomly distributed. It is important to ensure that large scale structure does not give rise to significantly larger errors. The clustering of X-ray sources appears to be stronger in low flux sources than in high flux, and can give rise to significant field to field variations (see for example Yang et al. 2003, Mullis et al. 2004 and Basilakos et al. 2005). To check the magnitude of this effect in this survey, subsamples of 1 to 5 fields were chosen at random from the blank field sample. The right panel of Figure 2.21

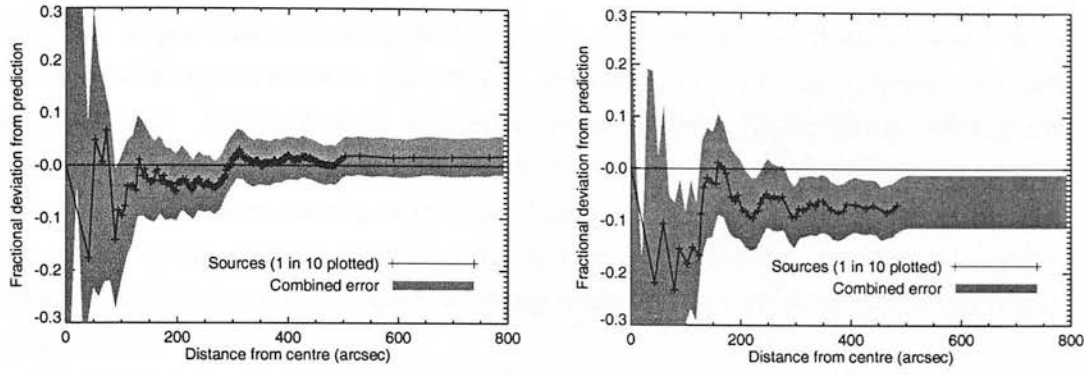

Figure 2.22: Deviation from the radial prediction for ACIS-I fields (left) and ACIS-S fields (right).

shows the ratio between the observed variation in the Log N(>S) - Log S and the expected variation from Poissonian errors, for 1000 subsamples of each size. At 10^{-14}erg/cm^2/sec the Poissonian errors completely explain the variance between the sub-samples (because the Poissonian errors are large, due to the small numbers of bright sources in these fields). At $10^{-14.5}$erg/cm^2/sec the variation in individual fields is 20% larger than that expected from the Poissonian errors, which is attributable to AGN clustering. This effect decreases as the sample size is increased, and for samples of 5 fields the variation is only slightly above the expected value; samples of this size are therefore sufficient to largely average out the effects of large scale structure. At 10^{-15}erg/cm^2/sec there are few blank fields available so only the variance for individual fields is shown. This is $\sim$ 10% higher than expected from Poissonian analysis, indicating that there is some effect due to large scale structure in faint sources too, although perhaps this is not as important as for the bright sources. This will also decrease with larger sample size, so should not be significant for samples of 5 fields. In taking small samples of fields it is therefore advisable to use at least 5 fields in order to ensure that the stated errors are not underestimated due to clustering.

The radial distributions for the ACIS-I and ACIS-S fields were also compared. The radial distribution for ACIS-I fields matches that predicted from the Log N($>$ S) - Log S distribution from ACIS-I fields alone, and the same applies for ACIS-S fields. Figure 2.22 shows the results for ACIS-I and ACIS-S blank fields against the predicted distribution from the complete blank field Log N(>S) - Log S. As expected, the ACIS-S fields end 1σ below the prediction, but otherwise both distributions are flat to within the errors, and there is no link between over or under prediction and radius.

As a final check the total excess or deficit of sources (over the full radius) compared to the prediction, was examined for each field. There was no correlation between offset and exposure time, or whether a field was merged or not. There was only a small correlation with ACIS array, as expected from the difference in Log N(>S) - Log S.

2.6.11 Corrections for gravitational lensing: The lensing model

The effect of gravitational lensing of X-ray sources by the galaxy cluster is small, but is expected to be significant over many fields. Johnson et al. (2003) calculate an expected deficit of X-ray sources of up to 10% in the central 0.5Mpc (at the cluster redshift) for MS1054-0321 (z=0.83). This is insignificant for a single field, since only a few sources are found in this region, but the cumulative effect over many fields may affect the sample. In addition, as the effect of lensing on the number counts is more significant for bright, moderate redshift clusters, gravitational lensing could bias, as well as reduce the magnitude of, any results.

To calculate exactly the difference between the cluster and blank fields that is due to gravitational lensing requires detailed knowledge of the dark matter distribution in the cluster and the redshift-flux distribution of the background sources. As this study is investigating a statistical excess of sources in a large number of fields, exact determination of the lensing is unnecessary (and unfeasible). Instead, the radial loss or gain of sources in each image due to the cluster is calculated using a simplified model of gravitational lensing, with the only inputs being the X-ray luminosity of the cluster (to give the mass), an assumed background distribution of X-ray sources, and the radial sensitivity distribution of the observation (the $S_{\rm min}$ map). As this technique is only an approximation, the results of this project will be evaluated with and without the lensing correction to ensure that they are robust.

As discussed by Refregier and Loeb (1997), the gravitational potential of the cluster has two effects on the X-ray background: the flux of each source is increased by a factor μ (due to an increase in source size at constant surface brightness), and the number density is decreased by the same factor due to a decrease in the apparent sky area of the image. This is equivalent to shifting the Log N($>S$) - Log S distribution to the right and downwards. Whether this results in a net increase or decrease in sources at a given flux depends on the slope of the Log N($>S$) - Log S distribution. At fluxes $\lesssim 10^{-14}$erg/cm^2/sec the slope becomes < -1 and the net result is a deficit in source counts, but at brighter fluxes the source counts are boosted. The size of this deficit/boost depends on μ which, for a simple model, can be expressed as

$$\mu(\theta) = |1 - \theta/\theta_E|^{-1} \tag{2.16}$$

$$\theta_E = 2.6'' \sigma_{300}^2 \frac{D_{LS}}{D_{OS}} \tag{2.17}$$

where θ is the angular separation between the cluster centre and the X-ray source, D_{LS} is the angular distance from the lens to the source, D_{OS} is the angular distance from the observer to the source and σ_{300} is the velocity dispersion of the cluster in units of 300 km/s. This equation is an approximation, calculated for an isothermal sphere where the image region is similar in scale to the mass distribution size (see Refregier and Loeb (1997), Blandford and Narayan (1992) and references therein). Although crude, this approximation is sufficient

for this analysis. It also is not valid in the region of very small θ, but in this case all but the brightest X-ray sources would be obscured by any cluster with a significant lensing potential, so it is sufficient to use this equation for all radii.

The velocity dispersion of the cluster can be found approximately from it's luminosity via the $L_X - \sigma$ relation. Mahdavi and Geller (2001) show that $L_X \propto \sigma^{4.4}$ is a good fit to the observed data for clusters and groups of galaxies with $z < 0.1$. The scatter in the distribution is around 0.3 dex, compared to an error of around 0.2 dex caused by the uncertainty in L_X in our cluster sample. For one field these errors may make a difference, but when a sample of cluster fields are combined the errors will largely cancel out. It is also possible that there is some redshift evolution in the normalisation of the $L_X - \sigma$ relation. Assuming a redshift evolution of $(1+z)^{1.8}$, as seen in the $L_X - T$ relation (Kotov and Vikhlinin 2005), introduces a maximum $\sim 25\%$ change in σ (at z $\sim$ 1). This is small but not insignificant, but as any evolution is not yet well quantified or for the $L_X - \sigma$ relation we apply the $z < 0.1$ relation to all clusters. As a final check the value of σ found using this method is compared to that found in the literature for some clusters, and is found to be a good match.

The change due to gravitational lensing for a population of sources depends on the distance to the sources, D_{OS}, as well as their flux. As the X-ray field has a distribution of sources at different luminosities and redshifts, models of the X-ray luminosity function and its evolution are used to produce luminosity functions at a range of redshifts. Three models of the X-ray background are used, as described below. They are all calculated for rest-frame 2-8 keV (hard band) sources, whereas the detected sources in the cluster images are observed in the 0.5-8 keV band. However, at the redshift of most AGN activity, and where the lensing from clusters will be strongest, the 2-8 keV rest-frame sources would be observed as 1-4keV sources, which is the central region of the full band. The models are therefore based on sources similar to those in our sample. Also the lensing factor calculated in this section is fractional, so only the shape and relative normalisation matter. It is therefore assumed that the population of hard sources in the model shows the same distribution and redshift evolution as the sources in the cluster image.

Barger et al. (2001) parameterise the X-ray luminosity function from $0.1 < z < 1.2$ by

$$\frac{d\phi(L_X, z)}{d\log L_x} \propto \frac{(1+z)^B}{(L/L_*)^{g1} + (L/L_*)^{g2}} \tag{2.18}$$

where

$$L_* = L_0 \left(\frac{1+z}{2}\right)^A \tag{2.19}$$

and A,B,L_*,$g1$ and $g2$ are parameters fit by Barger et al.. They also give the space densities of spectroscopically or photometrically identified sources at $z = 1.5 - 3.0$ and $3.0 - 5.0$ (in the Chandra deep fields and ASCA data analysed), and that which would be obtained if all

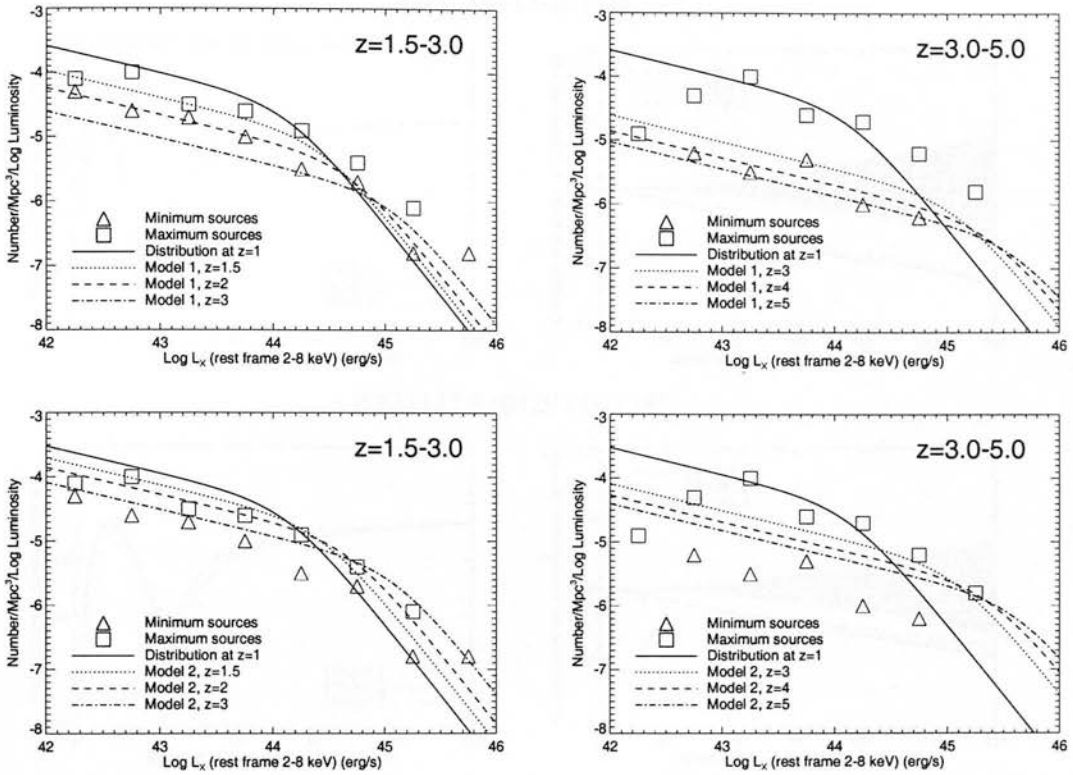

Figure 2.23: Two models of the X-ray luminosity function at high redshift. The solid line shows the $z = 1$ Barger luminosity function, and the triangles and squares show the minimum and maximum luminosity functions data points (from Figure 20 of Barger et al.). The top panel shows the first model, where at $z > 1$ the luminosity function follows the evolution at $z < 1$, but is scaled down by a factor of z^3. The model is a reasonable lower limit to the luminosity function. The lower panel shows a model where the normalisation at $z > 1$ is fixed such that the X-ray source population has a constant energy density, which is an upper limit to the luminosity function.

unidentified sources fell in each redshift interval, as shown in Figure 2.23.

Two of the models adopted here for the X-ray luminosity function use the Barger et al. model for $0.1 < z < 1.0$ and extend it using the data for $z > 1.2$. The first model is designed give a reasonable fit to the sources with confirmed redshifts: it uses the same luminosity function evolution as for $0.1 < z < 1.2$, but for $z > 1$ the distribution is scaled down by an additional factor of z^3. This underestimates the true distribution, as the unidentified sources are not assigned a redshift, but is useful as a lower limit. The top panel of Figure 2.23 shows this model and the data points at a range of redshifts.

A second model is produced by extending the Barger et al. model, scaling the space density such that the energy density remains flat at $z > 1$. This also gives fits which are within the minimum and maximum values in Figure 2.23, with most of the unidentified sources being placed in the $1.3 < z < 3.0$ interval. This gives an upper limit on the

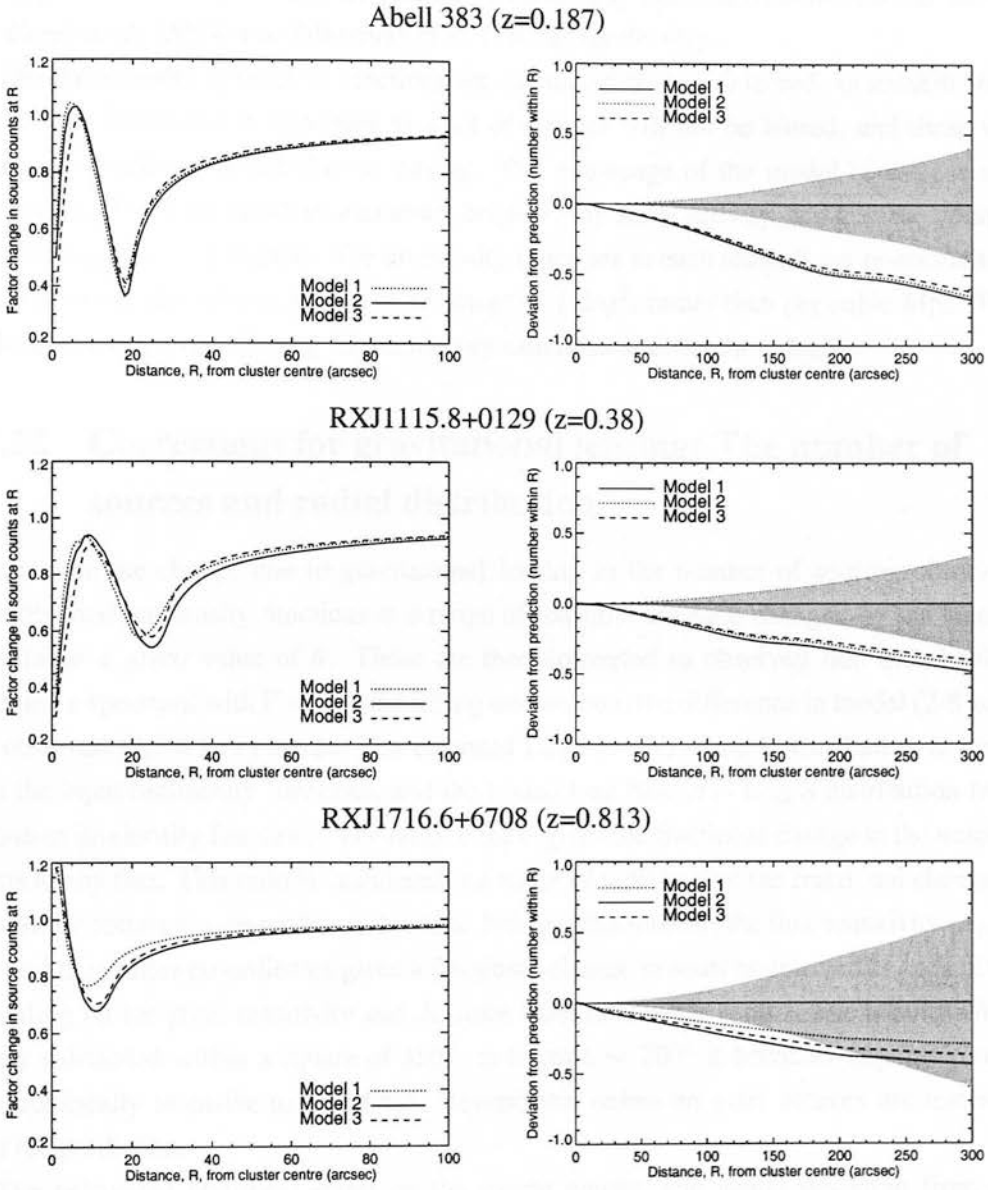

Figure 2.24: The effect of gravitational lensing on three clusters. Three models of the X-ray background luminosity function are shown, as described in the text. The plots in the left column show the factor change at a given radius, and on the right the actual cumulative change in the prediction is shown. The errors on the prediction, due to the number counts in the blank fields, are shown by the shaded area.

possible luminosity functions from these data: Barger et al. (2001) themselves state that at $z > 1$ the energy density production rate per comoving volume "is flat or, more realistically, slightly falling". The model and data points are shown in the lower panel of Figure 2.23.

The third model adopted here is a luminosity dependent density evolution (LDDE) model, with best fit parameters from Ueda et al. (2003), which is shown in Figure 1.2.

This appears to be the best fit to the hard X-ray luminosity function from the ChaMP survey (see Green et al. (2004) and Silverman et al. (2005a) for details).

The three model luminosity functions are calculated from z=0 to z=5, in redshift steps of 0.1. The lower end is important as a lot of sources will not be lensed, and these will reduce any fractional deficit due to lensing. The mid-range of the model (z=1-2) is also important as this is the epoch of maximum bright X-ray AGN activity, and also the point of most lensing by $z > 1$ clusters. The luminosity functions at each redshift are re-normalised to represent the sky volume visible in an image of 1 deg^2, rather than per cubic Mpc. This produces the desired weighting for luminosity functions at different redshifts.

2.6.12 Corrections for gravitational lensing: The number of sources and radial distribution.

To calculate the change due to gravitational lensing in the number of sources observed, the individual luminosity functions at a range of redshifts are each changed by the lensing potential at a given value of θ. These are then converted to observed flux distributions assuming a spectrum with $\Gamma = 1.7$ and taking into account the difference in model (2-8 keV) and observed (0.5-8 keV) bands. The unlensed Log N($< S$) - Log S distribution is found from the input luminosity functions, and the lensed Log N($< S$) - Log S distribution from the output luminosity functions. The ratio of these gives the fractional change in the number counts at any flux. This ratio is calculated at a range of radii to give the fractional change in the number counts at a given flux and radius. Folding this through the flux sensitivity ($S_{\rm min}$) map and the cluster co-ordinates gives a fractional change in sources detected at each pixel, depending on the pixel sensitivity and distance from the cluster centre. The lensing effect is only calculated within a square of 350″, as beyond $\sim$ 250″ it becomes negligible (and computationally intensive to calculate). Beyond this radius no extra sources are removed from the prediction.

The calculated fractional effect on the source counts, and actual deviation from the prediction, are shown for the three models in Figure 2.24. The left panel shows the fractional boost or deficit of sources at a given radius, taking into account the sensitivity of the image at each point. The right panel shows the effect of the three models on the predicted number of sources within a given radius. The errors on the prediction (before gravitational lensing), due to the errors in the blank field number counts, are shown by the shaded area. The gravitational lensing correction is a maximum of $\sim$ 1 source, and the difference between the three models is insignificant compared to the errors on the prediction. As the difference between the models is far smaller than the error on the predicted source distribution, only model 3 (the LDDE model) was used, as its prediction generally lies between those from the other two models.

The lensing model was also tested with a 10% error introduced in the cluster luminos-

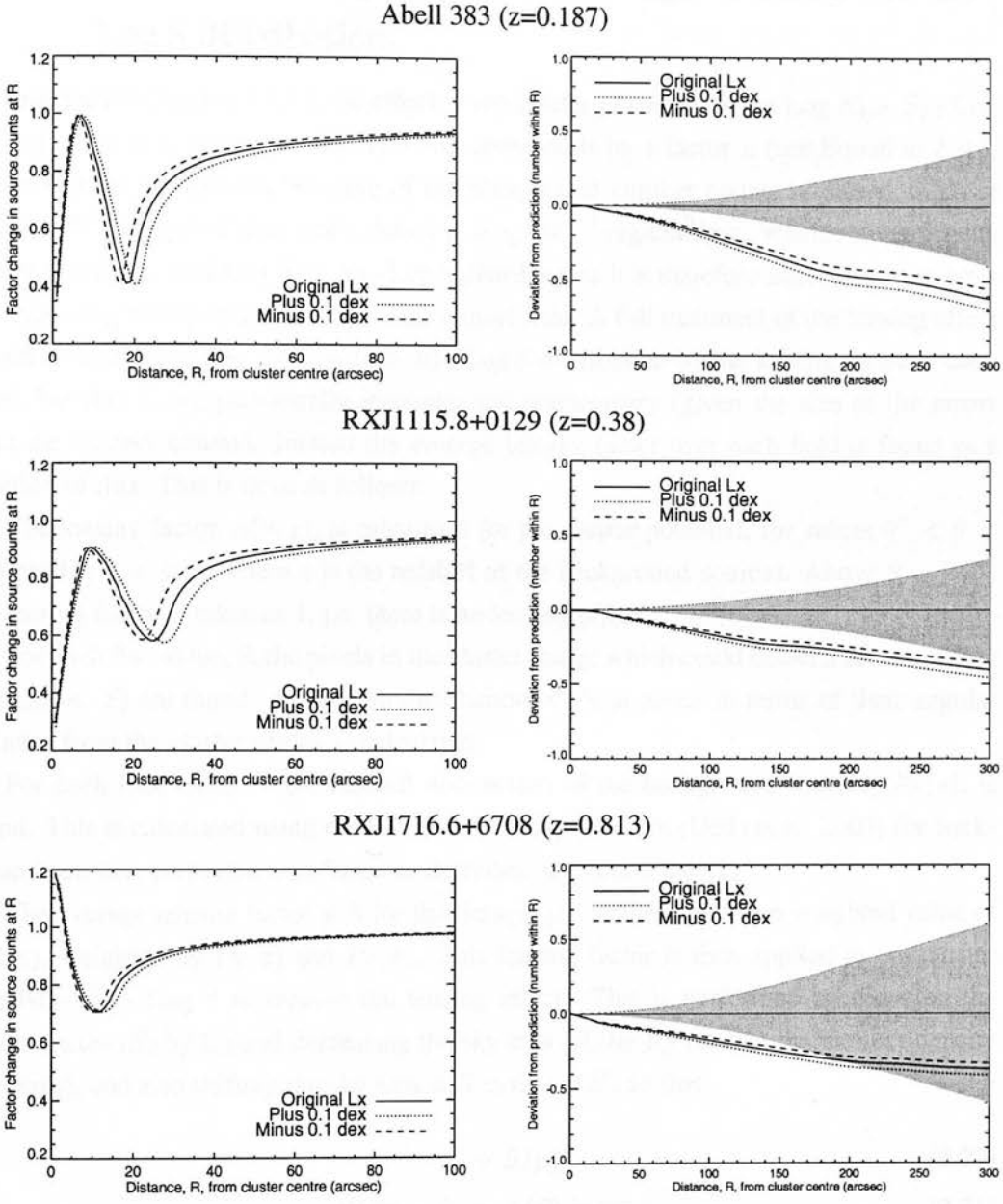

Figure 2.25: The effect of gravitational lensing on three clusters. The calculated lensing effect and the effect of a 10% error on the cluster luminosity are shown. The plots in the left column show the factor change at a given radius, and on the right the actual cumulative change in the prediction is shown. The errors on the prediction, due to the number counts in the blank fields, are shown by the shaded area.

ity. As Figure 2.25 shows, this does not introduce a significant error into the prediction compared to the errors in the prediction due to the blank field number counts (shaded area).

2.6.13 Corrections for gravitational lensing: The Log N($> S$) - Log S distribution.

As described in Section 2.6.11, the effect of the cluster potential on the Log N($> S$) - Log S distribution is to move it to the right and downwards by a factor μ (see Equation 2.16). This results in an apparent boosting of the background number counts in cluster fields at fluxes $\gtrsim 10^{-14}$ erg/cm^2/sec, and a deficit at $S \lesssim 10^{-14}$ erg/cm^2/sec. When comparing the cluster and blank field Log N($> S$) - Log S distributions it is therefore necessary to remove the effect of gravitational lensing for each cluster field. A full treatment of the lensing effect would involve correcting the Log N($> S$) - Log S distribution by the lensing factor at each pixel, but this is computationally intensive and unnecessary (given the size of the errors from the number counts). Instead the average lensing factor over each field is found as a function of flux. This is done as follows:

The lensing factor, $\mu(\theta, z)$, is calculated for the cluster potential, for values $0'' < \theta < 250''$ and $0 < z < 5$ (where z is the redshift of the background source). Above $\theta = 250''$ the lensing factor is taken as 1, i.e. there is no lensing effect.

For each flux value, S, the pixels in the cluster image which could detect a source of flux S ($S_{min} < S$) are found. $P_S(\theta)$, the distribution of these pixels in terms of their angular distance from the cluster centre, is calculated.

For each flux value, S, the redshift distribution of the background sources, $P_S(z)$, is found. This is calculated using the LDDE luminosity function (Ueda et al. 2003) for background sources, converted into fluxes as described in Section 2.6.12.

The average lensing factor at S for this image, $\overline{\mu_S}$, is then the mean weighted value of $\mu(\theta, z)$, weighted by $P_S(z)$ and $P_S(\theta)$. This lensing factor is then applied to the cluster Log N($> S$) - Log S to remove the lensing effect. This is performed by reducing the source fluxes (S) by $\overline{\mu_S}$ and decreasing the sky area (A) by $\overline{\mu_S}$ (so that the number density increases), and also shifting the sky area at S to that at S', so that;

$$S' = S/\overline{\mu_S} \tag{2.20}$$

$$A'(\overline{\mu_S} \times S) = A(S) \times \overline{\mu_S} \tag{2.21}$$

In this calculation the assumption that $\overline{\mu_S} = \overline{\mu_{S'}}$ has been made, which is valid given that $\overline{\mu_S}$ is of the order 1.1, and between S and $1.1S$, $\overline{\mu_S}$ changes by a maximum of 2% (and mean of 0.3%).

The maximum value of $\overline{\mu_S}$ for the cluster fields is, on average, ~ 1.12. To determine the magnitude of the lensing effect a typical distribution of $\overline{\mu_S}$ for the cluster fields is applied to the blank field Log N($> S$) - Log S distribution (which is similar in shape to the cluster field distributions). Removing the lensing effect decreases the source counts at $S > 10^{-13.5}$ erg/cm^2/sec by $\sim 7\%$, makes no change at $S > 10^{-14}$ erg/cm^2/sec, and increases the source

counts by $\sim 5\%$ at $S > 10^{-14.5}$ erg/cm^2/sec. The combined effect of the lensing correction on the sources at each flux depends on the individual cluster fields, and the sky area at each flux.

This method is accurate to first order, but does introduce additional uncertainties. As the average value of μ is applied to all sources, this method will overestimate the number of sources at the flux limit – it assumes that all the sources just below the flux limit are boosted by μ, whereas in reality some sources will be boosted by $< \mu$, and would not be detected. The lensing correction for the Log N($> S$) - Log S distribution is therefore over-calculated, and care should be taken when interpreting the results at low fluxes. To check the magnitude of this result, the lensing-corrected distribution for bright, low redshift clusters was compared to the distribution with half the lensing correction ($\mu/2$). The distributions differed by $\sim$ 10 sources (0.5% of the total, 0.2 per cluster) at low fluxes, but this is well within the 1σ error on the data. The lensing correction applied to the radial distribution does not suffer from the same problems, and so will be more accurate. The overall effect of lensing on the sample is shown in Chapter 3, where the cluster and blank fields are compared with and without the lensing correction.

2.6.14 Corrections for gravitational lensing: Using the NFW profile

The pipeline used in this thesis uses a lensing correction which is based on the single isothermal sphere (SIS) model, which is commonly used for such corrections. However the Navarro-Frenk-White (NFW) profile (e.g Navarro et al., 1997) is a better approximation to the mass distribution of a cluster, especially at higher radius where the SIS can significantly overestimate the mass. In this section the effect of applying the NFW profile is examined for three clusters to evaluate the errors in the SIS model.

The magnification factor, μ, for this model is derived in Appendix A of Myers et al. (2003), using formulae and data from Maoz et al. (1997), Bartelmann (1996) and Navarro et al. (1997). The magnification factor is given by

$$\mu(\theta) = |\,(r_s/D_L)^2\, x/\theta_q \;\; dx/d\theta_q| \tag{2.22}$$

where

$$x = \frac{D_L\theta}{r_s} \tag{2.23}$$

$$\frac{\theta_q}{x} = \frac{r_s}{D_L} - \frac{4GM_{1.5}D_{LS}}{D_S r_s c^2 g(1.5\mathrm{Mpc/r_s})}\frac{g(x)}{x^2} \tag{2.24}$$

$$\frac{d\theta_q}{dx} = \frac{r_s}{D_L} - \frac{4GM_{1.5}D_{LS}}{D_S r_s c^2 g(1.5\mathrm{Mpc/r_s})}\frac{d[g(x)/x]}{dx} \tag{2.25}$$

$$\tag{2.26}$$

$$g(x) = \ln(x/2) + \frac{2}{x^2-1}\tan^{-1}\sqrt{\frac{x-1}{x+1}} \quad (x > 1) \tag{2.27}$$

$$g(x) = \ln(x/2) + \frac{2}{1-x^2}\tanh^{-1}\sqrt{\frac{1-x}{1+x}} \quad (x < 1) \tag{2.28}$$

$$g(x) = \ln(x/2) + 1 \quad (x = 1) \tag{2.29}$$

$$\tag{2.30}$$

Here θ, D_{LS} and D_S are as described above, D_L is the angular distance to the lens, $M_{1.5}$ is the mass within 1.5 h^{-1} Mpc of the cluster centre and r_s is the characteristic scale in Mpc, approximated by

$$r_s = 0.3\left(\frac{M}{10^{15}M_\odot}\right)^{1/3} h^{-1}\text{Mpc} \tag{2.31}$$

The only free input to this model is therefore the cluster mass, M, which is approximately equal to the mass within 1.5 h^{-1} Mpc for the size of clusters being considered here, and to the degree of accuracy required for this model. To estimate the cluster mass from the X-ray luminosity, the self-similar relationship $L_X \propto M^{4/3}$ (e.g Kaiser 1986) was used, with the constant of proportionality taken as 10^{25} from the low redshift values in Figure 9 of Maughan et al. (2006).

The NFW magnification factor was applied to the cluster images in the same way as for the SIS model. The resulting changes to the predicted radial distribution, together with the original SIS changes, are shown in the first 3 panels of Figure 2.26. The NFW model clearly changes the shape of the radial correction, as well as reducing slightly the overall number of sources lost due to gravitational lensing.

These clusters are quite typical of the sample as a whole, although they are slightly brighter than average. When the results for the three clusters are combined in physical units, it is clear that the SIS profile underestimates the correction in the cumulative radial counts at low radius and overestimates at high radius. In all three fields the point at which the corrections agree is around 0.5 Mpc. Scaling these results to the whole sample would imply that the SIS correction for all 113 fields undercorrects the cumulative radial profile by around 17 sources at $\sim$0.2 Mpc, is approximately correct at $\sim$0.5 Mpc and adds an additional $\sim$12 sources at high radius compared to the NFW profile.

This error should be considered when examining the results of the pipeline, which uses the SIS model. It is desired that, when the final version of the pipeline is produced, the NFW model should be used rather than the SIS model. Examination of Figure 3.4(b) shows that using the NFW model would increase the excess at $\sim$0.2 Mpc by $\sim 1\sigma$ and decrease the excess at > 1 Mpc by $\sim 0.2\sigma$.

The net effect of using the NFW profile is to smooth out slightly the steep increase seen at 0.5 Mpc, with a few more sources in the central regions. However, the distinctive shape

of the radial excess is unchanged, and the large discrepancy between the observed profile and the galaxy distribution remains. The corrected radial profile, with a small excess of sources at low radius, is indicative of a shell of AGN in the cluster outskirts, as described in Section 3.

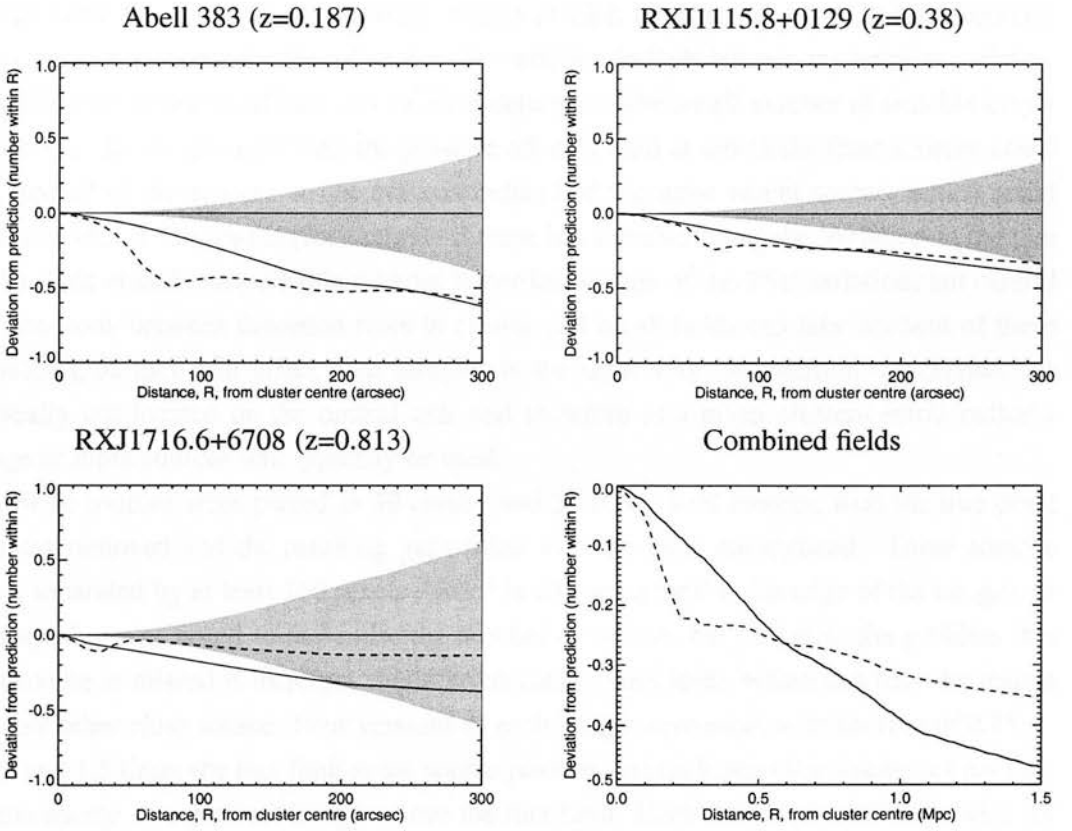

Figure 2.26: Panels 1:3 - the effect of the gravitational lensing correction for the SIS (solid line) and NFW (dashed line) models. The change in the cumulative prediction, as shown for the SIS model alone in Figure 2.25, is shown for both models along with the errors on the cumulative prediction (shaded region). Panel 4 - the combined radial correction due to lensing for the three fields, scaled by physical distance from the cluster centre.

2.7 Montecarlo simulations of faint sources

The statistical fluctuations in the background level in the regions of intra-cluster emission could cause sources in the central regions to be missed by a wavelet detection method. In order to evaluate the detection efficiency of WAVDETECT near the flux limit, montecarlo simulations of faint sources were performed on cluster and blank field images. The difference in the number of sources detected, and with significance > 3, could then be evaluated as a function of radial position for the cluster and blank field samples.

Because of the complex nature of the Chandra PSF it is not straightforward to simulate X-ray sources, especially those with very few photons. In particular, the variation of the PSF as a function of distance from the optical axis, and the non-gaussian profile make it very hard to model the sources accurately. To overcome this problem the faint sources used in the montecarlo simulations were extracted from bright sources at the same off-axis radius, which were not near a chip boundary, region of high background or other faint sources. This method accounts for the off-axis radial variation in PSF, but not any angular variation or difference between ACIS-I and ACIS-S detectors. The small number of suitable bright sources in the sample restricted the possible off-axis radii at which the false sources could lie, and all of the sources at one off-axis radius had the same parent source, which could lead to a bias in the results (for example if there is a significant angular variation in the true PSF). This error is unavoidable without better knowledge of the PSF variation, but careful comparisons between detection rates in cluster and blank fields can take account of these problems, as they will affect both samples in the same way. In addition the clusters are typically not located on the optical axis and therefore at a given cluster-centric radius a range of input sources will typically be used.

False sources were placed in 30 cluster and 30 blank field images, with the true point sources removed and the resulting gaps filled with the local background. These sources were separated by at least 160 pixels (which is 10 source radii at the edge of the image), as this spacing was found to maximise the number of sources but minimise the problem that if a source is missed it increases the inferred background level, which can bias the results for any other close source. Four versions of each image were used, with sources of 0.75, 1, 1.25 and 1.5 times the flux limit at the source position. At each point the number of photons in the source was the next integer above the flux limit. Each field was used only twice for each flux limit, since the restricted range of radii for the input sources meant that additional runs would begin to repeat the positions of the input sources, and cause correlations in the detection fraction. The two runs therefore used sources placed at very different radii. Since each image could only contain a maximum of 111 sources (for ACIS-I), there are quite large errors in the results.

There are possible correlations between radius and detection probability, introduced by using a small set of input bright sources for these simulations (due to the unknown angular variation of the PSF). To remove the effect of these errors the cluster and blank fields were paired, with each pair using the same ACIS detector. For each pair the radial distributions were calculated from the same position, which was found in 'chip' co-ordinates, so that each cluster – blank field pair had the same centre point regardless of the rotation of the detector. In this way the cluster and blank field samples use the same set of bright sources to produce the faint sources in each radial bin.

The sources were detected using WAVDETECT with the same settings used in the pipeline, and were also subject to the significance test applied all pipeline sources. Only detected

sources with $SIG > 3$ were included in the sample. The detection probabilities were calculated in annuli of width $75''$ starting from an inner radius of $25''$, in order to minimise the error bars whilst still being able to observe any radial trend.

The results of the simulations are shown in Figure 2.27. At all radii the detection probability decreases with decreasing flux, as expected. Sources at the flux limit are detected with $\sim 40\%$ probability, and this increases sharply for brighter sources. The missed sources are accounted for in the pipeline as they occur in both the blank and cluster fields, and the prediction for cluster fields is based on the blank field number counts.

However, in the central bin there is a deviation between the detection rates in blank and cluster fields. Surprisingly, the detection rate in the blank fields appears to increase in the central regions - this is most likely due to the problems with producing accurate input sources, as described above. If the detection rates are plotted as a function of off-axis angle then there are $\sim 10\%$ variations at different radii, with some of the more central sources having higher detection rates than expected. The inner radial bin is most likely to contain sources produced from just one or two bright sources, and will therefore be more biased by this effect than at outer radii. The important factor here is that the cluster and blank field samples contain the same input sources, so have the same bias.

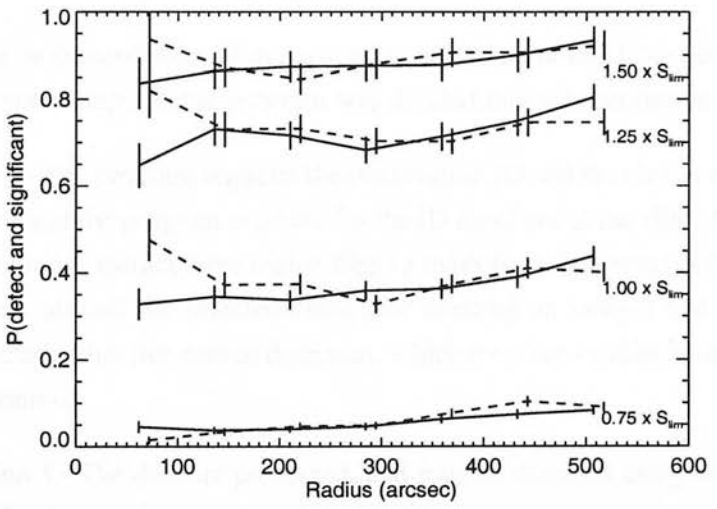

Figure 2.27: The results of montecarlo simulations of faint sources in cluster (solid line) and blank (dashed line) fields. The probability of a source in each radial bin being detected and significant is shown for sources of 0.75, 1.0, 1.25 and 1.5 times the flux limit (lower to upper lines respectively). The data points are plotted at the centre of each radial bin, with 1σ errors. The data for the blank fields are offset horizontally slightly for clarity.

The number of sources missed in the central regions of the cluster fields can be estimated roughly from the values in Figure 2.27 and the Log N($> S$) - Log S distribution. The number of sources expected in each image was estimated from the number per square degree

as a function of flux, the nearest detection probability to each flux value and the area of the radial bin. The difference between the blank and cluster fields was calculated for sources below 1.75 times the flux limit, as above this point the differences between blank and cluster field detection rates become statistically insignificant, and the number of sources per square degree decreases, such that the number of missed sources is negligible compared to that at lower flux. The difference is found to be ~ 0.12 sources per field, which are missed in the central $25'' - 100''$ of cluster images relative to the blank fields. In the central $25''$ the area is so low and flux limit so high that there will be less than 1 missed source over the 113 cluster fields.

The full sample of cluster fields should therefore have ~ 13 extra sources within the central $100''$. This corresponds to a $\lesssim 1\sigma$ increase in the excess at this radius (see Figure 3.3), and makes minimal difference at higher radii. When combined with the NFW lensing correction (Section 2.6.14) the two corrections result in a small ($\lesssim 2\sigma$) excess of sources at low cluster-centric radius. The interpretation of these results in Chapter 3 is therefore not changed significantly. It is possible that the small excess in the central regions is due to the projection of AGN in the cluster outskirts on the 2 dimensional image.

2.8 Summary of pipeline

The final pipeline automated most of the processes described in this Chapter. Manual input was required for some steps, so the program was divided into subsections as follows:

Manual Section 1 - The program requests the observation ID and the cluster name. The raw image is displayed and the program prompts for the ID numbers of the chips to be analysed. The user is required to construct three region files - a mask for bright sources (for calculating lightcurves), a box around the selected chips (for creating an image) and smaller boxes covering the selected chips (for source detection, which requires smaller image regions due to memory problems).

Automatic Section 1 - The data are processed, and sources detected using WAVDETECT, as described in Section 2.3.

Manual Section 2 - The user is required to examine the sources plotted on the image, and identify those which should be removed. Any detections of extended cluster emission should be removed, and also any sources which were detected twice. The latter are due to the image being cut into overlapping sections for the source detection, and can be identified by plotting the source detection boxes and examining the overlap regions, as shown in Figure 2.28. The redshift of the cluster is also input.

Automatic Section 2 - The source properties are calculated, and a list of significant sources

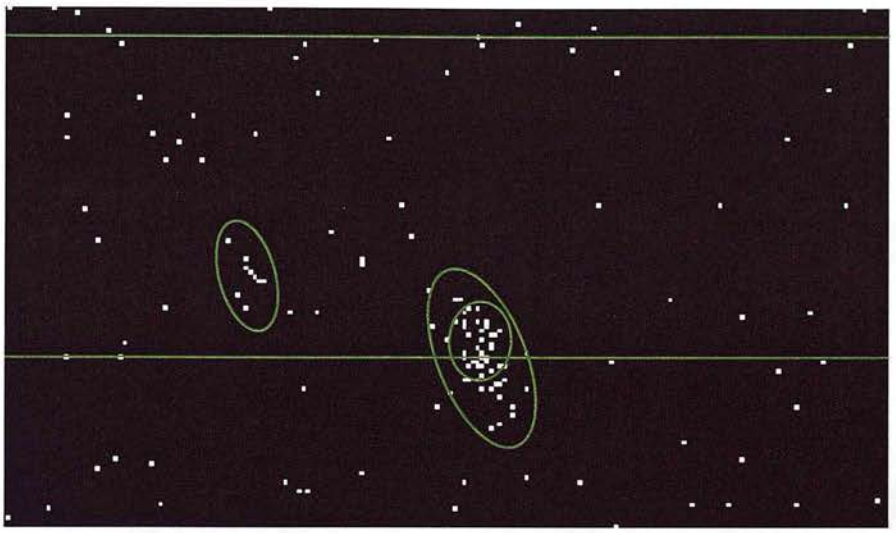

Figure 2.28: An example of sources detected twice due to cutting the image into sections. The area between the two green lines was included in both images - both sources are detected twice and so one detection of each needs to be removed. Whereas the source on the left is detected well in both images, for the source on the right one detection is too small due to the edge of the image, highlighting the need to have a bigger overlap region than the largest source.

is generated, as described in Section 2.5. The smoothed background image described in Section 2.6.3 is also produced.

Manual Section 3 - The smoothed background image and the full image are displayed. The user is required to select the cluster centre from a list of options (calculated from the peaks of the background image) or input another point. The user is also required to assign a morphology to the cluster.

Automatic Section 3 - The program now has all the inputs it requires. At this stage a combined Log N($> S$) - Log S distribution is made from the blank fields to compare to the cluster fields. The sky area for each field is calculated, and the individual Log N($> S$) - Log S distributions are made for the cluster fields and plotted against the blank field distribution. The cluster spectrum extraction region is found, and the spectrum, background file and calibration files are calculated and fit in XSPEC. Images are made in hard and soft bands only, and source hardness ratios are calculated. Finally, the predicted and actual radial distributions are calculated for each field, with and without the gravitational lensing correction. The data for each field can now be compared to determine the properties of AGN in galaxy clusters.

CHAPTER 3

Investigating AGN in galaxy clusters - the results

3.1 Introduction

In this Chapter the 0.5-8 keV sources found in the cluster fields and the predicted distributions from the blank fields are compared in order to determine the prevalence and distribution of AGN in galaxy clusters. The data used are produced by the pipeline as described in Chapter 2. In brief, this consists of a Log N($> S$) - Log S distribution for each blank and cluster field, including the number of sources and sky area at each flux, and a radial plot for each field, showing the actual distribution of sources and the predicted radial distribution (assuming no cluster AGN). To investigate the AGN in the cluster fields without being dominated by field-to-field statistical variance, the data from different subsets of fields are combined. The combined Log N($> S$) - Log S distribution is compared to that from the blank fields to determine the flux of the cluster sources. The combined radial distributions are compared to the combined prediction to find the radial distribution of cluster sources, and the total excess over the whole field.

Section 3.2 describes the analysis of the excess X-ray point sources found in the main cluster sample, focusing on the number, flux and radial distribution of the excess, and the effects of the gravitational lensing correction. In Section 3.3 the luminosity of the sources are calculated, to determine whether the excess is mainly due to star-forming galaxies or AGN. In Section 3.4 the results of previous studies (described in Sections 1.4.3 and 1.4.4) are compared to the pipeline results for the same fields, and the differences are discussed. In Section 3.6 the sample is split into subsamples, by cluster redshift, morphology and lu-

minosity. The distribution of clusters in these variables is discussed in Section 3.6 to define the subsamples. The dependence of the AGN properties on each variable are evaluated in Sections 3.7 to 3.9 respectively. Finally, in Section 3.10 the possible physical interpretations of the properties of AGN in galaxy clusters are discussed.

3.2 Excess point sources in the galaxy cluster sample

3.2.1 Excess sources in cluster fields

Figure 3.1 shows the excess or deficit of sources in each field in the 0.5-8 keV band, compared to the prediction (as described in Section 2.6.9 and illustrated in Figure 2.17). The predictions for each observation are calculated using the combined Log N ($> S$) - Log S distribution from the blank fields observed with the same ACIS array, and the lensing correction (see Section 2.6.12) is included in this analysis.

The histogram of deviations for the blank fields has a mean of -0.003 sources, and is fully consistent with a normal distribution. A K-S test against a normal distribution with a mean of 0 and standard deviation of $\sqrt{52}$, where 52 is the mean number of sources in a blank field, gives a probability of 60% that the blank field deviations are drawn from the normal distribution[1]. This is to be expected, as the prediction is based on the blank fields, but serves as a check of this method.

The histogram of deviations for the 131 cluster fields clearly shows that the cluster fields contain extra sources. The distribution has a mean of 2.1 sources, and is inconsistent with a normal distribution with a mean of 0 and standard deviation expected from the mean number of sources ($\sqrt{42}$) with $> 97.5\%$ confidence. If the same analysis is performed without the correction for gravitational lensing, the mean of the distribution is 1.4, and it is also inconsistent with a mean of 0 and standard deviation of $\sqrt{42}$, with $> 90\%$ confidence.

The lower panel of Figure 3.1 shows the difference between the uncontaminated (class 1, 2 and 3) and contaminated (class 1c and 2c) fields (see Section 2.4.2). The mean for the uncontaminated fields is 1.51 and that for the contaminated fields is 5.21, and there is a $\sim$ 18% chance that they are drawn from the same distribution. The contaminated fields have similar distributions of exposure time, main cluster morphology and redshift as the uncontaminated sample, so the extra sources are likely to be due to the contaminating clusters. The contamination appears to add around 3 sources to the excess, which seems very large considering that the contaminating clusters are generally small. This difference may be due to the statistical fluctuations in the small number of contaminated fields (as the

[1] In fact the standard deviation should be $\sim$ 10% larger due to large scale structure (see Section 2.6.10), but increasing it by 10% gives the same results.

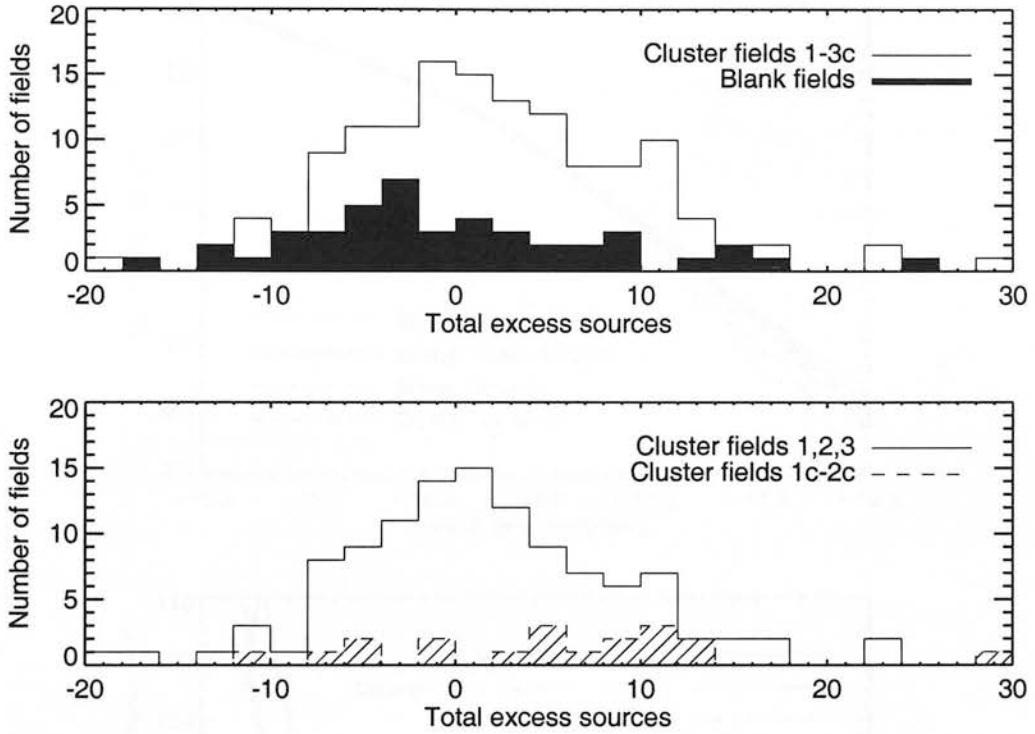

Figure 3.1: The difference between the predicted and actual number of sources over the whole field. The top histogram shows the excess or deficit for cluster fields (class 1-3c) and blank fields. The blank fields are distributed around 0, whereas the cluster fields clearly have an excess of sources on average. The lower histogram shows the excess sources in uncontaminated (1,2,3) and contaminated (1c,2c) cluster fields. There are slightly more sources on average in the contaminated fields, so the contaminating clusters may also contain X-ray sources.

difference is only significant at the $\sim 93\%$ level). It is possible that the excess is real and that the extra extended X-ray emission either indicates the presence of large-scale structure around the cluster, or an additional background cluster – investigation of this is beyond the scope of this work and so these fields are rejected for the rest of the analysis (unless specifically stated), and the term 'cluster fields' refers to class 1, 2 and 3 fields only.

We can therefore conclude that there are X-ray sources in the galaxy clusters, at the level of around 1 or 2 per uncontaminated cluster (although this may depend on the cluster properties and depth of the observation), and that this excess is smaller but still significant if the lensing correction (which adds ~ 0.7 sources per field) is not applied. As a typical cluster contains from ~ 30 to a few thousand galaxies, we are looking at activity at the few percent level, but as each image probes to a different flux limit it is not trivial to state here whether this is a higher or lower number of AGN than expected from the level of activity in the field. This issue is investigated in detail in Section 3.5.

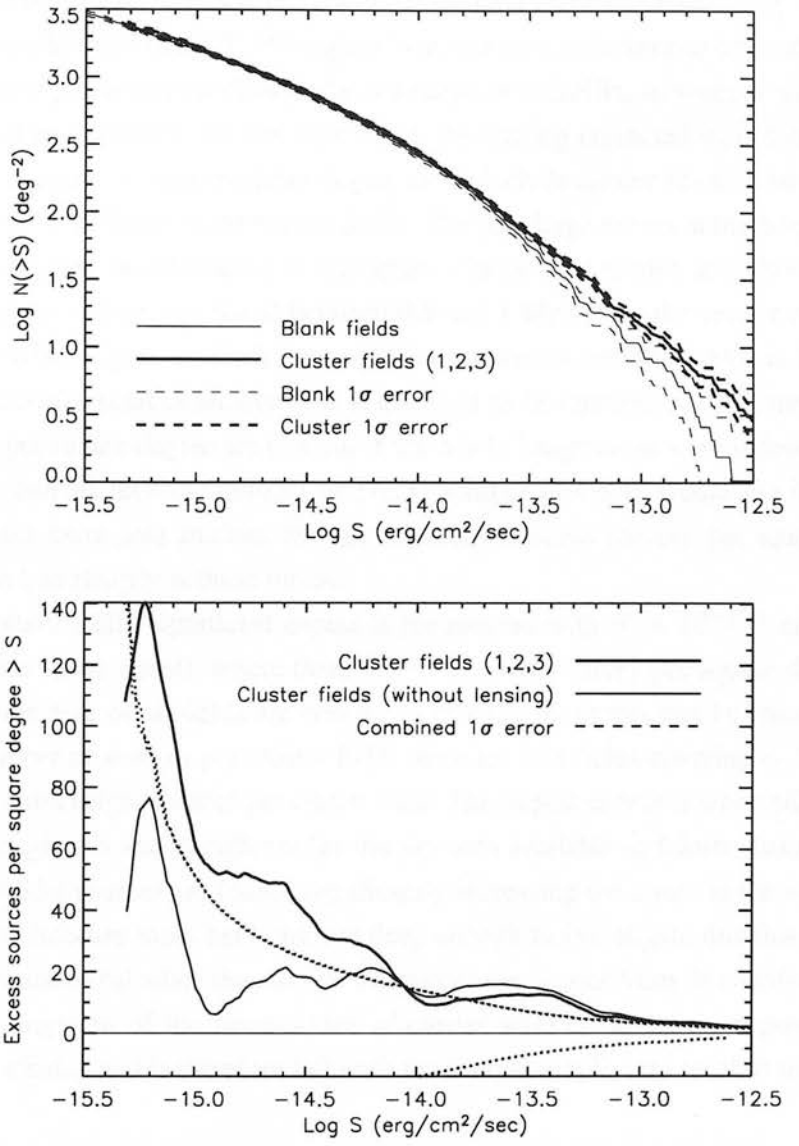

Figure 3.2: Upper panel: The Log N($> S$) - Log S distributions for the cluster and blank field samples, including the lensing correction. The cluster fields clearly contain more sources than the blank fields. Lower panel: The (smoothed) difference between the Log N($> S$) - Log S distributions, with combined errors. The distribution of excess sources is shown before (thin line) and after (thick line) the lensing correction is applied. An excess of sources is seen at all fluxes.

3.2.2 Cumulative number counts in cluster fields

The Log N($> S$) - Log S distributions for the cluster and blank field samples are shown in Figure 3.2. At all flux levels, S, the cluster fields contain more sources brighter than S than the blank fields. The lower panel shows the excess sources brighter than a given flux, with and without the lensing correction (see Section 2.6.13). As expected, correcting

for the effect of lensing decreases the number of bright, and increases the number of faint, sources. When the lensing effect is not corrected for then there is a statistically significant excess of sources brighter than $10^{-13.5}$ erg/cm^2/sec, but no significant rise beyond this. This seems unphysical given that the clusters lie at a range of redshifts, so sources with a range of fluxes would be expected. On the other hand, the lensing-corrected distribution shows an increase in excess sources per square degree as we include fainter sources, showing that there are sources at all fluxes in the cluster fields. The very large excess at the faintest fluxes ($< 10^{-15}$erg/sec) may be misleading in this figure – in the next section it is shown that the majority of cluster sources are found between 0.5 and 1 Mpc from the cluster centre, and this is similar to the region in which the very faintest sources are detectable. In Figure 3.2 the area in which the sources are detected is assumed to be representative of the full area, as the sources per square degree are plotted. If the whole image areas were indeed sensitive to the faintest sources then the number of excess sources probably would not increase in proportion to the extra area studied, and the number of excess sources per square degree would increase less sharply at these fluxes.

The most statistically significant excess is for sources with $S > 10^{-13.5}$ erg/cm^2/sec (as shown in the lower panel), where there are $\sim$ 12 extra sources per square degree. As almost the whole area of all fields are covered at this flux limit this can be translated into an average number of sources per cluster field; there are 113 fields covering ~ 5.33 deg^2, giving ~ 0.55 extra bright sources per cluster field. The largest excess is when all fluxes are included, although it is less significant (as the sky area available at fainter fluxes is much smaller so less faint sources are found, significantly increasing the errors in the number per square degree). Because most fields are not deep enough to investigate this flux limit it is not straightforward to calculate the number of sources per cluster from this analysis.

A full investigation of the luminosities of cluster sources obviously depends on the redshift of the cluster, and is therefore left until the sample is split into redshift bins.

3.2.3 Radial distribution of cluster sources

To investigate the radial distribution of cluster X-ray sources, the predicted and actual number of sources are calculated as a function of radius (see Section 2.6.9). The resulting excess in the cluster fields, as a function of angular distance from the cluster, is shown in Figure 3.3 (including the lensing correction described in Section 2.6.12). As described in Section 2.6.10, there is a 1σ offset between the ACIS-I and ACIS-S blank fields, so the excess is calculated in two ways; comparing ACIS-I cluster fields to the ACIS-I blanks, ACIS-S cluster fields to the ACIS-S blanks, and combining the two (left panel of Figure 3.3), and comparing the full sample to the combined blank fields, regardless of the array used (right panel of Figure 3.3). The results for the two methods are very similar. As there is not a significant increase in the errors between these methods, and as some subsamples of the clusters may

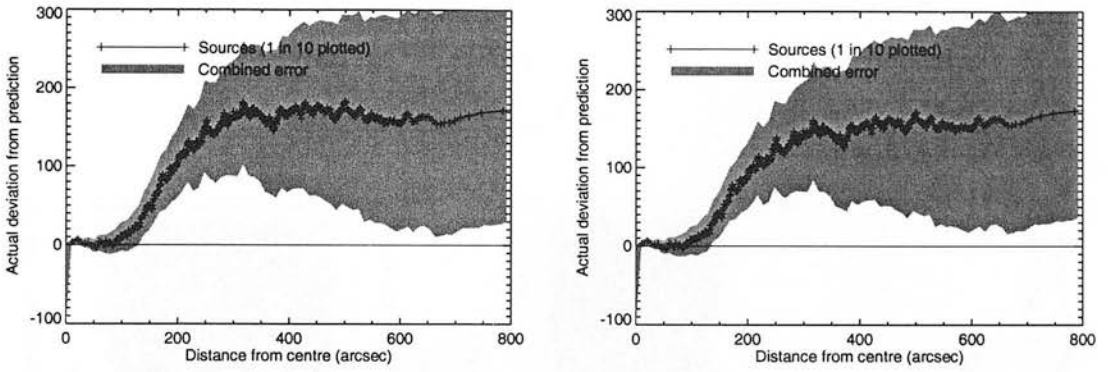

(a) - using ACIS array (b) - ignoring ACIS array

Figure 3.3: The (cumulative) number of excess sources within a given angular distance from the cluster centres, for all 113 good cluster fields and with the lensing correction applied: (a) - compared to a prediction for each cluster which uses only data from the blank fields observed with the same ACIS array as the observations, and (b) - compared to the prediction for each cluster using data from all blank fields, regardless of ACIS array. The first method gives very slightly higher results, but there is not much difference between results or errors for the two methods.

contain ratios of ACIS-I:ACIS-S fields that are vastly different to that of the blank fields, the former method is used in all future analysis to ensure that the analysis is robust.

To compare the radial distributions for the cluster fields in terms of physical distance from the cluster centre, the radial distribution for each cluster field was rescaled to the physical distance at the redshift of the cluster. The radial distribution and radial excess of cluster sources are shown in Figure 3.4(a) and (b). Panel (c) of Figure 3.4 shows the radial excess without the lensing correction. Removing the lensing correction makes a significant difference to the plots, reducing the significance of the excess, but also introducing a deficit of sources in the central 0.5 Mpc, corresponding to around 0.3 sources per cluster field, and significant at the $\sim 1\sigma$ level. When the lensing corrections for each field are applied, the deficit in the central regions is removed, as seen in Figure 3.4(b). This indicates that the lensing effect is important, particularly in the central regions, and that the lensing correction works well.

The radial distribution of the excess sources is striking – almost all of the sources are found between 0.5 and 1 Mpc from the cluster centre. This increase in sources is far more sudden than that seen when the radius is measured in arcseconds (Figure 3.3), and is significant at the $\sim 3\sigma$ level.

Before analysing the radial distribution it is worth explaining why the possible systematic sources of radial bias cannot account for this distribution. A possible concern is that the sensitivity of the cluster observations is lowest in the centre (within the cluster emission) and at the outskirts of the image: therefore, in each image, the area where the faintest sources can be detected is at moderate radius, which is also where the radial excess is seen

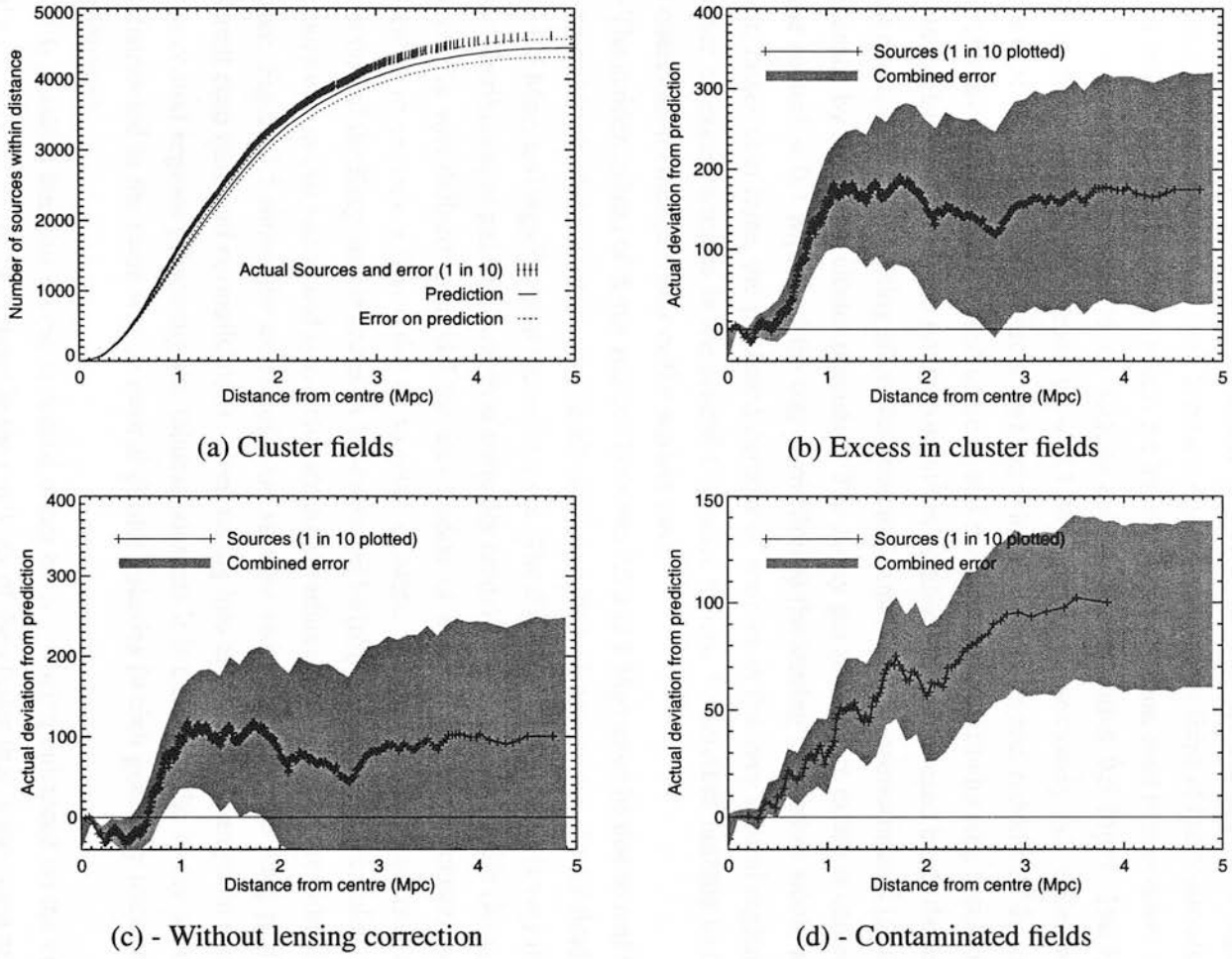

Figure 3.4: Cumulative radial distribution of sources for cluster fields. (a) - Radial distribution and prediction for 113 cluster fields (class 1,2,3) with the lensing correction. (b) - Radial excess for the cluster fields with the lensing correction. (c) - as (b) but without the lensing correction. (d) - as (b) but for the 19 contaminated (class 1c and 2c) fields.

(hence the problem with evaluating the number of faint sources per square degree over the whole field, discussed in the previous section). A potential problem therefore, is that cluster fields may contain more faint sources (near the flux limit) at all radii, but that these are only detected at moderate radius. However, since many fields with different distance scales and flux limits are combined, it is not the case that the 0.5 - 1 Mpc radius is probing a significantly different population of sources than any other radius. Also, as shown in Figure 3.2, the excess sources are found at all fluxes, not just near the flux limit of the observations.

A second potential concern is that the lensing approximation used breaks down at small radii - could this be related to the lack of excess sources within 0.5 Mpc? The Einstein radii of these clusters correspond to $\sim$ 0.1 Mpc (although obviously this varies with the redshift of the background sources and the velocity dispersion and redshift of the cluster), so problems with multiply lensed sources, and the inaccuracy of the lensing approximation within the Einstein radius are not important[2].In addition the model used treats the lens as a point mass, so that the lensing effect for sources at small radii is overestimated (as they are not lensed by the whole cluster potential). The X-ray gas (and hence mass) is concentrated in the central $\sim$ 0.1 Mpc, and the tiny correction to the lensing correction would actually lower, rather than raise, the predicted number of sources in the very central regions. The absence of excess sources in the central and outer regions is therefore nothing to do with the observation characteristics or the models used.

The sudden excess of X-ray sources between 0.5 and 1 Mpc must be due to real sources on the outskirts of the clusters. It is both sudden, with $>$ 1 source per cluster field within Δr = 0.5 Mpc, and significant at the $\sim 3\sigma$ level. The distribution of sources is very different to the distribution of galaxies, which is normally modelled with a King profile (King 1972): this profile was defined to model the distribution of mass in the Coma cluster, and can be scaled to provide a first order fit to other clusters. The cumulative two dimensional projection of the King profile scales as $M(<r) \propto ln(1+(r/r_0)^2)$, where r is the radius, M(<r) the mass within that radius and r_0 is a characteristic radius (known as the core radius) for the cluster. Figure 3.5 shows the excess of point sources and some example King profiles for different core radii and normalisations - even taking into account the changes in sensitivity in the central regions (obscuring the faintest sources) it is clear that the X-ray sources are not distributed in the same way as normal cluster galaxies (which generally trace the mass distribution).

It is possible that this excess is caused either by AGN being enhanced on the outskirts of the clusters, or by AGN activity in the outskirts of the cluster that is the same as that in the field, combined with suppression in the inner regions of the cluster. These possibilities are discussed further in Section 3.5.

[2]It could be argued that the more luminous clusters have larger Einstein radii, so may have an excess at $\sim$ 0.5 Mpc due to lensed sources. However, in Section 3.9 it will be shown that the radius of excess does not depend strongly on cluster luminosity, so it appears that the lensing correction is calculated correctly

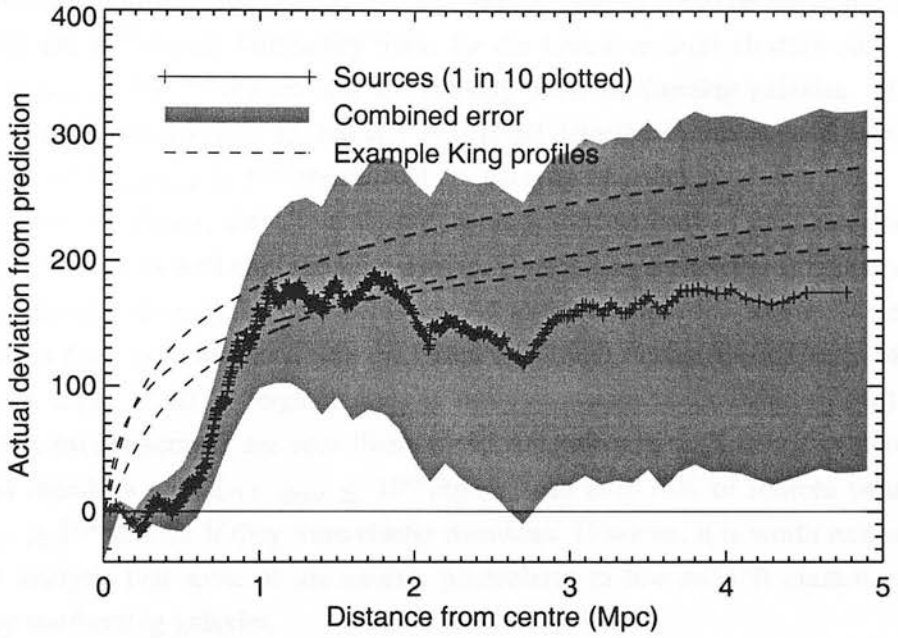

Figure 3.5: The radial distribution of cluster sources (as shown in Figure 3.4(b)) with examples of the King profile.

As an aside, the radial distribution of sources in the 19 contaminated (class 1c and 2c) fields was also investigated. The distribution of the excess sources is shown in Figure 3.4(d), and is clearly of a different shape to that for the uncontaminated fields. Although showing the same flat distribution from $\sim$ 0 to $\sim$ 0.5Mpc, followed by a rise in sources, the distribution continues to rise to give a total excess of $\sim$ 100 sources. This corresponds to an average of $\sim$ 5.3 sources per cluster field, of which only half are within the central 1Mpc. The number in the central regions is approximately that which would be expected for uncontaminated clusters, and so it seems that the conclusion in Section 3.2.1, that the extra sources are due to the contaminated nature of these fields, is true.

3.3 The brightest and faintest cluster sources

In order to investigate the properties of AGN it is important to identify the nature of the excess sources, as they could be powerful starbursts or AGN. The starforming and AGN population overlap at moderate luminosity, so here it is assumed that any source with around $L_{0.5-8\mathrm{kev}} > 1 \times 10^{41}\mathrm{erg/sec}$ is likely to be an AGN as although massive starbursts exist at this luminosity, they are far rarer than AGN (see Section 4.5.3). The faintest sources identi-

fied have $F_{0.5-8\mathrm{kev}} \sim 10^{-15.5}$erg/cm^2/sec which, if they lie in a z=0.1 cluster, correspond to sources with luminosities[3] of $L_{0.5-8\mathrm{kev}} \sim 10^{40}$erg/sec, and so could be starforming galaxies. Using the 10^{41}erg/sec luminosity limit, for the lowest redshift clusters only sources with $F_{0.5-8\mathrm{kev}} \gtrsim 10^{-14.4}$erg/cm^2/sec are unlikely to be starforming galaxies. However, this falls steeply with redshift, so that at $z = 0.25$ all detected sources would have cluster luminosities of $L_{0.5-8\mathrm{kev}} \gtrsim 10^{41}$erg/sec and are likely to be AGN.

As Figure 3.2 shows, there is a significant excess of sources at moderate fluxes ($\sim 10^{-14}$erg/cm^2/sec), as well as at the lowest fluxes (in addition the excess at the very lowest fluxes corresponds to many fewer detected sources as there is less sky area available, so the faint sources have even less effect on the radial results). Because the majority of excess sources are either $> 10^{-14.4}$erg/cm^2/sec, or lie in moderate ($z > 0.25$) redshift cluster fields, most excess sources are very likely to be AGN – only 0.9% of all sources could be cluster members with $L_{0.5-8\mathrm{kev}} \lesssim 10^{41}$erg/sec, and over 75% of sources would have $L_{0.5-8\mathrm{kev}} \gtrsim 10^{42}$erg/sec if they were cluster members. However, it is worth remembering in future analysis that some of the excess, particularly in low redshift clusters, may be caused by starforming galaxies.

An intriguing aspect of Figure 3.2 is the excess of very bright sources in the cluster fields (with flux $> 10^{-12.5}$erg/cm^2/sec). It is possible that these are associated with the cluster, but also that they are bright galactic stars. It is possible that the blank fields were selected to avoid these stars, and so the excess may not be due to the cluster. These sources are therefore worth investigating in detail.

The brightest sources in the cluster fields are all found in observations of $z < 0.5$ clusters, and if they lie in the cluster they correspond to very bright AGN, with $L_X \gtrsim 10^{44}$erg/sec (this population is not seen in the higher redshift cluster observations, but this may be due to the smaller number of fields, and is investigated in Section 3.7). As the number of sources is so small, it is possible to investigate them individually. Thirteen cluster (10%) and two blank (5%) fields contain sources with fluxes $> 10^{-12.5}$erg/cm^2/sec, and these were examined using the NED and the ESO digitised sky (version II). In both of the blank fields the sources are known AGN. Of the thirteen cluster fields, two contain close pairs of bright sources and two contain two distinct bright sources, the rest containing one each. Both of the close pairs, and two of the other sources, are emission from galactic stars. In addition, three of the sources have confirmed redshifts which are not in the galaxy cluster. Of the remaining 8 sources, 3 are confirmed to be cluster members either by redshift, or by position (located coincident with the central cluster galaxy), and five are associated with optical sources without known redshifts. The fraction of cluster fields (with $z < 1$) with bright non-cluster sources is therefore at least $\sim 5\%$, which is comparable to that for the blank fields (although none of the blank fields contain very bright X-ray stars). The fraction

[3]Fluxes are converted into luminosities in the rest frame 0.5-8 keV band assuming an unabsorbed spectrum with photon index $\Gamma = 1.7$

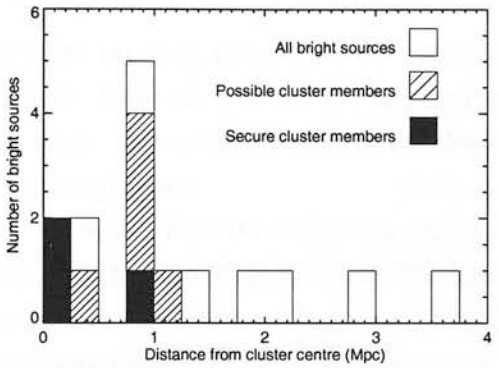

Figure 3.6: The radial positions of bright ($> 10^{-12.5}$erg/cm^2/sec) sources in cluster fields. When sources which cannot be cluster members, due to their redshifts or being a star, are excluded the radial distribution of the sources is very similar to that found for the excess sources in general, with the addition of two sources in the very centre of the clusters.

of cluster fields with bright cluster sources is between 2 and 6% if all cluster fields are considered.

If the positions of all of the bright sources are considered then there is not a strong radial trend, and the clustercentric distance in pixels is consistent with a random distribution. However, if the sources which cannot be cluster members are removed, and the distribution considered in physical distance at the cluster redshift, then the radial trend is extremely strong, as shown in Figure 3.6 – two sources lie in the central few kpc, one at 0.25 Mpc and five between 0.75 and 1.2 Mpc. The non-cluster sources are distributed randomly up to 3 Mpc, whereas there are no possible bright cluster sources at r$>$ 1.2 Mpc. It seems likely that most of these sources are associated with the cluster, and, like the cluster AGN population in general, the very bright cluster AGN are preferentially located at $\sim$ 1 Mpc from the cluster centre or in the central cluster galaxy. It could be that these sources are, like the general source population, lying in the cluster. However it is also possible that their luminosities are boosted due to lensing, as they all lie near moderate to massive clusters. The lensing correction is not well calculated for the very brightest sources, as the steep slope in the number counts means that the lensing effect is larger than normal. The radial distribution of these sources is very similar to that of the fainter sources, and the sources are not preferentially found in the fields of more luminous clusters, so it is most likely that these sources are in cluster galaxies.

3.4 Comparison to previous results

Sections 1.4.3 and 1.4.4 describe previous studies of point source distributions in Chandra observations of galaxy clusters. Most of these studies involved observations that are included in the sample in this thesis, and in this Section the previous results are compared to those produced by the automated pipeline.

In the majority of cases, the results from the pipeline agree with those of previous studies. The excesses found in A2104 (Martini et al. 2002), 3c295 Cappi et al. (2001), MS1054-03 (Johnson et al. 2003), three of the clusters investigated by Cappelluti et al. (2005) and the protocluster MRC 1138-262 (here called B1138-26, Pentericci et al., 2002) are all in agreement (within the errors) with the excesses found using the pipeline results. In addition, the lack of a point source excess in the field of MS0451-03 (Molnar et al. 2002), and three of the fields investigated by Cappelluti et al. are confirmed by this study. The radial distribution, number and flux of the sources are in agreement, but the values are often slightly different due to the more detailed analysis and lensing correction applied in the pipeline.

However, in a few cases the pipeline results do not agree with previous studies. In two fields, RDCS 1252-29 and 1E 0657-56, the pipeline results show an excess of sources where Cappelluti et al. (2005) found no excess. This is probably due to the fact that Cappelluti et al. only looked for excesses on a chip by chip basis, rather than a radial analysis. This, combined with the additional corrections in the pipeline, is probably also the reason that the pipeline finds no significant excess in MS1137+66, whereas Cappelluti et al. find a $> 2\sigma$ excess in two of the four chips. In addition, the 2σ excess of point sources found in RXJ003033.2+261819 (Cappi et al. 2001) is not seen in this study. This is because Cappi et al. only investigated the ACIS-S3 chip. The cluster is not situated in the centre of this chip, and if the full region within 1.5 Mpc of the cluster is investigated then the statistical excess disappears, as seen in the pipeline results.

The results from Ruderman and Ebeling (2005) used 51 clusters from the MACS (Massive Cluster Survey) with $0.3 < z < 0.6$. Of these, 21 have published redshifts and are included in this thesis. Ruderman and Ebeling find an excess within 0.5 Mpc, most of which is due to sources in the very central regions, and a secondary excess at 2-3 Mpc. In contrast, the pipeline results are similar to those for the whole field - the excess is found at 0.4-1 Mpc and there is no significant excess at higher radii or in the central regions. There are many possible reasons for this discrepancy. Ruderman and Ebeling only investigate the brightest ~ 10 sources per cluster field, whereas this study has ~ 40. In addition, the Ruderman and Ebeling results do not take into account the variation in sensitivity due to the cluster emission, and the Celldetect source detection algorithm they use is not accurate in regions of steeply varying background, and may over-detect sources in the outskirts of the cluster. A further concern with their analysis is the treatment of merged observations, as the flux limit for each cluster is scaled to the observation exposure time, and it is not clear how

this was accounted for in merged images.

Some of the clusters have also been studied using a combination of X-ray and optical data, as described in Section 1.4.3. In these studies, point sources were found to correspond to cluster galaxies, but no statistical excess of X-ray sources in the field was found (compared to blank fields). The more detailed pipeline results also fail to find a statistical excess in these fields, as either the number of sources was too low to be significant, or the non-cluster sources in the field were randomly much lower than the average (the spread of non-cluster sources from field-to-field is shown in Figure 3.1). Again, this highlights the advantages of combining X-ray and optical data, as many of the fields without statistical excesses will in fact contain cluster AGN.

3.5 AGN in low redshift galaxy clusters - suppression or triggering?

It is important to determine whether the number of AGN in galaxy clusters is higher (due to triggering) or lower (due to suppression) than expected given the increased number of potential AGN host galaxies compared to the field. To determine this the excess sources in uncontaminated clusters with $0.1 < z < 0.4$ were investigated. This redshift range contains 79 of the 113 uncontaminated cluster fields, and by selecting a moderately low redshift subsample we can compare the AGN to the field population without needing to consider the evolution of the galaxy clusters.

The excess of point sources in this sample, as a function of flux, is shown in Figure 3.7. The excess is calculated per square degree by comparing the observed (lensing corrected) Log N($> S$) - Log S distribution for the cluster fields to that for the blank fields. This is then scaled by the average area of a cluster field to give the number of excess sources per cluster field. A small excess per cluster field is seen at all fluxes.

To calculate whether the number of AGN observed is more or less than would be expected if AGN had the same prevalence (as a function of host optical magnitude) as in the field requires knowledge of the AGN luminosity function as a function of host galaxy magnitude, and the optical luminosity function of cluster galaxies. This is not available at the present time, but a first-order approximation can be made using published data. As powerful AGN are generally hosted by massive galaxies (Kauffmann et al. 2003), the X-ray luminosity function can be compared to the number density of galaxies $> L_*$ (the break in the optical luminosity function) to calculate the number of X-ray sources (above a given X-ray luminosity) per massive galaxy. Multiplying this by the number of galaxies $> L_*$ in a typical cluster gives the number of X-ray sources expected in the cluster, as a function of luminosity, assuming the same X-ray - optical correlation as in the field. The difference between the predicted and actual distributions will show whether AGN activity is suppressed

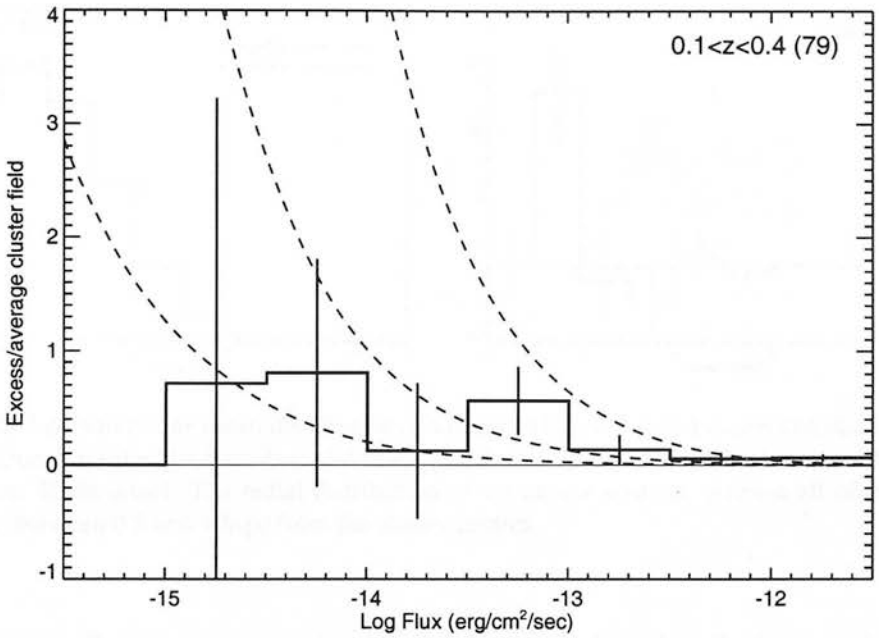

Figure 3.7: The excess sources per average cluster field area as a function of flux, for clusters with $0.1 < z < 0.4$. The excess per average field is given by the excess per square degree of sky area (which is a function of flux) scaled down by the total average area of the field of view ($0.046\,\mathrm{deg}^{-2}$). This therefore corrects for the variation in sensitivity across the field of view. The dashed lines mark the predicted flux distribution of hard X-ray sources in clusters with 1, 5 and 25 optical galaxies with $> L_*$, assuming that galaxies in the cluster have the same probability of being X-ray AGN as those in the field.

or enhanced in galaxy clusters.

In detail, this distribution was calculated for each cluster as follows:

$$N_{X,Cl}(\Delta \mathrm{logL}^{-1}) = \frac{N_{X,G}(\mathrm{Mpc}^{-3}\Delta \mathrm{logL}^{-1})}{N_{O,G}(>L_*)(\mathrm{Mpc}^{-3})} \times N_{O,Cl}(>L_*) \tag{3.1}$$

where N is the number of sources, with subscripts X and O referring to X-ray and optical sources, and Cl and G to cluster and global populations. The first two terms of the right hand side of the equation give the number of X-ray sources, as a function of luminosity, per L_* galaxy. As the sample is low redshift, to first order we can assume that the X-ray and optical luminosity functions do not evolve significantly. The number of X-ray sources per cluster is then given by the number of X-ray sources per L_* galaxy times the number of L_* galaxies in the cluster.

The X-ray luminosity function of Ueda et al. (2003) is used, as shown in Figure 1.2, and is evaluated at the mean redshift of the sample. This luminosity function only includes X-ray sources in the emitted 2-10 keV band, so is lower than the expected value from this survey, which consists of sources detected in the 0.5-8 keV band. However, as a first-order estimate

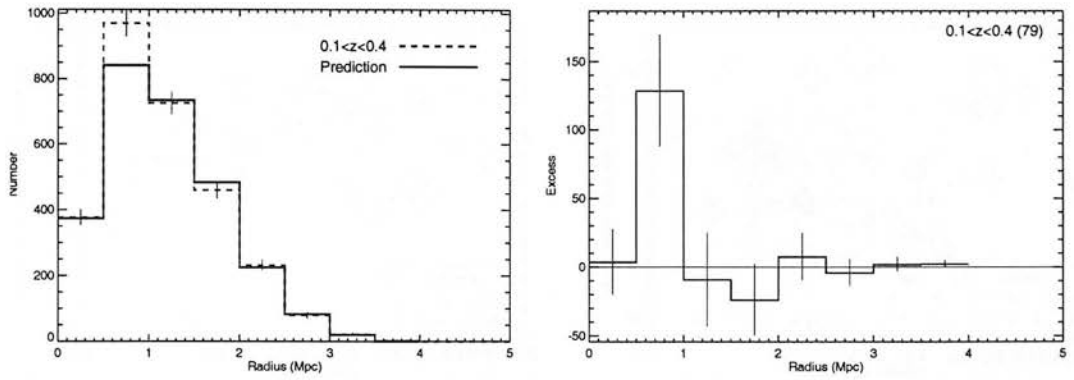

Figure 3.8: Left panel: The radial distribution of sources in $0.1 < z < 0.4$ clusters (dashed line) and the prediction from the blank fields (solid line). Combined 1σ error bars are shown on the cluster distribution. Right panel: The radial distribution of the excess sources. Almost all of the excess sources lie between 0.5 and 1 Mpc from the cluster centres.

it is sufficient. The average space density of galaxies brighter than L_* (averaged over the global population, including clusters and voids) is calculated from the mean luminosity function of Croton et al. (2005a) and using $L_* = M_{b_j} - 5\log h$ (from Norberg et al. 2002), and is found to be 0.0010 gal/Mpc^3 (assuming $h = 0.7$). The average number of cluster galaxies more luminous than L_* is harder to determine, but from Figure 1 of De Propris et al. (2004) the average number of cluster galaxies in the four 'representative' 2dFGRS clusters shown is ~ 6. Clearly, the number of massive cluster galaxies covers a large range (depending on the cluster luminosity), so this analysis is performed assuming 1, 5 and 25 massive galaxies per cluster, as shown in Figure 3.7.

To calculate the total expected flux distribution of sources in the $0.1 < z < 0.4$ clusters, the expected luminosity function for each cluster is converted to a flux distribution using the cluster redshift (assuming a $\Gamma = 1.7$ spectrum as usual) and the mean number of sources over all clusters is taken. Figure 3.7 shows the average number of sources per cluster field expected for if each cluster had 1, 5 or 25 galaxies $> L_*$.

At brighter fluxes, if the fraction of AGN is the same as in the field, then the observed distribution is consistent with ~ 5 massive galaxies per cluster, and this decreases to nearer ~ 1 per cluster at fainter fluxes. If, as the De Propris et al. (2004) results suggest, the average cluster contains ~ 6 massive galaxies, it is possible that lower flux AGN are suppressed but brighter AGN are unchanged. On the other hand, many of the X-ray clusters observed are massive, and might be expected to have an average of more than ~ 5 massive galaxies. It appears therefore that there is some degree of suppression overall in galaxy clusters. The suppression in the cluster centres might be even stronger if AGN are triggered on the cluster outskirts, giving a larger AGN population than predicted in the outer regions of the cluster.

To help understand whether clusters do trigger and suppress AGN activity, the radial

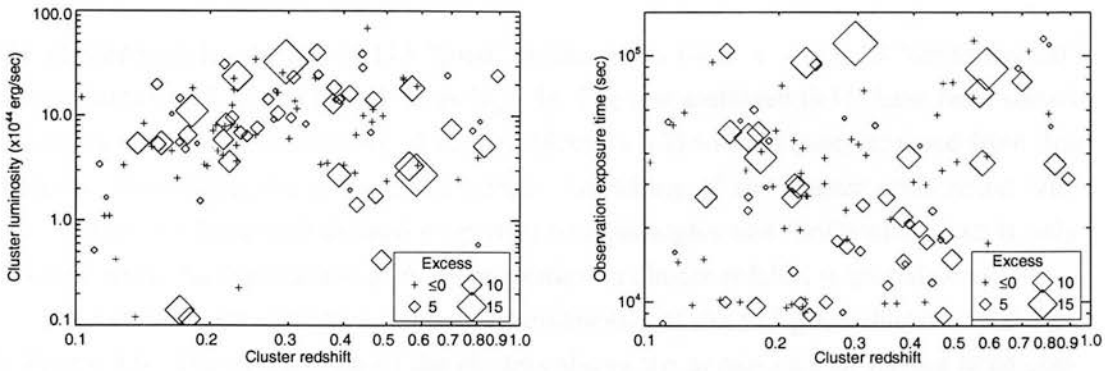

Figure 3.9: Left panel: The redshift and rest frame 0.5-8 keV luminosity of the good clusters. The symbol size is proportional to the excess found in each field. Right panel: The redshift and exposure time of the good cluster observations. Again the symbol size shows the excess in each observation.

distribution of the sources in these clusters are shown in Figure 3.8. Almost all of the excess sources lie between 0.5 and 1 Mpc from the cluster centres, and, as shown in the left panel, this is not due to a significant drop in the sky area covered beyond 1 Mpc. As explained in Section 3.2.3, this distribution is very different from the distribution of galaxies (as modelled by the King profile). It is clear that there is suppression in the central regions, with practically no excess of point sources despite the large number of potential host galaxies, and this may explain the low number of massive galaxies inferred from the number of AGN per cluster (Figure 3.7). It is harder to determine whether the peak at 0.5 - 1 Mpc is due to the excess galaxies at that radius or whether it is caused by triggering of AGN activity. The sharp peak would perhaps suggest the latter, as it is surprising that there are no excess sources beyond 1 Mpc, as even at this radii many cluster fields will still have a galaxy overdensity relative to the field.

From analysis of the number, luminosity and radial distribution of the excess sources in these cluster fields it is clear that AGN are suppressed in the central regions of galaxy clusters, and likely that they are triggered in the outskirts. Any such triggering serves to decrease the suppression signal over the whole cluster field. The conclusion that AGN are suppressed in the very central regions is clear from the radial distribution of the X-ray sources. However, without detailed knowledge of the number and radial distribution of the cluster galaxies no definitive conclusions can be drawn regarding whether AGN are triggered on the cluster outskirts.

3.6 Subdividing the cluster sample

The cluster sample consists of 113 'good' cluster fields (with $z < 1$), 19 'contaminated' cluster fields and 8 'protocluster' fields ($z > 1$). The contaminated fields have been shown to contain an unusual distribution of sources (Section 3.2) so have been removed from this analysis. In addition, the protocluster sample, consisting of any cluster observation with $z > 1$, does not have well defined properties (morphologies and luminosities), so is only included when the dependence of AGN properties on cluster redshift is investigated.

The redshifts and rest frame 0.5-8 keV luminosities of the 113 good clusters are shown in Figure 3.9. The distribution of the clusters shows the appearance of having been constructed from observations of two classes of clusters: the first resembles an X-ray flux-limited sample and consists of moderate luminosity, nearby clusters and high luminosity, distant clusters, most of which were presumably discovered in X-ray surveys. The second population consists of distant clusters with moderate X-ray luminosities, many of which were presumably discovered in optical data. The dominant population are moderate luminosity and moderate redshift ($0.15 < z < 0.3$) clusters, but there are enough clusters with other properties to split the sample by both luminosity and redshift.

The size of the symbols in Figure 3.9 indicates the number of excess sources over the whole field. As expected, there is a large degree of field-to-field variance, much of which is due to the small number of sources in each field. The scatter between clusters dominates over any strong correlation between the size of the excess and the galaxy properties, with the exception of an apparent lack of excess in the low redshift, low luminosity clusters. It is desired to cut the sample by redshift, morphology and cluster luminosity, such that the dependence of the AGN properties on each of these variables can be evaluated. In each case the subsamples must be selected so that as far as possible they only differ in one property - so that the sources in the different luminosity subsamples have similar redshift distributions, and vice versa. The definition of these subsamples is described in the next three sections.

It is also important that the exposure time is similar for the subsamples. The right panel of Figure 3.9 shows that deeper images tend to have a larger excess, which is to be expected as they can detect fainter AGN. There is only a moderate correlation between exposure time and redshift however, with $z > 0.5$ clusters having generally higher exposure times, but no particular correlation below this. This is important when considering the radial distributions, which include all detected sources. However, the difference will be clear in the Log N($> S$) - Log S distributions, as they will show how much of the excess in the higher redshift sample is due to an excess of sources near the flux limit. There is no clear correlation between cluster luminosity and exposure time, or between morphology and exposure time.

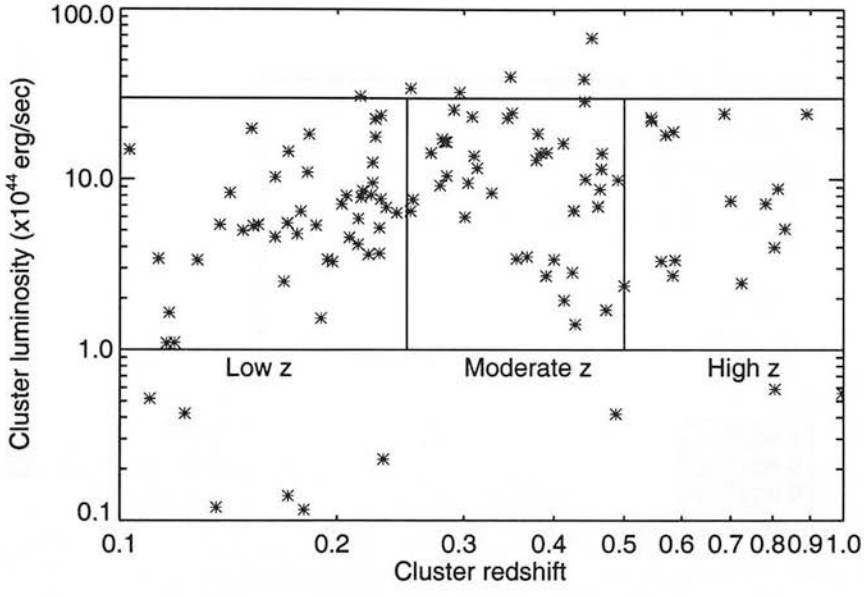

Figure 3.10: The definition of the subsamples split by redshift. Three sub-samples are marked, containing low, moderate and high redshift clusters, and excluding the most luminous and lowest luminosity clusters.

3.6.1 The redshift subsamples

The redshift subsamples were constructed as shown in Figure 3.10. These are defined such that the samples contain clusters with similar luminosities, but also retain as many clusters as possible. The redshift bins are $0.1 < z < 0.25$, $0.25 < z < 0.5$ and $0.5 < z < 1.0$, and only clusters with 10^{44}erg/sec $< L_X < 3 \times 10^{45}$erg/sec are retained, giving samples of size 44, 39 and 15 respectively. Kolmogorov-Smirnov (K-S) and Kuiper tests (see Appendix A.1.1) were used to compare the distribution of cluster luminosities in each sub-sample to that from all three sub-samples combined. The probabilities that they were drawn from the same distribution are 0.16, 0.16 and 0.70 respectively for the K-S test, and 0.49, 0.51 and 0.65 for the Kuiper test. Although there are small biases in the luminosity distributions in the lower redshift bins, these are only significant at around 1σ, so should not significantly affect the results.

In addition, the exposure times and morphologies of the clusters in the sub-samples were compared. The mean exposure time in the high redshift sample is around twice that in the lower redshift samples, but the cluster AGN are also further away - the samples are therefore probing different AGN populations, and care needs to be taken when investigating the radial distribution of these sources. The samples contain similar fractions of disturbed (type 2 and 3) clusters - 9 (20%) in the low redshift sample, 8 (21%) at moderate redshift and 2 (13%) at high redshift (when only Morphology type 3 clusters are considered the

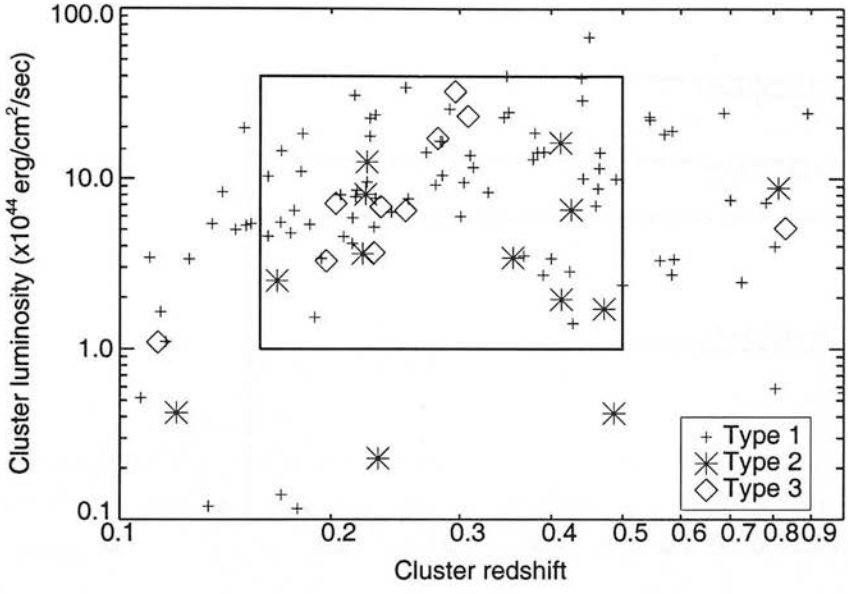

Figure 3.11: The sub-sample of clusters selected for investigating the dependence of AGN fraction on cluster morphology. Type 2 and 3 clusters are moderately and highly disturbed, and Type 1 appear to be relaxed, as described in Section 2.4.2.

fractions are also similar).

3.6.2 The morphology subsamples

The sample contains 90 good cluster observations, where the cluster appears to be relaxed, and 23 where it appears to be disturbed. The relaxed clusters are classed as Type 1 and the disturbed clusters are Type 2 and Type 3, depending on the degree of disturbance[4]. The disturbed clusters are not randomly distributed amongst the cluster population; this is partly due to the selection by the original observer, and partly due to the classification by eye, as in fainter or more distant clusters it is harder to see minor disturbances. To investigate whether cluster disturbance affects the prevalence of AGN a sub-sample of clusters was defined, such that the disturbed and relaxed clusters within the sub-sample have similar distributions in redshift, luminosity and exposure time. The boundaries of the subsample, shown in Figure 3.11, are $0.16 < z < 0.5$ and $10^{44} < L_X < 4 \times 10^{45}$erg/sec. Within these boundaries there are 58 relaxed and 17 disturbed clusters (the small sample size means that the errors become very large if the disturbed sample is split further into Type 2 and Type 3 clusters). The redshifts of the disturbed clusters are drawn from the whole sub-sample with a probability of 0.96, and the luminosities with a probability of 0.15 (from K-S tests) – there

[4]The morphologies were assigned by eye, see Section 2.4.2 for details

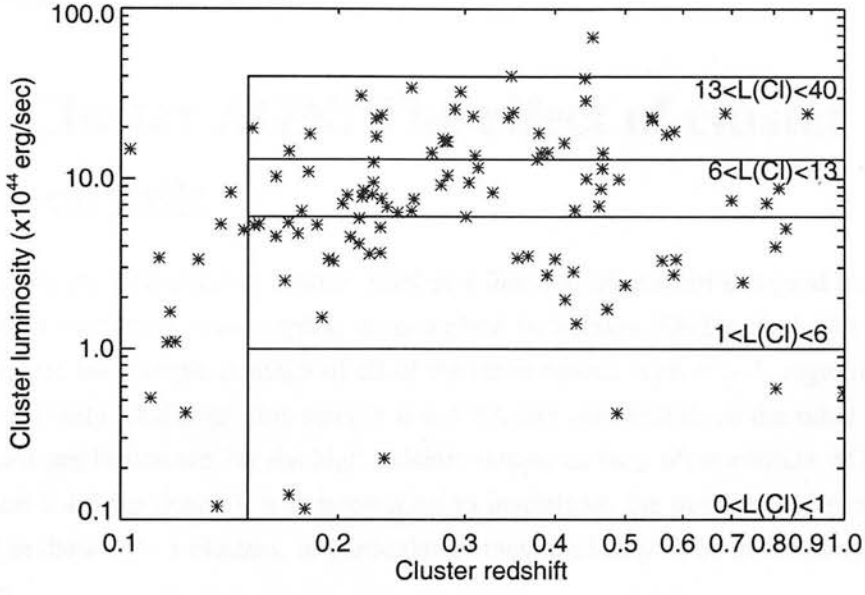

Figure 3.12: The sub-samples of galaxy clusters in the $L_{Cl} - z$ plane, selected to investigate the dependence of AGN activity on cluster rest-frame 0.5-8 keV luminosity.

are more low luminosity disturbed systems than high luminosity, but setting tighter limits in redshift and luminosity to reduce this effect would lead to smaller samples and significantly increased errors. As described in Section 3.9, more luminous clusters have more AGN, so this may have a slight effect on the interpretation of the results for these subsamples.

3.6.3 The cluster luminosity subsamples

The sample was cut by cluster rest-frame 0.5-8 keV luminosity to investigate the dependence of the AGN population on cluster mass. To simplify the analysis, the samples are selected to have the same redshift distribution so that any evolution in the $L_X - M$ relation can be ignored, and to be the same size so that the number per cluster can easily be compared. Three samples are selected, as shown in Figure 3.12, with $0.16 < z < 1$ and the highest and lowest luminosity clusters removed. The samples each contain 31 clusters, and are cut at $1 < L_{Cl}/10^{44}$erg/sec< 6, $6 < L_{Cl}/10^{44}$erg/sec< 13 and $13 < L_{Cl}/10^{44}$erg/sec< 40. A further sample of six clusters with the same redshift range and $L_{Cl} < 1 \times 10^{44}$erg/sec is also analysed, although the sample is too small to draw firm conclusions. The main three samples each have redshift distributions that are drawn from the combined distribution with probabilities 0.31, 0.94 and 0.46 respectively (from K-S tests). The samples contain 8, 7 and 4 disturbed clusters respectively, with each sample containing 3 highly disturbed (Type 3) systems. As disturbed clusters have more faint sources (see Section 3.8), this may make

a small difference to the results. There is no difference (at $> 99\%$) in the distribution of exposure times in the three samples.

3.7 Cluster AGN: The effect of cluster redshift

To investigate the properties of cluster AGN as a function of redshift the good cluster sample was split into three sub-samples, as described in Section 3.6.1 and shown in Figure 3.10. A fourth sub-sample consists of all of the observations with $z > 1$, regardless of the cluster luminosity. Although this sample is not directly comparable to the other three (the luminosities are inaccurate for the high redshift sample as they often contain AGN or jets, see Section 2.4.3 for details), it is interesting to investigate the number and properties of the AGN in these $z > 1$ clusters, in particular as they are likely to be in the early stages of formation.

The top panel of Figure 3.13 shows the flux distribution of sources in the four redshift-selected subsamples. The number of excess sources brighter than a flux S is found by comparing the number of sources detected in the cluster fields with a prediction from the weighted blank field source distribution as follows;

$$n(>S) = \sum_{S'=S}^{\infty} i_{c,S'} - \sum_{S'=S}^{\infty} i_{b,S'} \frac{A_{c,S'}}{A_{b,S'}} \tag{3.2}$$

where $n(>S)$ is the number of excess sources brighter than a given flux, $i_{c,S'}$ is the number of cluster sources at S' (including a lensing correction[5]), $i_{b,S'}$ the number of blank field sources at S' and $A_{c,S'}$ and $A_{b,S'}$ the sky areas sensitive to a source of flux S' in the cluster and blank field samples respectively, including a lensing correction in $A_{c,S'}$. The 1σ errors are calculated assuming the $\sqrt{n}$ approximation to Poissonian errors, and are given by

$$\sigma_n^2 = \sum_{S'=S}^{\infty} i_{c,S'} + \sum_{S'=S}^{\infty} i_{b,S'} \frac{A_{c,S'}^2}{A_{b,S'}^2} \tag{3.3}$$

This method takes no account of the reduction in sky area due to the different depths of the cluster observations, and it is important to note that at fluxes $\lesssim 10^{14.3}$erg/cm^2/sec the sky area begins to decrease, so for the faintest sources the number of additional excess sources is low due to the small sky area available.

The top panel of Figure 3.13 shows that while there are excess sources at all redshifts,

[5]Because the lensing correction for the Log N($>$ S) - Log S distributions is less accurate than that for the radial distributions (see Section 2.6.13) the total number of sources may vary between these two methods. These errors are always $< 1\sigma$ and do not affect the results significantly.

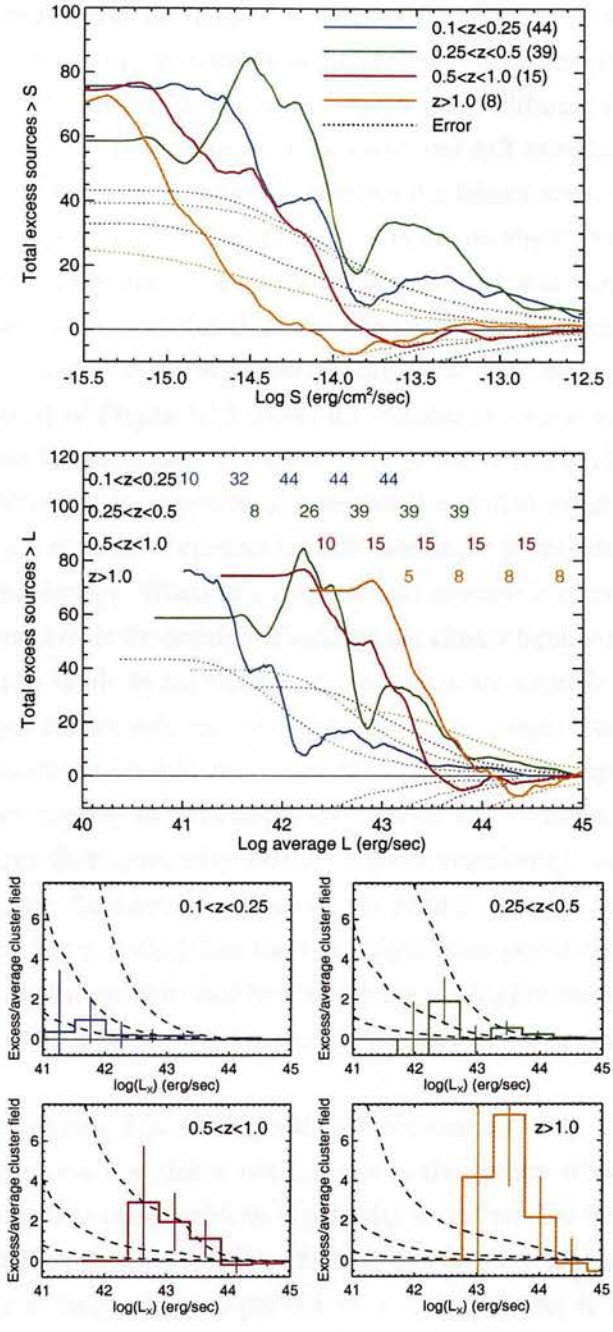

Figure 3.13: Top panel: The total number of excess sources brighter than a given flux in each sample, for four samples selected by cluster redshift. The number in brackets is the total number of fields in the sample. Middle panel: The same as the top panel, except that the fluxes are shifted to luminosities using the mean redshift for each sub-sample. The coloured numbers indicate the fall off in the number of fields sensitive to cluster AGN of lower luminosities. Lower panel (4 plots): The excess sources per average cluster field (for method, see Section 3.5) in each luminosity bin, where luminosity is calculated using the mean redshift for the subsample. The dashed lines mark the predicted distributions for hard X-ray sources in clusters with 1, 5 and 25 optical galaxies $> L_*$, if the probability of a galaxy hosting an AGN is the same in the clusters as in the field, as described in the text.

those found in the higher redshift samples are generally fainter than those at lower redshift. This serves to demonstrate that the observed excess is not simply a systematic error and we are indeed seeing an excess due to sources in the cluster. The excess in all four samples is significant to $\sim 2\sigma$ at the faintest fluxes, but is significantly different at brighter fluxes ($> 10^{-14}$erg/cm^2/sec), with far more sources in the lower redshift samples. To investigate the true nature of these sources, and in particular whether the fainter sources found in the more distant clusters are comparable to the bright sources in the nearby clusters, the luminosities of the excess sources were found. The fluxes were converted into luminosities[6] assuming that all sources lie at the mean redshift of the cluster bin. Although this method is not truly accurate, it is sufficient to get an understanding of the true luminosities of the cluster AGN. The middle panel of Figure 3.13 shows the number of excess sources as a function of luminosity, with the fall in number of cluster fields sensitive to each luminosity indicated by the coloured numbers. It is important to note that the plotted excess is the total for the subsample, and that the number of clusters in each subsample is very different (as indicated by the numbers in the figure). When this is taken into account it is evident that there is a sharp increase with redshift in the number of sources per cluster field. At $L_X > 10^{43}$erg/sec, where all of the cluster fields in the three $z < 1$ samples are capable of detecting excess sources, the excess per cluster field can be compared. This changes from 0.27 at the lowest redshift, to 0.85 at moderate redshift and 2.7 at high redshift. Although many fields in the $z > 1$ sample are not capable of detecting sources with $L_X = 10^{43}$erg/sec, the excess is at least 8.5 sources per field (assuming that all 8 fields contribute). At fainter fluxes it is not possible to calculate the number of sources per cluster $> S$, as not all clusters probe the fainter population, but it is clear that there is a significant population of fainter sources in the low redshift sample, and this may be mirrored in the higher redshift samples if more and deeper images were included. [The dip at low flux in the green line is $< 1\sigma$ and insignificant].

As mentioned in Section 3.3, the highest flux sources are only seen in the $z < 0.5$ clusters. Figure 3.13 shows that this is not just due to the greater distance to the $z > 0.5$ clusters. When the excess is converted into luminosity is is clear that the $L_X > 10^{44}$erg/sec sources are only found in the low redshift clusters, and in particular at $0.25 < z < 0.5$. However the number of bright sources per $0.1 < z < 0.5$ cluster is 11/83, and if this is applied to the higher redshift samples then the 2 and 1 bright AGN expected in the $0.5 < z < 1$ and $z < 1$ samples respectively are far less than the statistical errors at this luminosity. It is therefore not possible to say whether $z > 0.5$ clusters have different fractions of very luminous AGN than the $z < 0.5$ sample. Also, as mentioned in Section 3.3, the source of this excess could possibly be lensing of background sources, although the radial distribution is strikingly similar to that of other sources.

[6]Fluxes are converted into luminosities in the rest frame 0.5-8 keV band assuming an unabsorbed spectrum with photon index $\Gamma = 1.7$

3.7.1 Comparison with the evolution of field AGN

To investigate the number density of sources as a function of flux it is necessary to take account of the sky area available to detect sources of each flux. At fainter fluxes the number of fields, and area within each field, in which sources could be detected decreases rapidly, so by scaling by the area available, the number of sources per average cluster can be found. The lower panel of Figure 3.13 shows the average number of cluster AGN per cluster field as a function of luminosity, for the four samples. There are clearly far more AGN in higher redshift clusters. However, without further analysis it is not possible to say whether this is due to the general evolution of AGN, since in the field the number density of luminous AGN increases towards $z = 1$, or to some process specific to the cluster environment.

To determine whether the evolution is as would be expected from the field, the expected cluster X-ray luminosity function at the mean redshift was calculated by expanding the method in Section 3.5 to account for the redshift evolution of this sample. This method assumes that the probability of a galaxy having an X-ray AGN is the same in the cluster as in the field, in order to calculate the expected luminosity function of cluster AGN assuming no suppression or triggering.

To account for the redshift evolution, the X-ray global luminosity function is taken from Ueda et al. (2003), and because the number density of X-ray sources does not evolve significantly at the typical luminosities investigated, is evaluated at the mean redshift of each bin. In addition, for the optical luminosity function pure luminosity evolution is assumed (which is sufficient to first order for massive galaxies, see for example Drory et al. 2003). Using this method, the number of galaxies brighter than L_* does not evolve, so the evolution of optical galaxies can be removed from this calculation. This means that the number of moderate luminosity AGN per L_* galaxy does not evolve significantly over the redshift range considered. The expected X-ray luminosity functions for each cluster distribution are shown by the dashed lines, assuming that the number of optical galaxies $> L_*$ in the cluster are 1, 5 and 25 respectively.

The dashed lines shown on the lower panel of Figure 3.13 show that the evolution of cluster AGN is not consistent with that of field AGN (even taking into account the large errors introduced and the fact that the dashed lines are for hard sources only). The number of sources in the lowest redshift bin are consistent with ~ 1 luminous galaxy in each cluster, whereas at $0.5 < z < 1$ it is ~ 25 luminous galaxies per cluster. The number of L_* galaxies in a typical low redshift cluster is $\gg 1$, so the AGN activity is being suppressed at low redshift compared to the field, as discussed in Section 3.5. At $z > 1.0$ the predicted number density of sources with $L_X \sim 10^{43.5}$erg/sec should only be twice that at low redshift, whereas it is far higher. Either the higher redshift sample contain significantly more massive galaxies (unlikely given the similar luminosity distribution of the clusters in the redshift bins, shown in Figure 3.9), or the cluster AGN population has evolved far faster than that in the field. A full investigation of this effect requires more detailed knowledge of the cluster

properties, but this simple method indicates that the cluster environment has a significant effect on the evolution of AGN.

The larger number of AGN in the higher redshift bins could be due to higher activity, but it also may be due to massive galaxies associated with the cluster but at large radius, which are outside the field of view in the low redshift images. To investigate this further it is necessary to look at the radial distribution of the AGN. The cumulative excess within a given radius is shown in the top panel of Figure 3.14. The two lowest redshift samples have almost all their AGN within 0.5 - 1 Mpc, with no evidence for evolution in the radial distribution between $0.1 < z < 0.5$. In contrast, the AGN in the $z > 0.5$ clusters are distributed over a far larger area, up to 4 Mpc from the cluster centre, but the lack of AGN in the central ~ 0.5 Mpc is found in all clusters with $z < 1$.

The lower panels of Figure 3.14 show the predicted and actual number of sources as a function of radius (left column) and the difference between these (right column). It is clear that the lack of cluster AGN at > 1 Mpc in the two low redshift samples is not due to a lack of sky area at these radii. Many sources are found up to ~ 2 Mpc in the lowest redshift sample, and up to ~ 3 Mpc in the $0.25 < z < 0.5$ sample, but no excess is seen at these radii.

It is not possible to directly compare the number of AGN at a given radius between the different redshift samples, as they are probing to different luminosity limits. In most of the $0.5 < z < 1$ fields only $L_X > 10^{42.5}$erg/sec AGN are detectable, but the radial distribution of sources is very different from that at lower redshift, with a considerable number of excess AGN detected at > 1 Mpc from the cluster centre, compared to no excess for the $z < 0.5$ samples. Comparing this figure with the luminosities of the cluster AGN in Figure 3.13 shows that the evolution in the radial distribution cannot be explained by the difference in AGN luminosity probed by each sample: a scenario where the 0.5 - 1 Mpc peak is caused by AGN with $L_X < 10^{42}$erg/sec, and more luminous AGN are found at a range of radii, is clearly discounted by comparing the radial distributions in the $0.25 < z < 0.5$ and $0.5 < z < 1$ samples. These contain a similar total number of moderate luminosity AGN, but the excess at ~ 3 Mpc in the higher redshift sample is clearly missing from the lower redshift clusters.

The change in the radial distribution of the cluster AGN is even more evident in the $z > 1$ sample, where the AGN are distributed up to 4 Mpc from the cluster centre. Half of the excess sources are found within the central 2 Mpc, and so, comparing to the lower plot in Figure 3.13, even if all high-radius AGN are excluded the number of AGN in the high redshift sample is still significantly higher than at low redshift. This argument applies to all the subsamples, showing that the increased number of AGN in high redshift clusters is only partly due to the larger physical radius covered by the field of view.

The high number and extended radial distribution of the excess sources in the $z > 1$ sample is not dominated by one or two fields, but rather appear to be general characteristics

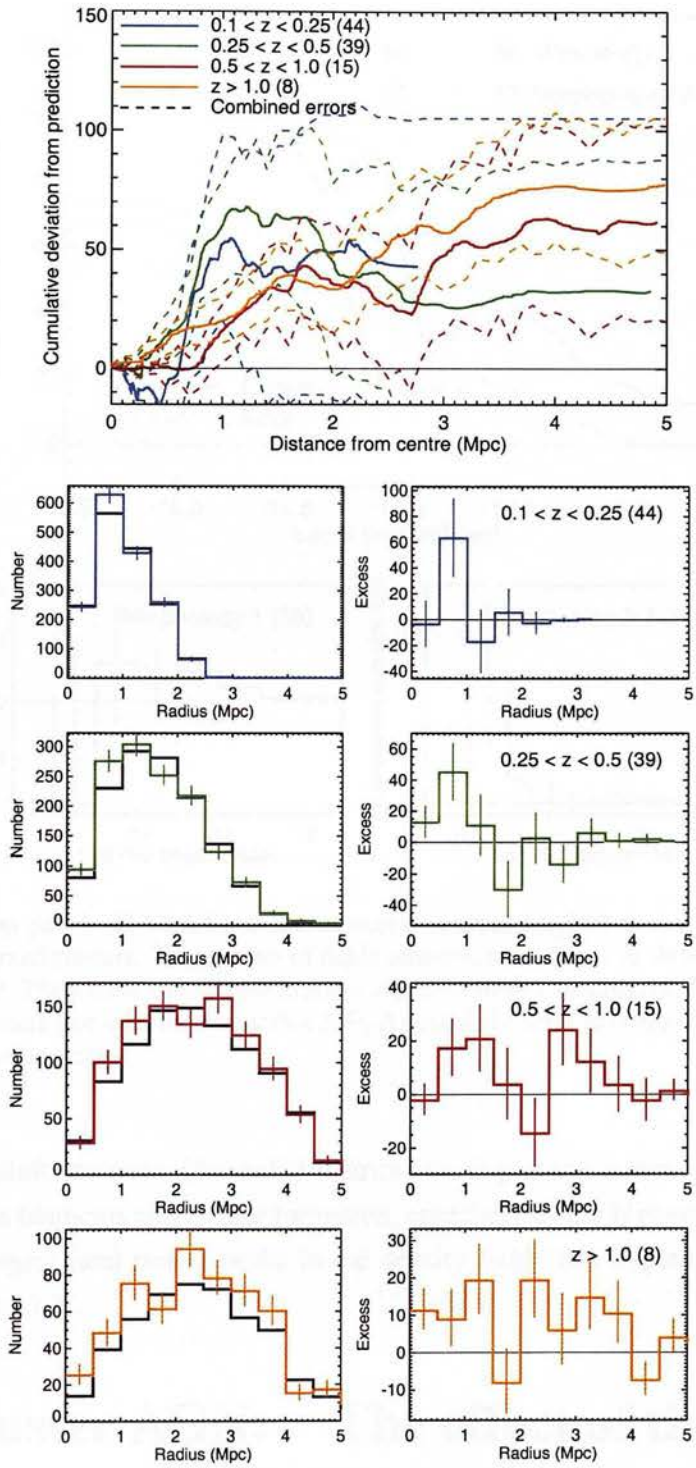

Figure 3.14: The radial distribution of cluster AGN as a function of cluster redshift. Top panel: The cumulative excess (within R) for the four redshift subsamples. 1σ errors are shown by the dashed lines, and the sample size is shown in brackets in the legend. Lower left panels: The number of predicted (black) and actual (colour) sources found at each radius, for each subsample. Lower right panels: The excess number of sources as a function of radius for each subsample. Vertical bars show the 1σ errors.

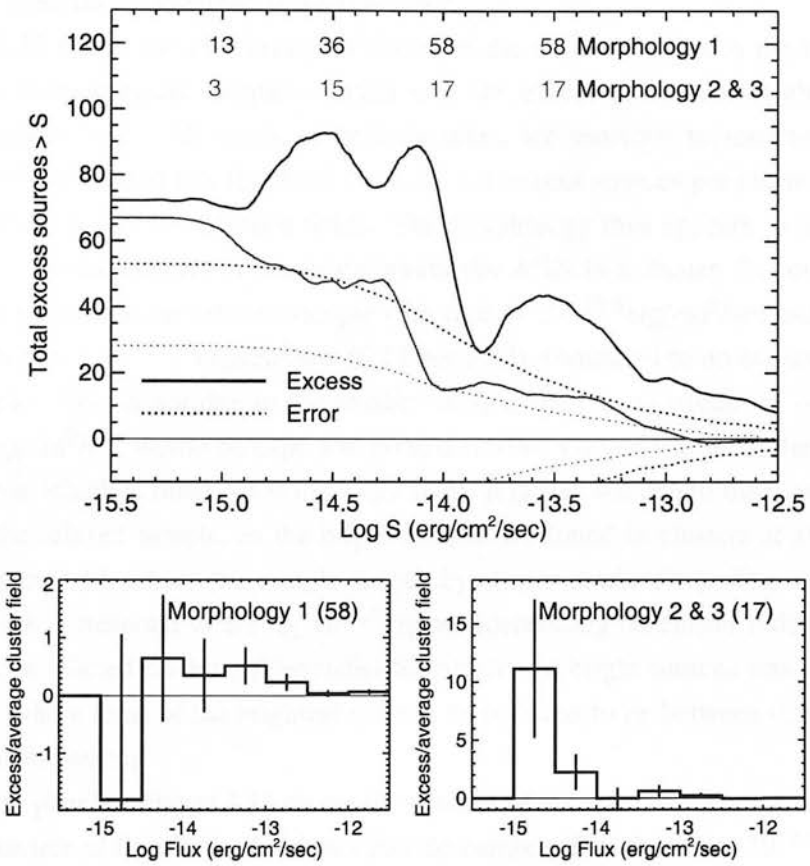

Figure 3.15: Top panel: The total number of excess sources brighter than a given flux, in the disturbed and relaxed clusters. The number of fields sensitive to each flux is shown at the top of the plot. Lower panel: The excess sources per average cluster field as a function of flux, for the relaxed and disturbed clusters (for method see Section 3.5). As usual, 1σ error bars are shown, based on the model and Poissonian errors.

of the high redshift clusters. The radial distribution is perhaps indicative of large-scale structure such as filaments and cluster formation, especially as the highest redshift clusters represent the largest (and rarest) peaks in the density field: this hypothesis is discussed further in Section 3.10.

3.8 Cluster AGN: The effect of the cluster morphology

The morphological classifications of the clusters can be used to determine whether disturbed systems (those undergoing cluster-cluster or cluster-group mergers, and those with highly asymmetric morphologies) have a higher fraction of AGN than clusters that appear to be

relaxed. Sub-samples of relaxed (Morphology Type 1) and disturbed (Morphology Type 2 and 3) were selected as described in Section 3.6.2.

Figure 3.15 shows the distribution of fluxes of the excess sources in the subsamples. Both of the morphological samples contain a $\sim 2\sigma$ excess of sources at all fluxes below 10^{-13}erg/cm^2/sec. All fields, in both samples, are sensitive to sources of flux $\sim 10^{-14}$erg/cm^2/sec, and at this flux limit there are 1.1 excess sources per cluster in relaxed fields, compared to 0.9 in disturbed fields. The morphology thus appears to have no significant effect on the number of moderate luminosity AGN in a cluster. In contrast, there are 8 excess sources in the relaxed sample with flux $\gtrsim 10^{-12.5}$erg/cm^2/sec and 14 excess sources with flux $\gtrsim 10^{-12.8}$erg/cm^2/sec (0.24 per field), compared to no excess in the disturbed sample. This is not due to the smaller sample size, as an excess of ~ 4 sources $\gtrsim 10^{-12.8}$erg/cm^2/sec would be expected if the disturbed sample had the same fraction of bright sources, which is ruled out at the $\sim 2\sigma$ level. It is also not due to the more luminous clusters in the relaxed sample, as the bright sources are found in clusters at all luminosities (see Figure 3.17, where the sample is split by cluster luminosity). The excess bright sources, which correspond to $L_X \gtrsim 10^{43.5}$erg/sec (depending on cluster redshift), appear to only exist in relaxed clusters. [The radial distribution of bright sources was discussed in Section 3.3, where most of the brightest sources were found to lie between 0.5 and 1 Mpc from the cluster centre].

The lower panel of Figure 3.15 shows the number of excess sources per average cluster fields as a function of flux. This plot shows that the number of moderate ($\gtrsim 10^{13.5}$erg/cm^2/sec) sources is similar in both samples, but there is a significant difference in the number of faint sources, even taking into account the large error bars (due to the small areas which are sensitive to faint sources). At $10^{-14.5}$ to 10^{-15}erg/cm^2/sec, there is no excess of sources in the 13 relaxed clusters which cover this depth. In contrast, there is a large and significant excess of similar sources in disturbed clusters. Although 10^{-15}erg/cm^2/sec sources can only be detected in 3 fields, the flux limit in 11 disturbed fields is fainter than $10^{-14.5}$erg/cm^2/sec. This excess is therefore not just due to sources in 3 fields, but the small number of fields covered means that field-to-field variance cannot be ruled out as the cause of this effect. If the excess is due to an increase in faint sources, the low flux means that part of this excess could be caused by luminous starforming galaxies in the lowest redshift clusters, but it is very unlikely to be completely due to star-formation due to the large redshift range of the sample.

The radial distributions of the excess sources in disturbed and relaxed clusters are shown in Figure 3.16. The relaxed clusters show the previously discussed distribution, with almost all of the sources lying between 0.5 and 1 Mpc from the cluster centre. In contrast, the sources in disturbed clusters have a far more extended distribution, with a significant increase between ~ 0.7 and 2 Mpc from the cluster core. It is worth noting that although these clusters are disturbed, in all but three of these systems the central point (from which

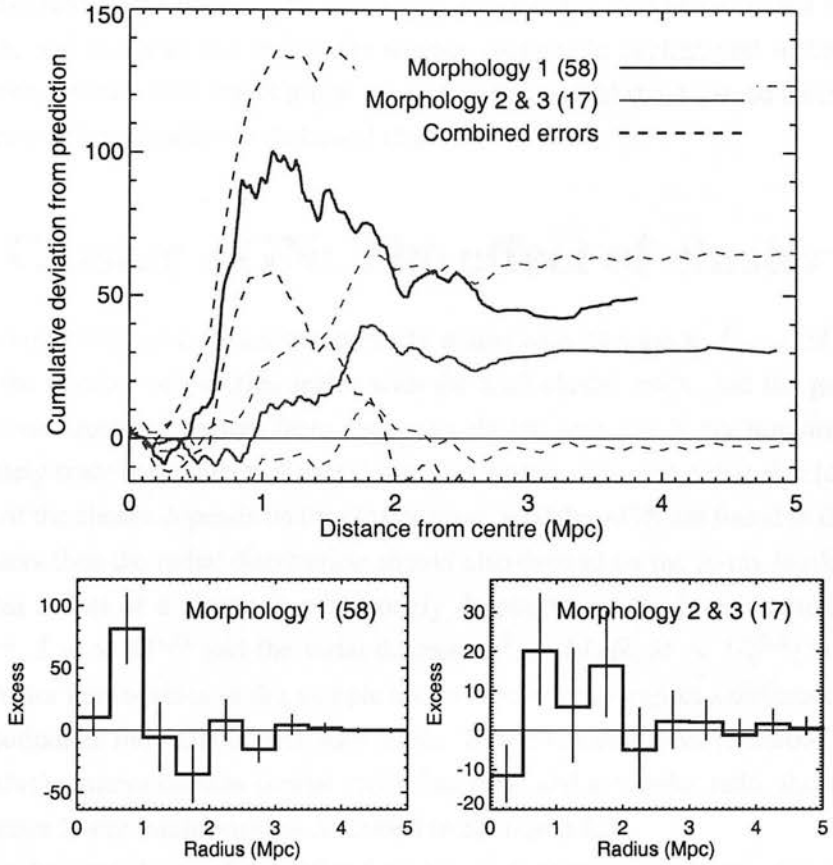

Figure 3.16: The radial distribution of sources in relaxed and disturbed clusters. The top panel shows the cumulative excess within a given radius, and the bottom plots show the excess within each 0.5 Mpc bin. The deficit of sources in the central 0.5 Mpc in the Morphology type 2 and 3 sample is purely due to the type 3 clusters, and is discussed further in the main text.

the radial excess is measured) of the dominant cluster is well defined, and that removing these three clusters makes no difference to the results. The distance from the central point to the disturbance (the secondary cluster, filament or spur near or on the edge of the cluster) varies significantly between clusters, but is typically in the range 0.5 - 1.5 Mpc. The extended distribution of sources can feasibly be explained by a distribution akin to that for a relaxed cluster, with the addition of further sources in the region of the disturbed area or secondary cluster. If this is the case then the direction of the extended region should correspond to that of the excess, but such analysis is beyond the scope of this study.

The radial histogram for the disturbed clusters also shows a deficit of sources in the central 0.5 Mpc at the few source level. It is likely that this is due to errors in the modelling of the expected source distribution, especially as all of the deficit occurs in the Morphology 3 cluster fields, which are the most disturbed. The gravitational lensing correction assumes

that the cluster is an isothermal sphere, which is clearly not the case in the most disturbed systems. In addition, the observation sensitivity is calculated using a smoothed background distribution, and this may not reflect the sharper changes in background in the disturbed clusters. These errors only affect a few sources in the central 0.5 Mpc, so cannot account for the excess at larger radius in disturbed clusters.

3.9 Cluster AGN: The effect of cluster mass

The X-ray luminosity of a cluster theoretically scales with its mass as $L_X \propto M^{4/3}$ (Kaiser 1986). If the number of galaxies scales with the total cluster mass, and the galaxy luminosity function does not change from cluster to cluster, then the X-ray luminosity should approximately trace the number of galaxies in the cluster. Also, the radial size (characteristic radius) of the cluster depends on the cluster mass, so if the AGN are found in the outskirts of the clusters then the radial distribution should also depend on the X-ray luminosity. The gravitational radius of a cluster is not strongly dependent on the X-ray luminosity [from $L_X \propto \sigma^{4.4}$, $L_X \propto M^{4/3}$ and the virial theorem $\sigma^2 \propto M/R$, $R \propto L_X^{\sim 0.3}$] but the large range in cluster luminosities in this sample means that we may expect a difference in the radial distributions of the AGN in each subsample. To test whether more luminous (and hence more massive) clusters contain similar AGN fractions, and at similar radii, the sample was split by cluster X-ray luminosity, as described in Section 3.6.3.

The number and fluxes of the AGN found in each cluster sample are shown in Figure 3.17. It is clear that the more luminous clusters contain more AGN per cluster at most fluxes. The very brightest sources ($> 10^{-13}$erg/cm^2/sec) have no dependence on cluster luminosity, but at moderate and low luminosities the more massive clusters have significantly more AGN. Excluding the small sample with $L_{Cl} < 10^{44}$erg/sec, the excess is $\sim 1.2\sigma$ for the lowest luminosity sample, $\sim 1.5\sigma$ for the moderate luminosity and $\sim 3\sigma$ for the highest luminosity sample, although the differences between the low and moderate samples are small. If the very low luminosity clusters are scaled by the number of fields then they have a similar number of AGN as the low and moderate luminosity samples. There is also some evidence that the $1 < L_{Cl} < 6 \times 10^{44}$erg/sec sample contains less moderate flux ($> 10^{-14}$erg/cm^2/sec) sources than the more massive clusters (with $L_{Cl} > 6 \times 10^{44}$ erg/sec), but otherwise the distributions of AGN luminosities are remarkably similar.

If the fraction of galaxies hosting AGN is independent of cluster luminosity, and the number of possible AGN host galaxies scales with cluster mass, then the number of AGN should be proportional to $L_{Cl}^{3/4}$. The mean luminosities of the clusters in each subsample are 21.5, 8.70 and 3.65×10^{44}erg/sec, ordered from most to least luminous, so the ratio of the excess in each sample should be 1:0.52:0.27 respectively. The actual ratio, taken from the total excess in Figure 3.17, are 1:0.55:0.49, with more sources per cluster mass in the low luminosity clusters relative to the higher luminosity samples. It is possible to obtain

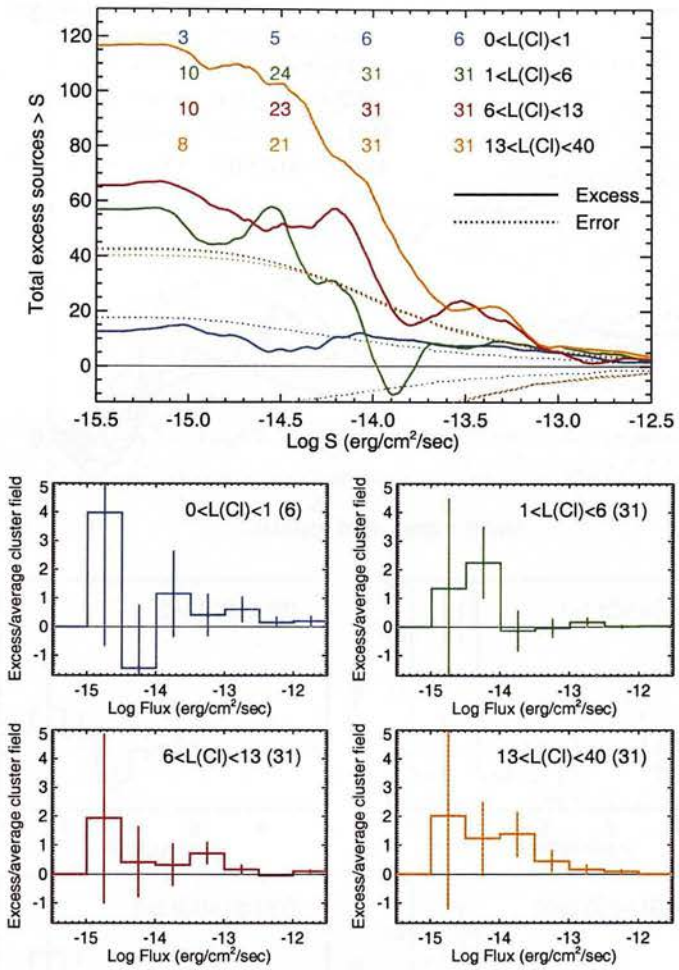

Figure 3.17: The number and flux of cluster AGN as a function of cluster luminosity (the cluster luminosity range is the rest-frame 0.5-8 keV value, given in units of 10^{44}erg/sec). Top panel: The number of excess sources brighter than a given flux in each sample. The coloured numbers show the number of fields in each sample which could detect sources at that flux, to illustrate the fall off in area at lower flux. Lower panel: The number of excess sources per average cluster field in each flux bin for each sample (for method see Section 3.5). The sample luminosity cut and size is shown in the top corner.

the theoretical values within the 1σ errors on the total excess, so it is possible that the AGN fraction is independent of cluster luminosity. However, the difference in the ratios does indicate that suppression may be greater in the most luminous clusters, possibly due to AGN lying only on the cluster outskirts.

Figure 3.18 shows the radial distribution of AGN as a function of cluster luminosity. The total excess sources are slightly different from those found from Figure 3.17 due to the different lensing correction (see Section 2.6.13), but are within the errors, and the ratio is the same. Interestingly there is not a large difference between the radial distributions of the

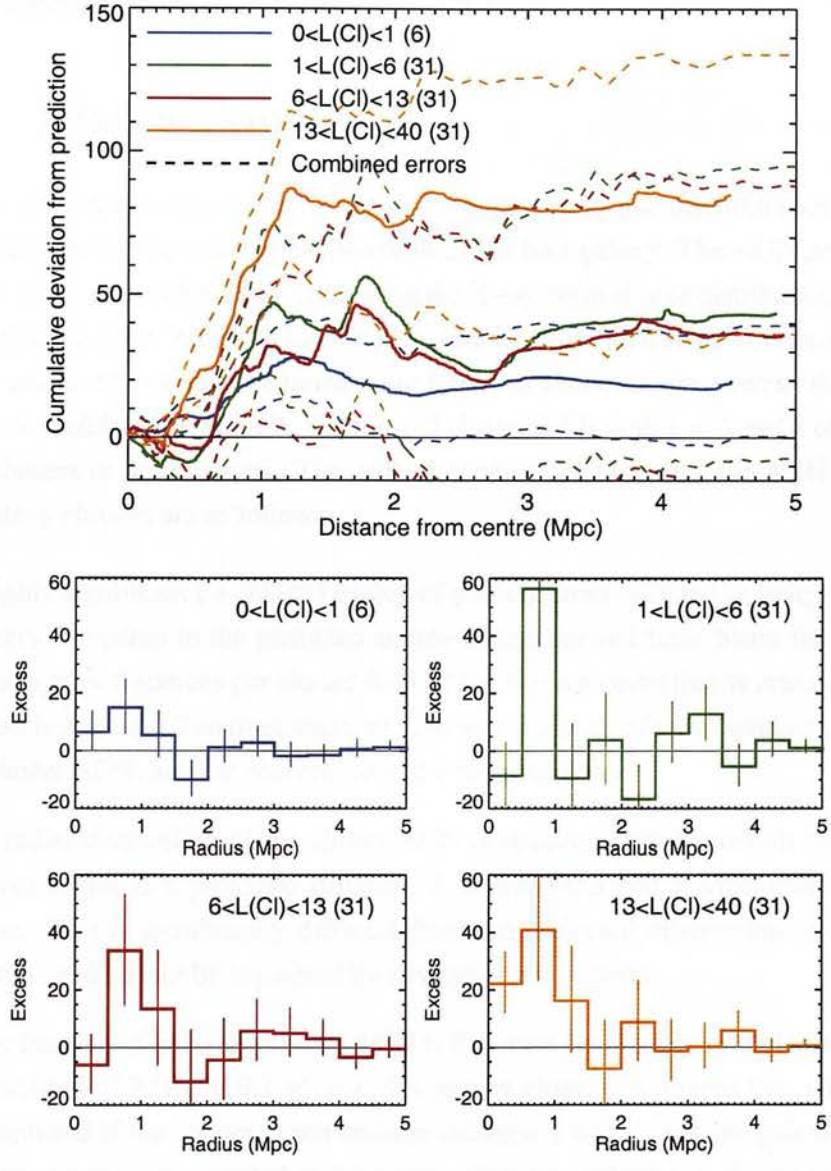

Figure 3.18: The radial distribution of AGN as a function of cluster luminosity. Top panel: The cumulative excess of sources within a given radius. Bottom panel: The excess of sources in each 0.5 Mpc bin. The cluster luminosities and number of clusters are marked on each plot.

different cluster samples. The distribution of AGN is slightly more spread out for massive clusters, with the excess starting ~ 0.2 Mpc further in, and extending very slightly further out, but within the errors it appears that the AGN are still found at $0.5 - 1$ Mpc, regardless of the cluster mass. If the radius at which the AGN are found traces the gravitational radii of the clusters, it should increase by a factor of ~ 1.3 between the lowest and middle subsamples, and ~ 1.7 between the lowest and highest subsamples. A factor 1.3 change between the low and moderate luminosity subsamples is not detectable within these errors,

but it is clear that the distribution for the highest luminosity clusters is not simply that for the lowest luminosity sample scaled by a factor of 1.7.

3.10 Discussion

The results presented in this chapter present compelling evidence that AGN activity is significantly affected by the external environment of the host galaxy. The AGN population in 140 cluster fields was evaluated by comparing the X-ray point source distribution to the predicted distribution from 'blank' fields. The 19 cluster fields which contained an unidentified secondary source of extended emission were found to contain more sources than average and were removed from the sample, leaving 113 cluster fields with $z < 1$ and 8 observations of $z > 1$ clusters or protoclusters. The general conclusions regarding the AGN population in these galaxy clusters are as follows:

- A highly significant ($> 99.9\%$) excess of point sources is found in images of galaxy clusters compared to the predicted source counts derived from blank fields, with an average of ~ 3 sources per cluster field (if the lensing correction is removed then the excess is around 0.7 sources smaller). The vast majority of these sources are likely to be cluster AGN, and the sources exist at a range of fluxes.

- The radial distribution of the cluster AGN is striking, with almost all of the excess sources found at a projected distance of between 0.5 and 1 Mpc from the cluster centre. This is significantly different from the projected distribution of galaxies in clusters, and cannot be explained by any systematic effects.

- If the fraction of galaxies hosting AGN is the same for cluster and field galaxies then the number of AGN in $0.1 < z < 0.4$ galaxy clusters is around that which would be expected if the clusters each contain between 1 and 5 massive galaxies ($> L_*$). As the clusters are expected to have more than five galaxies $> L_*$ on average, this indicates that AGN activity is suppressed relative to the field. The radial distribution of the sources clearly shows that there is suppression in the central areas. Without detailed analysis of the cluster galaxy distribution it is not possible to say for sure if the AGN found at 0.5-1 Mpc represent triggering on the cluster outskirts, but it seems likely given the sharpness of the radial distribution of the AGN.

- Up to 6% of all clusters contain AGN with flux $> 10^{-12.5}$erg/cm^2/sec. Like the general cluster AGN, it appears that these sources generally lie between ~ 0.5 and ~ 1 Mpc from the cluster centre, and if they are cluster AGN then they have luminosities of $\gtrsim 10^{44}$erg/sec, corresponding to very luminous AGN.

In addition to the general results, the cluster sample was split into subsamples to investigate the dependence of the cluster AGN population on cluster redshift, morphology and luminosity. The results from these subsamples are as follows:

- Higher redshift clusters contain significantly more AGN than those at low redshift, and this is only partly due to the higher physical radius in the observed field of view. This evolution is far larger than for field AGN (for example the number density of field sources with $L_X \sim 10^{42}$erg/sec does not evolve significantly to $z \sim 1$), and it appears that, in contrast to the $z < 0.4$ sample, the number of AGN found in $z > 1$ clusters is greater than expected from the field distribution at a similar redshift.

- The radial distribution of sources in $z > 0.5$ clusters is also very different from that at lower redshift. Rather than a sharp peak in the AGN distribution at 0.5 - 1 Mpc, followed by almost no additional AGN, at higher redshift the AGN are found over a far larger radius, and at $z > 1$ in particular the AGN are distributed up to 4 Mpc from the cluster centre. However, in all clusters at $z < 1$ it appears that almost no AGN are found in the central 0.5 Mpc.

- Disturbed and relaxed clusters have similar numbers of moderate luminosity AGN. However, all of the very luminous AGN ($L_X \gtrsim 10^{43.5}$erg/sec) are found in relaxed clusters, and there is an extra population of low luminosity sources in the disturbed clusters.

- In relaxed clusters the majority of AGN are found between 0.5 and 1 Mpc, whereas in the disturbed systems a similar distribution is seen up to 1 Mpc but the excess low luminosity X-ray sources extend to $\sim$ 2 Mpc. This is comparable to the distances to the disturbances, which are typically 0.5 - 1.5 Mpc from the cluster centre. The extra population of fainter sources are therefore likely to be directly associated with the disturbances, and may be AGN or luminous star-forming galaxies.

- More luminous clusters contain more AGN of all luminosities. The total number of extra AGN is, however, slightly lower than expected from the higher number of galaxies, assuming a constant AGN fraction. However within the errors it is possible that the fraction of galaxies hosting AGN does not depend on the cluster luminosity.

- The radial distribution of AGN is largely independent of cluster luminosity. In the high, medium and low cluster luminosity subsamples the majority of sources lie between 0.5 and 1 Mpc from the cluster centre, and the larger average radius of cluster galaxies in more massive clusters is not mirrored in the AGN population.

In moderate redshift clusters it is clear that almost no AGN are found in the centres of galaxy clusters. However, AGN are found on the outskirts of clusters and in regions of

morphological disturbance, such as sub-clusters. These AGN could either be an extension of the field population which are not yet suppressed by the cluster environment, or they could be triggered by their interaction with the cluster. The lack of a trend between the AGN radial distribution and cluster luminosity, and sudden lack of AGN at > 1.2 Mpc suggest that the AGN are triggered by some environmental process: if the AGN at moderate radii are purely an extension of the field population then the more massive clusters should have more AGN at higher radius, and a more gradual decline in AGN at higher radius should be seen.

It is also interesting that higher luminosity (more massive) clusters appear to have a slightly different AGN luminosity distribution from less massive clusters, with more moderate flux excess sources. In addition the luminosity distribution of the AGN is a strong function of cluster morphology; the extra AGN found in disturbed clusters, compared to the relaxed clusters, are generally faint, and some of the sources could be massive star-forming galaxies. These results also lend credence to the suggestion that AGN are triggered on interaction with the cluster environment, as different environments have different characteristic AGN luminosities. These results can be understood if AGN are triggered when galaxies, groups or other clusters join a galaxy cluster, with more AGN in more massive clusters and major cluster mergers triggering lower luminosity AGN. If, on the other hand, the results are purely due to AGN suppression then this would require a mechanism that suppresses the fainter AGN before affecting brighter AGN in massive clusters, but which suppresses brighter AGN before faint AGN in disturbed clusters. It is likely that AGN activity is enhanced relative to the field on cluster outskirts, and the lack of a strong trend with cluster luminosity suggests that this effect is dominated by local galaxy or gas density rather than global cluster properties.

The distribution of the very brightest sources, with $L_X > 10^{44}$erg/sec, suggests that local effects also have a large role in AGN activity. These AGN are found in clusters of all luminosities, but only at the radii of general AGN activity and surprisingly only in relaxed clusters. The first two correlations can be understood if it is the increase in local galaxy density that triggers the most luminous AGN. The third correlation is more complex; it can be postulated that a more disturbed cluster environment disrupts whatever mechanism drives fuel to the centre of the galaxy. However, a more detailed study of the host galaxies of these AGN is required to understand the fuelling of these luminous AGN.

The suppression of AGN in the centres of galaxy clusters is analogous to the suppression of star-formation in similar regions, as detailed in Section 1.3.2. However, there is no evidence that the fraction of blue star-forming galaxies increases in the cluster outskirts. It could be that the AGN are related to the population of dusty red star-forming galaxies found by Wolf et al. (2005), which exist preferentially in areas of moderate galaxy density. It is possible that either the star-formation triggers the AGN (for example if AGN are found in post star-burst galaxies, as found by Kauffmann et al. 2003), which would explain the

lack of AGN in cluster cores, or that the same processes which trigger star-formation also trigger AGN activity. To distinguish between these alternatives it is necessary to have some knowledge of the host galaxy properties of the cluster AGN.

The massive suppression of AGN within 0.5 Mpc from the cluster centre may be due to the direct effect of the environment, such as ram pressure stripping or evaporation of the gas in the galaxy due to the intra-cluster medium. It could also be due to a lack of fuel in the very central regions of these galaxies, caused by an increase in AGN or star-forming activity in the past. A third possibility, that the AGN activity in massive galaxies is highly obscured in the X-ray, is mentioned here for completeness, but is highly unlikely due to the high column densities required in every AGN host in order to obscure all AGN activity. Although the results from the low redshift cluster sample lead to the conclusion that AGN activity is suppressed in the centres, the results at higher redshift show that clusters contained far more powerful AGN in the past (even compared to the increase expected in the field galaxies), and at $z > 1$ there is some evidence that AGN exist near the centres of massive clusters. In addition, the apparent triggering of AGN on the outskirts of clusters, which was far larger in the past, could plausibly consume much of the fuel in the very central regions of the galaxy. This would make it harder to trigger an AGN in future as a larger disruption would be required to remove the angular momentum and drive fuel to the central regions of the galaxy. AGN outflows or central star-formation at $z > 1$ could also possibly reduce the available fuel in the central regions of these galaxies. It is not possible to distinguish between direct environmental suppression and lack of fuel in the host galaxies using the present data, but it is likely that a combination of the two produce the observed deficit of AGN in cluster cores.

The evolution of the AGN luminosity function in the fields of galaxy clusters is far faster than for similar luminosity AGN in the field. At $z > 1$ it appears that AGN are more prevalent around galaxy clusters than in the field, and they are found at large distances from the cluster centres, possibly tracing galaxy filaments. In comparison, at low redshift AGN are suppressed in clusters relative to the field population. This can be understood if a denser environment initially enhances AGN activity, due to the increased gravitational disturbance. The black holes in these galaxies will then consume most of the available fuel in the central regions, making it less likely that AGN activity is triggered in the future. The general result that activity was higher at $z \sim 1$ in the field is therefore even more true for galaxy clusters, and may explain some of the environmental dependence seen at lower redshifts.

In conclusion, the study of AGN in galaxy clusters can clearly help in the quest to understand AGN in general. This study has revealed that AGN are suppressed in cluster cores, and possibly triggered in the outskirts of clusters. It has also shown that the evolution of the AGN population in clusters is different to that in the field. However, more detailed, multi-wavelength analysis is required in order to understand the physical processes behind the observed results.

CHAPTER 4

AGN in Abell 901/2

4.1 AGN in superclusters

It is increasingly evident that many of the changes in galaxy properties between cluster cores and the field are triggered in intermediate density environments, and that a distinction between field and cluster populations is overly simplistic (see Chapter 1). To understand the links between AGN activity and their extended environment it is necessary to determine the effect of local ($\sim$ 100 kpc) and large scale ($\sim$ 1 Mpc) environment, from the field through groups and cluster outskirts to the cluster cores. Both the galaxy density and the type of galaxy in the local environment may be linked to the presence of AGN activity.

Superclusters are ideal testbeds for studying the effect of environment on AGN as they consist of a large number of galaxies in a range of environments, but at the same epoch. The correlations between environment and AGN properties can therefore be studied in one field, without complications due to galaxy or AGN evolution. For example, the AGN population in galaxy groups and cluster outskirts can be compared to distinguish between local and large scale environments. In addition galaxy superclusters contain both disturbed and relaxed regions, which may affect AGN in different ways.

As described in Section 1, deep X-ray data is the best way to detect a large sample of AGN, but optical data is required to identify the redshift of a source. By combining X-ray images and optical positions and redshifts, supercluster AGN can be identified. Comparing the local and extended environments of AGN hosts with other similar supercluster galaxies will determine the effect of a range of environments on AGN activity.

This chapter describes a study of the supercluster A901/2. Section 4.2 describes the large amount of data available for this supercluster, and the X-ray data which has recently been obtained. In Section 4.3 the X-ray data reduction is described, including a table of point sources. The distribution of the extended emission from the intra-cluster gas is detailed in Section 4.4. Section 4.5 explains how the optical and X-ray data were combined to determine a sample of AGN in the supercluster. In Section 4.6 the properties and local environments of the AGN host galaxies are compared to other similar galaxies to determine whether and how the environment affects the AGN activity. Finally, Section 4.7 contains a summary of the results, and a discussion of the possible physical explanations for the links between AGN activity and extended environment found in this supercluster.

4.2 The supercluster A901/2

4.2.1 Optical data

The supercluster consisting of Abell 901 and Abell 902 (A901/2) was first identified by Abell (1958) as two 'poor' clusters, Abell class 1 and 0 respectively. The low redshift (~ 0.17) and wealth of optical data available for this field make it ideal for a study of the effect of environment on AGN. It is one of the fields covered by the COMBO-17 survey (Classifying Objects by Medium-Band Observations in 17 Filters, Wolf et al. 2003), and in addition 2dF spectra are available for 282 supercluster galaxies, from observations with the two degree field (2dF) spectrograph on the Anglo-Australian telescope.

The COMBO-17 survey used the Wide Field Imager (WFI) at the MPG/ESO 2.2 m telescope on La Silla, Chile, to obtain images of a $0.56' \times 0.55'$ field with a pixel size of $0.238'' \times 0.238''$. Images were taken in 5 broad and 12 narrow band filters and matched to a set of template spectra, to determine photometric redshifts ($z_{\rm phot}$). The template spectra include QSOs, different types of galaxies and various types of star. In the deepest (R band) image almost 64000 objects were detected, and reliable photometric redshifts were found for the $\sim$18000 objects with $m_{\rm R} < 24$. The errors in the photometric redshifts for the supercluster galaxies are around $\sigma_z/(1+z) < 0.01$ at $m_{\rm R} < 20$ (which is comparable to the velocity dispersion of the supercluster) and $\sigma_z/(1+z) < 0.02$ for $m_{\rm R} < 23$ (Wolf et al. 2005). The small photometric redshift errors make it possible to select a supercluster sample with minimal contamination from interlopers and only a few percent loss of true supercluster galaxies.

A cut of $0.15 < z_{phot} < 0.18$ gives 1240 supercluster galaxies with $m_{\rm R} < 24$. This large sample makes it possible to determine very accurately the distribution and properties of the galaxies in A901/2 (Gray et al. 2002). In addition, by combining the three-dimensional positions with source shapes from the deepest (R band) image, Taylor et al. (2004) have determined the 3D mass distribution in the supercluster from weak lensing

analysis.

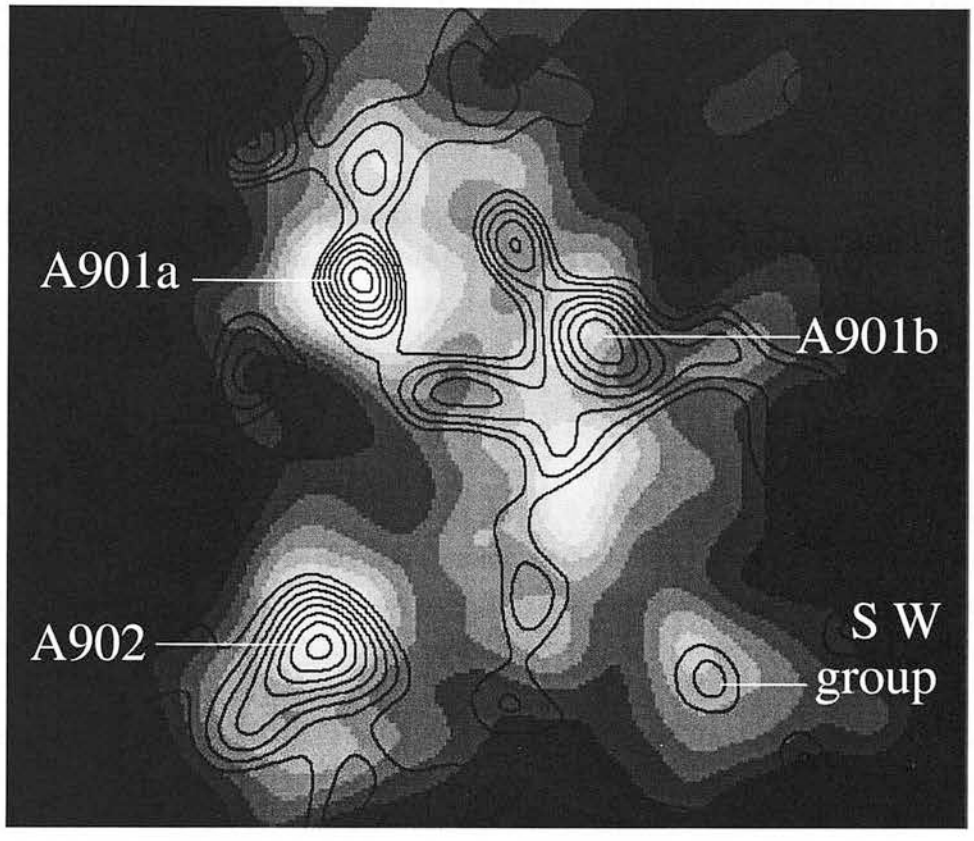

Figure 4.1: Galaxy number density in A901 (greyscale) and supercluster dark matter density (contours). Galaxies are selected in the range $0.15 < z_{\rm phot} < 0.18$. The optically identified clusters and group are marked.

The optically identified structure of A901/2 is shown in Figure 4.1. A901 consists of two dark matter halos of comparable size, A901a and A901b, each with a massive (BCG) galaxy in the centre. A901a contains far more galaxies and is far more concentrated than A901b. A tail of smaller, bluer galaxies extends south of A901b towards A902, which is a more optically diffuse cluster. There is also a group of galaxies in the south-west corner, and optical data and the 3D lensing have identified a cluster at redshift ~ 0.5 almost directly behind A902. It is clear that the supercluster contains a wide range of environments with differing ratios of dark to optically visible matter. The effect of these environments on the galaxy star-formation rate has been investigated by Gray et al. (2004), who found that the proportion of galaxies that are star-forming is a strong function of local dark-matter density.

The 2dF spectra cover 282 of the brightest galaxies in the supercluster, in the range 3900-6000A (Gray et al. in prep.). The COMBO-17 template spectra and 2dF spectra are not sufficient to compile a sample of AGN as many AGN are optically obscured. In comparison, X-ray samples are far more complete (see for example Martini et al. 2004 and Szokoly et al. 2004) but suffer from confusion with heavily star-forming galaxies. Combining an X-ray source list with the 2dF spectra and COMBO-17 data can help identify supercluster

X-ray sources and distinguish between X-ray emission from star-formation and that from AGN. Comparing the positions of AGN hosts with the other identified supercluster galaxies will determine whether AGN activity is enhanced or suppressed in a range of environments.

4.2.2 Infra-red data

This field is currently being surveyed using MIPS (Multi-band Imaging Photometer for Spitzer) on Spitzer. An early release catalogue of the 24 micron sources in this field (1/7 of the final data, from Bell and Papovich, private communication) will help in the identification of some AGN, as shown in Section 4.5.2.

4.2.3 X-ray data

The A901/2 supercluster region was observed for $\sim$ 0.4 ksec as part of the ROSAT All Sky Survey (Ebeling et al. 1996b) and in addition with the ROSAT High Resolution Imager for $\sim$ 12ksec. Two bright sources were found near the optical centre of A901, which coincide with A901a and A901b in Figure 4.1, as well as 5 fainter sources. Schindler (2000) concluded from the high resolution image that the only visible extended emission in the supercluster was from A901b. The bright emission from A901a, which coincides with an optical overdensity, was found to be a point source. No X-ray emission was found from A902.

A deep (90ksec) XMM-Newton image of the supercluster was obtained in 2003. Although the resolution of XMM is not significantly better than that of the ROSAT HRI, the superior collecting area, combined with the longer exposure, mean that this image is significantly deeper than the ROSAT high resolution image. AGN and star-forming galaxies in the supercluster can be detected by matching the X-ray and optical positions. Also the X-ray extended emission from the hot intra-cluster medium adds an additional dimension to the complex structure of the supercluster – combining the lensing analysis, galaxy distribution and X-ray emission it is possible to trace the dark matter, hot gas and galaxies.

4.3 X-ray data reduction

4.3.1 The XMM data

A 90ksec XMM image of A901/2 was taken on 6th/7th May 2003 using the three EPIC cameras (MOS1, MOS2 and PN) and a thin filter (see Appendix A.4 for details of XMM-Newton). The level 1 data are taken from the supplied pipeline products. These were reduced with SAS v5.4 and the calibration files available in May 2003. Due to a fault with

newer versions of SAS a more recent calibration could not be applied to the PN data, so for consistency the supplied level 1 data was used for all cameras.

Much of the signal was dominated by soft proton flares (Appendix A.2.1). To detect the times of high cosmic background the event lists were filtered for high energy single pixel events (PATTERN = 0 and energy $>$ 10 keV). Good time intervals were defined for each detector, with count rates in the filtered dataset of $<$ 0.2 counts/sec for MOS1 and MOS2 detectors and $<$ 0.67 counts/sec for PN. This reduced the exposure time for each detector to $\sim$ 67ksec for MOS and $\sim$ 61ksec for PN, and removed all regions of significant flaring.

The event lists were filtered for the good time interval, bad pixels, the standard good patterns of 0-12 and XMMEA_EM or XMMEA_EP (see Appendix A.4). Four energy bands were used: 0.5-2keV (soft band), 2-4.5keV (medium band), 4.5-7.5keV (hard band) and 0.5-7.5keV(full band). To account for variations in effective area the event lists were weighted with the vignetting factor described in Section A.4.1.

4.3.2 Source detection

For source detection, 600 x 600 pixel unvignetted full-band images and the corresponding exposure maps (Appendix A.3.5) were made for each detector, with a pixel size of 4.1″, and wavelet analysis was used to detect sources. The vignetting correction was not applied as wavelet detection methods only look at the local background, and require unscaled count levels to determine the source significance. To remove areas of low exposure and problems on the chip boundaries, a mask file was created from the exposure map. This mask removed areas with less than 25% of the maximum exposure or an exposure map gradient of over 0.4 for MOS or 0.03 for PN. Three areas of streaking (that were not due to out of time events[1]) were removed by hand in the PN mask.

Using the wavelet detection method described in Appendix A.4.3, 102 sources were detected in the MOS1 image, 96 in MOS2 and 128 in PN. The total number of unique sources detected, without applying any cut on source significance, was 150 (of which 64 were detected in all three images, 33 in two and 53 in one). The vast majority of those missed in one or two images were outside the field of view of those detectors, or only detected in the more sensitive PN image. The masked images and initial detections are shown in Figure 4.2 (a)-(c).

To construct a point source catalogue for each image, all detections of extended supercluster emission are removed. As the size and shape of the PSF is not well defined in XMM (see Section A.4.2) two methods were used to determine which were point sources:

- The FWHM was found using the 'Pick Object' tool in GAIA. As the sources become increasingly elliptical towards the edge of the image, it was required that the semi-

[1]Out of time events are received during the readout of the CCD, so have incorrect coordinates. Correcting for out of time events did not remove the streaks, so the areas were removed from the analysis.

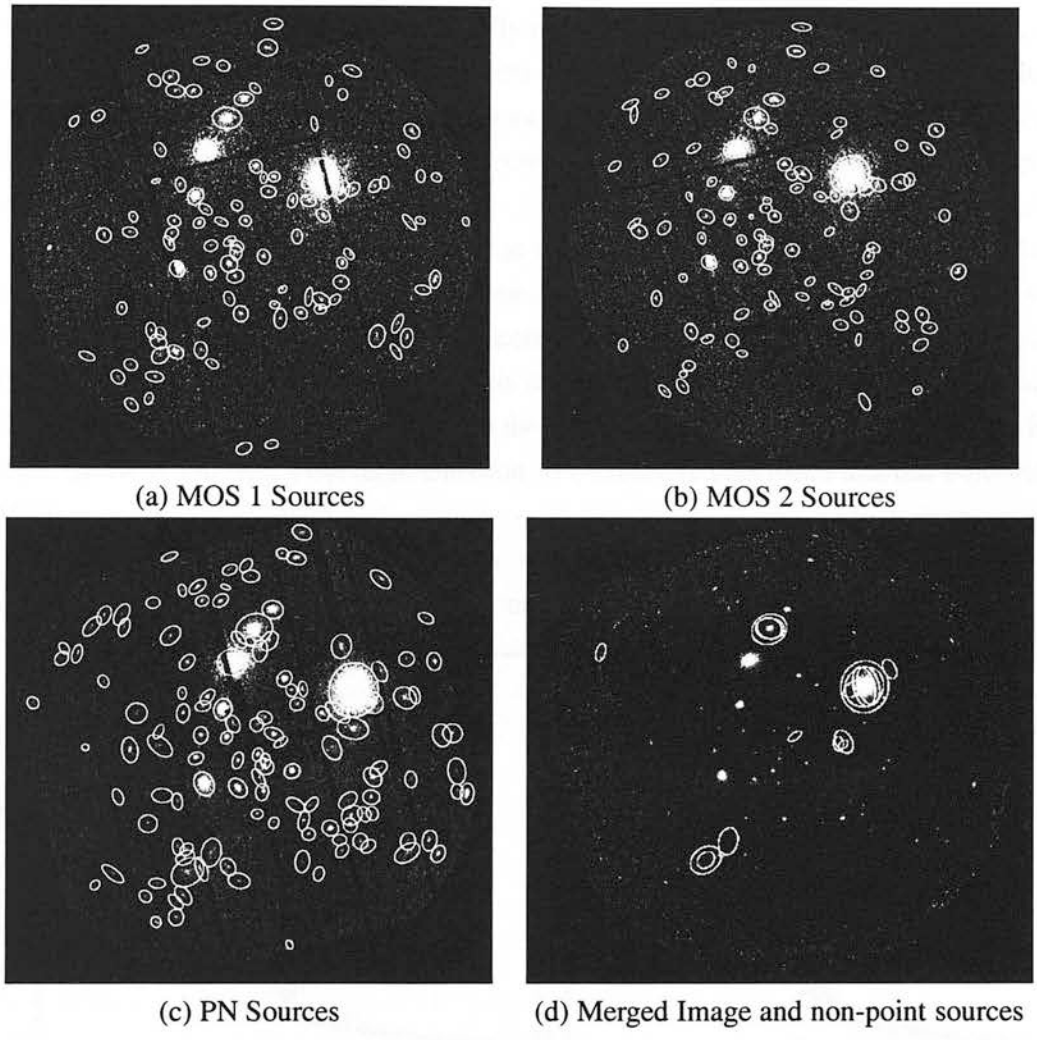

(a) MOS 1 Sources (b) MOS 2 Sources

(c) PN Sources (d) Merged Image and non-point sources

Figure 4.2: (a)-(c) - Images and 3-sigma source detections from each of the three EPIC cameras. (d) - Detections of non-point sources from images (a)-(c) are plotted over the merged, vignetted image. The sources were detected in the three images separately, and the three smallest sources are likely to be artefacts. The higher level of noise towards the outskirts of (d) is due to the vignetting weighting applied when combining the images, in order to give equal count levels across the field of view.

minor axis had a FWHM of < 3 pixels. This includes all bright on-axis point sources, which have a FWHM of 2.2 pixels, and allows some margin of error for the fainter sources. This method was only useful for moderate to bright sources.

- The catalogue was compared to the results for this field from the XCS survey (Davidson et al. 2005). This survey uses a sophisticated wavelet reconstruction method to find extended emission in XMM images. Due to the errors in the raw dataset (cf. Section 4.3.1), this method could only use the MOS data in the NE quarter of the image, whereas all data are used in the rest of the image. Detections of extended emission are therefore less accurate in the NE quarter.

The results of these methods are broadly in agreement, within the errors described, and identified eight areas of possible supercluster emission, shown in Figure 4.2 (d). Of these, the smallest three are likely to be artefacts as they all occur near the chip boundary of one image only. All of these sources were removed from the catalogue as none are true point sources.

A further consideration was the brightest source in the field, which has the FWHM of a point source. As this source is so bright (similar in flux to the cluster A901b) and lies very close to the centre of A901a, it could be concentrated cluster emission or a cooling flow. These scenarios were ruled out by analysis of the spectrum, which is a power law rather than thermal (Figure 4.3), and the fact that the X-ray emission is centred on a galaxy which is not the BCG and which has radio emission. It is therefore concluded that this object is an AGN.

After removing the extended emission, two catalogues of sources were made, one for use in point source subtraction and one for use in calculating the point source properties.

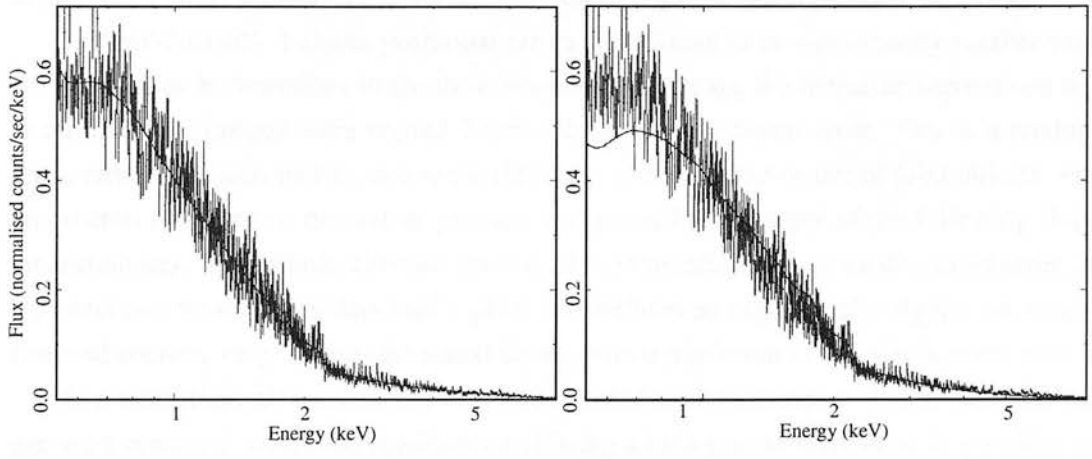

Figure 4.3: The spectrum of the bright source near the centre of A901a, fitted with an absorbed power law (left) and absorbed thermal model (right, from Raymond and Smith 1977). In both cases the plotted model has been combined with the response of the detector, and has a redshift of 0.166 and a fixed galactic neutral hydrogen density of 4.6×10^{-20} atoms/cm^2. The reduced χ^2 of the fits are 1.01 and 2.23 respectively. A cooling flow model is also a bad fit to the observed data.

Catalogue 1: Point sources for subtraction

For point source subtraction a conservative catalogue was made, the aim being to identify the vast majority of the counts from point sources, including sources that are detected at low significance, so that all remaining counts are background or extended emission. For this reason, when combining the three source lists, all point source detections were used and the largest area source ellipse was used for multiply detected sources, with the following exceptions:

1. If the detection in one image is near a chip boundary then detections in another image were used if possible.

2. If one image resolves two sources, and another merges them into one, the two sources were assumed to be real detections.

It is not necessary to use a 3σ source ellipse to mark all the source counts for the faintest sources, and similarly for the brightest sources a larger ellipse is required to include the counts in the wings of the PSF. Therefore the WAVDETECT 3σ source ellipse was scaled as a function of flux. An empirical function, $n\sigma = log(\text{counts}) - 0.5$, was used with a minimum source size of 1σ, which visually left no residuals after the source areas were removed from the image (see Section 4.3.3).

Catalogue 2: Point source properties

For the point source properties catalogue the important factor was to determine the reality, position and positional error of the sources. For sources that were detected in more than one image the position was defined as the midpoint of the two closest positions for that source. (In the most common case of three sources this removed errors due to one detection being near a chip boundary.) For singly detected sources the given position was used.

The WAVDETECT 1-sigma positional errors were found to be significantly smaller than the differences in detections in the three images - on average the detection separations between different images were around 7 times the stated positional error. This is a random error, rather than astrometric, due to the difficulty of finding the centre of faint objects. For this reason the error on the source position was given by the larger of the following three measurements: the distance between the two closest detections, 7 times the stated error, or 0.5 pixel (an error of less than half a pixel was defined as unphysical). Again, for singly detected sources, only 7 times the stated errors, with a minimum of 0.5 pixels, were used.

As a final stage, all sources that were not detected at significance > 3 in at least one image were removed, where the significance of being a background fluctuation is $\frac{C}{1+\sqrt{0.75+B}}$, for source counts C and background counts B (see Section 2.5.3). This cut removed 11 sources. At least one of these sources is real (at ~09:56:24 -10:01:52, probably matching a z=2.2 quasar in the COMBO-17 catalogue), as it has low significance but was detected in two images; however the removed source was very faint in both images and had very large positional errors, so for consistency and accuracy it was not included in the catalogue.

The final list of 139 point sources, including positional errors, is given in Table 4.1.

4.3.3 Detecting the extended emission

The extended emission from groups of galaxies is very faint, so careful subtraction of point sources and background events was required to distinguish real extended emission. In particular, it is important to take into account the level of the cosmic background and the spatial variation in the non-cosmic background (see Section A.2.1).

The residual background counts after filtering are still significant enough to cause con-

Table 4.1

Xray_ID	RA (J2000)	Dec (J2000)	Error (deg)	Cts/sec†($\times 10^{-3}$)	Detectors*
1	09:56:36.7	-10:02:39.2	0.00185	0.80	MOS1
2	09:56:35.9	-09:53:29.2	0.00095	2.11	MOS1,PN
3	09:56:35.8	-10:10:12.8	0.00132	5.17	MOS1,MOS2,PN
4	09:56:31.2	-09:53:28.9	0.00102	2.44	MOS1,MOS2,PN
5	09:56:28.0	-10:01:08.3	0.00155	0.75	MOS1,PN
6	09:56:20.4	-10:05:22.8	0.00113	1.21	MOS1,MOS2,PN
7	09:56:15.3	-09:53:19.0	0.00135	0.58	MOS1
8	09:56:12.1	-09:50:44.0	0.00112	5.06	MOS1,MOS2,PN
9	09:56:08.7	-10:08:03.0	0.00093	0.82	MOS1,PN
10	09:57:01.8	-09:55:27.5	0.00241	0.85	MOS1
11	09:56:41.0	-09:52:49.8	0.00123	0.77	MOS1,MOS2,PN
12	09:56:10.7	-10:16:05.7	0.00129	1.04	MOS1
13	09:56:01.4	-10:00:25.6	0.00070	1.90	MOS1,MOS2,PN
14	09:55:32.3	-09:58:54.8	0.00164	0.56	MOS1
15	09:55:31.6	-10:06:11.4	0.00289	0.73	MOS1
16	09:55:28.2	-09:58:59.6	0.00217	0.63	MOS1
17	09:56:54.1	-10:02:49.0	0.00085	2.85	MOS1,MOS2,PN
18	09:56:47.3	-10:13:29.3	0.00087	1.53	MOS1,MOS2,PN
19	09:56:20.0	-10:01:17.0	0.00116	0.40	MOS2
20	09:56:17.7	-10:01:49.3	0.00107	1.55	MOS1,MOS2,PN
21	09:56:10.3	-09:58:59.4	0.00080	2.27	MOS1,MOS2,PN
22	09:55:57.6	-10:01:27.5	0.00060	2.18	MOS1,MOS2,PN
23	09:55:52.6	-09:59:51.1	0.00060	6.77	MOS1,MOS2,PN
24	09:55:44.2	-09:59:33.0	0.00100	1.88	MOS1,MOS2,PN
25	09:55:41.7	-09:59:20.9	0.00127	0.77	MOS1,MOS2,PN
26	09:55:39.4	-10:13:25.9	0.00168	1.18	MOS2
27	09:55:34.6	-09:56:01.6	0.00094	4.24	MOS1,MOS2
28	09:56:33.6	-09:53:55.1	0.00134	1.29	MOS2
29	09:56:01.3	-10:06:40.0	0.00138	0.57	MOS1,MOS2
30	09:56:00.1	-10:09:03.5	0.00121	0.57	MOS2,PN
31	09:56:00.1	-09:55:32.8	0.00142	0.73	MOS1,MOS2
32	09:55:50.0	-09:59:44.8	0.00110	1.85	MOS1,MOS2
33	09:56:55.4	-10:02:18.0	0.00142	0.69	MOS2
34	09:56:48.2	-09:58:03.0	0.00156	0.85	MOS2
35	09:56:05.3	-09:51:52.6	0.00154	1.01	MOS2
36	09:55:53.6	-10:14:11.0	0.00296	0.84	MOS2
37	09:55:38.6	-10:10:15.9	0.00416	0.99	MOS1,MOS2
38	09:56:27.5	-10:08:19.5	0.00767	0.60	MOS2
39	09:57:07.4	-09:56:48.4	0.00060	1.77	PN
40	09:57:03.6	-09:55:04.7	0.00123	1.88	PN
41	09:57:00.7	-09:58:29.6	0.00146	0.90	MOS2,PN
42	09:57:00.6	-09:54:24.1	0.00117	2.17	PN
43	09:56:58.4	-10:10:29.8	0.00120	1.22	MOS1,MOS2,PN
44	09:56:56.3	-09:54:19.8	0.00123	1.45	MOS2,PN
45	09:56:55.6	-09:55:07.5	0.00096	1.48	MOS1,MOS2,PN

Continued on next page...

Table 4.1 – Continued

Xray_ID	RA (J2000)	Dec (J2000)	Error (deg)	Cts/sec†($\times 10^{-3}$)	Detectors*
46	09:56:49.5	-10:07:24.5	0.00195	1.21	MOS1,MOS2,PN
47	09:56:47.4	-10:02:34.7	0.00123	1.07	MOS1,MOS2,PN
48	09:56:43.8	-09:55:40.0	0.00105	1.09	PN
49	09:56:42.4	-10:13:11.6	0.00100	1.47	MOS1,MOS2,PN
50	09:56:41.9	-10:08:50.5	0.00108	0.90	MOS1,PN
51	09:56:42.2	-10:05:58.6	0.00138	0.56	MOS2,PN
52	09:56:40.8	-09:59:16.4	0.00092	0.44	MOS1,PN
53	09:56:40.6	-10:11:49.7	0.00124	1.54	MOS1,MOS2,PN
54	09:56:40.6	-10:00:30.4	0.00089	0.75	MOS2,PN
55	09:56:40.0	-10:09:30.1	0.00100	1.45	MOS1,MOS2,PN
56	09:56:39.6	-10:09:00.3	0.00126	0.72	MOS1,PN
57	09:56:39.7	-09:57:18.3	0.00086	1.12	MOS1,MOS2,PN
58	09:56:37.3	-10:03:16.2	0.00070	2.05	MOS1,MOS2,PN
59	09:56:37.0	-09:52:37.2	0.00079	3.36	MOS1,MOS2,PN
60	09:56:36.1	-10:01:49.9	0.00074	1.31	MOS1,MOS2,PN
61	09:56:35.6	-10:00:04.3	0.00097	0.34	PN
62	09:56:35.3	-10:04:55.2	0.00060	55.10	MOS1,MOS2,PN
63	09:56:34.5	-09:59:30.1	0.00098	1.10	MOS1,MOS2,PN
64	09:56:30.6	-10:00:16.4	0.00060	38.90	MOS1,MOS2,PN
65	09:56:29.9	-09:52:37.4	0.00167	0.31	PN
66	09:56:29.7	-10:02:01.3	0.00067	1.87	MOS1,MOS2,PN
67	09:56:29.1	-10:10:05.2	0.00093	1.13	MOS1,MOS2,PN
68	09:56:29.1	-09:51:33.0	0.00130	0.94	MOS1,MOS2,PN
69	09:56:26.7	-10:05:10.0	0.00060	3.74	MOS1,MOS2,PN
70	09:56:26.5	-10:03:24.6	0.00119	0.69	MOS1,MOS2,PN
71	09:56:26.4	-10:10:57.9	0.00166	0.68	MOS1,MOS2,PN
72	09:56:26.5	-09:55:55.3	0.00110	1.34	PN
73	09:56:22.6	-09:56:00.6	0.00066	1.60	PN
74	09:56:21.7	-10:03:06.8	0.00065	0.96	MOS1,MOS2,PN
75	09:56:21.2	-09:56:36.1	0.00093	1.14	PN
76	09:56:20.1	-10:03:50.3	0.00061	1.84	MOS1,MOS2,PN
77	09:56:20.0	-10:00:48.5	0.00090	0.54	MOS1,MOS2,PN
78	09:56:19.7	-10:03:27.1	0.00063	0.85	MOS1,MOS2,PN
79	09:56:18.8	-09:55:57.9	0.00139	1.06	MOS2,PN
80	09:56:18.1	-09:53:59.8	0.00078	16.40	MOS1,MOS2,PN
81	09:56:17.7	-10:07:20.2	0.00126	0.42	MOS2,PN
82	09:56:15.9	-10:02:19.2	0.00060	0.21	PN
83	09:56:15.5	-09:50:31.3	0.00150	0.66	PN
84	09:56:15.0	-09:58:20.6	0.00060	4.38	MOS1,MOS2,PN
85	09:56:13.1	-09:59:03.8	0.00114	0.44	MOS1,MOS2,PN
86	09:56:13.0	-10:04:07.3	0.00060	2.00	MOS1,MOS2,PN
87	09:56:11.8	-09:59:55.9	0.00100	0.65	MOS1,MOS2,PN
88	09:56:10.6	-09:49:12.0	0.00101	2.44	MOS1,MOS2,PN
89	09:56:10.0	-10:07:11.3	0.00086	0.72	MOS1,MOS2,PN
90	09:56:05.5	-10:00:30.0	0.00068	1.11	MOS1,MOS2,PN

Continued on next page...

Table 4.1 – Continued

Xray_ID	RA (J2000)	Dec (J2000)	Error (deg)	Cts/sec†($\times 10^{-3}$)	Detectors*
91	09:56:03.3	-10:07:41.1	0.00087	2.25	MOS1,MOS2,PN
92	09:56:00.9	-09:56:18.7	0.00251	2.31	PN
93	09:55:58.2	-10:07:27.4	0.00101	1.40	MOS1,MOS2,PN
94	09:55:57.9	-10:06:52.7	0.00121	1.40	MOS1,MOS2,PN
95	09:55:55.7	-10:08:30.7	0.00115	0.65	MOS2,PN
96	09:55:54.6	-10:06:46.5	0.00134	0.49	MOS1,MOS2,PN
97	09:55:53.7	-10:08:47.9	0.00162	0.39	PN
98	09:55:52.9	-10:05:43.7	0.00110	0.82	MOS1,MOS2,PN
99	09:55:52.6	-10:06:44.6	0.00121	0.43	PN
100	09:55:52.5	-10:04:28.7	0.00074	1.88	MOS1,MOS2,PN
101	09:55:51.2	-10:03:56.7	0.00133	1.04	MOS1,MOS2,PN
102	09:55:50.5	-09:52:06.2	0.00137	2.12	MOS1,MOS2,PN
103	09:55:43.9	-09:57:05.3	0.00148	0.74	MOS2,PN
104	09:55:43.6	-10:09:09.5	0.00113	2.03	MOS1,MOS2,PN
105	09:55:43.6	-10:08:28.1	0.00117	0.62	MOS2,PN
106	09:55:38.1	-10:08:25.3	0.00112	1.44	MOS1,MOS2,PN
107	09:55:36.9	-09:57:15.8	0.00114	2.17	MOS1,MOS2,PN
108	09:55:35.8	-10:09:15.8	0.00075	2.56	MOS1,MOS2,PN
109	09:55:35.1	-10:01:52.7	0.00102	0.59	MOS1,PN
110	09:55:32.3	-10:01:44.9	0.00126	0.96	MOS1,MOS2,PN
111	09:55:31.1	-10:05:22.5	0.00163	0.60	PN
112	09:55:28.5	-10:05:30.8	0.00060	7.21	MOS1,MOS2,PN
113	09:57:18.5	-09:59:51.5	0.00109	0.98	PN
114	09:57:11.3	-09:57:05.5	0.00140	1.17	PN
115	09:56:57.1	-10:05:43.7	0.00198	0.44	PN
116	09:56:52.4	-10:00:30.4	0.00124	1.11	PN
117	09:56:48.1	-09:53:36.4	0.00139	0.76	MOS2,PN
118	09:56:47.1	-10:11:04.2	0.00110	1.02	MOS1,PN
119	09:56:46.7	-10:01:37.5	0.00156	0.58	MOS1
120	09:56:44.2	-09:50:46.6	0.00253	0.99	MOS1,PN
121	09:56:42.3	-10:12:18.4	0.00211	0.59	MOS2,PN
122	09:56:24.8	-09:51:17.1	0.00157	0.62	PN
123	09:56:23.5	-09:51:54.8	0.00117	0.71	MOS1,PN
124	09:56:22.0	-10:01:13.7	0.00109	0.33	PN
125	09:56:08.1	-10:06:12.6	0.00129	0.30	MOS1,PN
126	09:56:06.2	-10:10:30.7	0.00170	0.30	PN
127	09:56:00.9	-10:08:24.2	0.00131	0.33	PN
128	09:55:58.8	-10:05:57.3	0.00124	0.38	PN
129	09:55:42.8	-10:04:37.7	0.00128	0.43	PN
130	09:55:39.1	-09:54:33.8	0.00155	0.47	PN
131	09:55:31.2	-10:04:07.4	0.00137	0.78	PN
132	09:57:10.6	-09:56:27.3	0.00118	0.66	PN
133	09:56:12.0	-10:06:13.8	0.00138	0.27	PN
134	09:56:10.4	-10:09:44.7	0.00214	0.33	PN
135	09:56:28.2	-09:57:19.3	0.00060	277.00	MOS1,MOS2,PN

Continued on next page...

Table 4.1 – Continued

Xray_ID	RA (J2000)	Dec (J2000)	Error (deg)	Cts/sec†($\times 10^{-3}$)	Detectors*
136	09:56:21.8	-10:04:34.9	0.00064	2.53	MOS1,MOS2,PN
137	09:56:18.8	-10:07:45.6	0.00101	1.95	MOS1,MOS2
138	09:56:21.8	-10:06:48.2	0.00091	0.42	MOS1,PN
139	09:56:50.2	-10:11:51.8	0.00215	1.15	MOS1,PN

Notes:

† – The count rate is given by the average of the WAVEDETECT count rates from the images listed in the 'Detectors' column. The PN count rate has been scaled down by a factor of 3.0 (calculated from the brightest sources) to match the rates to those from the MOS detectors, so all count rates are for the 0.5-7.5keV band for a MOS detector. The variations in the count rate between images range from a factor of $\sim$ 2 at $< 10^{-3}$counts/sec to $\sim$ 1.2 at 4×10^{-3}counts/sec, and give an estimate of the error.

$*$ – The detectors listed are those in which the source was detected with significance > 3 as described in Section 4.3.2. Many sources were found in images from additional detectors but had low significance so are not included here.

Table 4.1: Positions, positional errors and count rates of X-ray sources in the A901 field with significance > 3.

fusion for extended sources due to the spatial variation of the background. Arnaud et al. (2002) produced an event list for the residual background by combining 'blank field' observations and removing point sources. The resulting files can be used to remove the expected background counts from the image. The files supplied by Arnaud et al. were reduced with SAS v5.1, whereas these data were reduced with v5.4. As v5.4 was not a public release it was not possible to recalibrate the background data, but for imaging extended emission any changes in calibration should be negligible.

The background data were filtered for the same patterns, flag and energy as the A901 (source) image, and the same GTI cut was applied. Vignetting corrected images were made for each band and detector for the background and source data. To obtain the same spatial variations the background image was reprojected to the source image detector co-ordinates using the XMM-SAS tool ATTCALC.

To correct the background counts for changes in the observation conditions the data need to be corrected for cosmic X-ray background (CXB) and non-cosmic X-ray background (NXB). Following the method of Arnaud et al. this analysis was done with vignetting corrected count rates, so that all values refer to those expected at the detector assuming uniform spatial quantum efficiency. As the NXB (from within the detector) is not vignetted, the weighted source count rate per pixel, C, is related to the weighted image count rate per pixel, I, by

$$I = C + I_{CXB} + I_{NXB}W, \tag{4.1}$$

where W is the weight, I_{CXB} the image counts from the CXB, and I_{NXB} those from the

NXB. Similarly, for the background image count rate per pixel, T,

$$T = T_{CXB} + T_{NXB}W. \tag{4.2}$$

Assuming that the NXB is purely time variable, we can define a factor, Q, such that

$$I_{NXB} = QT_{NXB} \tag{4.3}$$

If we then define a residual change in the CXB, ΔCXB, given by the true CXB minus the *scaled* background CXB,

$$\Delta CXB = I_{CXB} - QT_{CXB} \tag{4.4}$$

then combining Equations 4.1 to 4.4

$$C = I - QT - \Delta CXB \tag{4.5}$$

The value of Q was calculated from the variation over the whole field of view with sources removed, in the 5-8keV band where NXB dominates (see Table 4.2), and is assumed to be the same in each energy band. To calculate ΔCXB for each band all source areas were removed, so that equation 4.5 becomes $0 = I_{\text{background}} - QT_{\text{background}} - \Delta CXB$, which can the be solved for ΔCXB (see Table 4.2). As spatial variation and energy of the NXB depends on the detector, the analysis was done for each detector and energy band separately. For each image, I, and corresponding background image, T, the values of Q and ΔCXB given in Table 4.2 were used to create a background subtracted image, C.

To create merged images in each energy band, from all 3 detectors, the individual background subtracted images were weighted by energy conversion factors (ECFs) to convert from counts/sec to erg/cm^2/sec as given in Table 4.2. These flux images for each detector were masked using the masks from the exposure maps, summed together and divided by the number of images used at each pixel to create merged background subtracted images in each band. This resulted in flux images for each band, with a mean background of 0 and minimal spatial variation.

Using point source catalogue 1, point source regions were removed and replaced with local background selected randomly from a source free area within 10 pixels (or 20 pixels if there are not enough background pixels within the smaller radius). Smoothed images were created in each band using a gaussian kernel of radius 4 pixels, and are shown in Figure 4.4.

In addition the background subtracted images in different energy bands, without point sources removed, were used to calculate hardness ratios for possible supercluster AGN as described in Section 4.5.3.

	PN	MOS1	MOS2
Q factor			
all bands	1.10	0.99	1.06
ΔCXB, ($\times 10^{-7}$counts/pixel/second)			
$0.5-2$keV	0.44	6.03	7.44
$2-4.5$keV	1.64	-0.68	0.96
$4.5-7.5$keV	-0.64	-0.12	-0.57
ECFs, ($\times 10^{11}$counts/cm^2/erg)			
$0.5-2$keV	6.596	1.980	1.977
$2-4.5$keV	1.953	0.741	0.7445
$4.5-7.5$keV	0.941	0.2644	0.2771

Table 4.2: Data for creating flux calibrated background subtracted images. (ECFs from 'Correction of SSC pipeline EPIC source list fluxes' 2003).

4.3.4 Spectra of bright extended sources

Spectra were extracted from the PN data for the regions with bright extended emission. The spectra were taken within circular apertures, with point sources and regions of low exposure and streaking removed. The background spectrum for each region was calculated from an annulus situated far enough away to exclude most cluster emission, also with other sources and bad regions removed, and normalised to the good source area.

The spectra were fit using an ARF and RMF made with the XMM tools ARFGEN and RMFGEN, and binned to a minimum of 25 counts per energy interval. The data were fit over the range 0.5-7.8keV, using a fixed galactic neutral hydrogen column density of 5×10^{20}cm^{-2} (Dickey and Lockman 1990), and redshift of 0.166 (the slight redshift differences between the clusters do not affect the results). An absorbed Raymond-Smith model was used, with all other parameters left free. The results are shown in Table 4.3 and discussed below.

4.4 Analysis of extended emission

Figure 4.4 shows the soft band extended emission. In a blank field observation of this depth less than one cluster per field should be found serendipitously (Davidson et al. 2005) so all the extended emission is expected to be associated with the supercluster. However, it is known from optical imaging and lensing analysis that there is a cluster behind A902, at redshift $\sim$0.5, which might have detectable X-ray emission.

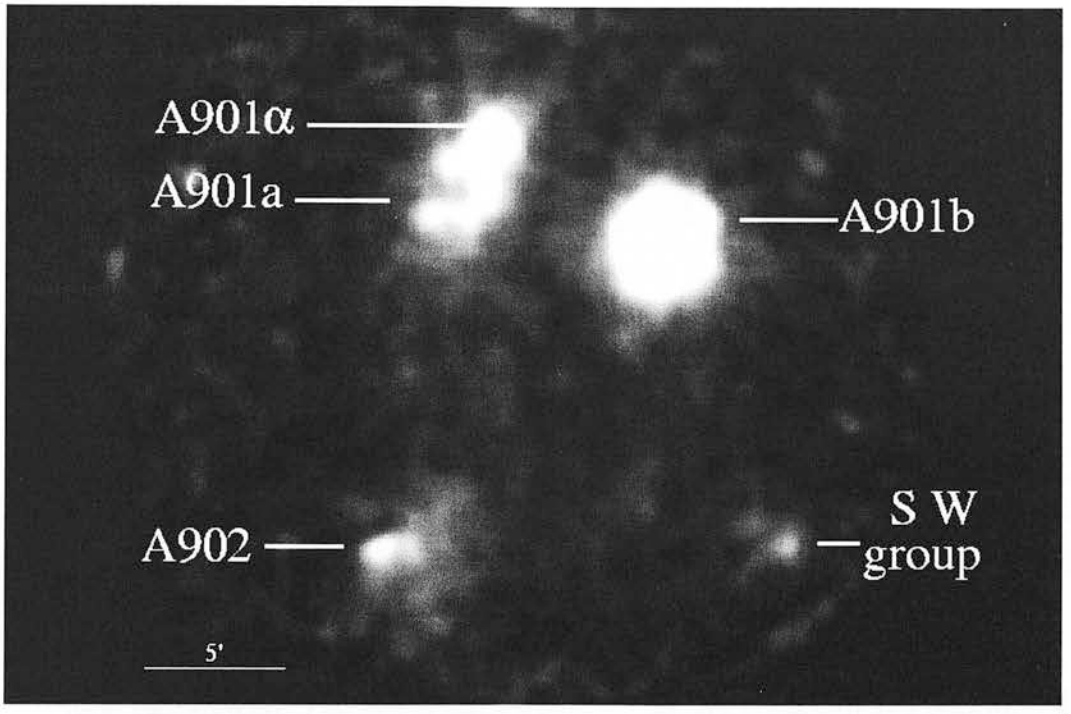

Figure 4.4: A smoothed image of A901 with point sources subtracted (0.5-2keV). Clusters are marked and described in Section 4.4.

- **A901**α This is a new detection of cluster emission in this field – the source was previously thought to be an AGN (Schindler 2000) but is clearly extended and is well fit by a thermal spectrum (Table 4.3 and Figure 4.5(a)). The emission is located coincident with a large red early-type galaxy in the COMBO-17 image, which is radio loud (14mJy at 1.4GHz, from the NVSS, Condon et al. 1998), so there may be emission from an AGN in addition to the cluster emission. The cluster nature of this object is confirmed by the galaxy number overdensity (at the cluster redshift) in this region, as shown in Figure 4.1. It lies on the cluster luminosity-temperature relation (Xue and Wu 2000) at the boundary between clusters and groups, and appears to be a small cluster merging with A901a.

- **A901a** The AGN in this area (see Section 4.3.2) dominates in this region, but there is also some evidence for cluster emission. Optically, the large number of galaxies and dominant BCG, together with the dark matter potential, suggest that there should be cluster gas in this region. Due to the uncertainties in the shape of the PSF it has not proved possible to subtract the AGN accurately, but there is some indication of asymmetry in the emission. Subtracting a circular region (centred on the well defined peak of the AGN emission), filling with local background and smoothing gives the image shown in Figure 4.4, with a hole in the centre (due to filling the region with

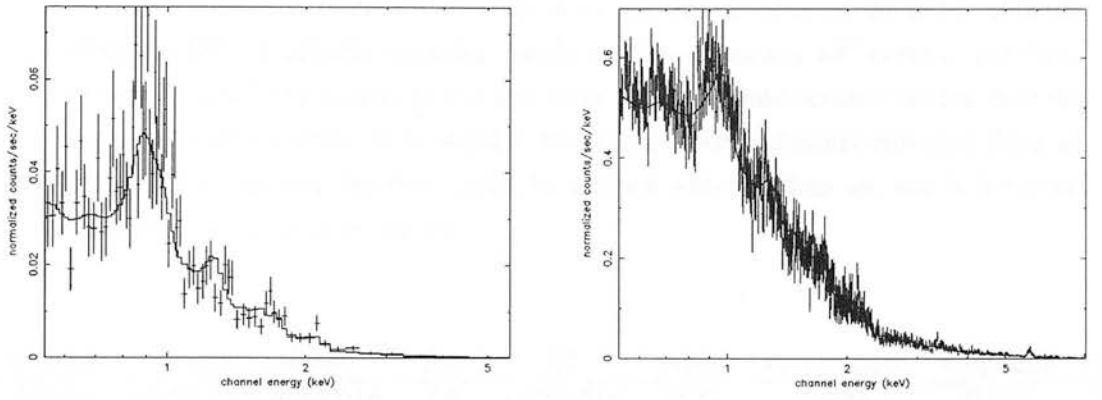

(a) A901α (b) A901b

Figure 4.5: Spectra and best fit thermal models (folded through the detector response) for A901α and A901b (see Table 4.3 for details).

local background). The remaining emission is very one sided with an offset towards the west, which is not the direction expected from variations in the PSF (which should be roughly arc-shaped around the aim-point). The BCG in this cluster is $\sim 25''$ west of the AGN host galaxy, so it is likely that this is the edge of cluster emission which is mainly hidden behind the AGN.

- **A901b** This is the only detected cluster emission in the ROSAT HRI analysis (Schindler 2000), and is by far the brightest cluster emission from this field. A spectral fit (see Table 4.3 and Figure 4.5(b)) shows that it lies on the cluster $L_X - T_X$ relation of Xue and Wu. Comparison with optical and radio data shows that the emission is located coincident with a central a BCG which is radio-loud, so a small fraction of the emission may be from an AGN. Although it has a lot of gas and dark matter, this cluster does not have many galaxies (Figure 4.1). This highlights the range of environments found in this supercluster.

- **A902** The cluster emission from this region is very diffuse, with a brighter peak towards the east. The centre of the brighter peak (~09:56:40,-10:10:24) coincides with the optical centre of the $z = 0.5$ cluster. The more diffuse emission is probably from gas in A902, and the brighter peak from the high redshift cluster. The superposition of the two clusters and low count level meant that spectra could not be fit to this emission.

- **SW group** The emission from the SW group is faint and centred at around 09:55:38.2,-10:10:18, which is near the brightest group galaxy (BGG). This galaxy is an AGN (and radio loud, see Section 4.5.4). Some of the extended X-ray emission in this

region could be due to under-subtraction of the large PSFs of the five X-ray point sources found here (three of which are in the group). In addition the radio emission from the BGG is slightly extended, implying that the galaxy 44″ north of the BGG is active. Low level activity in this and other galaxies could account for much of the emission in this region. It is possible that there is some thermal emission from an intra-cluster medium, but this cannot be verified with this data set, and it is far too faint to extract a reliable spectra.

Cluster	Position (J2000)	R_A	kT	Ab/$\odot$	$L_{0.1-2.4keV}$	$L_{0.5-8keV}$	rχ^2
A901α	09:56:22.7 -09:55:16	7.5	1.38±0.04	0.28	0.109	0.135	1.41
A901b	09:55:57.4 -09:59:04	21.5	2.84±0.04	0.33	1.38	2.35	1.04

Table 4.3: Details of the best-fit spectral models for the two brightest extended sources. The fit parameters are described in Section 4.3.4. Luminosities are given in 10^{44}erg/sec, R_A is the aperture radius in pixels, Ab/$\odot$ is abundance as a fraction of solar and rχ^2 is the reduced χ^2 .

4.5 Finding the Supercluster Active Galactic Nuclei

4.5.1 Matching X-ray and Optical catalogues

The COMBO-17 catalogue consists of 63776 sources detected using SExtractor on the R-band image (Wolf et al. 2003). These were matched with the XMM point sources to identify the X-ray sources in the supercluster. Some saturated stars and fainter sources near diffraction spikes are not included in the COMBO-17 catalogue, so the areas around each X-ray source were also examined for missing sources, and four such optical sources which could possibly match an X-ray source were added to the catalogue. Approximate magnitudes were assigned to these sources assuming a zero point magnitude derived from other objects in the field.

A maximum-likelihood technique was used to match the X-ray sources to the COMBO-17 optical catalogue. Matching was performed using a simple likelihood ratio, following Taylor (2005), which took account of angular separation and optical magnitude, but made no distinction between source classification or photometric redshift. This method treats optical quasars and galaxies of the same flux in the same way, and does not account for the fact that quasars are rarer and more likely to be X-ray sources. In addition, the method does not distinguish between the brightest galaxies, which are rare and quite likely to be X-ray sources, and stars of a similar magnitude. These issues become important when a

faint QSO is the only match and is assigned too low a probability, or when more than one possible match is identified, including a QSO or a bright star. The former case may lead to additional incompleteness in the X-ray matching, but will not affect the supercluster sample. In the latter case the source classifications, locations and errors of the possible matches were examined in detail to determine the true source of the X-rays.

The likelihood ratio was defined as

$$LR_{i,j} = \frac{e^{-r_{i,j}^2/2\sigma_j^2}}{\sigma_j^2 N(< m_i)} \tag{4.6}$$

where σ_j is the positional error on X-ray source j, $r_{i,j}$ the distance to optical source i from X-ray source j, and $N(< m_i)$ the number of optical sources brighter than source i in the r band image. The errors on the optical sources were small enough to neglect compared to those in the X-ray, and the astrometric errors were also found to be negligible as the minimum error on the X-ray position of 0.5 pixels is significantly larger than the astrometric error on this image.

As the X-ray errors vary significantly the likelihood values expected for a randomly placed X-ray source also vary, as there are more possible counterparts for a larger source error.

The expected distribution of likelihood values from an X-ray source randomly placed on the optical image is dependent on the X-ray positional error, which varies significantly from source to source. To account for the fact that, for example, there will be more random matches for a source with a larger positional error, the expected distribution of likelihood values was generated for each X-ray source, j, by randomly placing 14000 X-ray sources with σ_j over the optical catalogue. The resulting (normalised) distribution $N(LR)_j$ gives the probability of obtaining each likelihood ratio by chance (if source j had no optical counterpart), as shown for one source in Figure 4.6. This technique compares likelihoods to the average over the field and ignores any clustering, which gives slightly higher likelihood values for X-ray sources in the line of sight to cluster centres, and slightly lower for those in areas with few supercluster galaxies. This is very unlikely to change any results, especially as the catalogue is dominated at all optical magnitudes by non-supercluster galaxies ($> 80\%$ of optical sources are not in the supercluster at $m_{\rm R} < 20$, and $> 93\%$ at $m_{\rm R} < 24$).

The standard method of calculating the reliability of a match requires a large sample of sources, so instead the reliability for each source pair i, j was defined as the probability of not obtaining $LR_{i,j}$ randomly,

$$R_{i,j} = 1 - \Sigma N(LR_j > LR_{i,j}). \tag{4.7}$$

Most X-ray sources have more than one potential optical counterpart, as well as a significant probability of having no match. The probability that source i is the true counterpart to j, $(P_{i,j})$ and the probability that there is no counterpart $(P_{none,j})$, given a set of possible

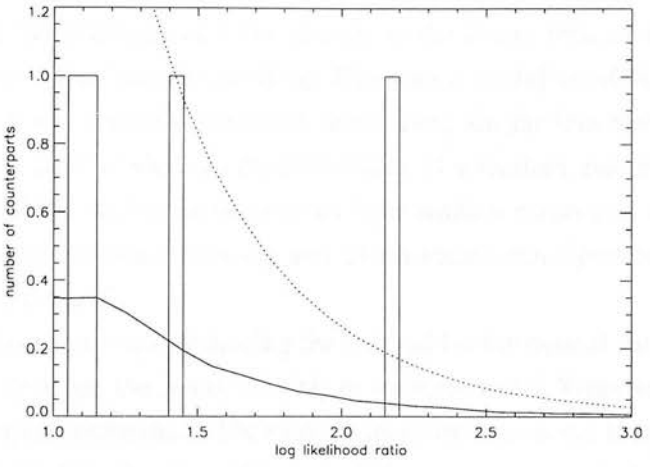

Figure 4.6: The expected distribution of likelihood ratios for one X-ray source based on 14000 trials (solid line), cumulative expected distribution (dashed line) and the histogram of actual likelihood ratios for the optical galaxies near this source (the vast majority of optical galaxies have log(likelihood) < 1). One likely match is identified, with a reliability of ~ 0.8.

counterparts, k, are calculated following Rutledge et al. (2000),

$$P_{i,j} = \frac{R_{i,j} \prod_{k \neq i}^{M} (1 - R_{k,j})}{S} \tag{4.8}$$

$$P_{none,j} = \frac{\prod_{k=1}^{M} (1 - R_{k,j})}{S} \tag{4.9}$$

where S is a normalisation factor so that the probabilities sum to 1, and M is the number of possible optical counterparts to the X-ray source.

For sources with only one likely optical counterpart, a secure match is defined as $P_{i,j} > 0.8$, which is confirmed by visual inspection. Although this is rather low compared to the probability cut used in many matched catalogues, the size of the X-ray positional uncertainties and depth of the optical catalogue means that the chance of a random association will always be high. For sources with more than one possible counterpart the conditions for i to be a unique counterpart given a set of options, k, were $\sum_k P_{k,j} > 0.8$ and $P_{i,j} / \sum_{k \neq i} P_{k,j} > 4$. This resulted in 66 secure identifications out of 139 sources, of which less than 6 are expected to be random associations.

For sources with multiple possible counterparts ($\sum_k P_{k,j} > 0.8$ and $P_{i,j} / \sum_{k \neq i} P_{k,j} \leq 4$) all sources with $P_{k,j} > 0.15$ were included as possible matches. This resulted in 17 sources with two possible counterparts and 3 sources with three options.

4.5.2 Matching with the 24-micron data

The Spitzer 24 micron catalogue of 1194 sources in the X-ray field of view was used to improve the X-ray to optical source matching. This data is useful as AGN often have infrared emission, but also in a purely statistical sense there are far less Spitzer sources than optical sources in the field of view, so the probability of a random association is far lower than for the optical data. As the 24μm sources have smaller errors and are rarer than the optical sources, a match between an X-ray and 24μm source can significantly improve the accuracy of the optical match.

A simple likelihood ratio test, following the method for the optical catalogue, produced 72 unique matches between the X-ray and 24μm sources, and 7 X-ray sources with more than one possible 24μm counterpart. The same probability cuts as the X-ray matching were applied, and the low surface density of 24μm and X-ray sources mean that we expect very few false matches. Examination of the optical images for the few X-ray sources with more than one possible 24μm counterpart shows that the 24μm points are likely to be multiple detections of extended objects.

The 24μm sources were then matched with the optical catalogue. The errors for the 24μm catalogue were taken as $1.2''$, which is half a pixel. This will underestimate the errors on faint sources, and give a more conservative catalogue. The advantage of taking the same errors for all sources is a reduction in computing time as only one expected distribution needs to be calculated. In addition, as the sample was large enough, a true reliability was calculated following by comparing the likelihood ratio distribution for the sample ($N_{true}(LR)$) with that of 10 random catalogues ($N_{random}(LR)$) following the method of Taylor (2005). The reliability is defined as a function of likelihood ratio,

$$R(LR) = \frac{N_{true}(LR) - N_{random}(LR)}{N_{true}(LR)}. \tag{4.10}$$

Probabilities for each possible match were calculated using Equations 4.8 and 4.9, and the criteria for unique and multiple matches used in the X-ray matching were applied. The 24μm sources that matched the X-ray catalogue were examined by eye to identify those which had good optical matches, but were rejected due to underestimated positional errors in the 24μm data.

In total, of the 79 of the X-ray sources with probable 24μm matches, the results of the 24μm-optical matching agreed with those of the X-ray-optical matching in 61 cases (including those where both the X-ray and 24μm matches detected multiple optical counterparts, or where both detected no match). Of the remainder, in 10 cases the 24μm data were able to distinguish between two or more possible optical counterparts to the X-ray source and produce a secure identification; in 1 case they reduced the possible optical matches from three to two; in 3 cases they showed that the identified optical match to the X-ray source was serendipitous, and there was actually no optical counterpart; and in the final 4 cases the

X-ray-24μm-optical match was less probable than the X-ray-optical match, so the optical counterpart was not changed.

The final lists of X-ray sources with unique and multiple counterparts are given in Tables 4.4 and 4.5, which list the X-ray IDs from Table 4.1 and COMBO-17 optical number, as well as the optical position, redshift, 24μm flux and probability that the match is not by chance.

4.5.3 Criteria for identifying supercluster AGN

To identify the AGN in the supercluster it is necessary to use the photometric redshifts from the COMBO-17 survey. A liberal cut of $0.15 < z_{\rm phot} < 0.18$ was used to ensure that all AGN associated with the supercluster were identified. This range also allows for the errors in the photometric redshifts, which may also be affected by the AGN emission, such that adding the maximum COMBO-17 redshift errors to each source does not add any sources to the supercluster sample. In addition some galaxies have bimodal photometric redshift distributions, and so for the X-ray loud sources it was checked that neither the first or second choice redshifts are in the supercluster.

The presence of an AGN may cause the template fitting in the COMBO-17 survey to give wrong photometric redshifts, as the COMBO-17 templates do not include Seyferts with spectra dominated by the galaxy emission. To check for missed supercluster X-ray sources we examined all optical counterparts with $21 > m_{\rm R} > 17.75$ (between the faintest supercluster AGN and the brightest BCG), and $B - R < 2.3$ (on or bluer than the supercluster main sequence) which were classified as galaxies[2]. The photometric data for these galaxies were manually compared to spectral templates at the supercluster redshift. Two optical counterparts (COMBO catalogue numbers 12953 and 41435, matching X-ray sources #3 and #135) were found to fit well with templates at $z \sim 0.16$, and are discussed in detail in Section 4.5.4.

To distinguish between X-ray emission from high levels of star formation and that from AGN, various methods were used depending on the information available for each source. Used alone most of these methods cannot distinguish absolutely between star-forming galaxies and those with AGN, but combining the available data can give a reliable indicator of the nature of the X-ray emission.

- **X-ray Luminosity -** Star forming galaxies generally have low X-ray luminosities. A source in the local universe with $L_{0.5-8\rm kev} > 3 \times 10^{42}$erg/sec is extremely unlikely be purely star forming (Bauer et al. 2004), and any source with $L_{0.5-8\rm kev} \gtrsim 1 \times 10^{41}$erg/sec is likely to be an AGN (see Figure 7 of Bauer et al. – most sources

[2]Photometric redshifts of objects classed as high redshift quasars are accurate as there is only a 1 in 10000 chance of a galaxy at $m_{\rm R} < 24$ being mistaken for a quasar (Wolf et al. 2004).

Table 4.4

Xray_ID	Optical_ID	RA(Opt) (J2000)	Dec(Opt) (J2000)	z(Opt)	24μm Flux [mJy]	Notes
1	28832	9:56:36.5	-10:02:43.5	0.253	0.67	
3	12953	9:56:35.7	-10:10:10.6	-	5.31	Z(a)
6	23122	9:56:20.3	-10:05:24.4	0.616		
8	54851	9:56:11.9	-09:50:47.2	1.353	1.11	
14	39465	9:55:31.9	-09:58:59.6	x		
17	28744	9:56:54.0	-10:02:45.9	0.754	1.14	
18	5514	9:56:47.1	-10:13:30.1	1.201	1.23	
20	31178	9:56:17.6	-10:01:49.4	0.171	2.29	Spec
21	36827	9:56:10.2	-09:58:59.2	1.886	0.58	
22	31519	9:55:57.5	-10:01:28.3	2.413	1.14	
23	35608	9:55:52.5	-09:59:51.3	x	0.39	
24	36966	9:55:44.3	-09:59:33.5	0.175		Spec
27	43454	9:55:34.6	-09:56:4.17	1.655	1.15	
28	47810	9:56:33.6	-09:53:58.4	2.109	0.45	
34	39549	9:56:48.1	-09:58:1.65	0.166		Spec
37	14161	9:55:38.4	-10:10:19.1	0.171		
39	42260	9:57:07.2	-09:56:44.9	x		
40	45295	9:57:03.7	-09:55:05.9	1.131	1.38	A
43	12232	9:56:58.4	-10:10:28.1	3.448	0.42	
47	29108	9:56:46.9	-10:02:32.8	0.797	0.37	A
49	6258	9:56:42.3	-10:13:11.2	0.337	0.80	
50	15780	9:56:42.0	-10:08:48.9	1.327		A
51	21892	9:56:42.1	-10:05:56.0	2.267	0.31	
55	14419	9:56:39.8	-10:09:30.1	0.292		
57	46236	9:56:39.6	-09:57:17.5	x	0.62	
58	27507	9:56:37.3	-10:03:17.1	1.458	0.54	
59	50887	9:56:37.0	-09:52:37.6	0.376	0.46	
60	30570	9:56:36.1	-10:01:51.3	0.948	0.33	
62	24409	9:56:35.3	-10:04:54.6	x	3.05	
63	35643	9:56:34.5	-09:59:30.1	0.965	1.11	
64	63780	9:56:30.6	-10:00:15.5	0.000	0.79	
66	63777	9:56:29.6	-10:01:59.7	x	0.62	
68	53095	9:56:28.9	-09:51:33.7	1.129	0.52	A
69	23665	9:56:26.8	-10:05:09.5	0.601	1.04	B
70	27071	9:56:26.7	-10:03:26.2	0.903	1.25	C
71	11827	9:56:26.1	-10:10:58.5	0.175	2.05	24μm
72	46335	9:56:26.5	-09:55:46.4	x	0.18	
73	43383	9:56:22.5	-09:56:00.0	1.253		
74	27810	9:56:21.7	-10:03:06.1	2.000		
75	42064	9:56:21.3	-09:56:37.7	3.493		
76	26320	9:56:20.1	-10:03:48.6	0.986		
78	27050	9:56:19.8	-10:03:27.1	0.974		
79	44351	9:56:18.8	-09:55:57.8	0.162		Spec
80	47978	9:56:18.0	-09:54:01.2	1.133	4.56	

Continued on next page...

Table 4.4 – Continued

Xray_ID	Optical_ID	RA(Opt) (J2000)	Dec(Opt) (J2000)	z(Opt)	24μm Flux [mJy]	Notes
81	19305	9:56:17.7	-10:07:18.7	0.175	0.44	Spec
84	38125	9:56:15.0	-09:58:21.3	0.902	0.92	
85	36939	9:56:13.1	-09:59:04.9	x		
86	25718	9:56:13.0	-10:04:06.9	2.267		
88	58384	9:56:10.5	-09:49:13.2	1.899	1.18	
89	19716	9:56:10.1	-10:07:10.8	0.260		
90	33381	9:56:05.4	-10:00:30.5	0.961	1.16	B
91	18874	9:56:03.3	-10:07:42.4	0.255	6.56	
93	18722	9:55:58.3	-10:07:27.3	1.304	0.70	
94	19933	9:55:57.9	-10:06:54.1	0.838	0.44	
95	16610	9:55:55.7	-10:08:31.9	0.516	1.44	
98	22404	9:55:52.9	-10:05:43.9	0.445	0.39	
100	24884	9:55:52.5	-10:04:28.8	0.416	0.44	
104	15698	9:55:43.7	-10:09:11.8	0.179	0.65	B Spec
105	17675	9:55:43.4	-10:08:26.5	0.170		Spec
106	16625	9:55:38.2	-10:08:24.6	0.562		
107	40605	9:55:36.8	-09:57:17.1	0.975	0.58	
108	14758	9:55:35.9	-10:09:15.7	1.693		
109	30592	9:55:35.0	-10:01:51.5	0.814	0.37	B
110	30855	9:55:32.6	-10:01:49.0	x		
111	63779	9:55:30.9	-10:05:18.9	x	0.39	
112	22807	9:55:28.6	-10:05:32.2	0.257	1.07	
116	35364	9:56:52.2	-10:00:29.7	0.079	1.92	24μm
118	10744	9:56:47.2	-10:11:03.8	0.941	0.32	D
119	31772	9:56:46.7	-10:01:38.6	0.168	8.69	Spec
124	31850	9:56:22.0	-10:01:14.5	3.373	0.41	
132	42725	9:57:10.4	-09:56:24.0	x	1.12	
135	41435	9:56:28.2	-09:57:19.0	-	1.17	Z(b)
136	24683	9:56:21.8	-10:04:35.7	1.088	0.28	
137	18034	9:56:18.7	-10:07:47.0	0.834	1.67	
138	20029	9:56:21.8	-10:06:47.4	0.719	0.19	
139	9020	9:56:50.0	-10:11:55.8	0.171	3.70	Spec

Notes: x – The source is too faint to have a reasonable COMBO-17 redshift.

A – X-ray data alone finds no secure match but the 24μm data identifies a unique optical counterpart.

B – 24μm data reduces two possible counterparts to one.

C – 24μm data reduces three possible counterparts to one.

D – The initial X-ray - optical match found three possible bright counterparts, but these were rejected as the 24μm data identified a secure match with a faint source.

Spec – 2dF spectra exist for this source.

Z – Dubious redshift, see section 4.5.3; Z(a) – COMBO-17 redshift is 1.4 but it may be 0.16. Z(b) – COMBO-17 redshift is 0.33 but 0.16 is more likely.

24μm – The 24μm catalogue includes multiple detections of the same object. The highest flux value is given, but this should be taken as a lower limit.

Table 4.4: X-ray sources with unique optical matches.

Table 4.5

Xray_ID	Optical_ID	RA(Opt) (J2000)	Dec(Opt) (J2000)	z(Opt)	24μm Flux [mJy]	Prob†	Notes
2	48944	9:56:35.7	-09:53:28.7	0.769	0.24	0.522	A
	48703	9:56:35.8	-09:53:30.0	0.759	0.24	0.386	A
5	32205	9:56:28.6	-10:01:07.8	x		0.605	
	32229	9:56:28.0	-10:01:03.5	1.301		0.207	QSO
11	51604	9:56:40.4	-09:52:49.8	0.164		0.681	Spec
	50205	9:56:41.2	-09:52:51.9	1.898		0.198	QSO
16	36617	9:55:28.1	-09:59:15.5	x		0.563	Star
	36776	9:55:27.7	-09:58:58.7	x		0.212	Star
26	5630	9:55:39.4	-10:13:22.9	0.662	0.40	0.532	B
	5612	9:55:39.3	-10:13:24.7	0.818	0.40	0.262	B
48	44635	9:56:43.9	-09:55:39.9	0.083	16.63	0.597	C
	45154	9:56:43.9	-09:55:43.2	0.053	27.48	0.391	C
52	36062	9:56:40.9	-09:59:16.0	0.728		0.541	
	36147	9:56:40.7	-09:59:14.2	x		0.289	
53	9081	9:56:40.6	-10:11:49.1	1.290	0.67	0.639	QSO
	9524	9:56:40.2	-10:11:52.0	0.176	0.82	0.318	
61	34255	9:56:35.9	-10:00:05.9	1.667		0.386	QSO
	34746	9:56:36.0	-09:59:57.8	x		0.204	Star
	34238	9:56:35.3	-10:00:09.0	0.426		0.204	
102	52252	9:55:50.4	-09:52:07.3	0.240		0.693	
	53126	9:55:50.6	-09:51:53.1	x		0.249	Star
121	8770	9:56:42.2	-10:12:19.1	0.324		0.482	
	7961	9:56:42.6	-10:12:22.6	x		0.369	Star
127	16637	9:56:00.9	-10:08:23.3	1.967		0.406	QSO
	17155	9:56:1.51	-10:08:19.1	0.173		0.289	Spec

Notes:

x – The source is too faint to have a reasonable COMBO redshift.

† – The probabilities given are for the X-ray - optical match alone (with the exception of note B). They are normalised as explained in the text, so are useful as a relative rather than absolute measure of the certainty of each match. In particular rejected sources with probabilities $< 20\%$ are not included here, but reduce the normalised probability for the other sources.

A – The X-ray source corresponds to one 24μm source, and they could both be either of the optical matches.

B – The optical source is identified by the 24μm match as the X-ray source had no clear optical counterparts but matches the 24μm source with high probability. The probabilities given are for the 24μm-optical match.

C – The two optical and two 24μm detections are both components of a local merging system.

QSO – The optical source is a QSO, and therefore has a higher likelihood of being the match than indicated by the probabilities.

Star – The optical source is a star, and as stars are often bright (and rare, giving a high probability) but not often X-ray loud the source may be a chance association.

Spec – This source has a 2dF spectrum

Table 4.5: X-ray sources with multiple optical matches.

with $L_X > 10^{41}$ which are not near the flux limit are securely identified as AGN by their column density or hardness ratio). Luminosities were calculated using aperture photometry on the background subtracted images described in Section 4.3.3. The redshift of the supercluster AGN (0.166) means that the observed 0.5-7.5 keV counts correspond to an emitted 0.58-8.7 keV luminosity. As this study does not require very accurate luminosities, and as the errors on the count rates are large, this is taken as an approximation to the 0.5-8 keV luminosity. The true luminosities may be slightly higher, but this depends on the X-ray spectrum.

- **[OII] Star-Formation Rates -** If the X-ray emission is purely due to star-formation, with no AGN present, then the star-formation rate (SFR) can be estimated from the X-ray luminosity as

$$SFR(\mathrm{M}_\odot/\mathrm{yr}) = 2.2 \times 10^{-47} L_{0.5-2\mathrm{kev}}(\mathrm{W}) \tag{4.11}$$

(Ranalli et al. 2003). If there is no AGN and minimal absorption then this must be near to the SFR derived from the [OII]λ3727 line flux (Hopkins et al. 2003);

$$SFR(\mathrm{M}_\odot/\mathrm{yr}) = \frac{L_{[OII]}}{2.97 \times 10^{33} W} \tag{4.12}$$

where $L_{[OII]}$ can be estimated for those sources with 2dF spectra from the equivalent width of the line and the COMBO-17 magnitude in the rest-frame Johnson U band. (This method assumes a flat spectrum in the U band, but will give an estimate of the flux at 3727$\AA$ to within at least a factor of two, as the U band magnitude has minimal contamination from flux above the 4000$\AA$ break).

- **X-ray / Optical Flux Ratio -** Sources with $f_{0.5-8\mathrm{kev}}/f_R > 1$ are very likely to be AGN, and those with $f_{0.5-8\mathrm{kev}}/f_R > 0.1$ are likely to be AGN (see Bauer et al. 2004 and references therein).

- **X-ray Hardness Ratio -** A good indication of the spectral properties and absorption of X-ray sources is given by the luminosity hardness ratio, $HR = \frac{H-S}{H+S}$, where $H = L_{2-8\mathrm{kev}}$ and $S = L_{0.5-2\mathrm{kev}}$. Sources with $HR > 0.8$ are unlikely be star-forming due to the very large amounts of absorption required (Mainieri et al. 2002) (unless the emission is dominated by hard X-ray binaries), and sources with $HR > -0.2$ are more likely to be AGN than star-forming (Szokoly et al. 2004). Hardness ratios were calculated from the background subtracted images described in Section 4.3.3.

- **Optical Line Ratios -** Line ratios in optical spectra can distinguish between star-forming galaxies and AGN. As the 2dF spectra are not flux calibrated only the [OIII] and Hβ lines were used, as they are close together in wavelength so considering the line equivalent widths, and assuming a flat continuum spectrum, will not introduce

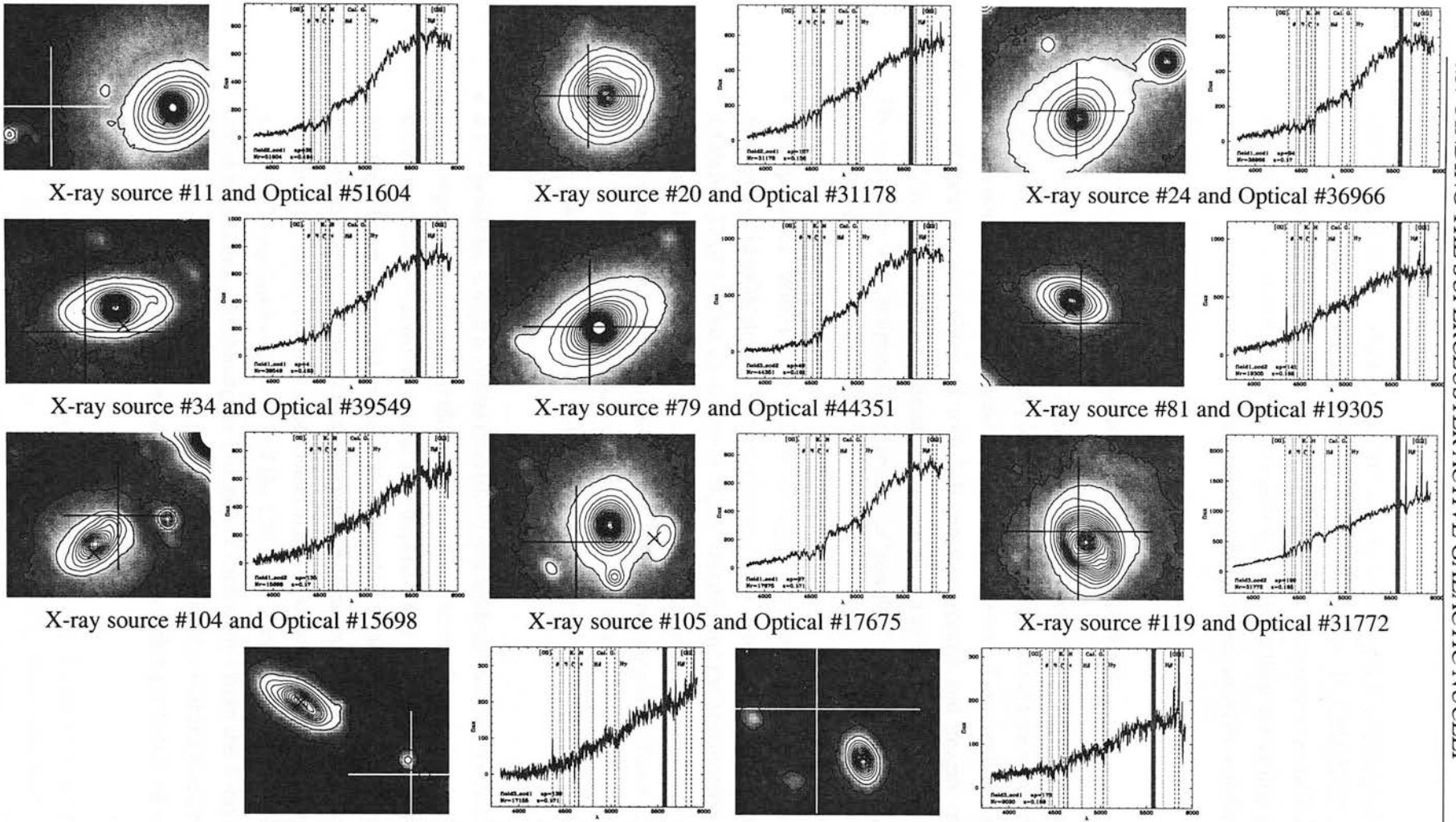

Figure 4.7: Images and spectra for candidate supercluster AGN which were observed with 2dF. The positions and 1σ error bars of the X-ray sources are marked with a large cross, and the smaller 'x' represent the positions of the Spitzer sources († for #127 the X-ray source error is misleading as the source is extended towards the North-East of the image). The images are $15.5'' \times 12.5''$ and the same scale and logarithmic contours are used throughout. The spectra are for the supercluster members, which are always the dominant object in each field. (Note that the 2dF spectra are not flux calibrated.)

overly large errors. Most of the 2dF spectra of the optical counterparts have very faint or no lines so only upper limits can be measured. If [OIII]λ5007/Hβ $\gtrsim$ 4.5 then the source is an AGN (Lamareille et al. 2004). However if the ratio is < 4.5 the source could still contain some AGN activity, and if no lines are visible it may be an obscured AGN, so this method can confirm the presence of AGN activity but cannot confirm star-formation.

4.5.4 Details of supercluster AGN candidates

After applying the redshift cut, the sample of possible supercluster AGN consists of eleven optical matches in the supercluster plus two matches with revised photometric redshifts and three possible matches with supercluster galaxies. Eleven of the candidate supercluster AGN host galaxies were observed with 2dF and their spectra and images are shown in Figure 4.7. The five candidates without spectra are shown in Figure 4.8.

The candidates were assigned to be 'secure' or 'possible' supercluster AGN, or rejected outright, as follows;

- **# 3 - possible.** With $L_X = 5.25 \times 10^{42}$erg/sec this source is clearly an AGN. The host galaxy identification is secure, with an initial photometric redshift assigned by COMBO-17 of 1.4, but the source is highly variable and the photometric data points taken on different days vary by up to 15%. This makes it difficult to assign a photometric redshift, but a visual fit to a $z = 0.158$ galaxy template, shown in Figure 4.9 is fair. The colours of this source place it on the cluster main-sequence, and the magnitude matches other cluster AGN hosts. It is therefore considered to be a possible supercluster AGN.

- **# 11 - possible.** A high hardness ratio (0.49) and moderate luminosity (6.2×10^{41}erg/sec at the supercluster redshift) indicate that the X-ray source is probably an AGN. However, there are two possible optical counterparts, only one of which is in the supercluster. The spectrum and image of the supercluster member show a very bright red early-type galaxy with no detectable emission lines, but this is unremarkable for X-ray detected AGN. The non supercluster member is both closer and a quasar, which are often X-ray luminous ($\sim$ 2% of the QSOs are X-ray sources) and are rare compared to galaxies. Combining the distance of each source from the X-ray source and the number of QSOs in the field to that of bright galaxies, neither association is likely to be random. The X-ray emission could be from either (or both!) of the counterparts.

- **# 20 - certain.** This X-ray source is securely associated with a galaxy in the supercluster. The image and 2dF spectrum of the host galaxy show a red early-type galaxy in the supercluster with weak emission lines. The X-ray luminosity could be caused

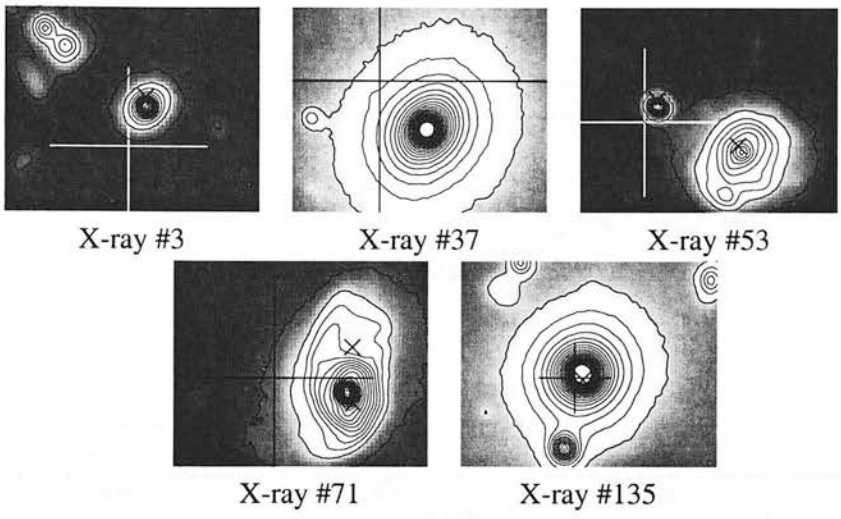

Figure 4.8: Images of candidate supercluster AGN which were not observed with 2dF. The positions and 1σ error bars of the X-ray sources are marked with a large cross, and the smaller 'x' represent the positions of the Spitzer sources. The images are $15.5'' \times 12.5''$ and the same scale and logarithmic contours are used throughout.

by a galaxy with a SFR of $96 M_{\odot}/\mathrm{yr}$ and no AGN; this is inconsistent with both that implied by the [OII] line luminosity ($1.2 M_{\odot}/\mathrm{yr}$) and the nature of the galaxy in the 2dF spectrum. It is therefore concluded that this galaxy contains an AGN which is optically obscured. This conclusion is backed by the moderate X-ray luminosity (8.1×10^{41} erg/cm^2/sec), hardness ratio (0.03) and X-ray to optical flux ratio (0.12).

- **# 24 - certain.** This source is securely identified with a supercluster galaxy, and the image and 2dF spectrum of the host show a red early-type galaxy. The upper limit on the SFR from [OII] of $< 1 M_{\odot}/\mathrm{yr}$ is 500 times less than that required to explain the X-ray emission. Again, this must be due to optically obscured AGN activity. The X-ray/Optical flux ratio also indicates an AGN.

- **# 34 - certain.** The X-ray emission clearly originates from a supercluster galaxy. A high hardness ratio (0.7) and moderate [OIII] and [OII] emission indicate an AGN. Due to uncertainties in the strength of the Hβ line some degree of star formation can not be ruled out, but it is at least 25 times too low to account for all of the X-ray emission.

- **# 37 - certain.** Moderate X-ray luminosity (2.4×10^{41} erg/cm^2/sec) and no detectable hard X-ray emission indicate a weak AGN or moderately powerful starburst. The optical counterpart is identified securely as a supercluster galaxy - there is no spectral information on this source, but it is the brightest galaxy in the south-west group and falls on the main sequence of the colour magnitude diagram. Other sources with

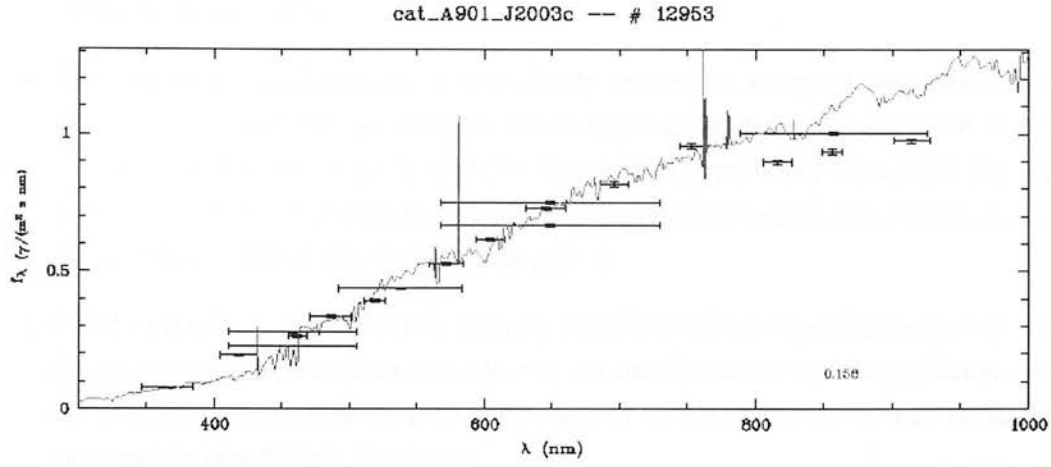

Figure 4.9: The COMBO-17 data and a z=0.158 galaxy template for optical source 12953, associated with X-ray source # 3. High levels of variability were observed in the B and R bands, which were reobserved over multiple runs, and which encompass the [OII] and [OIII] emission lines at this redshift, indicating that the galaxy could be at $z \sim 0.15$. Above 800nm the data and template do not match well as the illustrated template is not dust reddened - a bluer galaxy template with dust reddening would fit far better. It is possible, but by no means certain, that this is the correct redshift for this source.

similar properties but with optical spectra (in particular #79 and #24) are confirmed to be AGN by the lack of emission lines in their spectra. The COMBO-17 best fit galaxy template for this source is also an old red early-type galaxy with no emission lines, and the galaxy was detected in the NVSS (Condon et al. 1998) so is a radio source. It seems most likely that this source is a supercluster AGN.

- **# 53 - reject.** A soft, moderate luminosity X-ray source with two possible optical counterparts, both of which are 24μm sources but only one of which is in the supercluster. The non-supercluster source is twice as likely to be the match by position and luminosity only, and is also an optical quasar. Taking into account both the positions and classifications of the possible matches, the quasar is seven times less likely to be a random association, so this source is not considered to be a supercluster member.

- **# 71 - certain.** This source is securely identified with a supercluster galaxy which does not have a 2dF spectrum. A moderate X-ray luminosity and $f_X/f_R = 0.05$ could be caused by star formation or an AGN. However the high hardness ratio (0.53) makes star formation very unlikely, so this source is classified as a secure supercluster AGN.

- **# 79 - certain.** This source is securely identified as a supercluster galaxy. A moderate X-ray luminosity and low hardness ratio and f_X/f_R (-0.75 and 0.01) make this source

very similar to #37. However the optical spectrum is that of a red early-type galaxy, whose emission lines indicate at least 150 times too little star formation to account for the X-ray emission.

- **# 81 - certain.** The X-ray emission is clearly centred on a supercluster galaxy. The line ratios from the 2dF spectrum (taking an upper limit on the non detection of Hβ) clearly show that this source is an AGN. Despite being prominent, the [OII] line flux is still 12 times too low to account for the X-ray emission through star formation, and the spectrum is that of an red early-type galaxy.

- **# 104 - certain.** This source is securely identified with a supercluster galaxy. Although the optical line ratios can not rule out star formation due to confusion with Hβ absorption and emission, a hardness ratio of 0.95 and f_X/f_R of 0.22 make this an unambiguous AGN in the X-ray.

- **# 105 - certain.** This X-ray source is securely identified as a galaxy in the supercluster. A moderate X-ray luminosity, $f_X/f_R = 0.05$ and hardness ratio ~ 0 could be caused by star formation or an AGN. Again, star-formation is ruled out by the optical spectrum, which is a red early-type galaxy with no detectable emission lines.

- **# 119 - reject.** The X-ray emission clearly emanates from a galaxy in the supercluster. A hard (hardness ratio = 0.43) but moderate X-ray luminosity and low f_X/f_R appear to indicate an AGN or highly obscured star-burst. The optical spectrum is clearly a blue star-forming galaxy in the supercluster. However the observed [OII] flux is not enough to account for all of the X-ray emission through star-formation. To test whether this is due to a significant amount of dust extinction the Hβ/Hγ ratio was calculated, using the equivalent widths of the lines and the continuum flux density in the $\lambda_{cen} = 5710\mathring{A}$ narrow-band filter to calculate the flux from Hβ, and the mean flux densities in the $\lambda_{cen} = 5190\mathring{A}$ and $\lambda_{cen} = 4860\mathring{A}$ COMBO-17 bands to calculate the flux from Hγ. The ratio is 1.35 times lower than it should be, which can be accounted for by a E(B-V) dust extinction of 0.677 magnitudes. Accounting for this, the [OII] SFR is 43 $M_\odot$/yr, which agrees (within errors) with the X-ray SFR of 30 $M_\odot$/yr. The source is clearly a star-forming supercluster galaxy, so is removed from the sample.

- **# 127 - possible.** A hardness ratio of 0.25 indicates a probable AGN. This source has two possible optical counterparts, with the non-supercluster source being both ten times closer to the X-ray position and a quasar. Accounting for the number of QSOs in the sample (2074), compared to galaxies brighter than the possible supercluster host (263) gives very similar likelihood ratios for the sources. However, the spectrum of the supercluster source has [OII] and [OIII] emission lines, so it is a probable source of X-rays from star-formation or an AGN. Closer examination of the X-ray image finds tentative evidence of a blend of two sources, with an elongation in the

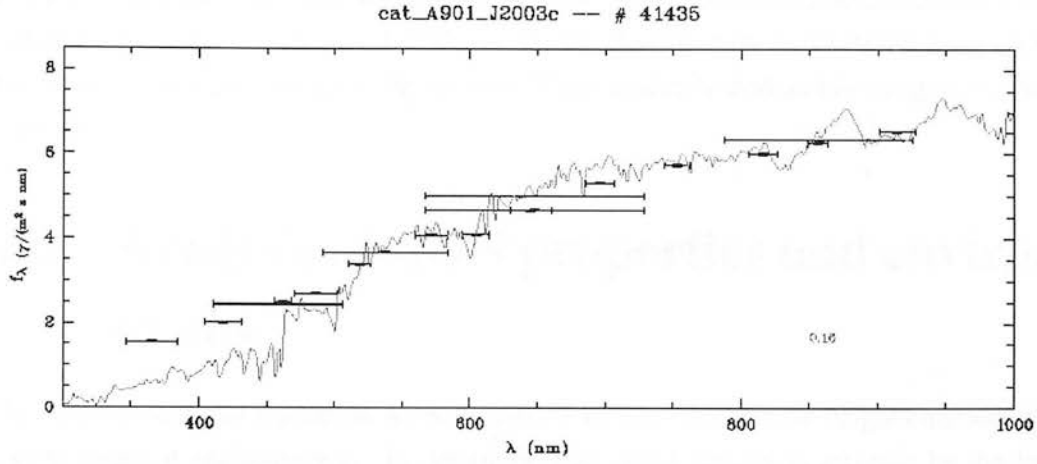

Figure 4.10: The COMBO-17 data and a z=0.16 template for optical source 41435, associated with X-ray source # 135. The template has been selected by eye as a best-guess early-type template at this redshift. Adding excess UV light from an obscured AGN would give a good fit, indicating that this source is likely to be in the supercluster.

direction of the supercluster galaxy - if this is the case, and $\sim$ 10% of the X-ray emission is from the supercluster galaxy, it could be caused by star-formation. If $\gtrsim$ 10% of the X-ray emission in this region is from the supercluster galaxy then it is likely to contain an AGN. This source is therefore retained as a possible supercluster AGN.

- **# 135 - certain.** This X-ray source is securely identified with a large red galaxy. It has $L_X = 1.55 \times 10^{44}$erg/cm^2/s, so must be an AGN. The initial COMBO-17 photometric redshift was 0.33, but the colours and position (a large red galaxy near the centre of A901a) indicate supercluster membership. A visual fit to a $z = 0.16$ red early-type galaxy template is excellent above 4000$\AA$ as shown in Figure 4.10. The discrepancy can be accounted for by adding a UV excess caused by the emission from the AGN.

- **# 139 - certain.** A hardness ratio of 1, [OIII]λ5007/H$\beta > 20$ and $L_X > 10^{42}$erg/cm^2/s make this a certain AGN, and it is unambiguously associated with a supercluster galaxy.

The final sample therefore consists of 11 certain supercluster AGN and 3 possible members. All of the AGN hosts appear to be early-type galaxies and some appear to be morphologically disturbed. Detailed study of the morphologies of the AGN hosts is beyond the scope of this work, and will be left until Hubble Space Telescope images of this field are obtained (scheduled for late 2005). It is worth noting that all of the supercluster AGN candidates are classed as galaxies in the COMBO-17 survey as the photometric method is not

sensitive to Seyfert-like AGN and obviously misses optically obscured AGN. In addition, of the 8 certain members with optical spectra only 5 have emission lines, and only 2 have emission line ratios which would lead to a secure classification as an AGN using optical data alone. This highlights again the need for X-ray studies to find and investigate the AGN population.

4.6 Analysis of AGN properties and environments

The 11 confirmed and 3 possible AGN in A901/2 are in a very diverse neighbourhood, with a wide range of environments. To determine how AGN activity is affected by the local environment it is first necessary to define a control sample of similar galaxies without an AGN. Comparing the environments of this control sample with the AGN hosts will reveal whether local or extended environment can affect AGN.

4.6.1 Properties of the AGN hosts

The supercluster sample contains 1240 galaxies, where all sources with $0.15 < z_{\rm phot} < 0.18$ and $m_{\rm R} \leq 24$ were identified as supercluster members. The large redshift range (the same as applied for the AGN in Section 4.5.3) allows for the errors in the photometric redshifts, and the magnitude cut removes faint sources, which have far less accurate photometric redshifts.

The colour-magnitude diagram for the supercluster is shown in Figure 4.11, with the supercluster AGN host galaxies indicated (it is important here to note that the R band magnitudes of the host galaxies are not significantly changed by the presence of an AGN, as can be seen directly from the 2dF spectra). It is intriguing that all of the AGN and possible AGN lie in bright ($m_{\rm R} < 20$) galaxies. The X-ray luminosity of the AGN, as indicated by the size of the symbols in Figure 4.11, shows that the lack of AGN in lower mass galaxies is not due to fainter X-ray AGN being found in optically fainter galaxies, which would lead to AGN in lower mass galaxies falling below the detection threshold. In fact the opposite is true - there is a trend towards more X-ray luminous AGN in optically fainter host galaxies. The inverse correlation between $m_{\rm R}$ and $\log(L_X)$ is significant at 92% using a Spearman rank test. This result is in contrast to that found by Pellegrini (2005), who found no correlation between L_X and M_{BH} in local AGN, but in addition to the A901/2 AGN being almost an order of magnitude brighter than the Pellegrini samples, they are also different due to their unusual environment. The possible effect of environment on accretion rate is discussed in Section 4.6.5.

To find out the range of accretion rates covered by this sample, $L_{\rm AGN}/L_{\rm eddington}$ was

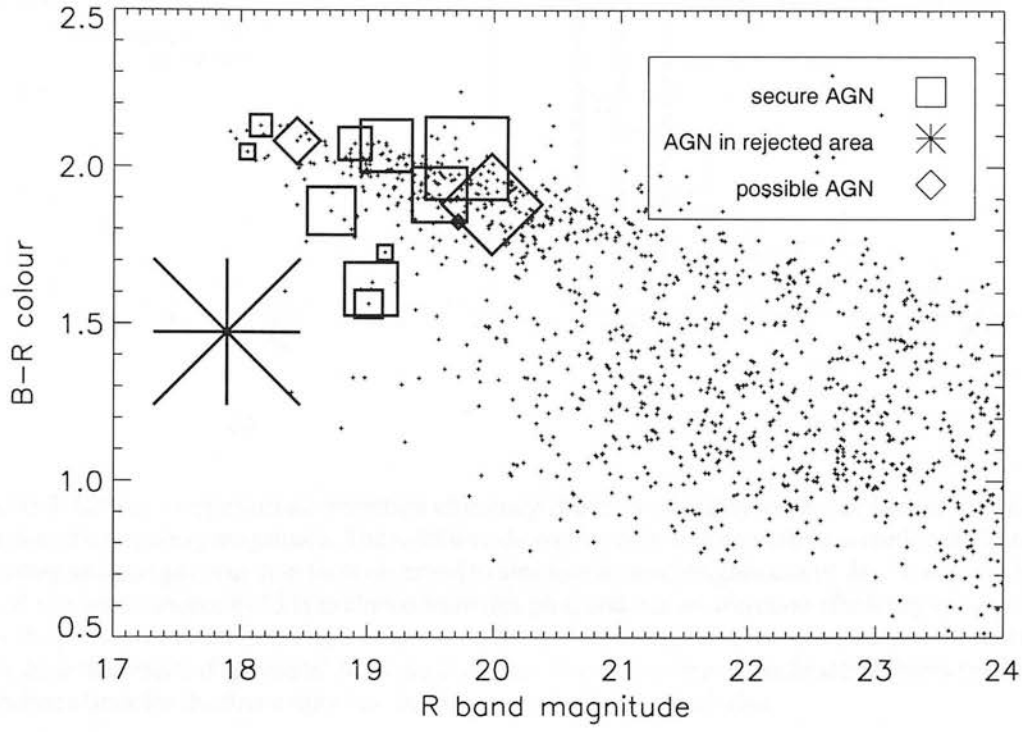

Figure 4.11: The colour-magnitude plot for all supercluster galaxies (small dots) and AGN hosts. The area of the AGN symbols is proportional to log(L_X(0.5-8keV)). The X-ray source #135 is marked with a star as it is not in the control area described in Section 4.6.1.

calculated for each AGN, where it was assumed that 10% of the AGN luminosity is emitted in the 0.5-8keV band. The relation $log(M_{BH}/M_{\odot}) = -0.5M_{\rm R} - 2.96$ of McLure and Dunlop (2002) was used to calculate the black hole mass from the rest frame R-band absolute magnitude ($M_{\rm R}$) given in the COMBO-17 catalogue (as derived from the galaxy template). The resulting plot (Figure 4.12(a), excluding the bright source #135), although crude due to the approximations made, shows a clear correlation between $m_{\rm R}$ and $L_X/L_{eddington}$. However, fainter galaxies may have undetected AGN with low accretion efficiencies, as these would be below the detection threshold, so this sample of AGN selected by X-ray luminosity is missing low mass galaxies with low efficiencies. It is clear that the brighter galaxies only have low accretion efficiencies, but this may also be due to the smaller number of bright galaxies. To calculate whether the lack of more efficient AGN in massive galaxies is due to the smaller sample size or a physical effect, we need to know the number of possible AGN hosts as a function of M_R.

To determine the proportion of galaxies with AGN and the properties of the AGN hosts it is necessary to define a control area in which the AGN could have been detected. To

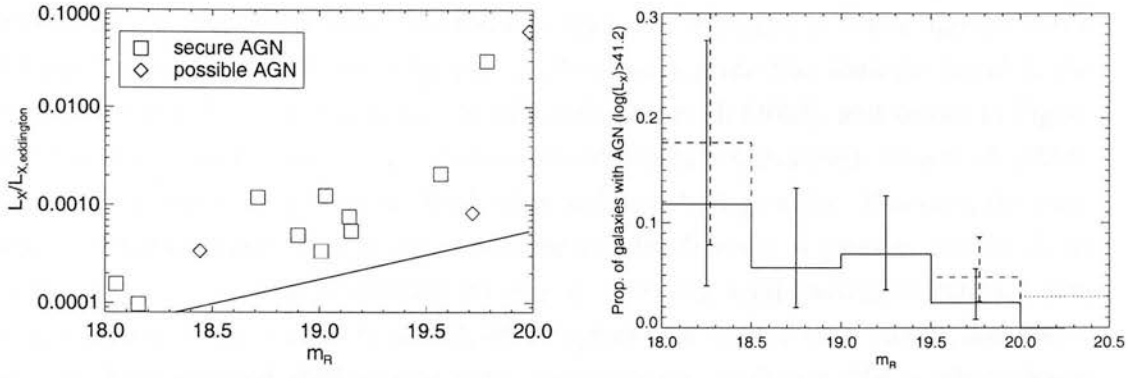

(a) (b)

Figure 4.12: (a) - Approximate accretion efficiency (fraction of eddington X-ray luminosity) as a function of host galaxy magnitude. The solid line shows the minimum detectable accretion efficiency assuming an average correction from observed to absolute R-band magnitudes of $M_{\rm R} = m_{\rm R} - 40.7$. The X-ray bright source #135 is excluded from this plot, and has an accretion efficiency of $\sim 30\%$. (b) - Proportion of AGN hosts as a function of X-ray luminosity, with 1σ error bars. The dashed lines show the results if 'possible' AGN are included. The dotted line in the final bin shows the 95% confidence limit for the first empty bin. Again source #135 is not included.

select the control area the COMBO-17 catalogue was cut to remove sources within $160''$ of the top and sides and $300''$ of the bottom of the image. This cut ensures the returned area is 97% covered by the X-ray image, and also ensures that the edge of the catalogue does not affect properties such as local density. In addition areas where AGN could not be detected due to extended or very bright X-ray emission were removed from the control area: three areas were deemed to be bright enough to obscure moderate luminosity AGN: a $30''$ circle around A901α, $67''$ around the AGN in A901a and $83''$ around A901b. The small changes in detection sensitivity due to emission from A902 and the SW group and the changes in PSF were not included as they only affect marginal detections and are not significant in a sample of this size. This cut also removes the AGN in A901a (#135) from the sample, which is necessary as it obscures possible AGN activity from all of the surrounding large galaxies so will bias the sample. In addition its accretion efficiency (30% of Eddington) and luminosity show that it is the only X-ray Type-I AGN in the sample. The control sample contains 911 supercluster galaxies, as 150 were removed in the edge cut and 179 were in regions where AGN could not be detected.

The number of AGN hosts in the supercluster can be directly compared to the number of possible host galaxies in the control sample area. The number of AGN per possible host galaxy is shown in Figure 4.12(b) for a range of host luminosities. When interpreting this plot it is important to note that this is a flux limited sample, and, as Figure 4.12(a)

shows, misses low efficiency AGN at fainter host magnitudes. All conclusions therefore relate to AGN in the supercluster with luminosity $L_X > 10^{41.2}$erg/sec. Despite the large error bars (1σ Poissonian error from Gehrels 1986, see Appendix A.1.4) it appears that a brighter galaxy is more likely to have an AGN above a given flux limit (as found in the optically selected $z < 0.3$ field sample of Kauffmann et al. (2003), and shown in Figure 1.5, but not the higher activity, $z > 0.5$ sample of Sánchez et al. 2004). Best et al. (2005) also find the same result for radio-loud AGN and their host galaxies. However, the error bars on Figure 4.12(b) show that it is possible that the fraction of galaxies hosting AGN with $L_X > 10^{41.2}$erg/sec is constant for $m_R < 19.5$. The total fraction of galaxies with $m_{\rm R} < 20$ hosting these AGN is 10/193, which agrees with Martini et al. (2002), who found a $\sim 5\%$ X-ray detected AGN fraction at the same magnitude limit in A2104, a galaxy cluster at z=0.154.

The lack of AGN with $L_X/L_{X,eddington} > 5 \times 10^{-4}$ and $m_R < 18.5$ is probably due to the lack of bright galaxies, rather than a tendency for more massive host galaxies to have lower efficiencies. There are only 17 galaxies in this field with $m_R < 18.5$ in which AGN activity could have been detected, and if the same fraction of galaxies have moderate accretion efficiencies as the $18.5 < m_R < 19.5$ sample ($\sim 6\%$), then only one $m_R < 18.5$ galaxy would be expected to have an AGN with $L_X/L_{X,eddington} > 5 \times 10^{-4}$. Similarly, the one secure AGN with efficiency > 0.01 only corresponds to $\sim 1\%$ of the galaxies in that 0.5 magnitude bin, and only ~ 1 galaxy with $m_R < 19.5$ would be expected to have accretion above this efficiency. It is plausible that there is no relationship between efficiency and host galaxy mass (for $m_{\rm R} < 20$) for the AGN in this sample. However this is not the case at fainter host magnitudes: there must be a significant decrease in the efficiency of any AGN in galaxies with $m_{\rm R} > 20$ as the number of supercluster galaxies is very large yet no AGN are observed above the X-ray flux limit.

4.6.2 Defining a control sample

To compare the AGN environments and properties, control samples were created, consisting of similar galaxies to the AGN hosts, where AGN activity could have been detected but was not found. Whereas a randomly selected control sample would contain many faint galaxies, it is instead preferable to define a control sample with a similar distribution of galaxy properties as the AGN hosts. Any difference between the AGN hosts' environments and the control sample environments would therefore be due to an environmental effect on AGN.

100 control samples were made, each consisting of 66 of the 193 supercluster galaxies in the control area which are not AGN hosts. These samples were selected at random such that there are equal numbers of galaxies in each 0.5 magnitude bin to replicate the distribution of AGN host magnitudes. This method ignores the apparent increase in the number of AGN

in brighter galaxies (Figure 4.12(b)) but given the small number of galaxies available it is a reasonable sample and should not affect any results significantly.

The 100 samples are identical at $m_{\rm R} < 18.5$, due to the small number of available galaxies, but at $18.5 < m_{\rm R} < 20$ different sets of galaxies were chosen, although the samples still have considerable overlap with each other. Each of the 100 control samples was compared to the AGN sample and the median statistic taken to reduce the errors. A Kolmogorov-Smirnov (K-S) test (to identify changes in the mean) and Kuiper test (a K-S test using Kuiper's statistic which is better at identifying changes in spread, see Appendix A.1.1) confirm that the control samples and AGN hosts are drawn from the same R-band magnitude distribution (at at least 56% confidence for the 'secure' AGN and 94% confidence if possible AGN are included).

The colour-magnitude diagram in Figure 4.11 also shows that at least three AGN hosts are significantly bluer than the colour-magnitude main sequence. K-S and Kuiper's tests on the deviation from the main sequence give 37% and 34% probabilities that the secure AGN hosts and control galaxies are drawn from the same distribution (increasing to $\sim 75\%$ when the possible AGN are added). This deviation is possibly significant, especially as similar results were found by Martini et al. (2002) for the cluster A2104, with a propensity for AGN hosts to be bluer than similar galaxies. This may be due to AGN light, or to star-formation or post star-formation light associated with the AGN, as found by Kauffmann et al. (2003) and Sánchez et al. (2004).

4.6.3 The local properties of galaxies around AGN

The local environment of the AGN was evaluated by considering all supercluster galaxies within $1.5'$ (250kpc at the supercluster redshift) of the AGN hosts, excluding the host itself. The properties investigated were; total luminosity, average B-R colour, and number of galaxies with $m_{\rm R} < X$ for a range of X. For each property the results for the AGN hosts and possible AGN hosts were compared to those of the 100 control samples, using a K-S test and Kuiper's test. Adding the 'possible' AGN is found to weaken any statistical differences found in most cases, probably indicating that some of these are not true matches, so unless stated only the 'secure' AGN were considered.

These tests indicate that there are no significant differences between the AGN and the control sample in terms of the total ($m_{\rm R} < 24$) number (at least at the 31% confidence level, from Kuiper's test), total luminosity (at 39%) or average colour (at 30%, from the K-S test) of galaxies within $1.5'$.

The number of local ($< 1.5'$) galaxies with $m_{\rm R} < 20$, 22 and 24 is shown for the control sample and secure AGN in Figure 4.13. There is a statistically significant difference between the control samples and AGN hosts in the second plot, which shows the number of local galaxies with $m_{\rm R} < 22$. The AGN hosts live preferentially in areas of moderate

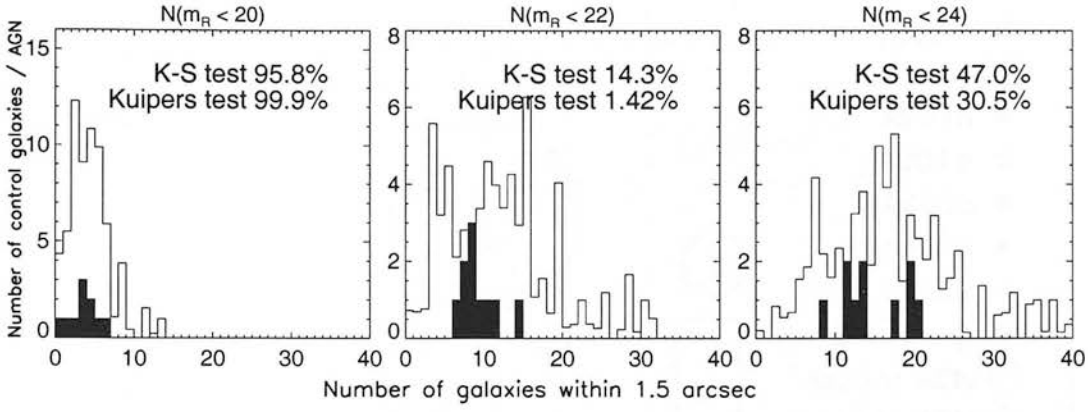

Figure 4.13: The number of galaxies within $1.5'$ of the control samples (mean value, empty histograms) and AGN hosts (filled histograms). Histograms are shown for the number of nearby galaxies with $m_{\rm R} < 20$, $m_{\rm R} < 22$ and $m_{\rm R} < 24$. The statistical deviation of the AGN hosts from the control samples is given using the K-S and Kuiper's tests.

density, compared to other similar galaxies, and do not exist in areas of very high or very low density, such as field environments and near cluster centres (the densest environments are excluded due to the extended X-ray emission). The same pattern is seen for the $m_{\rm R} < 24$ plot, but the statistical strength of the signal is diluted, so it appears that the effect is dominated by moderately large galaxies (the lack of signal for $m_{\rm R} < 20$ galaxies could be due to the low numbers of galaxies).

In addition, to investigate large-scale and very local effects, the same properties were evaluated within $3.0'$ and $0.5'$. No significant deviations were found between the AGN and control samples within $0.5'$ or $3.0'$ for any of the investigated properties. This result is inconsistent very local effects, such as mergers, and also large scale effects. (To check for mergers the distance to the nearest supercluster neighbour was also compared and the AGN and control samples were not significantly different).

4.6.4 The types of environments which contain AGN

To better classify the environments within A901/2, areas which fell into a clear environmental category were selected as shown in Figure 4.14. Cluster and group regions are defined by circles of $1'$ radius, centred on the brightest cluster galaxy. As A902 does not have a clear centre, a radius of $2'$ was used to include the whole cluster. For the rich cluster A901a and the SW group a second region out to $3'$ radius is considered, marking the cluster and group edge environments. The filament region, with a large number of blue galaxies, is marked with a rectangle.

It is found that these environments can be well separated on a plot of local galaxy number density ($m_{\rm R} < 24$) and local mean B-R colour (as defined in Section 4.6.3). The

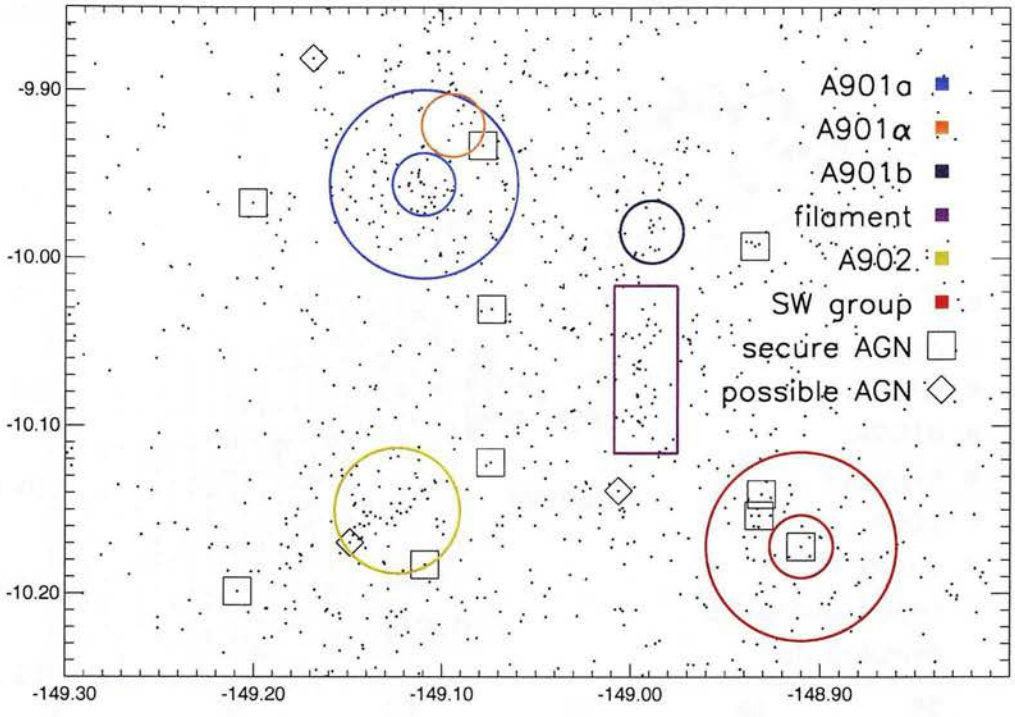

Figure 4.14: Regions with a clear environmental category in the supercluster (the X axis is RA and Y axis is Declination). Supercluster galaxies are marked with a dot, and for comparison the AGN are also marked.

galaxies defined in the regions of Figure 4.14 are shown in a number density vs. mean colour plot in Figure 4.15. By plotting local colour, rather than deviation from the colour-magnitude main sequence, this plot also has a mass dependence, as the bluer galaxies are generally less massive.

The clusters all lie on a local number density and local colour 'main sequence', whereas the filament is considerably bluer. Locations in this plane can therefore be used as a means of defining the local environment for other supercluster galaxies. The regions are separated as shown on the plot: a line parallel to the 'main sequence' is used to mark the boundary between cluster and filament-like environments, and a line perpendicular to this marks the beginning of group-like environments. The edges of clusters are included in the group-like environment category, and to help distinguish between edges and groups the category is split into red group-like and blue group-like environments, where the edges of clusters are generally in redder environments as they are influenced by the red cluster galaxies. The distinction between blue group-like and red group-like environments is not very clear, and so it was decided to define two samples of approximately equal size.

Figure 4.16 shows the distribution of supercluster galaxies in each type of environment -

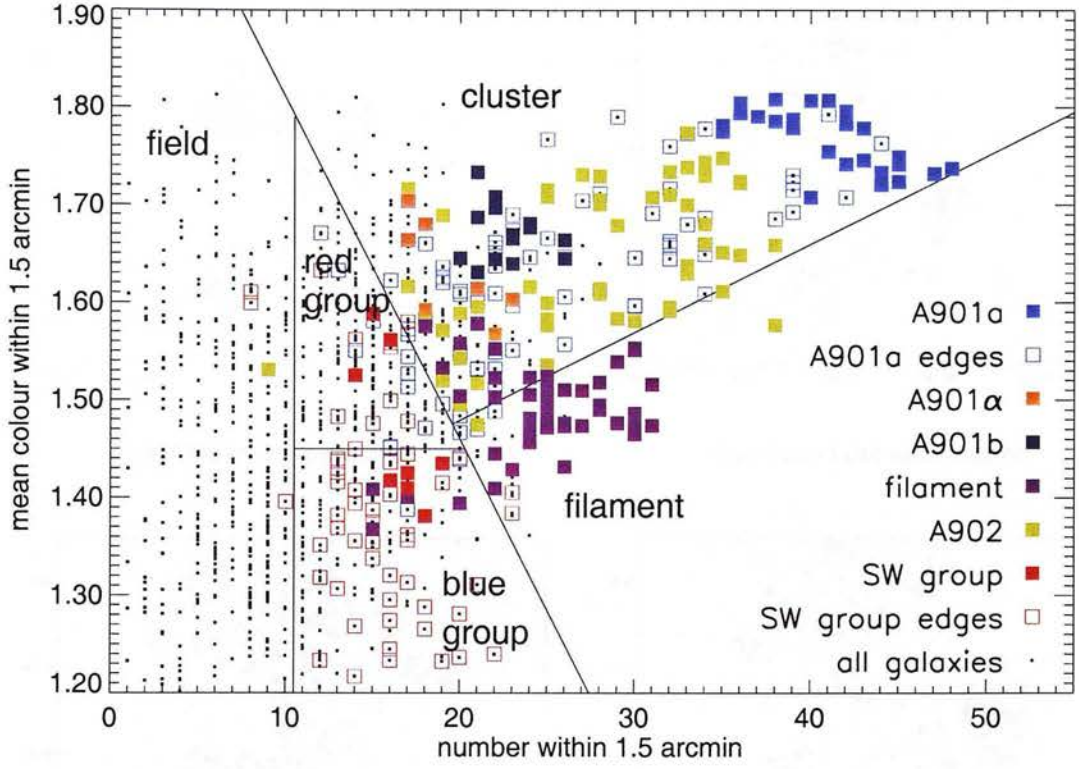

Figure 4.15: The local number density (counting all galaxies with $m_R < 24$) and mean local B-R colour for galaxies in well defined environments. The plot is split into five regions corresponding to different types of environment. A901a and the SW group are split into inner and outer regions, marked by the concentric circles, and the galaxies in A901α are excluded from the outer regions of A901a.

it is clear that local colour and density are indeed excellent at separating environments. This classification by local environment rather than by arbitrarily defined region is important - for example, although some galaxies in the cluster-like environment (Figure 4.16(a)) are not actually in the defined clusters, the galaxy will experience the same local effects as a cluster galaxy. In addition this method identifies regions such as small groups which are difficult to define by eye. It is worth noting that the same analysis for local density alone is far less successful, with mixing between filaments and cluster cores, and also groups and smaller clusters.

The secure AGN all lie within or very close to the red and blue group-like environments (Figure 4.17). This is very different from the distribution of the control samples, where a significant proportion lie in filament or cluster-like environments, as well as in the field. In particular the AGN hosts in slightly higher density areas (15 to 20 local galaxies) are all found in bluer areas, whereas in the control sample the average local colour at this density is far redder. A two-dimensional K-S test (see Appendix A.1.2) in the local number vs local

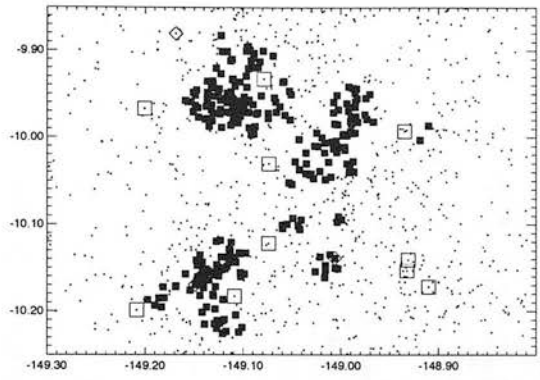

(a) Cluster-like environments

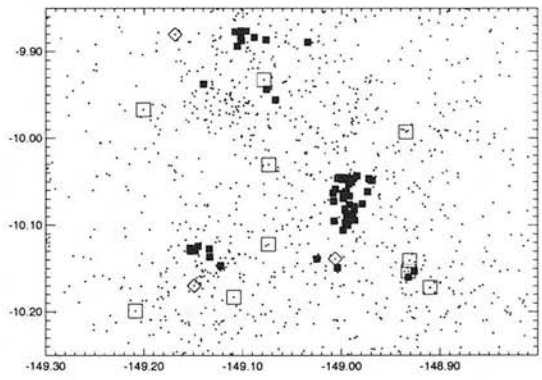

(b) Filament-like environments

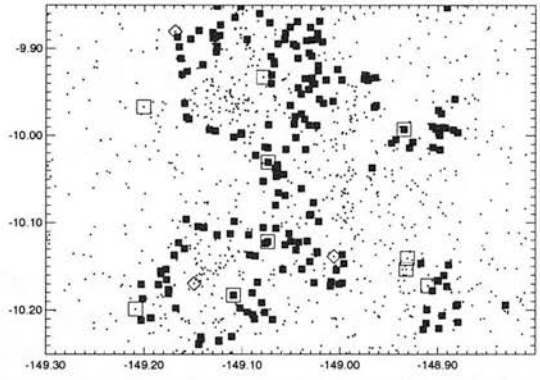

(c) Red Group-like environments

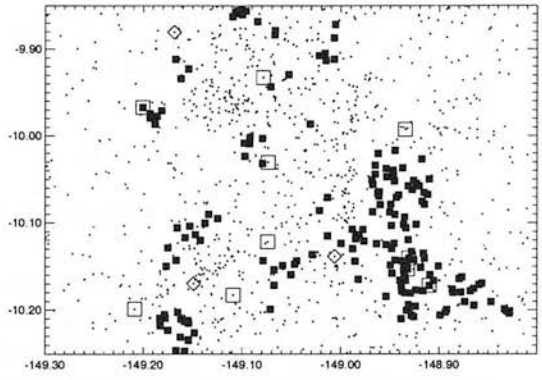

(d) Blue Group-like environments

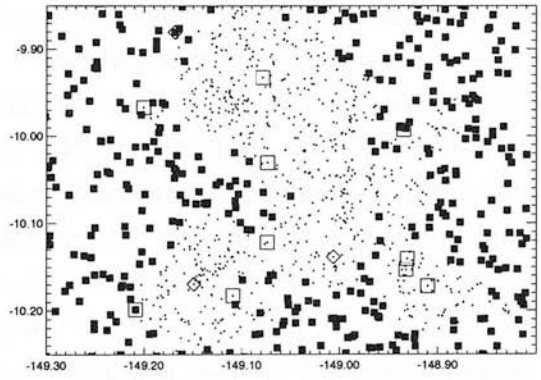

(e) Field-like environments

Figure 4.16: Supercluster galaxies segregated according to environment, as defined in Figure 4.15. The filled squares show galaxies in each type of environment, and dots show other supercluster galaxies. Secure and possible AGN are marked with open squares and diamonds respectively.

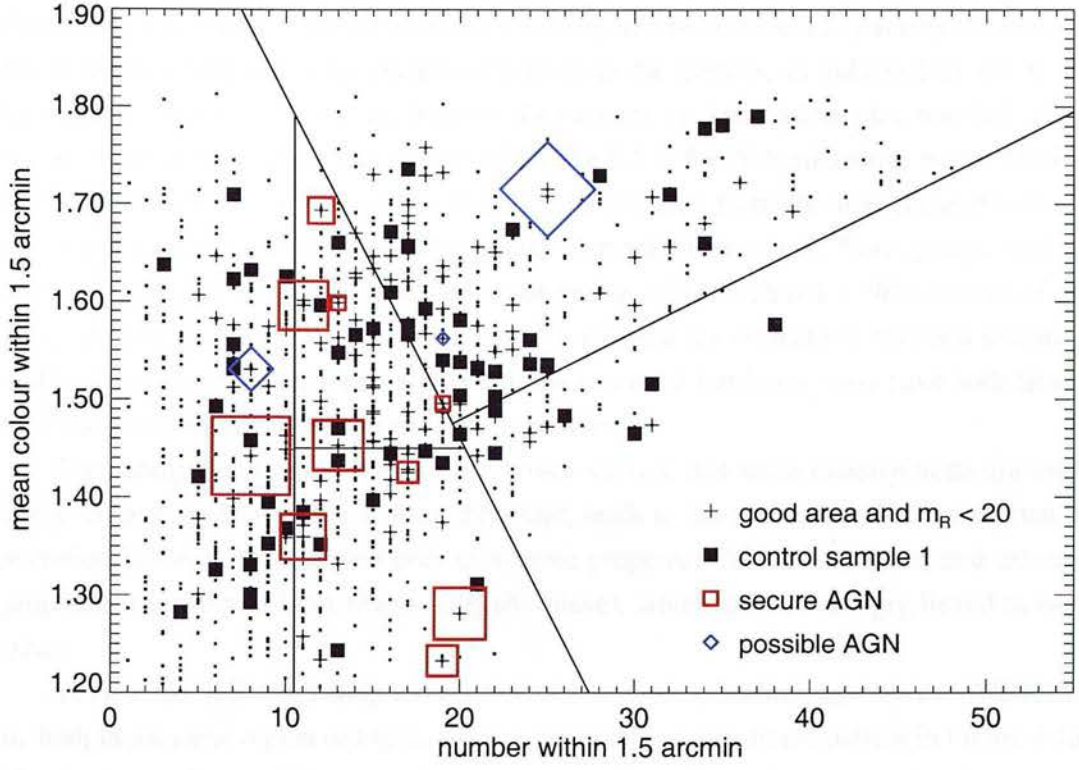

Figure 4.17: Local number density and local mean colour for the AGN and one control sample, with the regions defined in Figure 4.15. The dots mark all supercluster galaxies, and the crosses and filled squares those which are as bright as the AGN hosts and in regions where AGN emission could be detected (the selected control sample and other control galaxies). The size of the AGN symbols is proportional to $\mathrm{Log}(L_X)$.

mean colour plane gives a probability of only 3.3% that the secure AGN were drawn from the control samples. Comparing with the control samples in each region separately, the probability that the AGN are drawn purely from the red and blue group-like environments is 18%, compared to $< 0.1\%$ for the other environments. In addition a Kuiper's test on the deviation from the line perpendicular to the local colour / density 'main sequence' gives a probability of 4.0% that the AGN hosts are drawn from the same population as the control samples (compared to 30% for deviation in density only). We can therefore assert (at a $>$ 95% confidence level) that the AGN are affected by the environment, and favour moderate density red or blue environments or slightly denser environments if the local environment is also bluer.

4.6.5 Linking X-ray properties to environments

Further evidence for the link between AGN activity and environment is given by the relation between environment and the amount of activity in the nucleus, as indicated by the X-ray luminosity. Figure 4.17 shows the local number density vs. local colour plot, now indicating the positions of the control sample and AGN. The $0.5 - 8$ keV luminosities of the AGN in terms of the size of their symbols. Plotting the distance from the line perpendicular to the 'main sequence', that divides cluster and filament environments from groups, against $\log(L_X)$ (Figure 4.18) gives a distribution for secure AGN that has a $> 98\%$ chance of not being random (using a Spearman rank test). In contrast the correlation between deviation and host luminosity is far weaker, although the two most luminous hosts have both fainter AGN and are towards more cluster-like environments.

Comparing this result to Figure 4.12, which showed that more massive hosts are more likely to have an AGN above a given flux limit, leads to the conclusion that the amount of accretion in the AGN is related both to internal properties (black hole mass) and external properties (position in local colour - density plane), which are not strongly linked to each other.

As an aside, it is interesting to note that of the three 'possible' supercluster AGN, two lie both in the same region of Figure 4.17 as the AGN and also fit the pattern in Figure 4.18. The third is both in a different environment and with an X-ray luminosity that does not at all fit with Figure 4.18. This is X-ray source #3, which had a secure optical counterpart but unsure photometric redshift. It is worth postulating that source #3 is not a supercluster AGN, but that the other two 'possible' AGN are real, which would then bolster the results drawn from the sure AGN sample.

4.7 Conclusions

4.7.1 AGN host galaxies and properties

This sample consists of 11 AGN with $L_{X,(0.5-8keV)} \gtrsim 10^{41.2}$erg/sec which have host galaxies in the supercluster A901/2. Three additional sources, which may be supercluster AGN, are also investigated. The properties of the AGN host galaxies and a comparison with the galaxies without AGN led to the following results;

- The AGN host galaxies are all massive, early-type galaxies, with $m_R < 20$. Although most of the host galaxies lie on the cluster colour-magnitude main sequence, a significant fraction are bluer, possibly due to emission from the AGN. Of the 8 AGN with optical spectra, only 2 would have been identified as AGN from optical data alone.

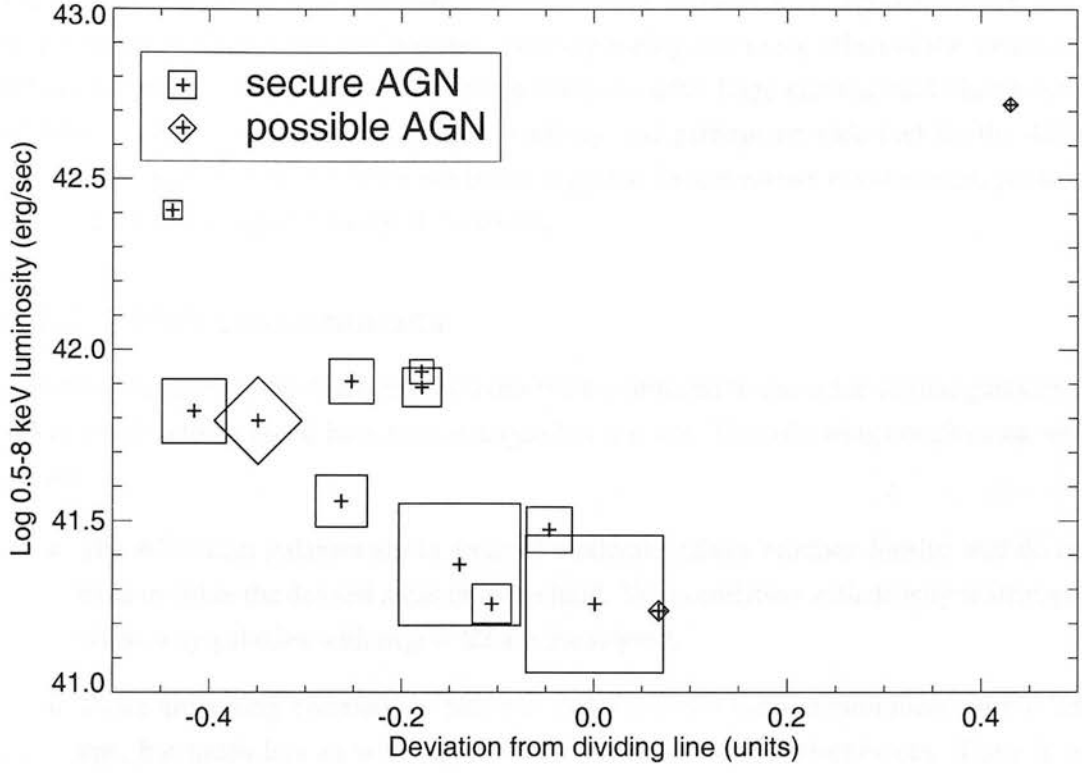

Figure 4.18: X-ray luminosity against deviation from the local colour - number dividing line. The deviation is in physical distance in Figure 4.17 (such that one unit is 1 magnitude in B-R colour or 50 galaxies in density, or combinations of the two). Again the squares are secure AGN and the diamonds possible AGN. The symbol sizes are scaled such that the area is proportional to the optical luminosity of the host galaxy.

- There is a significant inverse correlation between the AGN luminosity and the mass of the host galaxies, with the brightest AGN lying in galaxies with $m_R \sim 20$.
- It appears that more massive galaxies are more likely to host an AGN above this flux limit. However, when the AGN accretion is measured in terms of luminosity per unit black hole mass, the small sample size and flux limits mean that that no clear correlation can be seen, and it is plausible that the accretion efficiency is unrelated to the galaxy luminosity.

These results are generally unsurprising, with the exception of the inverse correlation between L_X and m_R. The preference for optically detected AGN to lie in massive galaxies, and the increase with optical host mass, is well known (see Figure 1.5 and the discussion in Chapter 1). The fraction of galaxies hosting AGN is comparable to the Martini et al. (2002) result for the cluster A2104.

The correlation between L_X and m_R is the opposite of what might be expected – galaxies with smaller bulges, and hence smaller black holes, actually have higher accretion rates, as measured by their X-ray luminosities. This is possibly due to the effect of the supercluster environment. Smaller galaxies are more likely to suffer large gravitational disturbances which can affect the central regions of the galaxy, and perhaps provide fuel for the AGN. This result suggests that the AGN are being triggered by the cluster environment, possibly due to the increased gravitational disturbance.

4.7.2 AGN environments

The environments of the AGN host galaxies were compared to those for similar galaxies in which AGN activity could have been detected but was not. The following conclusions were drawn;

- The AGN host galaxies are in areas of moderate galaxy number density, and do not exist in either the densest areas or in the field. The correlation with density is strongest when only galaxies with $m_R < 22$ are considered.
- There are strong correlations between AGN and the local environment within 250 kpc, but much less so with larger scale or smaller scale environments. There is no correlation with distance to the nearest neighbour.
- The environments in A901/2 can be split according to local galaxy number density and local mean B-R colour (which also traces mass as smaller galaxies are bluer). The AGN host galaxies lie in areas of moderate density, or slightly higher density and bluer colour, similar to cluster outskirts and groups. Galaxies in cluster-like environments, the blue filament and the field are less likely to host AGN. No AGN are found in areas with ~ 20 nearby galaxies but red colours, such as the centres of small clusters.
- The X-ray luminosity of the AGN is linked to the environment, with more luminous AGN being found in less cluster-like environments (as measured by distance along the local density – local colour main sequence shown in Figure 4.15).

It is clear from these results that the AGN are affected by their environment. The lack of AGN in low density regions shows that the AGN activity is enhanced relative to the field, and the lack of AGN in the highest density regions shows that this enhancement is followed by either suppression or a return to the field values. The enhancement occurs in areas of moderate density, but also in slightly denser areas which are dominated by bluer galaxies. There are two possible interpretations for this – either the bluer mean colour indicates a higher level of activity in the surrounding galaxies, or it shows that the local environment is dominated by smaller galaxies. The first interpretation agrees with the results of Coldwell

and Lambas (2003), who find that optically identified AGN lie in regions containing more emission line galaxies. Martini et al. (2002) find that their AGN hosts have higher velocity dispersions than normal cluster galaxies, indicating that they have recently joined the cluster, and this would explain the lack of AGN in red regions with moderate galaxy density ($\sim$ 20 nearby galaxies), such as small clusters, compared to bluer areas of the same galaxy density.

If the bluer environments of some AGN are due to a larger number of small galaxies then it appears that the same number density of large galaxies is less likely to trigger an AGN. This would suggest minor mergers with small galaxies as the trigger for AGN activity. Adding a third dimension of local mean m_{R} to this analysis may help to resolve this issue, but the current sample is considered too small for this analysis.

If, on the other hand, the bluer environments of some AGN are due to areas with enhanced star-formation, it suggests that the same processes that trigger star-formation also trigger AGN activity. However, the correlations between star-formation and density show that star-formation is suppressed in cluster cores, rather than triggered in cluster outskirts (see Section 1.3.2). The dusty star-forming galaxies found by Wolf et al. (2005) show that activity can be triggered in medium density environments. Of the 10 secure AGN hosts (excluding the very bright AGN, which is significantly contaminated with AGN optical light) the fraction of old red, dusty star-forming and blue host galaxies (as defined by Wolf et al., see Section 1.3.2) are 0.5, 0.2 and 0.3, compared to fractions in the intermediate density galaxy population of $\sim$ 0.54, $\sim$ 0.26 and $\sim$ 0.20 (see Figure 1.4). There is therefore no propensity for AGN to reside in galaxies of any particular type. Also no correlation was found between the host type and AGN luminosity, AGN position or local density. The transformation processes which create the dusty red population (probably either minor mergers or gravitational disruption) could also cause AGN activity, but the two populations do not appear to be linked directly.

The correlation between environment and L_X is more tenuous, and with a sample this small we can only postulate as to the possible links between luminosity and extended environment. From Figure 4.18 it appears that AGN in less cluster-like environments have higher X-ray luminosities. If this is true in general then it may be that more luminous AGN are easier to trigger: if the more luminous AGN are in galaxies with a large amount of gas in the central regions, it would require a smaller gravitational instability to start the fuel falling towards the black hole (possibly via central star-formation). In contrast, galaxies which have less gas in the central regions require a larger degree of disruption and will have lower accretion rates. A second possibility is that galaxies loose their gas gradually on joining a cluster environment. The increased gravitational disturbance in denser environments could therefore trigger AGN, but galaxies in denser regions would have less remaining gas and hence lower X-ray luminosities.

In conclusion, it appears that AGN activity is triggered in moderate density environments, which are often bluer than expected, similar to (but not limited to) cluster outskirts and blue groups. This evidence shows that the properties of cluster AGN are significantly different to those in the field, and indicates that this is due to the gravitational disturbance caused by the environment.

CHAPTER 5

Conclusions and Future Work

This Thesis presents two very different studies of AGN in the densest regions of the universe, which give very similar results. In the first study the distribution of X-ray point sources in Chandra fields containing galaxy clusters was compared statistically to the expected distribution, calculated from blank fields, in order to determine the number and position of cluster AGN. It was found that AGN are suppressed in the centres of galaxy clusters, and possibly triggered on the outskirts of the cluster. The second study looked at the distribution of 11 X-ray detected and optically confirmed AGN in the supercluster A901/2 ($z \sim 0.17$). The AGN were preferentially found in areas of moderate density, avoiding both the field and the cluster cores, showing that they are triggered in moderate density environments and either suppressed in denser regions, or return to the low level of activity found in the field. Combining the results of these studies leads to the conclusion that AGN are triggered by moderate density environments, and suppressed in the densest environments. The suppression in cluster cores is in agreement with the recent optical AGN samples of Coldwell et al. (2002) and Kauffmann et al. (2004), but there is no evidence for an increase in AGN activity in moderate density regions in these studies.

The AGN activity appears to be affected by the local ($\sim$ 250 kpc) rather than cluster-scale ($\sim$ 1 Mpc) environment, as evidenced by the strong correlation between AGN and local properties in A901/2. This is backed up by the Chandra statistical study, as the number, luminosity and distribution of AGN in a cluster is not a strong function of cluster mass, apart from the expected increase in number due to the extra galaxies in more massive clusters. This is similar to the results seen for the fraction of star-forming galaxies, which is found to be dependent on local galaxy density, but not on the general cluster properties (Gómez et al. 2003, Lewis et al. 2002).

Both of the studies presented here also indicate that AGN activity is increased in more

'active' environments. A901/2 would be classified in the Chandra study as a 'disturbed' system, with an X-ray morphology indicating a merging group or cluster. The Chandra study shows that more X-ray point sources are found in such 'disturbed' systems compared to 'relaxed' clusters, and that these are found at cluster-centric distances similar to the distance to the disturbance. These could be massive star-forming galaxies or AGN which are triggered in the merging group or cluster. The results from the A901/2 study indicate that the majority of such X-ray emitting galaxies are not star-forming (11/12 supercluster sources are AGN), and that some of these AGN are indeed found in the small groups associated with the supercluster. The AGN are preferentially found in environments such as small groups and cluster outskirts (which are moderate density, or slightly higher density and blue), and are not found in environments such as small clusters (with the same density as groups, but far more red galaxies). These results show that AGN activity is linked with infalling groups as well as the outskirts of galaxy clusters.

The correlation between AGN activity and areas with more bluer galaxies in A901/2 may be an observation of the link between AGN and areas with more emission line galaxies seen by Coldwell and Lambas (2003), and the links between higher fractions of blue galaxies and faint radio AGN (Dwarakanath and Owen 1999). Combining this result with the suppression in the cluster cores suggests that AGN suppression may be linked with the suppression of star-formation in denser regions (see Section 1.3.2). Although the AGN hosts in A901/2 do not correspond directly to star-forming or post-starforming galaxies, the regions in which they are found suggest that the same processes, such as the removal of gas by galaxy-galaxy interactions, may be responsible for truncating both types of activity. Unlike the AGN, there is no evidence that normal star-forming galaxies are triggered on the outskirts of clusters. However, like the AGN, the dusty star-forming galaxies found by Wolf et al. (2005) only exist in areas of moderate density. Again, although these galaxies are not more likely to be AGN hosts, both populations are triggered by joining moderate density regions, and the same physical processes may be responsible for both effects.

Finally, it is clear from the Chandra study that the evolution of AGN in clusters is not the same as that for field AGN, and that the suppression seen in cluster cores at low redshift is not seen at $z > 1$. In addition, in moderately high redshift clusters ($z > 0.5$) AGN are far more prevalent than at lower redshift, and are found at far higher clustercentric distances. Determining the reasons for the faster evolution of the number of AGN in clusters than the field, and for the evolution of the environmental dependence of AGN activity, will require further, more detailed studies of cluster and supercluster AGN and their host galaxies.

5.1 Future projects

5.1.1 Improvements to the current studies

The current study of AGN in Chandra observations of galaxy clusters uses data from the Chandra archive, and all good cluster observations with published redshifts > 0.1 have been analysed (see Section 2.2). This study can be extended as more observations become public (~ 4 per month), and as redshifts are published for the ~ 50 clusters which have been observed but have no published redshift (in particular for the MACS sample of galaxy clusters, Ebeling et al. 2001a). This will increase the statistical significance of these results, and hopefully fill in some of the gaps in the cluster luminosity - redshift plane (Figure 3.9). In particular, there is a deficit in the current sample of low to moderate luminosity clusters with $z \sim 0.3$, and of high redshift ($z > 1$) cluster observations.

A further enhancement to the current studies would be to greatly improve the comparison with the optical cluster galaxy population. At present the conclusion that AGN are suppressed (on average, over all radii) in galaxy clusters is made assuming that the field X-ray luminosity function is produced by galaxies with $L > L_*$, and then calculating the expected number of sources per cluster galaxy $> L_*$ if the probability of being an X-ray source is the same. This shows that there is suppression if clusters on average contain > 5 galaxies $> L_*$ (see Section 3.5). Using current large surveys, this analysis can be significantly improved upon: optical follow up of X-ray surveys such as the ChaMP (Kim et al. 2004a) will allow a more accurate determination of the fraction and luminosity of X-ray sources in the field as a function of host galaxy luminosity. In addition, comparing the optical galaxies in the Sloan Digital Sky Survey (SDSS) with the cluster X-ray luminosity from the ROSAT All Sky Survey for a range of clusters will give a relationship between cluster X-ray luminosity and the number of bright galaxies. This can be compared to the cluster sample to determine the number of AGN per cluster galaxy at a given host luminosity, and compare it to the value in the field.

The radial distribution of galaxies in the SDSS as a function of cluster X-ray luminosity can also be calculated. This will give a definitive answer to the question of whether AGN are triggered on the cluster outskirts, as the radial distribution of the AGN can be compared to that of the galaxies to find the fraction of galaxies hosting AGN as a function of radius. Furthermore, it will allow a far more detailed interpretation of the number and radial distribution of AGN as a function of cluster luminosity, as at present this analysis is based on the assumption that the number of galaxies and typical radius of a cluster scales with X-ray luminosity according to simple theoretical cluster scaling relations (see Section 3.9).

Finally, the analysis of the Chandra Log N($> S$) - Log S distributions for the cluster fields can also be improved by using a more accurate lensing correction, as described in Section 2.6.13.

5.1.2 Optical observations of a subsample of clusters

The results presented in this thesis give strong evidence for the interaction between AGN and their extended environment, but, with the exception of the small sample of AGN in A901/2, are limited to statistical analysis. To understand the effect of the cluster environment on AGN in more detail it is essential to determine exactly how many AGN lie in each cluster, and their positions and properties.

The sample of X-ray sources in the Chandra cluster fields provides an excellent basis for such a study into the properties of individual AGN in these clusters. Optical photometric or spectroscopic redshifts can identify which AGN lie in the clusters, so that the actual number of AGN per cluster can be determined, and the actual radial and luminosity distributions of the AGN can be found. This will allow the results of this Chandra statistical study to be verified, and significantly reduce the errors due to field-to-field variance. It will also show whether the results of this study are enhanced or biased by massive star-forming galaxies. The luminosities and hardness ratios of the cluster AGN can be found and compared to typical values for field AGN, to determine whether the cluster environment affects the properties of AGN.

To this end, a sub-sample of 13 clusters with $0.22 < z < 0.4$ have been observed with the Wide Field Camera on the Isaac Newton Telescope (INT) in four bands[1]. This subsample is selected at moderate redshift so that the clusters contain a significant number of AGN and the Chandra images probe to > 3 Mpc from the cluster centres, but also the clusters are close enough that a significant number of cluster galaxies can be detected in an observation with a moderate exposure time. These data will enable cluster members less than 4 magnitudes fainter than a typical brightest cluster galaxy to be selected in each field. As most AGN hosts are above this magnitude, and have typical colours of cluster ellipticals (or slightly bluer, as shown in the A901/2 study) this will allow the cluster AGN to be identified. In addition, the photometric redshifts will enable the cluster richness and local projected galaxy density around the AGN to be evaluated.

One of the key questions raised by this thesis is whether the AGN are actually triggered on the outskirts of clusters, as much of the evidence presented here suggests, as well as being suppressed in the central regions. Using the cluster galaxies identified from the photometric data the fraction of moderate luminosity galaxies that host AGN, as a function of radius and local density, will be evaluated on a cluster by cluster basis. Comparing this value to that found in field samples will solve the issue of whether AGN are triggered by denser environments, and whether this is a function of local or global properties. The results from the small sample of AGN in A901/2 can also be confirmed or disproved by the photometric data; in particular the lack of a link between the distance to the nearest neighbour and AGN

[1]The Harris B and V and Sloan-Gunn r' and i' filters were used, giving three bands above and one band below the 4000Å break for most clusters.

activity, and the correlation between local colour and AGN activity, can be investigated for galaxy clusters in general.

Martini et al. (2002) find evidence that cluster galaxies in A2104 with AGN have higher peculiar velocities than non-AGN hosts, suggesting that they have recently joined the cluster. To test whether cluster AGN hosts in general have a higher velocity dispersion than expected it is necessary to obtain spectroscopic redshifts for galaxies and AGN hosts in the cluster. Spectroscopic data can also identify cluster host galaxies for Type 1 AGN, which have unusual colours due to the AGN emission. Multi-object spectroscopy of the cluster AGN and other large cluster galaxies identified through the photometric data will show whether there is a significant offset between the cluster population and AGN hosts, and in particular whether the AGN hosts have higher peculiar velocities than other galaxies in similar density environments.

5.1.3 Investigating the host galaxies of cluster AGN

It is important to know what sort of galaxies in the cluster have AGN activity, so that the mechanisms for fuelling the AGN can be determined. It appears that AGN in general are linked to post-starforming galaxies, and it is possible that the suppression of star-formation and morphological transformations of galaxies in clusters may be related to the presence of AGN. This can be investigated using deep optical imaging and spectroscopy which will provide details of the properties of the AGN hosts. The study of AGN in A901/2 suggests that less massive galaxies tend to have higher X-ray luminosities; further optical studies, such as the INT data already obtained for $z \sim 0.3$ clusters, will show whether this result is true of cluster AGN in general. In addition deep Hubble Space Telescope images of A901/2, to be taken in late 2005 [P.I. Meghan Gray], will show whether the supercluster AGN hosts have undergone, or are undergoing, morphological disturbance (indicated by the detection of minor mergers or asymmetric profiles), or have features such as stellar bars, and whether this is atypical for cluster galaxies in similar environments.

5.1.4 Extending the supercluster sample

A picture is starting to emerge of how AGN are affected by galaxy density, but if it is gravitational disturbance that changes AGN activity then both the X-ray emitting intra-cluster medium and the dark matter may play a crucial role, as they dominate the large scale gravitational potential. Distinguishing between the roles of the different constituents of clusters and superclusters will help to determine whether ram-pressure stripping, mergers, or strangulation and suffocation affect AGN. The study of AGN in the well studied supercluster A901/2 has highlighted the advantages of studying superclusters rather than galaxy clusters, and shown that the dark matter, galaxy density and X-ray gas do not precisely trace each other. The A901/2 supercluster does not contain enough AGN to separate the effects

of the different supercluster components, but further studies of AGN in superclusters may be able to determine whether there are any links between the dark matter, or X-ray gas, distributions and the positions of the AGN. In the short term it is feasible to extend the study of AGN in superclusters via Chandra and XMM images of well studied superclusters such as A851 (z=0.4) and CL1604+43 (z=0.9), which have extensive archival optical observations. Using these data, and the combination of optical and X-ray data for some of the cluster sample, the dependence of AGN activity on the galaxy density and the X-ray gas will be able to be determined. Further superclusters can be studied with dedicated optical observations, and in the longer term, as dark matter profiles for superclusters and clusters become available, the dependence of AGN activity on the dark matter distribution will also be able to be found.

5.1.5 Investigating cluster AGN at $z > 1$

Finally, the epoch of highest X-ray AGN activity is at $z \gtrsim 1$, and the studies presented here show a striking increase in the number of moderate luminosity AGN in high redshift galaxy clusters, with evolution to the present time that is far larger than that in the field. It may be the case that AGN activity is higher in galaxy clusters than the field at $z \sim 1$, and that the lack of AGN in the cores of nearby clusters is due to the fuel being used up in the past. At present the evolution of AGN as a function of environment is not well defined, and although this study presents some evidence for a faster evolution, it is necessary to investigate high redshift clusters in far more detail in order to understand how the AGN population evolves in different environments. This will become an achievable goal in the next two years with the publication of major catalogues of X-ray detected and optically confirmed galaxy clusters from ongoing dedicated (Valtchanov et al. 2004) and archival (Romer et al. 2001) XMM surveys. Deep Chandra images and optical spectroscopy of the richest of these clusters will determine whether the evolution of AGN is faster in denser environments, and whether the feedback from AGN can be large enough to affect the temperature of the intra-cluster medium, and help to explain the cooling flow problem.

In conclusion, the results of the studies presented in this Thesis form an excellent basis for further studies into AGN in clusters and superclusters. Our understanding of what causes AGN activity in galaxies can be significantly improved in the near future, using currently available data and new dedicated observations. In the next few years it is hoped that the links between AGN and their extended environment will be quantified and that the physical processes which that cause this link will be able to be identified.

APPENDIX A

Glossary of terms and definitions

A.1 Statistical tests and mathematical methods

A.1.1 Kuiper test

The Kuiper test is similar to the Kolmogorov-Smirnov (K-S) test in that it tests the significance of the deviation between two cumulative distribution functions. Unlike the K-S test, the Kuiper test is sensitive to differences at the extreme ends of the distribution, and is useful to distinguish between distributions with similar means but different variances. The test uses Kuiper's statistic, which finds the maximum positive and negative deviation between the two cumulative distribution functions:

$$K = max(P(x) - Q(x)) + max(Q(x) - P(x)) \tag{A.1}$$

where P(x) and Q(x) are the two cumulative distributions to be compared. The probability of finding a value of K greater than the observed value is given in Numerical Recipes (Press et al. 1992):

$$\text{Probability}(K > \text{Observed}) = Q\left(K \times \left(\sqrt{N_e} + 0.155 + 0.24/\sqrt{N_e}\right)\right) \tag{A.2}$$

where N_e is found from the number of data points in P and Q, N_P and N_Q:

$$N_e = \frac{N_P N_Q}{N_P + N_Q} \tag{A.3}$$

and the function Q is given by

$$Q(\lambda) = 2\sum_{j=1}^{\infty}(4j^2\lambda^2 - 1)e^{-2j^2\lambda^2} \tag{A.4}$$

A.1.2 2-Dimensional Kolmogorov-Smirnov test

To compare two 2-dimensional distributions, a variant on the Kolmogorov-Smirnov (K-S) test can be used (based on a method developed by Peacock (1983), as described in Press et al. 1992). For a distribution, P(x,y), the cumulative distribution function can be found by the fraction of data in four quadrants around a data point (x_i, y_i), i.e. in $(x > x_i, y > y_i), (x > x_i, y < y_i), (x < x_i, y > y_i)$ and $(x < x_i, y < y_i)$. The K-S statistic, D, is given by finding the maximum difference between these cumulative distribution functions (in any quadrant) for two distributions, P(x,y) and Q(x,y). As the value of D depends whether the distribution calculated at each point in P (i.e. at x(P),y(P)) or at each point in Q, the true value is taken as the mean of D for the two methods.

Monte Carlo analysis of the distribution of D gives a probability

$$\text{Probability}(D > \text{Observed}) = Q\left(\frac{D\sqrt{N_e}}{1 + \sqrt{1 - r^2}(0.25 - 0.75/\sqrt{N_e})}\right) \tag{A.5}$$

where N_e is given by Equation A.3 and r is the linear correlation coefficient for the data,

$$r = \frac{\sum_i (x_i - \bar{x})(y_i - \bar{y})}{\sqrt{\sum_i (x_i - \bar{x})^2}\sqrt{\sum_i (y_i - \bar{y})^2}} \tag{A.6}$$

This is accurate for $N_e \gtrsim 20$. For probabilities of > 0.2 the value is less accurate, but one can conclude that data are not significantly different.

A.1.3 Wavelet detection

Wavelets are mathematical functions which are used to separate out different frequencies within a signal, in a method similar to Fourier analysis. In contrast to Fourier transforms, wavelets are limited in spatial size and Fourier space, and they are normalised such that the area under the function is zero. They are therefore ideal for detecting peaks in data, and are used in fields as diverse as geology, music and quantum physics.

Source detection using wavelets involves choosing a range of wavelet scales, and convolving the scaled wavelet functions with the data to detect signals at each scale. This method is ideal for detecting X-ray sources, as the PSF size in X-ray images varies significantly across the image. WAVDETECT (Freeman et al. 2002) is a source detection algorithm which has specifically been designed for X-ray image analysis. The wavelet used is a "Mexican Hat" function, which resembles a typical X-ray PSF (where it is >0). The input image

is convolved with the wavelets at a range of scales, and the significance of each detection is determined. Sources are detected iteratively – detected sources are removed and the image is re-processed to determine the correct background level for each source.

For point source analysis the source list at each scale is then compared to the expected source size, and true point sources are found. This is very important in X-ray image analysis as a point source on the edge of the image will have a very different scale from one in the centre. In addition, the fact that wavelets detect fluctuations at different scales makes it far easier to detect small sources which are surrounded by larger sources. In this project the detection of AGN within the cluster emission is very important, and this is possible with wavelet detection.

The WAVDETECT program consists of two parts: WTRANSFORM, which convolves the image with the wavelet scales, and WRECON, which uses the input expected source size distribution to determine which sources are real. For a full description of wavelet analysis, and the different algorithms used in WAVDETECT, see Freeman et al. (2002).

A.1.4 Gehrels approximation of errors

The calculation of errors in the low-count regime requires careful analysis. Applying the standard treatment of errors used in, for example, optical data analysis, will significantly underestimate the true positive error. The positive and negative errors are not equal in the low-count regime, and the $\sqrt{N}$ approximation for the 1σ error breaks down at $N \lesssim 100$. A better numerical approximation is given by Gehrels (1986). This is described in detail below, but to summarise in brief, the 1σ error on N data points is approximated by $1 + \sqrt{N + 0.75}$ for the positive error, and $\sqrt{N - 0.25}$ for the negative error.

A confidence limit is defined as the region around the $measured$ value in which there is an $x\%$ chance that the $true$ value lies. It is therefore not always valid to use the distribution of the true value to estimate the errors.

The probability of a measurement, a, drawn from a distribution with given (but here unknown) true mean, $\bar{a}$, is

$$P(a|\bar{a})$$

Suppose that we observe a value n. The chances of observing n or less is

$$P(a < n|\bar{a}) = \int_{-\infty}^{n} P(a|\bar{a})da$$

There is some value of $\bar{a}$, call it a_+, where this is equal to the confidence limit we are seeking, $1 - \beta$,

$$P(a < n|\bar{a} = a_+) = \int_{-\infty}^{n} P(a|a_+)da = \beta$$

Assuming that the shape of $P(a|\bar{a})$ doesn't change significantly between $\bar{a} = n$ and $\bar{a} = a_+$, we can say that

$$\beta = \int_{a_+}^{\infty} P(n|\bar{a})d\bar{a}$$

which is the value we are looking for, the probability that a_+ is greater than the true value of $\bar{a}$. A similar derivation for the lower confidence limit, α gives

$$\int_{-\infty}^{a_-} P(n|\bar{a})d\bar{a} = \int_{n}^{\infty} P(a|a_-)da = \alpha$$

This is illustrated in Figure A.1, showing the required quantities on the left and the distributions of a_+ and a_- used to obtain these values. The shaded areas are β and α, the regions in which if $a_\pm$ was the true mean then a value below/above n would be expected less than $\beta\%$ or $\alpha\%$ of the time.

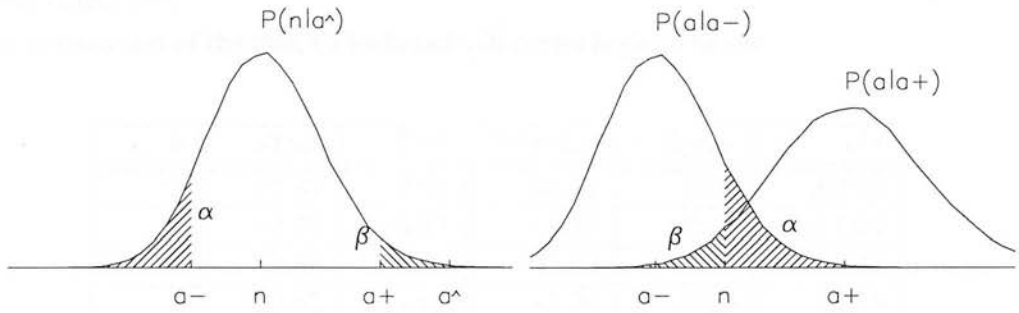

Figure A.1: The probability of measuring n, given a true mean â , gives regions α and β on the left. The values of a_- and a_+ are calculated using $P(a|a_\pm)$ as shown on the right.

The most commonly used confidence interval is the 68.3% two sided level, corresponding to $\alpha = \beta = 100 - 84.13\%$. This is the 1σ gaussian level, but is used generally as a $"1\sigma"$ error in the general case.

In most situations in X-ray astronomy, the random errors are described by the Poisson distribution, which describes a small number of random events taken from a large parent distribution. This is defined as

$$P(n|\bar{a}) = \frac{\bar{a}^n\, e^{-\bar{a}}}{n!}$$

where n is the integer number of events recorded, and $\bar{a}$ is the true mean of the distribution. As described above, the confidence limits on this are

$$\beta = \sum_{x=0}^{n} \frac{{a_+}^x\, e^{-a_+}}{x!}, \qquad 1 - \alpha = \sum_{x=0}^{n-1} \frac{{a_-}^x\, e^{-a_-}}{x!}$$

so that the errors are $n^{+(a_+ - n)}_{-(n-a_-)}$. As this is a discrete distribution, this is the range in which there is *at least* a $1 - \alpha - \beta$ chance that the the true value lies. These equations cannot be solved exactly, but Gehrels (1986) calculates approximations which are valid in most cases. The Poisson sum is related to the χ^2 distribution by

$$\sum_{x=0}^{n-1} \frac{a^x\, e^{-a}}{x!} = P(\chi^2|\nu)$$

where $\chi^2 = 2a$ and $\nu = 2n$.

Using standard approximate relations for χ^2, we find that for the "1σ" case

$$a_+ = n + 1 + \sqrt{n + \frac{3}{4}}, \qquad a_- = n - \sqrt{n - \frac{1}{4}}$$

The expression for a_+ is commonly referred to as the 'Gehrels error' , although other approximations are derived by Gehrels which are more complex, but more accurate for various ranges of n.

A comparison of the true, Gehrels and $\sqrt{n}$ errors is given below

n	+True	-True	Gehrels+	Gehrels-	$\sqrt{n}$
0	+1.84	-0.00	+1.87	-0.00	±0.00
1	+2.30	-0.83	+2.32	-0.67	±1.00
2	+2.63	-1.92	+2.66	-1.33	±1.41
3	+2.92	-1.63	+2.94	-1.66	±1.73
4	+3.16	-1.91	+3.18	-1.94	±2.00
5	+3.38	-2.16	+3.40	-2.18	±2.24
10	+4.27	-3.11	+4.28	-3.12	±3.16
50	+8.12	-7.05	+8.12	-7.05	±7.07
100	+11.00	-9.98	+11.00	-9.99	±10.00
10000	+101.00	-100.00	+101.00	-100.00	±100.00

For most purposes it is sufficient to use the approximation $\sigma = 1 + \sqrt{n + 0.75}$ for the upper limit, which is accurate to $< 1\%$ for $n > 0$. At $N > 100$ the error in the $\sqrt{n}$ approximation is $< 10\%$, and the difference between the Gehrels and $\sqrt{n}$ approximations become negligible.

A.2 X-ray detectors

X-ray telescopes are significantly different from optical telescopes, due to the high energies and low number of photons received, and the need to observe from space. The primary difficulty in forming an X-ray image is focusing the X-rays, as they pass through or are

absorbed by most materials. The X-rays are therefore focused using total external reflection off a combination of parabolic and hyperbolic mirrors. However, as the grazing angle for X-rays is energy dependent this results in different optical paths for X-rays of different energies. The resulting image is therefore blurred, and the point spread function (PSF) is quite strongly energy dependent.

Like optical photons, X-rays can be detected using a charge-coupled device (CCD), which has the advantage of a fast readout and small pixels. The high energy and low number of X-ray photons emitted by a typical source means that almost every detected X-ray photon can be individually recorded – a typical readout time is 3 seconds and it is highly unlikely that more than one X-ray will hit any one pixel (or any two adjacent pixels) in that time, unless a very bright source is being observed. As the signal at each pixel corresponds to just one X-ray photon, the charge in that pixel (and the surrounding pixels, as the charge can spill between pixels) is directly related to the energy of the X-ray photon.

In addition, as the time of arrival of each X-ray is recorded, it is straightforward to analyse the time variability of X-ray sources. An X-ray data set therefore contains the position, energy and time of each photon, and can easily be formed into an image, lightcurve or spectrum.

A.2.1 Sources of background

Unfortunately, the vast majority of the received signals in an X-ray source list are not true X-rays from the observed sources, but are either X-rays produced within the detector, bad pixels or signals from energetic particles. The fact that each signal has an energy, position and time (and in addition a grade, or 'pattern' in XMM data, and status: see Appendices A.3.2 and A.3.3) means that it is relatively straightforward to remove the majority of these signals, but in doing so some of the true X-ray events are also removed.

The main source of background from outside the telescope is due to flares, where the background increases significantly for a period of time, probably due to soft protons scattering through the mirror system. These can be removed by filtering for times of particularly high signal rate, which removes the majority of these events, but also removes the source X-rays received during the flare. This problem is worse for CCDs which are "back illuminated" (see Appendix A.3.1), as detectors using this technique have an improved detection efficiency but are particularly sensitive to proton flares. Each detector therefore needs to be filtered separately for times of high background.

The non-quiescent background is due mainly to cosmic rays and protons, which can be removed by investigating the energies, grades and status of the events. There will be a residual level of cosmic rays which are not removed by this filter, and this background is spatially varying due to the shielding of the detector by parts of the telescope. The level of cosmic ray background is largest above 5 keV. If required, this residual can be removed by

investigating blank fields, but alternatively it can be treated as background noise.

In addition, fluorescent X-rays are produced within the detector, due to the interaction of charge particles with the body of the detector. This emission can be identified by the energy of the X-rays, with the most dominant lines being Al K (1.478 keV), Si K (1.74 keV) and Cu K (8.048 keV). Again these lines can be removed by filtering for energy, but this removes much of the signal. Alternatively, as they vary spatially, they can be removed by comparing the positions and energies of the events to those in blank fields, or they can be retained and treated as another source of background.

Bad pixels can contribute significantly to the background level, but they are generally easy to identify, either via the most recent calibration files, or by a characteristic signal such as a very high signal rate, or signals being received in successive readouts.

The final source of background is the true, extragalactic X-ray background, which is made up of unresolved sources from which only 1 or 2 X-rays are received during the exposure time. There have been many studies investigating the nature of this background, but when studying individual sources it can again be treated as background, and does not need to be removed.

A.3 The Chandra X-ray telescope

The Chandra X-ray Observatory was launched in July 1999, and with XMM-Newton has heralded a new generation of X-ray astronomy. It consists of four nested pairs of parabolic and hyperbolic mirrors, and a range of detectors for imaging (with moderate energy resolution) and high resolution spectroscopy.

X-ray imaging is performed using the ACIS-I and ACIS-S detectors described below. The data are generally reduced using the CIAO (Chandra Interactive Analysis of Observations) package, which consists of mission specific software and calibration files. The following sections describe some of the characteristics of Chandra data.

A.3.1 Detectors

The ACIS detectors consist of ten 1024 x 1024 pixel CCDs, split into four ACIS-I chips (generally used for imaging) and six ACIS-S chips (designed for use in spectroscopy, but also used for imaging), as shown in Figure A.2. Any six chips can be operated at any one time, and observations can be taken with the focal point on ACIS-I3 or ACIS-S3. Two of the ACIS-S chips (S1 and S3) have a different design, being 'back illuminated', and have higher efficiency than the other chips. Observations which don't require a large field of view are therefore often focused on ACIS-S3 rather than using ACIS-I.

The pixels on the ACIS chips are 24μm square, corresponding to 0.492 arcseconds, although the actual resolution is less than this due to the point spread function. Each chip

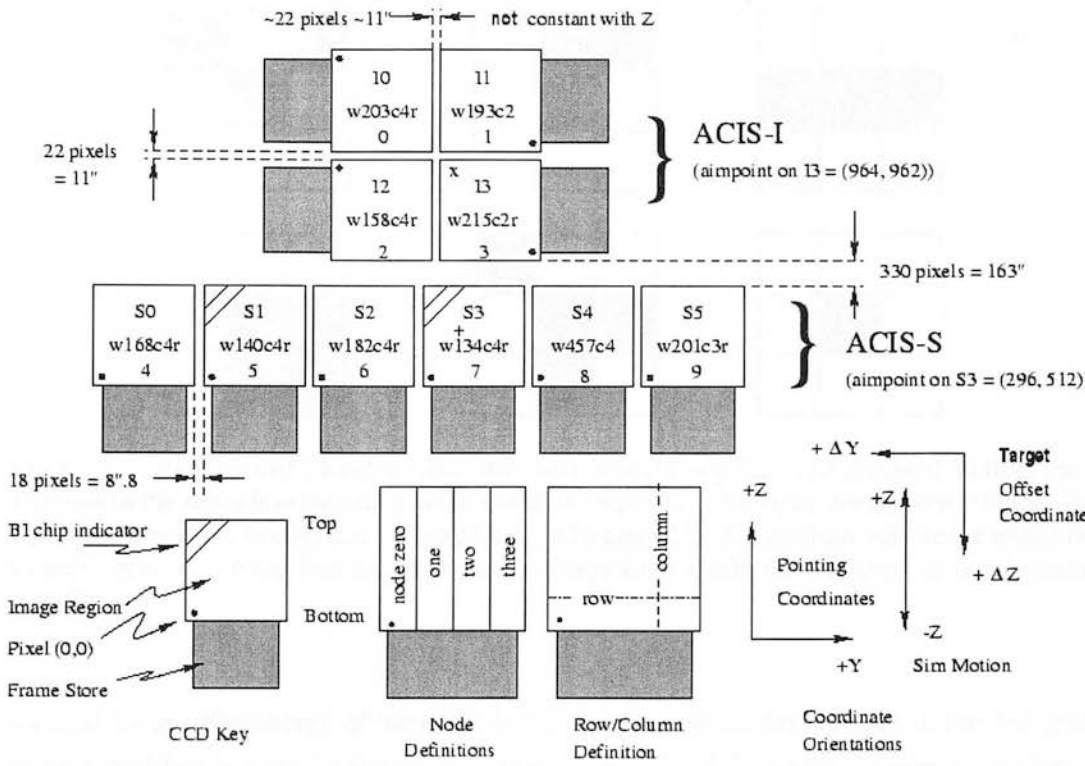

Figure A.2: The layout of the Chandra ACIS detector. The ten ACIS chips are shown, with the possible focal points marked by crosses. The lower part of the figure shows the definition of nodes, rows and columns and the co-ordinate systems.

therefore covers a field of view of $\sim$ 8 arcminutes, and the image is dithered to fill the gaps between the chips. Details of the telescope pointing at each frame readout are stored in the observations files included with each dataset, in order to determine the sky co-ordinates corresponding to each pixel at each time. The energy resolution of the ACIS array varies from $\sim$60eV at 1 keV to $\sim$150eV at 8 keV, but this is also spatially variant across the detector.

A.3.2 Chandra grades

At each readout of the CCD, particle detections ('events') are selected. Each X-ray (or other particle) can produce a signal in one or more pixels, due to the charge spilling between pixels or the particle travelling through adjacent pixels. The distribution of the signal is used to distinguish between true X-ray events and contaminants, by assigning a grade to each event.

To assign the grade the local maximum is selected and a 3x3 grid around this point is investigated. Examples of some events are shown in Figure A.3 - the top line shows some events that were rejected, and the bottom some that were accepted. For example, a signal in three pixels in a row is likely to be caused by a particle hitting at an angle, rather than a

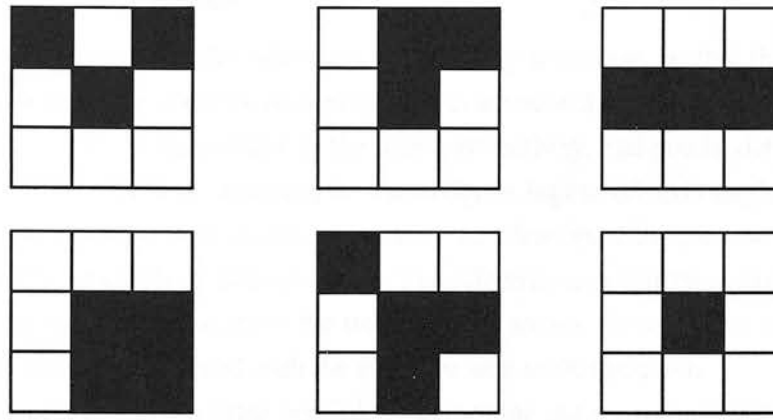

Figure A.3: Examples of Chandra events that were rejected (top line) and accepted (bottom line). The peak of the signal is in the centre pixel, and all other pixels with a signal are marked in black. The signal patterns in the bottom line are very likely to be caused by X-rays from outside the telescope, whereas those in the top line are likely to be X-rays from inside the telescope or other cosmic particles.

focused X-ray. The energy of the event is found by summing the energies in the 3x3 grid, and the position is given by the local maximum. 97.7% of all events are rejected on board Chandra, and further filtering removes $\sim 90\%$ of the remaining 0.5-8keV events to produce a 'Level 2' event list. Although this process removes some true source X-rays, the signal-to-noise ratio is significantly increased, and the vast majority of the remaining events are not contaminants.

A.3.3 Chandra event status

In addition to a grade, each event is assigned a status, which flags potential problems such as the energy being > 130 keV or the event occurring at a bad pixel. Events with status = 0 have no identified problems, and so only these events are generally used in data analysis.

A.3.4 Destreaking

CCD-8 (ACIS-S4) has large streaks in the image due to a fault with the readout of the ACIS chips. The problem results in extra charge being deposited in some rows, which is then identified as true X-rays by the on-board analysis. These can be removed using the CIAO *destreak* tool, which identifies where two or more events occur in any one node and at the same time, and removes these events. This will only remove true source events if a very bright source is being investigated, which isn't an issue in this thesis.

A.3.5 Exposure maps

A number of factors reduce the efficiency of the X-ray telescope, so that the effective detector area is reduced. The effective area takes into account the obscuration of the detector by the telescope, energy dependence of the mirror reflectivity, bad pixels, detector quantum efficiency and the vignetting (decrease in sensitivity at higher off axis angles, particularly for higher energy X-rays). It also takes account of the telescope dither, as one sky position is covered by different pixels at different times. The effective area is both spatially and energy dependent, and in order to calculate the true flux of a source the spectrum and position of the source needs to be combined with the effective area at that position.

For faint sources it is not often possible to determine the source spectrum, so instead a typical spectrum is assumed. The effective area (as a function of energy and time) can then be combined with the assumed spectrum create an exposure map. This gives the effective exposure at each point on the sky for a source with a given spectrum, in units of cm^2sec.

A.3.6 Spectral calibration files

Two calibration files are needed in order to analyse the spectrum of a source. The Auxiliary Response File (ARF) contains information on the detector response and efficiency, and the Response Matrix File (RMF) contains the conversion from detected signal to the X-ray energy.

The ARF is both spatially and energy dependent, and combines the area of the detector sensitive to X-rays of each energy, the dither of the telescope, the response of the filters and the quantum efficiency of the detectors. The resulting ARF at any one point is a plot of response vs. energy, in units of cm^2counts/photon. Multiplying a model spectrum by the ARF gives the observed spectrum assuming that the detector has infinite energy resolution.

The RMF takes into account the uncertainties when converting from detected signal (pulse height) to the X-ray energy for each detection, and is dependent on the detector conditions (temperature, degree of degradation) and position on the detector. The RMF is given by a probability matrix in X-ray energy – pulse height space, and most of the response is diagonal, i.e. a one-to-one correspondence between pulse height and energy. However, there is a non-negligible response that is not diagonal, as particles of a given energy can produce signals with a range of different pulse heights. The probability distribution of pulse heights for each energy needs to be taken into account when fitting a model to an observed spectrum. In reality it is not trivial to determine the true X-ray spectrum from the received pulse heights, so instead a model spectrum is combined with the ARF and RMF and compared to the actual data. This results in a decrease in the resolution of the model spectrum, so that it is comparable to that for the actual data.

A.4 XMM-Newton

XMM consists of three detectors with the same aim point, each covering most of a 15′radius field of view. The two MOS detectors each consist of seven 600 x 600 pixel detectors rotated at 90°to each other. The PN detector consists of twelve 192 x 63 pixel detectors and as it is more advanced (being 'back illuminated') it has around twice the quantum efficiency of a MOS detector. The MOS pixel size is 1.1″whereas PN is 4.1″, so they cover a similar field of view. When combining the images, the data in this thesis was reprojected and rebinned to 4.1″pixels, which is slightly less than the on-axis PSF.

As with Chandra, most of the XMM events are background. The majority of these can be removed by filtering for event PATTERN and FLAG. Filtering for PATTERN $\leq$ 12 selects events that triggered four or less pixels, which removes many non-cosmic events. FLAG describes conditions such as hot pixels and events outside the field of view. The standard screening for flags is encoded in the filters #XMMEA_EM and #XMMEA_EP.

A large fraction of background events can also be removed by restricting the energy to a maximum of 7.5keV, as the PN detector has a significant number of internal X-rays from fluorescent metal lines above this energy, even after filtering. The analysis is also improved if a minimum energy of 0.5keV is applied, as the quantum efficiency of XMM is not well calibrated below 0.4keV.

XMM data is generally reduced with the mission specific software, XMM-SAS. The on-board analysis of the data in this thesis was carried out using SAS v5.4, and subsequent analysis used version 6.0.

A.4.1 Vignetting

The effective area (the sensitivity across the detector), is both energy and spatially dependent. To account for the spatial dependence, or vignetting, a weight can be assigned to each event such that the weight in the centre is 1 for all energies. This weight is defined as

$$w_j = \frac{A_{(0,0)}(E_j)}{A_{x_j,y_j}(E_j)} \tag{A.7}$$

where $A_{x,y}(E)$ is the effective area at (x,y) for a photon of energy E. The weighted event list then gives uniform sensitivity over the detector at each energy.

A.4.2 XMM Point Spread Function

The point spread function (PSF) for XMM is rather complex, due to the difficulties in focusing X-rays, and this introduces significant complications when investigating particularly bright or particularly faint sources. The shape of the PSF varies with the detector, off-axis angle and energy of the source. Broadly speaking, around 90% of the energy is contained

within $48''$ of an on-axis source, although 50% is found within $\sim 10''$. In a faint source over half of the counts are likely to be obscured by the background. For the brightest sources a pattern of radial spikes can be seen out to $> 50''$ from the source centre, which are caused by the telescope supports.

At larger radii ($\gtrsim 3'$) the PSF degrades significantly, in particular for low energy X-rays: at $6'$, 90% of the energy of a 1.5 keV source is contained within $\sim 55''$, and by $12'$ this becomes $\sim 65''$. At higher energies the increase is less significant, but when detecting sources up to $\sim 14'$ from the X-ray axis it is important to take into account the change in source size.

In addition, the shape of the PSF also changes, as shown in the calibration measurements included in the XMM-Newton Users' Handbook. Whereas in some parts of the image, such as the north-east corner, it becomes arc shaped, in areas like the extreme west it is elongated in a radial direction. The current modelling of the PSF does not take into account these variations, and so the easiest way to identify point sources is by eye, via comparisons with other point sources in similar areas of the image.

A.4.3 Detection in XMM images

As described in Section A.4.2, variations in the XMM PSF means that the source sizes vary significantly across the image. Section A.1.3 describes the WAVDETECT program, which detects sources of different sizes using wavelets.

For the XMM images wavelets of 1 to 16 pixels were used to cover the whole range of source sizes in the image. A significance threshold of 1×10^{-5} was used, corresponding to an average of ~ 1.4 false sources per XMM image at the resolution used.

APPENDIX B

Table of detected sources in cluster fields

The first few pages of the table of the sources detected in each cluster field are shown. For the full table see http://www.roe.ac.uk/∼red . The acronym CXOGBA (Chandra X-ray Observatory, Gilmour Best Almaini, where Gilmour is the married name of the author of this thesis) has been registered with the International Astronomical Union for this sample.

Sources are listed for each cluster field, in the same order as Table 2.3. Fluxes are calculated in the 0.5-8keV band, assuming a spectrum with $\Gamma = 1.7$, and are given in units of 10^{-15}erg/cm^2/sec. Sig is the source significance, as defined in Equation 2.8, and HR is the hardness ratio (in counts), as described in Section 2.5.4.

Table B.1

Name	RA (J2000)	DEC (J2000)	Net Counts	F_X	Sig	HR
MS0015+16: 00:18:33.6 +16:26:12.6						
CXOGBA J001756.7+163008	00:17:56.8	+16:30:08.9	35.4	6.06	3.4	-1.00± 0.00
CXOGBA J001758.9+163118	00:17:58.9	+16:31:19.0	51.7	8.17	13.9	-1.00± 0.00
CXOGBA J001801.1+163139	00:18:01.2	+16:31:39.8	29.0	5.05	7.5	-0.12± 0.30
CXOGBA J001801.6+163236	00:18:01.6	+16:32:36.5	24.0	3.74	5.2	1.00± 0.00
CXOGBA J001801.6+163426	00:18:01.7	+16:34:26.1	76.7	12.13	7.0	-0.08± 0.23
CXOGBA J001803.3+162753	00:18:03.4	+16:27:53.8	17.2	2.81	4.1	-1.00± 0.00
CXOGBA J001805.7+162855	00:18:05.7	+16:28:55.3	14.4	2.20	5.1	1.00± 0.00
CXOGBA J001806.0+163040	00:18:06.0	+16:30:40.5	19.4	3.05	4.3	-1.00± 0.00
CXOGBA J001806.9+162518	00:18:06.9	+16:25:18.7	13.0	1.95	4.0	-1.00± 0.00
CXOGBA J001807.3+163553	00:18:07.3	+16:35:53.8	47.7	6.73	6.4	0.04± 0.27
CXOGBA J001807.9+163120	00:18:07.9	+16:31:20.6	102.5	15.42	30.8	-0.13± 0.12
CXOGBA J001808.5+163231	00:18:08.6	+16:32:31.7	81.2	12.26	19.2	-0.27± 0.16
CXOGBA J001809.3+162532	00:18:09.3	+16:25:32.6	91.3	13.98	17.0	-0.35± 0.16

Continued on next page...

Table B.1 – Continued

Name	RA (J2000)	DEC (J2000)	Net Counts	F_X	Sig	HR
CXOGBA J001809.8+162557	00:18:09.9	+16:25:57.7	32.1	6.00	6.9	-0.27± 0.31
CXOGBA J001810.1+163207	00:18:10.1	+16:32:07.5	16.3	2.43	6.3	1.00± 0.00
CXOGBA J001810.2+162943	00:18:10.3	+16:29:43.1	21.0	3.10	7.8	-1.00± 0.00
CXOGBA J001810.2+163224	00:18:10.3	+16:32:24.5	238.4	35.72	83.6	-0.49± 0.09
CXOGBA J001812.4+162714	00:18:12.5	+16:27:14.2	16.4	2.40	5.8	0.02± 0.42
CXOGBA J001816.6+163214	00:18:16.6	+16:32:14.7	10.5	1.52	4.2	0.00± 1.00
CXOGBA J001817.6+163107	00:18:17.6	+16:31:07.6	28.5	4.07	13.3	0.17± 0.27
CXOGBA J001818.0+163315	00:18:18.1	+16:33:15.3	47.1	6.75	16.2	-0.33± 0.22
CXOGBA J001818.8+163748	00:18:18.9	+16:37:48.6	22.8	3.55	3.6	0.00± 1.00
CXOGBA J001821.9+161943	00:18:21.9	+16:19:43.6	152.6	24.81	12.8	-0.57± 0.16
CXOGBA J001822.1+162927	00:18:22.2	+16:29:27.8	9.3	1.29	4.2	1.00± 0.00
CXOGBA J001822.3+163747	00:18:22.3	+16:37:47.2	13.2	2.08	4.1	1.00± 0.00
CXOGBA J001824.5+163733	00:18:24.5	+16:37:33.8	24.3	3.81	6.7	1.00± 0.00
CXOGBA J001824.6+162931	00:18:24.6	+16:29:31.6	8.6	1.19	4.2	1.00± 0.00
CXOGBA J001825.0+163652	00:18:25.0	+16:36:52.9	59.2	9.11	14.5	-0.28± 0.19
CXOGBA J001825.8+163028	00:18:25.8	+16:30:28.6	19.5	2.68	9.2	-1.00± 0.00
CXOGBA J001827.0+162900	00:18:27.1	+16:29:00.3	65.8	9.26	27.2	-0.39± 0.18
CXOGBA J001828.3+163610	00:18:28.4	+16:36:11.0	15.4	2.32	3.8	1.00± 0.00
CXOGBA J001828.5+162800	00:18:28.5	+16:28:00.2	155.0	22.00	67.2	-0.39± 0.11
CXOGBA J001828.7+162752	00:18:28.7	+16:27:52.1	9.4	1.34	4.4	1.00± 0.00
CXOGBA J001828.6+163418	00:18:28.7	+16:34:18.2	52.0	8.06	22.4	-0.49± 0.22
CXOGBA J001828.6+163529	00:18:28.7	+16:35:29.2	13.7	2.04	5.0	1.00± 0.00
CXOGBA J001828.9+162725	00:18:28.9	+16:27:25.5	7.9	1.12	3.3	1.00± 0.00
CXOGBA J001829.8+163426	00:18:29.8	+16:34:26.8	11.0	1.60	4.8	-1.00± 0.00
CXOGBA J001831.3+162043	00:18:31.4	+16:20:43.2	240.6	38.79	28.1	-0.45± 0.10
CXOGBA J001831.7+163747	00:18:31.8	+16:37:47.3	13.4	2.09	4.3	1.00± 0.00
CXOGBA J001832.0+162926	00:18:32.0	+16:29:26.4	738.8	233.77	369.7	-0.59± 0.06
CXOGBA J001832.5+163632	00:18:32.5	+16:36:32.5	31.7	5.14	7.8	0.24± 0.31
CXOGBA J001833.4+163154	00:18:33.5	+16:31:54.5	217.5	30.24	103.3	-0.45± 0.09
CXOGBA J001833.5+162652	00:18:33.6	+16:26:52.4	38.7	5.52	11.1	-0.36± 0.27
CXOGBA J001834.2+163759	00:18:34.3	+16:37:59.7	37.7	5.88	7.8	-0.19± 0.27
CXOGBA J001835.2+163748	00:18:35.2	+16:37:48.2	11.8	1.84	3.9	-1.00± 0.00
CXOGBA J001836.1+163549	00:18:36.2	+16:35:49.4	8.2	1.22	3.6	-1.00± 0.00
CXOGBA J001836.6+162230	00:18:36.6	+16:22:30.3	16.9	2.62	4.0	-1.00± 0.00
CXOGBA J001836.7+163614	00:18:36.8	+16:36:14.9	24.0	3.61	5.4	-0.03± 0.37
CXOGBA J001836.9+162737	00:18:37.0	+16:27:37.7	8.7	1.94	3.6	1.00± 0.00
CXOGBA J001837.2+163411	00:18:37.2	+16:34:11.0	12.4	1.79	4.9	0.00± 1.00
CXOGBA J001837.3+163446	00:18:37.4	+16:34:46.8	120.0	18.26	44.9	-0.57± 0.15
CXOGBA J001837.4+163046	00:18:37.5	+16:30:46.5	32.8	4.49	16.6	-0.40± 0.28
CXOGBA J001837.5+163756	00:18:37.5	+16:37:57.0	103.6	16.25	31.4	-0.46± 0.15
CXOGBA J001837.5+163610	00:18:37.6	+16:36:10.5	42.8	6.42	10.9	-0.13± 0.23
CXOGBA J001837.9+163910	00:18:37.9	+16:39:10.2	175.4	28.07	25.4	-0.41± 0.11
CXOGBA J001838.1+163320	00:18:38.2	+16:33:20.2	49.2	7.00	21.9	-0.45± 0.22
CXOGBA J001838.4+163437	00:18:38.4	+16:34:37.8	13.4	2.06	4.7	-1.00± 0.00
CXOGBA J001838.6+163237	00:18:38.7	+16:32:37.1	14.5	2.04	6.8	-1.00± 0.00
CXOGBA J001839.6+163824	00:18:39.6	+16:38:24.9	22.0	3.45	3.9	-1.00± 0.00
CXOGBA J001839.7+162245	00:18:39.7	+16:22:45.3	14.3	2.20	4.0	-1.00± 0.00
CXOGBA J001841.0+163036	00:18:41.1	+16:30:36.7	7.7	1.11	3.8	0.00± 1.00
CXOGBA J001842.0+163425	00:18:42.1	+16:34:25.3	13.9	2.02	5.1	1.00± 0.00
CXOGBA J001842.3+163943	00:18:42.3	+16:39:43.0	24.8	3.46	3.8	1.00± 0.00
CXOGBA J001844.2+163103	00:18:44.2	+16:31:03.4	18.5	2.79	8.7	-0.17± 0.37

Continued on next page...

Table B.1 – Continued

Name	RA (J2000)	DEC (J2000)	Net Counts	F_X	Sig	HR
CXOGBA J001845.0+163243	00:18:45.0	+16:32:43.1	18.3	5.97	8.4	-1.00± 0.00
CXOGBA J001845.2+162538	00:18:45.2	+16:25:38.2	34.7	6.27	10.5	-0.49± 0.31
CXOGBA J001845.3+163528	00:18:45.3	+16:35:28.3	32.4	4.84	8.5	1.00± 0.00
CXOGBA J001845.7+163346	00:18:45.7	+16:33:46.6	292.1	42.33	110.6	-0.28± 0.07
CXOGBA J001846.1+162213	00:18:46.2	+16:22:13.6	26.3	8.31	6.4	0.26± 0.35
CXOGBA J001846.1+162815	00:18:46.2	+16:28:15.5	11.5	1.62	5.5	0.00± 1.00
CXOGBA J001847.1+163204	00:18:47.1	+16:32:04.5	8.8	1.25	3.7	1.00± 0.00
CXOGBA J001847.5+163330	00:18:47.6	+16:33:30.4	9.4	1.32	3.7	-1.00± 0.00
CXOGBA J001848.2+163503	00:18:48.2	+16:35:03.2	11.0	1.76	3.2	-1.00± 0.00
CXOGBA J001849.3+162339	00:18:49.4	+16:23:39.3	8.2	1.83	3.1	0.00± 1.00
CXOGBA J001850.1+162756	00:18:50.1	+16:27:56.6	111.3	17.30	43.4	-0.43± 0.14
CXOGBA J001851.7+162739	00:18:51.8	+16:27:39.8	10.6	1.82	4.2	0.00± 1.00
CXOGBA J001851.9+162630	00:18:52.0	+16:26:30.8	14.8	2.18	5.4	-1.00± 0.00
CXOGBA J001853.5+162751	00:18:53.6	+16:27:51.9	175.7	25.39	58.0	-0.07± 0.09
CXOGBA J001853.5+162840	00:18:53.6	+16:28:40.8	12.1	1.73	4.6	0.00± 1.00
CXOGBA J001854.8+162953	00:18:54.9	+16:29:53.1	55.5	7.98	22.1	-0.42± 0.21
CXOGBA J001855.5+162940	00:18:55.5	+16:29:41.0	22.5	3.24	8.0	-1.00± 0.00
CXOGBA J001856.0+163055	00:18:56.1	+16:30:55.6	12.4	1.80	4.9	1.00± 0.00
CXOGBA J001856.5+163316	00:18:56.6	+16:33:16.5	15.3	2.26	3.8	1.00± 0.00
CXOGBA J001856.8+162941	00:18:56.9	+16:29:41.1	20.1	2.91	7.6	0.16± 0.36
CXOGBA J001859.8+162649	00:18:59.8	+16:26:49.7	354.6	53.24	85.1	-0.42± 0.07
CXOGBA J001900.0+163337	00:19:00.0	+16:33:38.0	16.3	2.45	4.5	-1.00± 0.00
CXOGBA J001902.7+163212	00:19:02.8	+16:32:12.2	14.4	2.16	4.0	0.00± 1.00
CXOGBA J001905.9+162843	00:19:05.9	+16:28:43.0	55.2	8.39	10.6	-0.23± 0.21
CXOGBA J001909.2+163101	00:19:09.2	+16:31:01.0	55.6	8.40	9.1	-0.28± 0.23
CL0024+17: 00:26:35.8 +17:09:41.1						
CXOGBA J002603.4+171349	00:26:03.5	+17:13:49.1	30.7	7.46	7.1	-1.00± 0.00
CXOGBA J002605.0+171355	00:26:05.1	+17:13:56.0	37.1	8.96	10.1	-0.40± 0.28
CXOGBA J002606.8+171216	00:26:06.8	+17:12:16.4	22.3	5.29	10.1	-1.00± 0.00
CXOGBA J002606.9+171213	00:26:07.0	+17:12:13.4	16.5	3.91	6.6	-0.13± 0.41
CXOGBA J002607.4+171246	00:26:07.5	+17:12:46.3	24.8	6.50	5.3	-1.00± 0.00
CXOGBA J002609.8+171600	00:26:09.8	+17:16:00.4	19.9	4.82	5.4	-1.00± 0.00
CXOGBA J002610.6+171439	00:26:10.6	+17:14:39.3	44.9	11.19	10.0	0.18± 0.24
CXOGBA J002611.0+171009	00:26:11.1	+17:10:09.8	7.1	1.63	3.1	0.00± 1.00
CXOGBA J002612.5+171253	00:26:12.6	+17:12:53.5	15.1	3.47	6.5	-1.00± 0.00
CXOGBA J002615.6+170927	00:26:15.6	+17:09:27.9	35.8	10.91	15.1	-0.37± 0.26
CXOGBA J002615.6+171208	00:26:15.7	+17:12:08.8	13.6	3.08	5.5	-1.00± 0.00
CXOGBA J002617.4+170944	00:26:17.5	+17:09:44.4	19.8	3.31	6.6	0.12± 0.37
CXOGBA J002618.1+170949	00:26:18.2	+17:09:49.4	65.2	10.99	22.4	-0.47± 0.20
CXOGBA J002620.2+171705	00:26:20.3	+17:17:05.4	38.2	9.34	9.1	-1.00± 0.00
CXOGBA J002624.3+171134	00:26:24.3	+17:11:34.6	20.5	5.97	9.6	-1.00± 0.00
CXOGBA J002626.0+171117	00:26:26.1	+17:11:17.0	11.3	1.83	5.2	0.00± 1.00
CXOGBA J002626.3+170939	00:26:26.4	+17:09:39.8	366.2	58.80	164.6	-0.66± 0.08
CXOGBA J002627.6+171428	00:26:27.7	+17:14:28.2	19.2	4.28	8.6	-1.00± 0.00
CXOGBA J002628.8+171517	00:26:28.8	+17:15:18.0	16.7	3.77	6.9	-1.00± 0.00
CXOGBA J002629.5+171118	00:26:29.6	+17:11:18.1	6.5	1.03	3.0	0.00± 1.00
CXOGBA J002629.9+171636	00:26:30.0	+17:16:37.0	15.3	3.33	3.6	-1.00± 0.00
CXOGBA J002630.9+171030	00:26:31.0	+17:10:30.4	22.4	3.57	10.5	-1.00± 0.00
CXOGBA J002631.0+171017	00:26:31.1	+17:10:17.3	310.1	51.48	135.9	-0.56± 0.09
CXOGBA J002631.5+171358	00:26:31.5	+17:13:58.4	8.6	1.88	4.2	-1.00± 0.00
CXOGBA J002631.6+171022	00:26:31.7	+17:10:22.5	22.5	3.73	10.5	-1.00± 0.00

Continued on next page...

Table B.1 – Continued

Name	RA (J2000)	DEC (J2000)	Net Counts	F_X	Sig	HR
CXOGBA J002632.0+170941	00:26:32.0	+17:09:42.0	21.6	3.46	8.8	1.00± 0.00
CXOGBA J002633.0+170800	00:26:33.0	+17:08:00.3	43.5	7.09	17.4	-0.63± 0.28
CXOGBA J002633.9+170733	00:26:34.0	+17:07:33.5	29.5	4.83	10.5	-0.29± 0.29
CXOGBA J002636.4+170735	00:26:36.4	+17:07:35.4	69.9	11.48	25.9	-0.41± 0.18
CXOGBA J002636.5+171158	00:26:36.5	+17:11:58.1	20.7	3.31	10.2	-1.00± 0.00
CXOGBA J002637.4+171355	00:26:37.4	+17:13:55.7	8.6	1.50	4.1	0.00± 1.00
CXOGBA J002638.5+171448	00:26:38.5	+17:14:48.9	24.9	4.68	7.7	-1.00± 0.00
CXOGBA J002638.7+170703	00:26:38.7	+17:07:03.8	8.1	1.34	3.1	0.00± 1.00
CXOGBA J002639.7+171248	00:26:39.8	+17:12:49.0	6.6	1.09	3.2	-1.00± 0.00
CXOGBA J002639.9+170804	00:26:39.9	+17:08:04.6	12.3	2.00	3.4	-1.00± 0.00
CXOGBA J002641.3+170732	00:26:41.3	+17:07:32.2	13.5	2.22	4.1	0.00± 1.00
CXOGBA J002641.9+170953	00:26:41.9	+17:09:53.9	7.6	1.60	3.1	0.00± 1.00
CXOGBA J002642.0+170641	00:26:42.1	+17:06:41.7	19.3	3.22	5.4	-1.00± 0.00
CXOGBA J002642.5+171113	00:26:42.6	+17:11:13.9	17.3	2.81	7.8	-1.00± 0.00
CXOGBA J002643.0+170832	00:26:43.0	+17:08:32.8	70.9	11.62	23.8	-0.55± 0.20
CXOGBA J002643.7+170721	00:26:43.7	+17:07:21.1	56.5	9.82	13.8	-0.48± 0.23
CXOGBA J002643.8+171317	00:26:43.9	+17:13:17.9	43.3	7.91	16.7	0.10± 0.21
CXOGBA J002643.9+171136	00:26:44.0	+17:11:36.5	30.7	5.07	12.7	-0.53± 0.32
CXOGBA J002644.5+170232	00:26:44.6	+17:02:32.3	42.4	10.85	9.6	-1.00± 0.00
CXOGBA J002645.0+170811	00:26:45.0	+17:08:11.3	19.7	3.24	7.1	-1.00± 0.00
CXOGBA J002645.3+170716	00:26:45.3	+17:07:16.6	72.6	12.09	20.7	0.25± 0.17
CXOGBA J002645.8+171305	00:26:45.8	+17:13:05.6	32.5	5.83	12.9	-1.00± 0.00
CXOGBA J002646.0+171232	00:26:46.1	+17:12:32.3	385.0	67.56	120.0	-0.57± 0.08
CXOGBA J002646.3+171025	00:26:46.3	+17:10:25.1	15.5	2.58	5.0	1.00± 0.00
CXOGBA J002646.4+170648	00:26:46.4	+17:06:49.0	32.3	5.46	7.8	-1.00± 0.00
CXOGBA J002648.7+170554	00:26:48.7	+17:05:54.9	22.8	2.59	3.7	0.00± 1.00
CXOGBA J002653.0+170041	00:26:53.1	+17:00:41.5	79.7	22.37	10.2	-1.00± 0.00
CXOGBA J002657.9+170849	00:26:58.0	+17:08:49.3	51.5	9.42	18.3	-0.70± 0.27
CXOGBA J002701.0+170803	00:27:01.0	+17:08:03.5	79.6	20.38	8.4	-1.00± 0.00
CXOGBA J002703.9+170724	00:27:03.9	+17:07:24.7	82.2	20.94	6.6	-1.00± 0.00
CXOGBA J002704.2+170234	00:27:04.2	+17:02:34.8	31.1	8.36	4.4	0.00± 1.00
CXOGBA J002707.5+170619	00:27:07.5	+17:06:19.2	154.7	40.37	19.9	-0.46± 0.13
CXOGBA J002707.7+170751	00:27:07.7	+17:07:51.3	433.8	114.91	51.3	-0.38± 0.06
RXJ0027+26: 00:27:45.4 +26:16:22.5						
CXOGBA J002713.9+262334	00:27:14.0	+26:23:34.6	7.7	8.60	3.8	0.00± 1.00
CXOGBA J002717.3+262021	00:27:17.4	+26:20:21.6	9.9	10.64	5.2	-1.00± 0.00
CXOGBA J002720.7+262430	00:27:20.7	+26:24:30.3	8.4	9.96	3.9	0.00± 1.00
CXOGBA J002721.0+262248	00:27:21.1	+26:22:49.0	15.8	18.02	7.9	-1.00± 0.00
CXOGBA J002728.7+261446	00:27:28.7	+26:14:46.2	9.8	10.55	5.0	0.00± 1.00
CXOGBA J002747.7+261346	00:27:47.8	+26:13:46.1	11.5	12.33	5.5	-1.00± 0.00
CXOGBA J002750.3+261835	00:27:50.4	+26:18:35.3	13.9	13.95	7.3	-0.15± 0.44
CXOGBA J002751.1+262437	00:27:51.1	+26:24:37.6	9.7	10.32	4.8	-1.00± 0.00
CXOGBA J002753.9+261842	00:27:54.0	+26:18:42.4	7.0	7.03	3.7	-1.00± 0.00
CXOGBA J002756.5+261652	00:27:56.6	+26:16:52.0	335.6	346.37	160.2	-0.78± 0.10
CXOGBA J002758.3+262735	00:27:58.3	+26:27:35.1	16.4	18.64	3.7	-1.00± 0.00
CXOGBA J002758.5+261738	00:27:58.6	+26:17:38.7	13.8	14.44	6.9	-1.00± 0.00
CXOGBA J002759.1+262251	00:27:59.2	+26:22:51.9	7.7	8.09	3.8	0.00± 1.00
CXOGBA J002801.4+262044	00:28:01.5	+26:20:44.5	38.3	39.34	17.4	-1.00± 0.00
CXOGBA J002803.8+261903	00:28:03.8	+26:19:03.9	7.9	8.10	4.0	0.00± 1.00

For the full table see http://www.roe.ac.uk/~red

APPENDIX C

Bibliography

Bibliography

Abadi, M. G., Moore, B., and Bower, R. G.: 1999, *MNRAS* **308**, 947

Abell, G. O.: 1958, *ApJS* **3**, 211

Abell, G. O., Corwin, H. G., and Olowin, R. P.: 1989, *ApJS* **70**, 1

Allen, S. W., Edge, A. C., Fabian, A. C., Boehringer, H., Crawford, C. S., Ebeling, H., Johnstone, R. M., Naylor, T., and Schwarz, R. A.: 1992, *MNRAS* **259**, 67

Allen, S. W., Schmidt, R. W., Ebeling, H., Fabian, A. C., and van Speybroeck, L.: 2004, *MNRAS* **353**, 457

Aller, M. F., Aller, H. D., and Hughes, P. A.: 1992, *ApJ* **399**, 16

Arnaud, M.: 1992, in *Environment Observation and Climate Modelling Through International Space Projects*, pp 177–178

Arnaud, M., Majerowicz, S., Lumb, D., Neumann, D. M., Aghanim, N., Blanchard, A., Boer, M., Burke, D. J., Collins, C. A., Giard, M., Nevalainen, J., Nichol, R. C., Romer, A. K., and Sadat, R.: 2002, *A&A* **390**, 27

Böhringer, H., Schuecker, P., Guzzo, L., Collins, C. A., Voges, W., Cruddace, R. G., Ortiz-Gil, A., Chincarini, G., De Grandi, S., Edge, A. C., MacGillivray, H. T., Neumann, D. M., Schindler, S., and Shaver, P.: 2004, *A&A* **425**, 367

Böhringer, H., Voges, W., Huchra, J. P., McLean, B., Giacconi, R., Rosati, P., Burg, R., Mader, J., Schuecker, P., Simiç, D., Komossa, S., Reiprich, T. H., Retzlaff, J., and Trümper, J.: 2000, *ApJS* **129**, 435

Baldwin, J. A., Phillips, M. M., and Terlevich, R.: 1981, *PASP* **93**, 5

Balogh, M., Bower, R. G., Smail, I., Ziegler, B. L., Davies, R. L., Gaztelu, A., and Fritz, A.: 2002, *MNRAS* **337**, 256

Balogh, M. L., Morris, S. L., Yee, H. K. C., Carlberg, R. G., and Ellingson, E.: 1999, *ApJ* **527**, 54

Balogh, M. L., Navarro, J. F., and Morris, S. L.: 2000, *ApJ* **540**, 113

Barger, A. J., Cowie, L. L., Mushotzky, R. F., and Richards, E. A.: 2001, *AJ* **121**, 662

Barnes, J. E.: 2002, *MNRAS* **333**, 481

Barr, J. M., Bremer, M. N., Baker, J. C., and Lehnert, M. D.: 2003, *MNRAS* **346**, 229

Bartelmann, M.: 1996, *A&A* **313**, 697

Barton Gillespie, E., Geller, M. J., and Kenyon, S. J.: 2003, *ApJ* **582**, 668

Basilakos, S., Plionis, M., Georgakakis, A., and Georgantopoulos, I.: 2005, *MNRAS* **356**, 183

Bauer, F. E., Alexander, D. M., Brandt, W. N., Schneider, D. P., Treister, E., Hornschemeier, A. E., and Garmire, G. P.: 2004, *AJ* **128**, 2048

Bechtold, J., Forman, W., Jones, C., Schwarz, J., van Speybroeck, L., Giacconi, R., and Tucker, W.: 1983, *ApJ* **265**, 26

Benoist, C., da Costa, L., Jørgensen, H. E., Olsen, L. F., Bardelli, S., Zucca, E., Scodeggio, M., Neumann, D., Arnaud, M., Arnouts, S., Biviano, A., and Ramella, M.: 2002, *A&A* **394**, 1

Benson, A. J., Bower, R. G., Frenk, C. S., Lacey, C. G., Baugh, C. M., and Cole, S.: 2003, *ApJ* **599**, 38

Best, P. N.: 2004, *MNRAS* **351**, 70

Best, P. N., Kauffmann, G., Heckman, T. M., Brinchmann, J., Charlot, S., Ivezić, Ž., and White, S. D. M.: 2005, *MNRAS* **362**, 25

Best, P. N., van Dokkum, P. G., Franx, M., and Röttgering, H. J. A.: 2002, *MNRAS* **330**, 17

Blakeslee, J. P., Franx, M., Postman, M., Rosati, P., Holden, B. P., Illingworth, G. D., Ford, H. C., Cross, N. J. G., Gronwall, C., Benítez, N., Bouwens, R. J., Broadhurst, T. J., Clampin, M., Demarco, R., Golimowski, D. A., Hartig, G. F., Infante, L., Martel, A. R., Miley, G. K., Menanteau, F., Meurer, G. R., Sirianni, M., and White, R. L.: 2003, *ApJ* **596**, L143

Blandford, R. D. and Narayan, R.: 1992, *ARA&A* **30**, 311

Böhringer, H., Schuecker, P., Guzzo, L., Collins, C. A., Voges, W., Cruddace, R. G., Ortiz-Gil, A., Chincarini, G., De Grandi, S., Edge, A. C., MacGillivray, H. T., Neumann, D. M., Schindler, S., and Shaver, P.: 2004, *A&A* **425**, 367

Borgani, S. and Guzzo, L.: 2001, *Nature* **409**, 39

Bower, R. G. and Balogh, M. L.: 2004, in *Clusters of Galaxies: Probes of Cosmological Structure and Galaxy Evolution*, pp 326–+

Bower, R. G., Lucey, J. R., and Ellis, R. S.: 1992, *MNRAS* **254**, 601

Brandt, W. N., Hornschemeier, A. E., Alexander, D. M., Garmire, G. P., Schneider, D. P., Broos, P. S., Townsley, L. K., Bautz, M. W., Feigelson, E. D., and Griffiths, R. E.: 2001, *AJ* **122**, 1

Butcher, H. and Oemler, A.: 1984, *ApJ* **285**, 426

Caccianiga, A., Maccacaro, T., Wolter, A., Della Ceca, R., and Gioia, I. M.: 2000, *A&AS* **144**, 247

Cao, L., Wei, J.-Y., and Hu, J.-Y.: 1999, *A&AS* **135**, 243

Cappelluti, N., Cappi, M., Dadina, M., Malaguti, G., Branchesi, M., D'Elia, V., and Palumbo, G. G. C.: 2005, *A&A* **430**, 39

Cappi, M., Mazzotta, P., Elvis, M., Burke, D. J., Comastri, A., Fiore, F., Forman, W., Fruscione, A., Green, P., Harris, D., Hooper, E. J., Jones, C., Kaastra, J. S., Kellogg, E., Murray, S., McNamara, B., Nicastro, F., Ponman, T. J., Schlegel, E. M., Siemiginowska, A., Tananbaum, H., Vikhlinin, A., Virani, S., and Wilkes, B.: 2001, *ApJ* **548**, 624

Caretta, C. A., Maia, M. A. G., Kawasaki, W., and Willmer, C. N. A.: 2002, *AJ* **123**, 1200

Cohen, J. G. and Kneib, J.: 2002, *ApJ* **573**, 524

Coldwell, G. V. and Lambas, D. G.: 2003, *MNRAS* **344**, 156

Coldwell, G. V., Martínez, H. J., and Lambas, D. G.: 2002, *MNRAS* **336**, 207

Cole, S., Lacey, C. G., Baugh, C. M., and Frenk, C. S.: 2000, *MNRAS* **319**, 168

Condon, J. J., Cotton, W. D., Greisen, E. W., Yin, Q. F., Perley, R. A., Taylor, G. B., and Broderick, J. J.: 1998, *AJ* **115**, 1693

Correction of SSC pipeline EPIC source list fluxes: 2003, *XMM Survey Science Centre public release SSC-LUX-TN-0059_3*

Couch, W. J., Balogh, M. L., Bower, R. G., Smail, I., Glazebrook, K., and Taylor, M.: 2001, *ApJ* **549**, 820

Couch, W. J., Barger, A. J., Smail, I., Ellis, R. S., and Sharples, R. M.: 1998, *ApJ* **497**, 188

Cowie, L. L., Barger, A. J., Bautz, M. W., Brandt, W. N., and Garmire, G. P.: 2003, *ApJ* **584**, L57

Croton, D. J., Farrar, G. R., Norberg, P., Colless, M., Peacock, J. A., Baldry, I. K., Baugh, C. M., Bland-Hawthorn, J., Bridges, T., Cannon, R., Cole, S., Collins, C., Couch, W., Dalton, G., De Propris, R., Driver, S. P., Efstathiou, G., Ellis, R. S., Frenk, C. S., Glazebrook, K., Jackson, C., Lahav, O., Lewis, I., Lumsden, S., Maddox, S., Madgwick, D., Peterson, B. A., Sutherland, W., and Taylor, K.: 2005a, *MNRAS* **356**, 1155

Croton, D. J., Springel, V., White, S. D. M., De Lucia, G., Frenk, C. S., Gao, L., Jenkins, A., Kauffmann, G., Navarro, J. F., and Yoshida, N.: 2005b, *astro-ph/0508046, submitted to MNRAS*

Daddi, E., Cimatti, A., and Renzini, A.: 2000, *A&A* **362**, L45

Davidson et al.: 2005, *in preperation*

Davis, D. S., Miller, N. A., and Mushotzky, R. F.: 2003, *ApJ* **597**, 202

de Grandi, S., Böhringer, H., Guzzo, L., Molendi, S., Chincarini, G., Collins, C., Cruddace, R., Neumann, D., Schindler, S., Schuecker, P., and Voges, W.: 1999, *ApJ* **514**, 148

De Grandi, S. and Molendi, S.: 2002, *ApJ* **567**, 163

De Propris, R., Colless, M., Peacock, J. A., Couch, W. J., Driver, S. P., Balogh, M. L., Baldry, I. K., Baugh, C. M., Bland-Hawthorn, J., Bridges, T., Cannon, R., Cole, S., Collins, C., Cross, N., Dalton, G., Efstathiou, G., Ellis, R. S., Frenk, C. S., Glazebrook, K., Hawkins, E., Jackson, C., Lahav, O., Lewis, I., Lumsden, S., Maddox, S., Madgwick, D., Norberg, P., Percival, W., Peterson, B. A., Sutherland, W., and Taylor, K.: 2004, *MNRAS* **351**, 125

De Propris, R., Stanford, S. A., Eisenhardt, P. R., and Dickinson, M.: 2003, *ApJ* **598**, 20

Della Ceca, R., Scaramella, R., Gioia, I. M., Rosati, P., Fiore, F., and Squires, G.: 2000, *A&A* **353**, 498

Dickey, J. M. and Lockman, F. J.: 1990, *ARA&A* **28**, 215

Disney, M. J., Boyce, P. J., Blades, J. C., Boksenberg, A., Cane, P., Deharveng, J. M., Macchetto, F., Mackay, C. D., Sparks, W. B., and Phillipps, S.: 1995, *Nature* **376**, 150

Donahue, M., Scharf, C. A., Mack, J., Lee, Y. P., Postman, M., Rosati, P., Dickinson, M., Voit, G. M., and Stocke, J. T.: 2002, *ApJ* **569**, 689

Donahue, M., Voit, G. M., O'Dea, C. P., Baum, S. A., and Sparks, W. B.: 2005, *ApJ* **630**, L13

Dressler, A.: 1980, *ApJ* **236**, 351

Dressler, A.: 1984, *ARA&A* **22**, 185

Dressler, A., Oemler, A. J., Couch, W. J., Smail, I., Ellis, R. S., Barger, A., Butcher, H., Poggianti, B. M., and Sharples, R. M.: 1997, *ApJ* **490**, 577

Dressler, A., Smail, I., Poggianti, B. M., Butcher, H., Couch, W. J., Ellis, R. S., and Oemler, A. J.: 1999, *ApJS* **122**, 51

Dressler, A., Thompson, I. B., and Shectman, S. A.: 1984, *BAAS* **16**, 881

Drory, N., Bender, R., Feulner, G., Hopp, U., Maraston, C., Snigula, J., and Hill, G. J.: 2003, *ApJ* **595**, 698

Dwarakanath, K. S. and Owen, F. N.: 1999, *AJ* **118**, 625

Ebeling, H., Edge, A. C., Bohringer, H., Allen, S. W., Crawford, C. S., Fabian, A. C., Voges, W., and Huchra, J. P.: 1998, *MNRAS* **301**, 881

Ebeling, H., Edge, A. C., and Henry, J. P.: 2001a, *ApJ* **553**, 668

Ebeling, H., Jones, L. R., Fairley, B. W., Perlman, E., Scharf, C., and Horner, D.: 2001b, *ApJ* **548**, L23

Ebeling, H., Voges, W., Bohringer, H., Edge, A. C., Huchra, J. P., and Briel, U. G.: 1996a, *MNRAS* **281**, 799

Ebeling, H., Voges, W., Bohringer, H., Edge, A. C., Huchra, J. P., and Briel, U. G.: 1996b, *MNRAS* **281**, 799

Eckart, M. E., Laird, E. S., Stern, D., Mao, P. H., Helfand, D. J., and Harrison, F. A.: 2005, *ApJS* **156**, 35

Eddington, A. S.: 1913, *MNRAS* **73**, 359

Edge, A.: 1992, in R. Robinson, A. & Terelevich (ed.), *The Nature of Compact Objects in Active Galactic Nuclei*, pp 125–128, CAP

Edge, A. C., Ebeling, H., Bremer, M., Röttgering, H., van Haarlem, M. P., Rengelink, R., and Courtney, N. J. D.: 2003, *MNRAS* **339**, 913

Ellis, S. C. and Jones, L. R.: 2004, *MNRAS* **348**, 165

Eskridge, P. B., Frogel, J. A., Pogge, R. W., Quillen, A. C., Berlind, A. A., Davies, R. L., DePoy, D. L., Gilbert, K. M., Houdashelt, M. L., Kuchinski, L. E., Ramírez, S. V., Sellgren, K., Stutz, A., Terndrup, D. M., and Tiede, G. P.: 2002, *ApJS* **143**, 73

Fabian, A. C.: 1999, *MNRAS* **308**, L39

Fabian, A. C., Barcons, X., Almaini, O., and Iwasawa, K.: 1998, *MNRAS* **297**, L11+

Fabian, A. C., Mushotzky, R. F., Nulsen, P. E. J., and Peterson, J. R.: 2001, *MNRAS* **321**, L20

Fabian, A. C., Sanders, J. S., Crawford, C. S., and Ettori, S.: 2003, *MNRAS* **341**, 729

Franceschini, A., Manners, J., Polletta, M. d. C., Lonsdale, C., Gonzalez-Solares, E., Surace, J., Shupe, D., Fang, F., Xu, C. K., Farrah, D., Berta, S., Rodighiero, G., Perez-Fournon, I., Hatziminaoglou, E., Smith, H. E., Siana, B., Rowan-Robinson, M., Nandra, K., Babbedge, T., Vaccari, M., Oliver, S., Wilkes, B., Owen, F., Padgett, D., Frayer, D., Jarrett, T., Masci, F., Stacey, G., Almaini, O., McMahon, R., Johnson, O., Lawrence, A., and Willott, C.: 2005, *AJ* **129**, 2074

Freeman, P. E., Kashyap, V., Rosner, R., and Lamb, D. Q.: 2002, *ApJS* **138**, 185

Gómez, P. L., Hughes, J. P., and Birkinshaw, M.: 2000, *ApJ* **540**, 726

Gómez, P. L., Nichol, R. C., Miller, C. J., Balogh, M. L., Goto, T., Zabludoff, A. I., Romer, A. K., Bernardi, M., Sheth, R., Hopkins, A. M., Castander, F. J., Connolly, A. J., Schneider, D. P., Brinkmann, J., Lamb, D. Q., SubbaRao, M., and York, D. G.: 2003, *ApJ* **584**, 210

Gandhi, P., Crawford, C. S., Fabian, A. C., and Johnstone, R. M.: 2004, *MNRAS* **348**, 529

Gebhardt, K., Bender, R., Bower, G., Dressler, A., Faber, S. M., Filippenko, A. V., Green, R., Grillmair, C., Ho, L. C., Kormendy, J., Lauer, T. R., Magorrian, J., Pinkney, J., Richstone, D., and Tremaine, S.: 2000, *ApJ* **539**, L13

Gebhardt, K., Lauer, T. R., Kormendy, J., Pinkney, J., Bower, G. A., Green, R., Gull, T., Hutchings, J. B., Kaiser, M. E., Nelson, C. H., Richstone, D., and Weistrop, D.: 2001, *AJ* **122**, 2469

Gehrels, N.: 1986, *ApJ* **303**, 336

Gilli, R., Daddi, E., Zamorani, G., Tozzi, P., Borgani, S., Bergeron, J., Giacconi, R., Hasinger, G., Mainieri, V., Norman, C., Rosati, P., Szokoly, G., and Zheng, W.: 2005, *A&A* **430**, 811

Gioia, I. M. and Luppino, G. A.: 1994, *ApJS* **94**, 583

Gioia, I. M., Shaya, E. J., Le Fevre, O., Falco, E. E., Luppino, G. A., and Hammer, F.: 1998, *ApJ* **497**, 573

Goto, T., Sekiguchi, M., Nichol, R. C., Bahcall, N. A., Kim, R. S. J., Annis, J., Ivezić, Ž., Brinkmann, J., Hennessy, G. S., Szokoly, G. P., and Tucker, D. L.: 2002, *AJ* **123**, 1807

Gray, M. E., Taylor, A. N., Meisenheimer, K., Dye, S., Wolf, C., and Thommes, E.: 2002, *ApJ* **568**, 141

Gray, M. E., Wolf, C., Meisenheimer, K., Taylor, A., Dye, S., Borch, A., and Kleinheinrich, M.: 2004, *MNRAS* **347**, L73

Green, P. J., Silverman, J. D., Cameron, R. A., Kim, D.-W., Wilkes, B. J., Barkhouse, W. A., LaCluyzé, A., Morris, D., Mossman, A., Ghosh, H., Grimes, J. P., Jannuzi, B. T., Tananbaum, H., Aldcroft, T. L., Baldwin, J. A., Chaffee, F. H., Dey, A., Dosaj, A., Evans, N. R., Fan, X., Foltz, C., Gaetz, T., Hooper, E. J., Kashyap, V. L., Mathur, S., McGarry, M. B., Romero-Colmenero, E., Smith, M. G., Smith, P. S., Smith, R. C., Torres, G., Vikhlinin, A., and Wik, D. R.: 2004, *ApJS* **150**, 43

Grogin, N. A., Conselice, C. J., Chatzichristou, E., Alexander, D. M., Bauer, F. E., Hornschemeier, A. E., Jogee, S., Koekemoer, A. M., Laidler, V. G., Livio, M., Lucas, R. A., Paolillo, M., Ravindranath, S., Schreier, E. J., Simmons, B. D., and Urry, C. M.: 2005, *ApJ* **627**, L97

Grupe, D., Thomas, H.-C., and Beuermann, K.: 2001, *A&A* **367**, 470

Henry, J. P. and Briel, U. G.: 1991, *A&A* **246**, L14

Henry, J. P., Gioia, I. M., Mullis, C. R., Clowe, D. I., Luppino, G. A., Boehringer, H., Briel, U. G., Voges, W., and Huchra, J. P.: 1997, *AJ* **114**, 1293

Hewitt, A. and Burbidge, G.: 1991, *ApJS* **75**, 297

Ho, L. C.: 1999, *ApJ* **516**, 672

Ho, L. C., Filippenko, A. V., and Sargent, W. L. W.: 1997a, *ApJS* **112**, 315

Ho, L. C., Filippenko, A. V., and Sargent, W. L. W.: 1997b, *ApJ* **487**, 591

Holden, B. P., Stanford, S. A., Squires, G. K., Rosati, P., Tozzi, P., Eisenhardt, P., and Spinrad, H.: 2002, *AJ* **124**, 33

Hopkins, A. M., Miller, C. J., Nichol, R. C., Connolly, A. J., Bernardi, M., Gómez, P. L., Goto, T., Tremonti, C. A., Brinkmann, J., Ivezić, Ž., and Lamb, D. Q.: 2003, *ApJ* **599**, 971

Huchra, J. and Burg, R.: 1992, *ApJ* **393**, 90

Iono, D., Yun, M. S., and Mihos, J. C.: 2004, *ApJ* **616**, 199

Johnson, O., Best, P. N., and Almaini, O.: 2003, *MNRAS* **343**, 924

Jones, L. R., Ponman, T. J., Horton, A., Babul, A., Ebeling, H., and Burke, D. J.: 2003, *MNRAS* **343**, 627

Kaiser, N.: 1986, *MNRAS* **222**, 323

Kauffmann, G., Heckman, T. M., Tremonti, C., Brinchmann, J., Charlot, S., White, S. D. M., Ridgway, S. E., Brinkmann, J., Fukugita, M., Hall, P. B., Ivezić, Ž., Richards, G. T., and Schneider, D. P.: 2003, *MNRAS* **346**, 1055

Kauffmann, G., White, S. D. M., Heckman, T. M., Ménard, B., Brinchmann, J., Charlot, S., Tremonti, C., and Brinkmann, J.: 2004, *MNRAS* **353**, 713

Kim, D.-W., Cameron, R. A., Drake, J. J., Evans, N. R., Freeman, P., Gaetz, T. J., Ghosh, H., Green, P. J., Harnden, F. R., Karovska, M., Kashyap, V., Maksym, P. W., Ratzlaff, P. W., Schlegel, E. M., Silverman, J. D., Tananbaum, H. D., Vikhlinin, A. A., Wilkes, B. J., and Grimes, J. P.: 2004a, *ApJS* **150**, 19

Kim, D.-W., Wilkes, B. J., Green, P. J., Cameron, R. A., Drake, J. J., Evans, N. R., Freeman, P., Gaetz, T. J., Ghosh, H., Harnden, F. R., Karovska, M., Kashyap, V., Maksym, P. W., Ratzlaff, P. W., Schlegel, E. M., Silverman, J. D., Tananbaum, H. D., and Vikhlinin, A. A.: 2004b, *ApJ* **600**, 59

King, I. R.: 1972, *ApJ* **174**, L123+

Kirhakos, S., Bahcall, J. N., Schneider, D. P., and Kristian, J.: 1999, *ApJ* **520**, 67

Knapen, J. H., Shlosman, I., and Peletier, R. F.: 2000, *ApJ* **529**, 93

Kodama, T. and Smail, I.: 2001, *MNRAS* **326**, 637

Kotov, O. and Vikhlinin, A.: 2005, *ApJ* **633**, 781

Lamareille, F., Mouhcine, M., Contini, T., Lewis, I., and Maddox, S.: 2004, *MNRAS* **350**, 396

LaRoque, S. J., Joy, M., Carlstrom, J. E., Ebeling, H., Bonamente, M., Dawson, K. S., Edge, A., Holzapfel, W. L., Miller, A. D., Nagai, D., Patel, S. K., and Reese, E. D.: 2003, *ApJ* **583**, 559

Laurikainen, E., Salo, H., and Buta, R.: 2004, *ApJ* **607**, 103

Lazzati, D., Campana, S., Rosati, P., Chincarini, G., and Giacconi, R.: 1998, *A&A* **331**, 41

Ledlow, M. J. and Owen, F. N.: 1996, *AJ* **112**, 9

Lewis, I., Balogh, M., De Propris, R., Couch, W., Bower, R., Offer, A., Bland-Hawthorn, J., Baldry, I. K., Baugh, C., Bridges, T., Cannon, R., Cole, S., Colless, M., Collins, C., Cross, N., Dalton, G., Driver, S. P., Efstathiou, G., Ellis, R. S., Frenk, C. S., Glazebrook, K., Hawkins, E., Jackson, C., Lahav, O., Lumsden, S., Maddox, S., Madgwick, D., Norberg, P., Peacock, J. A., Percival, W., Peterson, B. A., Sutherland, W., and Taylor, K.: 2002, *MNRAS* **334**, 673

Liang, H., Lémonon, L., Valtchanov, I., Pierre, M., and Soucail, G.: 2000, *A&A* **363**, 440

Lira, P., Lawrence, A., and Johnson, R. A.: 2000, *MNRAS* **319**, 17

Magorrian, J., Tremaine, S., Richstone, D., Bender, R., Bower, G., Dressler, A., Faber, S. M., Gebhardt, K., Green, R., Grillmair, C., Kormendy, J., and Lauer, T.: 1998, *AJ* **115**, 2285

Mahdavi, A. and Geller, M. J.: 2001, *ApJ* **554**, L129

Maia, M. A. G., Willmer, C. N. A., Rossetto, B. M., and Machado, R. S.: 2004, in *IAU Symposium*, pp 435–438

Mainieri, V., Bergeron, J., Hasinger, G., Lehmann, I., Rosati, P., Schmidt, M., Szokoly, G., and Della Ceca, R.: 2002, *A&A* **393**, 425

Malzac, J., Jourdain, E., Petrucci, P. O., and Henri, G.: 1998, *A&A* **336**, 807

Manners, J. C.: 2002, *Ph.D. thesis*, University of Edinburgh

Manners, J. C., Johnson, O., Almaini, O., Willott, C. J., Gonzalez-Solares, E., Lawrence, A., Mann, R. G., Perez-Fournon, I., Dunlop, J. S., McMahon, R. G., Oliver, S. J., Rowan-Robinson, M., and Serjeant, S.: 2003, *MNRAS* **343**, 293

Maoz, D., Rix, H.-W., Gal-Yam, A., and Gould, A.: 1997, *ApJ* **486**, 75

Martin, C. L.: 1999, *ApJ* **513**, 156

Martini, P., Kelson, D. D., and Mulchaey, J. S.: 2004, *American Astronomical Society Meeting Abstracts* **205**,

Martini, P., Kelson, D. D., Mulchaey, J. S., and Trager, S. C.: 2002, *ApJ* **576**, L109

Maughan, B. J., Jones, L. R., Ebeling, H., and Scharf, C.: 2006, *MNRAS* **365**, 509

McLure, R. J. and Dunlop, J. S.: 2002, *MNRAS* **331**, 795

Mihos, J. C.: 2004, in *Clusters of Galaxies: Probes of Cosmological Structure and Galaxy Evolution*, pp 278–+

Miller, C. J., Nichol, R. C., Gómez, P. L., Hopkins, A. M., and Bernardi, M.: 2003, *ApJ* **597**, 142

Miller, N. A. and Owen, F. N.: 2003, *AJ* **125**, 2427

Molinari, E., Banzi, M., Buzzoni, A., Chincarini, G., and Pedrana, M. D.: 1994, *A&AS* **103**, 245

Molnar, S. M., Hughes, J. P., Donahue, M., and Joy, M.: 2002, *ApJ* **573**, L91

Morrison, R. and McCammon, D.: 1983, *ApJ* **270**, 119

Mulchaey, J. S. and Regan, M. W.: 1997, *ApJ* **482**, L135+

Mullis, C. R., Henry, J. P., Gioia, I. M., Böhringer, H., Briel, U. G., Voges, W., and Huchra, J. P.: 2004, *ApJ* **617**, 192

Mullis, C. R., McNamara, B. R., Quintana, H., Vikhlinin, A., Henry, J. P., Gioia, I. M., Hornstrup, A., Forman, W., and Jones, C.: 2003, *ApJ* **594**, 154

Mushotzky, R.: 2004, *How are AGN Found?*, pp 53–+, ASSL Vol. 308: Supermassive Black Holes in the Distant Universe

Myers, A. D., Outram, P. J., Shanks, T., Boyle, B. J., Croom, S. M., Loaring, N. S., Miller, L., and Smith, R. J.: 2003, *MNRAS* **342**, 467

Nandra, K., Laird, E. S., Adelberger, K., Gardner, J. P., Mushotzky, R. F., Rhodes, J., Steidel, C. C., Teplitz, H. I., and Arnaud, K. A.: 2005, *MNRAS* **356**, 568

Narayan, R., Igumenshchev, I. V., and Abramowicz, M. A.: 2000, *ApJ* **539**, 798

Navarro, J. F., Frenk, C. S., and White, S. D. M.: 1997, *ApJ* **490**, 493

Norberg, P., Cole, S., Baugh, C. M., Frenk, C. S., Baldry, I., Bland-Hawthorn, J., Bridges, T., Cannon, R., Colless, M., Collins, C., Couch, W., Cross, N. J. G., Dalton, G., De Propris, R., Driver, S. P., Efstathiou, G., Ellis, R. S., Glazebrook, K., Jackson, C., Lahav, O., Lewis, I., Lumsden, S., Maddox, S., Madgwick, D., Peacock, J. A., Peterson, B. A., Sutherland, W., and Taylor, K.: 2002, *MNRAS* **336**, 907

Oemler, A. J.: 1974, *ApJ* **194**, 1

Palunas, P., Collins, N. R., Gardner, J. P., Hill, R. S., Malumuth, E. M., Smette, A., Teplitz, H. I., Williger, G. M., and Woodgate, B. E.: 2000, *ApJ* **541**, 61

Pascarelle, S. M., Windhorst, R. A., Driver, S. P., Ostrander, E. J., and Keel, W. C.: 1996, *ApJ* **456**, L21+

Peacock, J. A.: 1983, *MNRAS* **202**, 615

Pellegrini, S.: 2005, *ApJ* **624**, 155

Pentericci, L., Kurk, J. D., Carilli, C. L., Harris, D. E., Miley, G. K., and Röttgering, H. J. A.: 2002, *A&A* **396**, 109

Pentericci, L., Kurk, J. D., Röttgering, H. J. A., Miley, G. K., van Breugel, W., Carilli, C. L., Ford, H., Heckman, T., McCarthy, P., and Moorwood, A.: 2000, *A&A* **361**, L25

Peres, C. B., Fabian, A. C., Edge, A. C., Allen, S. W., Johnstone, R. M., and White, D. A.: 1998, *MNRAS* **298**, 416

Perlman, E. S., Horner, D. J., Jones, L. R., Scharf, C. A., Ebeling, H., Wegner, G., and Malkan, M.: 2002, *ApJS* **140**, 265

Pierre, M., Oukbir, J., Dubreuil, D., Soucail, G., Sauvageot, J.-L., and Mellier, Y.: 1997, *A&AS* **124**, 283

Pizzolato, F. and Soker, N.: 2005, *ApJ* **632**, 821

Ponman, T. J., Allan, D. J., Jones, L. R., Merrifield, M., McHardy, I. M., Lehto, H. J., and Luppino, G. A.: 1994, *Nature* **369**, 462

Porciani, C., Magliocchetti, M., and Norberg, P.: 2004, *MNRAS* **355**, 1010

Postman, M., Geller, M. J., and Huchra, J. P.: 1988, *AJ* **95**, 267

Press, W. H., Teukolsky, S. A., Vettering, W. T., and Flannery, B. P.: 1992, *Numerical Recipes in C - The Art of Scientific Computing*, Chapt. 14, Cambridge University Press, second edition

Quilis, V., Moore, B., and Bower, R.: 2000, *Science* **288**, 1617

Ranalli, P., Comastri, A., and Setti, G.: 2003, *A&A* **399**, 39

Raymond, J. C. and Smith, B. W.: 1977, *ApJS* **35**, 419

Reddy, N. A. and Yun, M. S.: 2004, *ApJ* **600**, 695

Refregier, A. and Loeb, A.: 1997, *ApJ* **478**, 476

Reiprich, T. H. and Böhringer, H.: 2002, *ApJ* **567**, 716

Romer, A. K., Viana, P. T. P., Liddle, A. R., and Mann, R. G.: 2001, *ApJ* **547**, 594

Rosati, P., Borgani, S., and Norman, C.: 2002, *ARA&A* **40**, 539

Roukema, B. F. and Bajtlik, S.: 1999, *MNRAS* **308**, 309

Ruderman, J. T. and Ebeling, H.: 2005, *ApJ* **623**, L81

Rutledge, R. E., Brunner, R. J., Prince, T. A., and Lonsdale, C.: 2000, *ApJS* **131**, 335

Sánchez, S. F., Jahnke, K., Wisotzki, L., McIntosh, D. H., Bell, E. F., Barden, M., Beckwith, S. V. W., Borch, A., Caldwell, J. A. R., Häussler, B., Jogee, S., Meisenheimer, K., Peng, C. Y., Rix, H.-W., Somerville, R. S., and Wolf, C.: 2004, *ApJ* **614**, 586

Sakelliou, I., Peterson, J. R., Tamura, T., Paerels, F. B. S., Kaastra, J. S., Belsole, E., Böhringer, H., Branduardi-Raymont, G., Ferrigno, C., den Herder, J. W., Kennea, J., Mushotzky, R. F., Vestrand, W. T., and Worrall, D. M.: 2002, *A&A* **391**, 903

Sánchez, S. F., Becker, T., Garcia-Lorenzo, B., Benn, C. R., Christensen, L., Kelz, A., Jahnke, K., and Roth, M. M.: 2005, *A&A* **429**, L21

Schade, D., Barrientos, L. F., and Lopez-Cruz, O.: 1997, *ApJ* **477**, L17+

Schindler, S.: 2000, *A&AS* **142**, 433

Schindler, S., Castillo-Morales, A., De Filippis, E., Schwope, A., and Wambsganss, J.: 2001, *A&A* **376**, L27

Schindler, S., Guzzo, L., Ebeling, H., Boehringer, H., Chincarini, G., Collins, C. A., de Grandi, S., Neumann, D. M., Briel, U. G., Shaver, P., and Vettolani, G.: 1995, *A&A* **299**, L9+

Schwope, A., Hasinger, G., Lehmann, I., Schwarz, R., Brunner, H., Neizvestny, S., Ugryumov, A., Balega, Y., Trümper, J., and Voges, W.: 2000, *Astronomische Nachrichten* **321**, 1

Sheth, K., Regan, M. W., Scoville, N. Z., and Strubbe, L. E.: 2003, *ApJ* **592**, L13

Shimada, M., Ohyama, Y., Nishiura, S., Murayama, T., and Taniguchi, Y.: 2000, *AJ* **119**, 2664

Shlosman, I., Frank, J., and Begelman, M. C.: 1989, *Nature* **338**, 45

Silk, J. and Rees, M. J.: 1998, *A&A* **331**, L1

Silverman, J. D., Green, P. J., Barkhouse, W. A., Cameron, R. A., Foltz, C., Jannuzi, B. T., Kim, D.-W., Kim, M., Mossman, A., Tananbaum, H., Wilkes, B. J., Smith, M. G., Smith, R. C., and Smith, P. S.: 2005a, *ApJ* **624**, 630

Silverman, J. D., Green, P. J., Barkhouse, W. A., Kim, D.-W., Aldcroft, T. L., Cameron, R. A., Wilkes, B. J., Mossman, A., Ghosh, H., Tananbaum, H., Smith, M. G., Smith, R. C., Smith, P. S., Foltz, C., Wik, D., and Jannuzi, B. T.: 2005b, *ApJ* **618**, 123

Smail, I., Ellis, R. S., Aragon-Salamanca, A., Soucail, G., Mellier, Y., and Giraud, E.: 1993, *MNRAS* **263**, 628

Spinrad, H., Marr, J., Aguilar, L., and Djorgovski, S.: 1985, *PASP* **97**, 932

Stanford, S. A., Holden, B., Rosati, P., Eisenhardt, P. R., Stern, D., Squires, G., and Spinrad, H.: 2002, *AJ* **123**, 619

Stern, D., Holden, B., Stanford, S. A., and Spinrad, H.: 2003, *AJ* **125**, 2759

Stocke, J. T., Morris, S. L., Gioia, I. M., Maccacaro, T., Schild, R., Wolter, A., Fleming, T. A., and Henry, J. P.: 1991, *ApJS* **76**, 813

Stocke, J. T., Perlman, E. S., Gioia, I. M., and Harvanek, M.: 1999, *AJ* **117**, 1967

Stoughton, C. e.: 2002, *AJ* **123**, 485

Streblyanska, A., Hasinger, G., Finoguenov, A., Barcons, X., Mateos, S., and Fabian, A. C.: 2005, *A&A* **432**, 395

Struble, M. F. and Rood, H. J.: 1999, *ApJS* **125**, 35

Szokoly, G. P., Bergeron, J., Hasinger, G., Lehmann, I., Kewley, L., Mainieri, V., Nonino, M., Rosati, P., Giacconi, R., Gilli, R., Gilmozzi, R., Norman, C., Romaniello, M., Schreier, E., Tozzi, P., Wang, J. X., Zheng, W., and Zirm, A.: 2004, *ApJS* **155**, 271

Taylor, A. N., Bacon, D. J., Gray, M. E., Wolf, C., Meisenheimer, K., Dye, S., Borch, A., Kleinheinrich, M., Kovacs, Z., and Wisotzki, L.: 2004, *MNRAS* **353**, 1176

Taylor, E. L. Mann, R. J.: 2005, *in preperation*

The CIAO detect manual (CIAO Software release V3.0.1): 2003, *CIAO detect manual (CIAO Software release V3.0.1)*

Tozzi, P., Rosati, P., Nonino, M., Bergeron, J., Borgani, S., Gilli, R., Gilmozzi, R., Hasinger, G., Grogin, N., Kewley, L., Koekemoer, A., Norman, C., Schreier, E., Szokoly, G., Wang, J. X., Zheng, W., Zirm, A., and Giacconi, R.: 2001, *ApJ* **562**, 42

Tucker, W., Blanco, P., Rappoport, S., David, L., Fabricant, D., Falco, E. E., Forman, W., Dressler, A., and Ramella, M.: 1998, *ApJ* **496**, L5+

Ueda, Y., Akiyama, M., Ohta, K., and Miyaji, T.: 2003, *ApJ* **598**, 886

Véron-Cetty, M.-P. and Véron, P.: 2001, *A&A* **374**, 92

Valtchanov, I., Pierre, M., Willis, J., Dos Santos, S., Jones, L., Andreon, S., Adami, C., Altieri, B., Bolzonella, M., Bremer, M., Duc, P.-A., Gosset, E., Jean, C., and Surdej, J.: 2004, *A&A* **423**, 75

van Dokkum, P. G., Franx, M., Fabricant, D., Kelson, D. D., and Illingworth, G. D.: 1999, *ApJ* **520**, L95

van Dokkum, P. G., Franx, M., Kelson, D. D., Illingworth, G. D., Fisher, D., and Fabricant, D.: 1998, *ApJ* **500**, 714

van Dokkum, P. G. and Stanford, S. A.: 2003, *ApJ* **585**, 78

Vikhlinin, A., McNamara, B. R., Forman, W., Jones, C., Quintana, H., and Hornstrup, A.: 1998, *ApJ* **502**, 558

Virani, S. N., Treister, E., and Urry, C. M.: 2005, *ApJ, in press (astro-ph/0506551)*

Voit, G. M. and Donahue, M.: 2005, *ApJ* **634**, 955

Wake, D. A., Collins, C. A., Nichol, R. C., Jones, L. R., and Burke, D. J.: 2005, *ApJ* **627**, 186

Wei, J. Y., Xu, D. W., Dong, X. Y., and Hu, J. Y.: 1999, *A&AS* **139**, 575

White, D. A.: 2000, *MNRAS* **312**, 663

Willick, J. A., Thompson, K. L., Mathiesen, B. F., Perlmutter, S., Knop, R. A., and Hill, G. J.: 2001, *PASP* **113**, 658

Wolf, C., Gray, M. E., and Meisenheimer, K.: 2005, *astroph/0506150*

Wolf, C., Meisenheimer, K., Kleinheinrich, M., Borch, A., Dye, S., Gray, M., Wisotzki, L., Bell, E. F., Rix, H.-W., Cimatti, A., Hasinger, G., and Szokoly, G.: 2004, *A&A* **421**, 913

Wolf, C., Meisenheimer, K., Rix, H.-W., Borch, A., Dye, S., and Kleinheinrich, M.: 2003, *A&A* **401**, 73

Xue, Y. and Wu, X.: 2000, *ApJ* **538**, 65

Yang, Y., Mushotzky, R. F., Barger, A. J., Cowie, L. L., Sanders, D. B., and Steffen, A. T.: 2003, *ApJ* **585**, L85

Yang, Y., Mushotzky, R. F., Steffen, A. T., Barger, A. J., and Cowie, L. L.: 2004, *AJ* **128**, 1501

Yee, H. K. C., Ellingson, E., Abraham, R. G., Gravel, P., Carlberg, R. G., Smecker-Hane, T. A., Schade, D., and Rigler, M.: 1996, *ApJS* **102**, 289